THREE-DIMENSIONAL ANALYSIS OF SLOPES

by

AMR SAYED AZZOUZ

BS, Cairo University
Cairo, Egypt
(1970)
MS, Northwestern University
Evanston, Illinois
(1974)

SUBMITTED IN PARTIAL FULFILLMENT
OF THE REQUIREMENTS FOR THE
DEGREE OF

DOCTOR OF SCIENCE

at the

MASSACHUSETTS INSTITUTE OF TECHNOLOGY

December, 1977
(i.e. February, 1978)

Signature of Author .....
Department of Civil Engineering, December, 1977

Certified by .....
Thesis Supervisor

Accepted by.....
Chairman, Department Committee on Graduate Students
of the Department of Civil Engineering

Archives

MAR 31 1978

LIBRARIES

THREE-DIMENSIONAL ANALYSIS OF SLOPES

by

AMR SAYED AZZOUZ

Submitted to the Department of Civil Engineering on December 13, 1977, in partial fulfillment of the requirements for the degree of Doctor of Science.

ABSTRACT

This thesis investigates the three-dimensional stability of slopes. The classical circular arc method of analysis is extended to three-dimensional problems by considering failures with finite lengths along shear surfaces of revolution. A computer program (STAB3D) is developed to evaluate the three-dimensional factor of safety of slopes.

Results of analyses are presented in the form of charts which illustrate the importance of different factors on stability and can be used for the design of slopes with a uniform cross section in the following cases:

1. the undrained stability of: a - homogeneous slopes which may exhibit an anisotropic shear strength; b - slopes with homogeneous cross sections and a variable strength along their axis; and c - homogeneous slopes with isotropic strength subjected to surcharge loads;
2. the drained stability of homogeneous slopes.

Four case studies of embankments rapidly loaded to failure on saturated clay foundations are thoroughly analyzed. The three-dimensional factor of safety, which accounts for strength anisotropy and strain compatibility along the shear surface, is compared to the actual value of unity at failure. Conclusions regarding the selection of an adequate shear strength for stability computations on clay foundations are derived. A new correction factor for field vane shear strength data is obtained from the above four case studies and from fourteen additional embankment failures. This correction factor includes three-dimensional effects and is about 10% lower than that recommended by Bjerrum (1972).

Thesis Supervisor: Mohsen M. Baligh

Title: Associate Professor of Civil Engineering

ACKNOWLEDGEMENTS

I wish to thank Professor Mohsen M. Baligh for suggesting and developing the basic concepts of this research, and for the inspiration, encouragement and friendship he has supplied me with for the past three years. His personable manner and guidance have made my experience at MIT most useful, rewarding, and memorable.

I also wish to thank Professor Charles C. Ladd for his invaluable suggestions and constructive criticisms regarding this thesis, as well as for his willingness to share his widespread knowledge on soil behavior.

Special thanks are due to Professor Gregory B. Baecher for his helpful discussions regarding Chapter 7, and Mr. Walter Steiner, the author's colleague, for his assistance in performing the work in Chapter 6.

Important suggestions regarding this research were also received from the author's colleagues including Messrs: Jacques N. Levadoux and Vitoon Vivatrat. I wish to sincerely thank Jacques N. Levadoux for the immense amount of time he sacrificed during the final preparation of this thesis.

This thesis is dedicated to my wife, Moushira, and my parents, without whose support, encouragement, and patience, my graduate work would not have been possible.

TABLE OF CONTENTS

	PAGE NO.
TITLE PAGE	1
ABSTRACT	2
ACKNOWLEDGEMENTS	3
TABLE OF CONTENTS	4
LIST OF TABLES	9
LIST OF FIGURES	11
NOTATION	17
CHAPTER 1: INTRODUCTION	23
CHAPTER 2: THREE-DIMENSIONAL MODEL	28
2.1 MECHANISM OF SLOPE STABILITY	28
2.1.1 Two-Dimensional Problems	28
2.1.2 Three-Dimensional Problems	32
2.2 SHEAR SURFACES OF REVOLUTION	37
2.2.1 Cone Attached to a Cylinder	37
2.2.2 Ellipsoid Attached to a Cylinder	39
CHAPTER 3: UNDRAINED STABILITY OF HOMOGENEOUS SLOPES	41
3.1 UNDRAINED STABILITY OF A VERTICAL CUT	42
3.1.1 Closed-Form Solutions	42
3.1.2 Numerical Solutions	47
3.2 UNDRAINED STABILITY OF HOMOGENEOUS SLOPES	52
3.3 SUMMARY AND CONCLUSIONS	57
CHAPTER 4: UNDRAINED STABILITY OF HOMOGENEOUS SLOPES SUBJECTED TO SURCHARGE LOADS	59

PAGE NO.

4.1 INTRODUCTION 59

4.2 BACKGROUND OF RELATED WORK 62

4.2.1 Two-Dimensional Solutions 62

Janbu's Analysis 62
Meyerhof's Analysis 65
Bowles' Analysis 68
The Modified Bowles' Analysis . . . 70

4.2.2 Three-Dimensional Solutions 73

Brinch Hansen's Analysis 73
Giger and Krizek Analysis 76

4.3 PLANE STRAIN PROBLEMS 80

4.3.1 Vertical Line Loads of Infinite Extent 80

4.3.2 Uniform Vertical Strip Loads 88

4.4 THREE-DIMENSIONAL PROBLEMS 93

4.4.1 Line Loads of Finite Length 93

4.4.2 Square Loaded Areas 98

4.5 METHODOLOGY EVALUATION 103

4.5.1 Evaluation of Two-Dimensional Methods 103

4.5.2 Evaluation of Three-Dimensional Methods 106

4.6 SUMMARY AND CONCLUSIONS 112

CHAPTER 5: UNDRAINED STABILITY OF HOMOGENEOUS SLOPES WITH ANISOTROPIC STRENGTH 117

5.1 STRENGTH ANISOTROPY MODELS 124

5.2 TWO-DIMENSIONAL ANALYSIS OF HOMOGENEOUS SLOPES 131

5.3 THREE-DIMENSIONAL ANALYSIS OF HOMOGENEOUS SLOPES 138

PAGE NO.

5.4 SUMMARY AND CONCLUSIONS 144

CHAPTER 6: DRAINED STABILITY OF HOMOGENEOUS SLOPES 145

6.1 THE ORDINARY METHOD OF SLICES 148

6.2 THE M.I.T. METHOD 152

6.3 DRAINED STABILITY OF HOMOGENEOUS SLOPES . . . 157

6.3.1 Two-Dimensional Analysis 158

6.3.2 Three-Dimensional Analysis 161

6.4 SUMMARY AND CONCLUSIONS 167

CHAPTER 7: LENGTH OF FAILURE 171

7.1 MODELS FOR STRENGTH VARIABILITY 173

7.2 UNDRAINED STABILITY OF A VERTICAL CUT 175

7.2.1 Closed-Form Solutions 175

7.2.2 Numerical Solutions 178

7.3 UNDRAINED STABILITY OF HOMOGENEOUS SLOPES . . 183

7.4 LENGTH OF FAILURE-APPROXIMATE ANALYSIS . . . 186

7.4.1 Factor of Safety and Critical Failure Length 186

7.4.2 Constants α and γ 188

7.4.3 Results 188

7.4.4 Design Methodology 193

7.5 LENGTH OF FAILURE - A PROBABILISTIC APPROACH 195

7.5.1 Probabilistic Model 196

7.5.2 Reduction Factors 201

7.5.3 Risk or Probability of Failure 203

PAGE NO.

7.5.4. Results 207

7.6 SUMMARY AND CONCLUSIONS 213

CHAPTER 8: CASE STUDIES 217

8.1 I-95 EMBANKMENT, SAUGUS, MASSACHUSETTS . . . 219

8.1.1 Description of the Site 219

8.1.2 Failure 222

8.1.3 Soil Properties 222

8.1.4 Stability Analyses 236

8.1.5 Summary and Conclusions for the I-95 Failure 252

8.2 EXPERIMENTAL TEST SECTION, PORTSMOUTH, NEW HAMPSHIRE 256

8.2.1 Site Description 256

8.2.2 The Failure 256

8.2.3 Determination of the Soil Properties . 259

8.2.4 Stability Analyses 266

8.2.5 Summary and Conclusions for the ETS, PORTSMOUTH, N.H. 278

8.3 NEW LISKEARD EMBANKMENT FAILURE, NEW LISKEARD, CANADA 282

8.3.1 Site Description 282

8.3.2 Failure 282

8.3.3 Soil Properties 285

8.3.4 Stability Analyses 292

8.3.5 Summary and Conclusions for the New Liskeard Case Study 304

8.4 FORE RIVER TEST SECTION, PORTLAND, MAINE 307

PAGE NO.

8.4.1 Site Description 307

8.4.2 The Failure 307

8.4.3 Soil Properties 309

8.4.4 Stability Analyses 311

8.4.5 Summary and Conclusions for the FRT Case Study 316

8.5 DESIGN OF EMBANKMENTS USING THE FIELD VANE STRENGTH 319

8.6 SUMMARY AND CONCLUSIONS 326

CHAPTER 9: SUMMARY AND CONCLUSIONS 330

REFERENCES 342

BIOGRAPHY 350

APPENDIX A: COMPUTER PROGRAM STAB3D 352

A-1 USER'S MANUAL 354

LIST OF TABLES

Table No.	Title	Page
4.1	Equations and Unknowns Associated with Bowles' Analysis (1975).	71
4.2	Methods for Estimating the Undrained Ultimate Pressure of Footings on Slopes.	79
4.3	Critical Values of Stability Number, $(\gamma H/c)_{cr}$ (after Taylor 1937).	82
4.4	Comparison of Predictions according to Different Methods.	107
5.1	Undrained Strength Anisotropy of Normally Consolidated Clays (from Ladd et al., 1977).	121
6.1	Results of Two-Dimensional Drained Stability Analysis.	159
7.1	Constants α and γ in the Equation $F = [1+\alpha(2L/DR)^{\gamma}]F_0$	189
8.1	Undrained Strength Ratio vs. OCR for Boston Blue Clay.	228
8.2	Strain Compatibility Effects for Boston Blue Clay.	232
8.3	Undrained Strength Ratios Corrected for Strain Compatibility for Boston Blue Clay.	234
8.4	STAB3D Input Parameters Utilizing the Field Vane Strength Model for Boston Blue Clay, I-95, Station 263.	242
8.5	SHANSEP-$S_u(\theta)$ Undrained Strength for Boston Blue Clay, I-95, Station 263.	244
8.6	STAB3D Input Parameters Utilizing the SHANSEP-$S_u(\theta)$ Strength Model for Boston Blue Clay, I-95 Station 263.	246
8.7	Undrained Shear Strength Ratios for the Portsmouth Clay, N.H.	265
8.8	STAB3D Input Parameters Utilizing the Field Vane Strength Model for Portsmouth Clay.	268

Table No.	Title	Page
8.9	SHANSEP-$S_u(\theta)$ Undrained Strength for Portsmouth Clay.	271
8.10	STAB3D Input Parameters Utilizing the SHANSEP-$S_u(\theta)$ Strength Model for Portsmouth Clay.	273
8.11	Summary of Plane Strain Stability Analysis of the ETS, N.H.	275
8.12	STAB3D Input Parameters Utilizing the Field Vane Strength Model for New Liskeard Varved Clay.	295
8.13	SHANSEP-$S_u(\theta)$ Undrained Strength for New Liskeard Varved Clay Based on the Minimum $\bar{\sigma}_{vm}$ Profile.	298
8.14	STAB3D Input Parameters Utilizing the SHANSEP-$S_u(\theta)$ for New Liskeard Varved Clay.	300
8.15	SHANSEP-DSS Undrained Strength for Maine Organic Clay, Me.	313
8.16	STAB3D Input Parameters for Maine Organic Clay.	314
8.17	Field Vane Correction Factors.	322
8.18	Summary of Case Studies.	327

LIST OF FIGURES

Figure	Title	Page
2.1	Typical Slope Failure	30
2.2	Failure Surfaces in Three-Dimensional Slope Stability	33
3.1	Stability of a Vertical Cut	43
3.2	End Effects on the Stability of a Vertical Cut	48
3.3	Plan View of the Failure Surfaces for a Vertical Cut	50
3.4	End Effects on the Stability of Homogeneous Isotropic Slopes	54
4.1	Problems Description	61
4.2	Janbu's Analysis	64
4.3	Meyerhof's Analysis	67
4.4	Bowles' Analysis	69
4.5	The Modified Bowles' Analysis	72
4.6	Brinch Hansen's Analysis	74
4.7	Giger's and Krizek's Analysis	77
4.8	Stability Charts for Line Loads of Infinite Extent	84
4.9	Effect of Bedrock Location for Line Loads of Infinite Extent	87
4.10	Stability Charts for a Uniform Strip Load	90
4.11	Three-Dimensional Failure Surfaces	94
4.12	End Effects for Line Loads of Finite Length ($A/H \geq 0.5$)	96
4.13	End Effects for Line Loads of Finite Length ($A/H \leq 0.5$)	97
4.14	End Effects for Square Loaded Areas	100
4.15	Critical Concentrated Load Causing Failure Along a Conical Surface	109

Figure	Title	Page
4.16	Concentrated Load Causing Failure of a Vertical Cut in Frictionless Soil	110
4.17	Prediction Method of the Ultimate Surcharge Load	116
5.1	Definition of Strength Variation with Direction in Two-Dimensional Problems	118
5.2	State of Stress Along a Typical Failure Circle	123
5.3	Elliptic Strength Plots	127
5.4	Strength as a Function of Orientation for Two Normally Consolidated Clays	130
5.5	Definition of Geometric Parameters of a Typical Failure Circle	132
5.6	Effect of Strength Anisotropy on the Toe Failure of Homogeneous Slopes	136
5.7	Definition of Strength Variation with Direction in Three-Dimensional Problems	139
5.8	Definition of Geometric Parameters of a Typical Three-Dimensional Failure Surface	141
5.9	End Effects on the Stability of a Vertical Cut with Anisotropic Strength	143
6.1	Three-Dimensional Failure of a Prismatic Slope	147
6.2	Influence of Base Inclination of Slices in Two-Dimensional Slope Stability Analysis	151
6.3	Results of the Drained Stability Analysis of Homogeneous Slopes According to the Ordinary Method of Slices	163
6.4	Results of the Drained Stability Analysis of Homogeneous Slopes According to the MIT Method	165
7.1	Models for the Variation of Shear Strength Along the Longitudinal Axis of Embankments	174
7.2	End Effects on the Stability of a Vertical Cut with Non-uniform Shear Strength Along the Longitudinal Axis (Conical Shear Surface)	179

Figure	Title	Page
7.3	End Effects on the Stability of a Vertical Cut with Non-uniform Shear Strength Along the Longitudinal Axis (Ellipsoidal Shear Surface)	181
7.4	End Effects on the Stability of Slopes with Homogeneous Cross Sections and Non-uniform Shear Strength Along Their Axis	184
7.5	Average Strength Along Length 2L of an Embankment (Centered at z = 0)	187
7.6	A Comparison Between the Results of the Approximate Analysis, Eq. 7.27, and Results from STAB3D	191
7.7	Minimum Safety Factors and Critical Failure Lengths for Slopes with Homogeneous Cross Sections and Non-uniform Shear Strength Along Their Axis	192
7.8	Sinusoidal Probability Distribution Model	199
7.9	Reduction Factors Describing the Strength Variability	202
7.10	Definitions Regarding the Reliability Analysis of Embankments	206
7.11	Relationship between the Probability of Failure and the Reliability Index	208
7.12	Results of the Probabilistic Analysis of Toe Failures of Slopes with Homogeneous Cross Sections	210
7.13	Results of the Probabilistic Analysis of Base Failures of Slopes with Homogeneous Cross Sections	211
8.1	Location Map, I-95 (From Silva, 1975).	220
8.2	Cross Section of the I-95 Embankment at Station 263	221
8.3	Field Vane Strength, I-95, Station 263	224
8.4	Evaluation of Existing Stresses August 1974,I-95, Station 263 Centerline to 35 Feet East (from Ladd, 1975b)	225

Figure	Title	Page
8.5	Initial Stress History, I-95, Station 263	227
8.6	Stress-Strain Curves from $\overline{CK_oU}$ Tests on Normally Consolidated Boston Blue Clay	230
8.7	Stress-Strain Curves from $\overline{CK_oU}$ Tests on Boston Blue Clay at OCR = 4	231
8.8	Interpretation of the $\overline{CK_oU}$DSS Test Results for the Normally Consolidated Boston Blue Clay	237
8.9	Interpretation of the $\overline{CK_oU}$DSS Test Results for Boston Blue Clay at OCR = 2	238
8.10	Normalized Polar Strength Plots for Boston Blue Clay	239
8.11	Anisotropic Undrained Strength Parameters for Boston Blue Clay	240
8.12	Field Vane Total Stress Stability Analysis, I-95 Station 263	241
8.13	SHANSEP-$S_u(\theta)$ Undrained Strength for Boston Blue Clay, I-95, Station 263	245
8.14	Results of Two-Dimensional Stability Analysis Utilizing the SHANSEP-$S_u(\theta)$ Strength Model, I-95 Station 263	247
8.15	Three-Dimensional Effects for the I-95 Embankment, Station 263	250
8.16	Effect of the Longitudinal Stress on the Stability of the I-95 Embankment, Station 263	253
8.17	Cross Section Through Centerline of Experimental Test Section Looking North (from Ladd, 1972)	257
8.18	Plan of Experimental Test Section Showing Location of Instrumentation and Mode of Failure (from Ladd, 1972)	258
8.19	Soil Profile, Index Properties and Field Vane Strengths at Experimental Test Section (from Ladd, 1972)	260
8.20	Stress History at Experimental Test Section (after Ladd, 1972)	262

Figure	Title	Page
8.21	Decrease in Strength with Rebound for Boston Blue Clay	264
8.22	Anisotropic Undrained Strength Parameters for Portsmouth Clay, N.H.	267
8.23	Field Vane Total Stress Stability Analysis at the Experimental Test Section, N.H.	269
8.24	SHANSEP-$S_u(\theta)$ Undrained Strength for Portsmouth Clay, N.H.	272
8.25	Results of Two-Dimensional Stability Analysis Utilizing the SHANSEP-$S_u(\theta)$ Strength Model, Experimental Test Section, N.H.	274
8.26	Three-dimensional Effects for the Experimental Test Section, N.H.	277
8.27	Determination of the Cylinder Length for the Experimental Test Section, N.H.	279
8.28	Project Location (from Lacasse et al., 1977)	283
8.29	Description of Project and Soil Conditions (from Lacasse et al., 1977)	284
8.30	Plan of Test Section and Failure Area (from Lacasse et al., 1977)	286
8.31	Maximum Past Pressures from Oedometer Tests (from Lacasse et al., 1977)	288
8.32	Average Field Vane Strength in Failure Area (from Lacasse and Ladd, 1973)	289
8.33	Interpretation of the $\overline{CK_0U}$DSS Test Results for the Normally Consolidated New Liskeard Varved Clay	293
8.34	Normalized Polar Strength Plot for the Normally Consolidated New Liskeard Varved Clay	294
8.35	Field Vane Total Stress Stability Analysis, New Liskeard Embankment	296
8.36	SHANSEP-$S_u(\theta)$ Undrained Shear Strength for the New Liskeard Varved Clay	299

Figure	Title	Page
8.37	Results of Two-Dimensional Stability Analysis Utilizing the SHANSEP-$S_u(\theta)$ Model, New Liskeard Embankment	302
8.38	Three-Dimensional Effects for the New Liskeard Embankment	303
8.39	Plan of Fore River Test Section (from Ladd et al., 1969)	308
8.40	Soil Properties of the Maine Organic Clay (from Ladd et al., 1969)	310
8.41	Anisotropic Shear Strength Parameters for the Maine Organic Clay	312
8.42	Results of Two-Dimensional Stability Analyses, Fore River Test Section	315
8.43	Three-Dimensional Effects for the Fore River Test Section	317
8.44	Field Vane Correction Factor	320
8.45	The Use of the Field Vane Strength in the Design of Embankments	324
A.1	Pore Pressure Specification in STAB3D	357

NOTATION

A	edge distance from the crest of the slope
a	average undrained shear strength = $0.5[q_f(V) + q_f(H)]$
$\bar{a}$	average undrained shear strength adjusted for strain compatibility = $0.5[\tau_{ff}(V) + \tau_{ff}(H)]$
a*,b*	decaying parameters of the strength variability reduction factors
B	width of the surcharge load
b/a	axes of Davis-Christian elliptical strength relationship in terms of q_f
$\bar{b}/\bar{a}$	axes of Davis-Christian elliptical strength relationship in terms of τ_{ff} adjusted for strain compatibility
c,$\bar{c}$	intercept of Mohr-Coulomb failure envelope
c*	average shear strength along the axis of the embankment
$\tilde{c}$	standard deviation of the shear strength
D	depth of footing below ground surface
d	$1 - b^2/a^2$
$\bar{d}$	$1 - \bar{b}^2/\bar{a}^2$
DR	difference between the maximum and minimum radii of the shear surface
e	$(1-K_s)/(1+K_s)$
$\bar{e}$	$(1-\bar{K}_s)/(1+\bar{K}_s)$
F	three-dimensional factor of safety
F^0	plane strain factor of safety
F_{2L}	factor of safety associated with a failure length of 2L
$\bar{F}_{2L}, \tilde{F}_{2L}$	mean and standard deviation of the factor of safety associated with a failure length 2L
f	angle between the normal to the failure plane and the direction of σ_{1f}

f_L	influence ratio for expressing the three-dimensional effects
H	height of the slope
i	angle between the major principal stress at failure and the vertical direction
j,h	angles
K	ratio between the effective longitudinal stress and the effective vertical stress
K_a	active earth pressure coefficient
K_o	at-rest coefficient of earth pressure
K_p	passive earth pressure coefficient
K_s	anisotropic strength ratio = $q_f(H)/q_f(V)$
$\bar{K}_s$	anisotropic strength ratio = $\tau_{ff}(H)/\tau_{ff}(V)$
2L	total failure length
L_p	length of the surcharge
L.I.	liquidity index
$2\ell_c$	the cylinder length
ℓ_e	semi-axis of the ellipsoid shear surface
ℓ_n	cone height
M_d	three-dimensional driving moment
M_r	three-dimensional resisting moment
M_d^0	two-dimensional driving moment
M_r^0	two-dimensional resisting moment
m	amplitude of the strength variation model
$\bar{N}$	effective normal force on the base of the shear surface
$N_c, N_\gamma, \bar{N}_c, \bar{N}_\gamma$	bearing capacity coefficients
N_S, N_{Sf}	stability numbers
N_ϕ	$(1+\sin \bar{\phi})/(1-\sin \bar{\phi})$

n	parameter expressing the location of the bedrock
$\underset{\sim}{n}$	outward normal vector to the failure surface
OCR	overconsolidation ratio = $\bar{\sigma}_{vm}/\bar{\sigma}_{vo}$
$P(\cdot)$	cumulative probability
P.I.	plasticity index
$p(\cdot)$	probability density function
p	intensity of a line load of finite length
p^0	intensity of a line load of infinite length
p_{cr}	intensity of the critical line load of finite length
p^0_{cr}	intensity of the critical line load of infinite length
q	intensity of a uniform surcharge of finite length
q^0	intensity of a uniform surcharge of infinite length
q_{cr}	intensity of a uniform critical surcharge of a finite length
q_f	$0.5(\sigma_1-\sigma_3)$ at failure
q^0_{cr}	intensity of a uniform critical surcharge of an infinite length
R	radius of the shear surface
R_i	reliability index
R_{max}	maximum radius of the shear surface
r_u	pore pressure ratio
S	arc length of the failure surface
s_u	undrained shear strength = q_f or $\tau_{ff} = q_f \cos \bar{\phi}$
$s_u(H)$	s_u from horizontal loading
$s_u(i)$	s_u from loading where the angle between σ_{1f} and the vertical direction is i.
$s_u(V)$	s_u from vertical loading
$s_u(45)$	s_u from inclined (45°) loading

$s_{u\theta}$	s_u corresponding to a failure plane inclined θ to the horizontal
s_{uh}	s_u corresponding to a horizontal failure surface
s_{uv}	s_u corresponding to a vertical failure surface
s_u(DSS)	s_u from direct simple shear test
s_u(FV)	s_u from field vane test
s_u(PSC)	s_u from plane strain compression test
s_u(PSE)	s_u from plane strain extension test
T	integral of the shearing stresses acting along the shear surface
u	pore water pressure
u_f	pore water pressure at failure
W	weight of the soil mass above the failure arc
w_ℓ	liquid limit
w_n	natural water content
w_p	plastic limit
x,y,z	the x,y and z axes
β	slope angle
Γ	soil variability reduction factor
γ	total unit weight of soil
Δ	indicates an increment
δ	half the length of the strength variation model
δ^*	autocorrelation distance
θ	angle between the failure plane and the horizontal axis
λ	normalized half wave length = δ/H or δ/DR
μ	field vane correction factor based on three-dimensional factor of safety

μ^0	field vane correction factor based on two-dimensional factor of safety
ρ	angle between the tangent plane to the shear surface and the z-axis, or the cone angle
$\sigma_f, \bar{\sigma}_f$	normal stress on failure plane at failure
σ_{ij}	stress tensor
$\sigma_\ell, \bar{\sigma}_\ell$	longitudinal (out-of-plane) stress
$\sigma_N, \bar{\sigma}_N$	normal stress on shear surface
$\sigma_v, \bar{\sigma}_v$	vertical stress
$\bar{\sigma}_{vc}$	vertical consolidation stress
$\bar{\sigma}_{vo}$	initial vertical stress
$\bar{\sigma}_{vm}$	maximum past pressure
σ_x, σ_y	normal stresses in the x-y plane
$\sigma_1, \sigma_2, \sigma_3$	principal stresses
$\sigma_{1f}, \bar{\sigma}_{1f}$	major principal stress at failure
τ	shear stress
τ_h	τ on a horizontal plane (direct simple shear test)
τ_{ff}	τ on the failure plane at failure
τ_{xy}	τ in the x-y plane
$\phi, \bar{\phi}$	slope of Mohr Coulomb failure envelope

CONSOLIDATION AND STRENGTH TESTS

CRSC	constant rate of strain consolidation test
CU	consolidated-undrained shear test
$\overline{\text{CIU}}$	isotropically consolidated-undrained shear test
$\overline{\text{CIU}}$C	$\overline{\text{CIU}}$ triaxial compression test
$\overline{\text{CIU}}$E	$\overline{\text{CIU}}$ triaxial extension test
$\overline{\text{CK}_o\text{U}}$	K_o consolidated-undrained shear test

$\overline{CK_oUC}$	$\overline{CK_oU}$ triaxial compression test
$\overline{CK_oUDSS}$	$\overline{CK_oU}$ direct simple shear test
$\overline{CK_oUE}$	$\overline{CK_oU}$ triaxial extension test
$\overline{CK_oUPSC}$	$\overline{CK_oU}$ plane strain compression
$\overline{CK_oUPSE}$	$\overline{CK_oU}$ plane strain extension
UC	unconfined compression test
UU	unconsolidated-undrained shear test
UUC	UU triaxial compression test

MISCELLANEOUS

BBC	Boston Blue Clay
CVVC	Connecticut Valley Varved Clay
ETS	Experimental test section, Portsmouth, N.H.
FRT	Fore River test section, Portland, Me.
MB	Modified Bishop method of analysis
MIT	M.I.T. method of analysis
NLVC	New Liskeard Varved Clay
OMS	Ordinary Method of Slices

CHAPTER 1

INTRODUCTION

Stability is an important consideration in the design of dams, levees, breakwaters, embankments for transportation facilities, cut slopes and excavations. The result of a failure can be costly, involving the loss of property, time, and even lives. Nevertheless, the margin of safety against failure for typical earth structures and excavations is one of the lowest amongst all engineering designs. Using present analysis techniques, designs are often performed on the basis of a factor of safety of 1.5 or less, even for important and expensive structures such as high earth dams. Hence, the design of important earth structures and excavations should employ methods of stability analysis that are as realistic and accurate as possible.

Existing methods of stability analysis are based almost entirely on limit equilibrium techniques that are only applicable to plane strain conditions (Wright, 1969). Strictly speaking, for a plane strain analysis to be correct, the failure surface should extend for an infinite distance along its axis. Practically, a "reasonably long" failure makes the plane strain analysis "reasonably applicable" to what is always a three-dimensional failure. In some cases, however, the validity of a plane strain analysis is clearly inappropriate and the results involve significant errors. Examples of such problems include:

1. High dams built in narrow rock-walled valleys where the length of failure is restricted by rock abutments. A design based on a plane strain analysis of the central cross section, as often performed in practice, may be too conservative and thus uneconomical (Marsal and de Arellano, 1967 and Anagnosti, 1969).

2. Embankments having a variable cross section along their axis. The I-95 embankment failure (MIT, 1975) represents such a case. The fill that was added on a 300-ft.-long section of the embankment caused a failure which extended about 1000 ft.

3. Embankments and slopes having variable soil properties along their axis. This causes the failure to take place along one particular segment of the embankment rather than another. Realistic factors of safety and modes of failure cannot be based on either the average or the worst conditions.

4. Slopes and embankments subjected to concentrated loads or to finite loaded areas from heavy equipment, constructed facilities, etc.

5. Slopes and embankments which are curved in plan.

In contrast to the voluminous literature on plane strain stability analysis, little work has been done regarding three-dimensional problems. Sherard et al. (1963) present a method of analysis for three-dimensional problems which is specifically intended to evaluate end effects for high dams in narrow valleys. This method essentially gives a "weighted" average

of the stability of various sections of the embankment. The length of the dam is divided into a series of segments of equal length. The average cross section of each segment is analyzed as a two-dimensional problem. The factor of safety is then defined as the ratio of the sum of the resisting forces to the sum of the driving forces for all segments of dam length. Lambe and Whitman (1969) recommend a similar approximate approach for the analysis of three-dimensional problems. It consists of considering three parallel cross sections through the slope, calculating the factor of safety of each, and then computing a weighted average safety factor using the total weight above the failure surface in each cross section as the weighting factor. However, these approaches do not take into consideration the additional soil resistance resulting from the actual shape of the shear surface, and hence, they underestimate the end effects. In a recent work, Hovland (1977) presented a three-dimensional slope stability method. This method is valid for failure surfaces of general shape and assumes that all side forces are equal to zero. This assumption underestimates the frictional resistance on vertical planes and, as will be shown later, leads to unsatisfactory results.

The objective of this thesis is to investigate the three-dimensional stability of slopes. This is achieved by:

1. Developing a new analytical method to account for the mechanism of the three-dimensional stability of slopes;

2. Extending the existing two-dimensional soil behavior models to three dimensions;

3. Incorporating the new analytical method and soil behavior models into a computerized numerical procedure;

4. Performing parametric studies of the influence of end effects on slope stability and hence develop a better understanding of the different factors affecting this problem; and

5. Reevaluating case studies involving actual slope failures to check the predictive capabilities of the new method of analysis and the soil behavior models.

The three-dimensional model is presented in Chapter 2. Chapters 3 through 7 present solutions to the following problems:

1. The undrained stability of homogeneous slopes which may exhibit an anisotropic strength (Chapters 3 and 5).

2. The undrained stability of homogeneous slopes with isotropic strength subjected to surcharge loads (Chapter 4).

3. The undrained stability of slopes with homogeneous cross sections and a variable shear strength along their axis (Chapter 7).

4. The drained stability of homogeneous slopes (Chapter 6).

For each of these problems, extensions of the relevant two-dimensional soil behavior models to three-dimensions are first introduced and then the solutions are presented in the form of design charts. Chapter 8 presents the results from the analy-

sis of four case studies of embankments rapidly loaded to failure on saturated clay foundations. The major findings of this study are concluded in Chapter 9, and Appendix A gives a description of the computer program STAB3D.

CHAPTER 2

THREE-DIMENSIONAL MODEL

2.1 MECHANISM OF SLOPE STABILITY

The stability of slopes has traditionally been treated as a problem in limiting equilibrium mechanics. A condition of failure is postulated along a known (or assumed) failure surface, and the necessary shear resistance of the soil to maintain equilibrium of the resulting free body is calculated. This shear resistance is then compared to the estimated shear strength of the soil to indicate the margin of safety of the slope.

2.1.1. Two-Dimensional Problems

A number of methods for the two-dimensional analysis of slope stability which are based on limit equilibrium techniques are presently available. For a description of these methods, the reader may refer to Fellenius, 1936; Taylor, 1937; Janbu, 1954; Bishop, 1955; Lowe and Karafiath, 1960; Morgenstern and Price, 1965; Spencer, 1967; and Janbu, 1973. Wright (1969) made a comprehensive study of some of these methods and compared their merits and shortcomings.

These methods differ from one another in one or more of the following aspects:

1. The assumptions introduced to achieve statical determinancy.

2. The conditions of equilibrium which are satisfied.

3. The shape of the failure surface or the shape of the cut to be analyzed. The analysis performed herein is limited to circular arc modes of failure.

For a typical slope such as the one shown in Fig. 2.1, the circular arc method assumes that the shear surface consists of a cylinder with an infinite length. The mechanism of failure consists of a rigid body rotation of the cylinder about its axis o-$\bar{o}$ (z-axis, Fig. 2.1). If we now consider a unit length along the z-axis, the driving moment, M_d^0, and the resisting moment, M_r^0, are given by:

$$M_d^0 = W \cdot a \tag{2.1}$$

$$M_r^0 = T \cdot R_{max} \tag{2.2}$$

where,

W = weight of soil above the circular arc bd

a = moment arm of W about the cylinder axis (the z-axis)

R_{max} = radius of the cylinder

T = integral of the shearing stresses acting along the arc bd.

For soils obeying the Mohr-Coulomb yield criterion, the shear strength, τ_f, is given by:

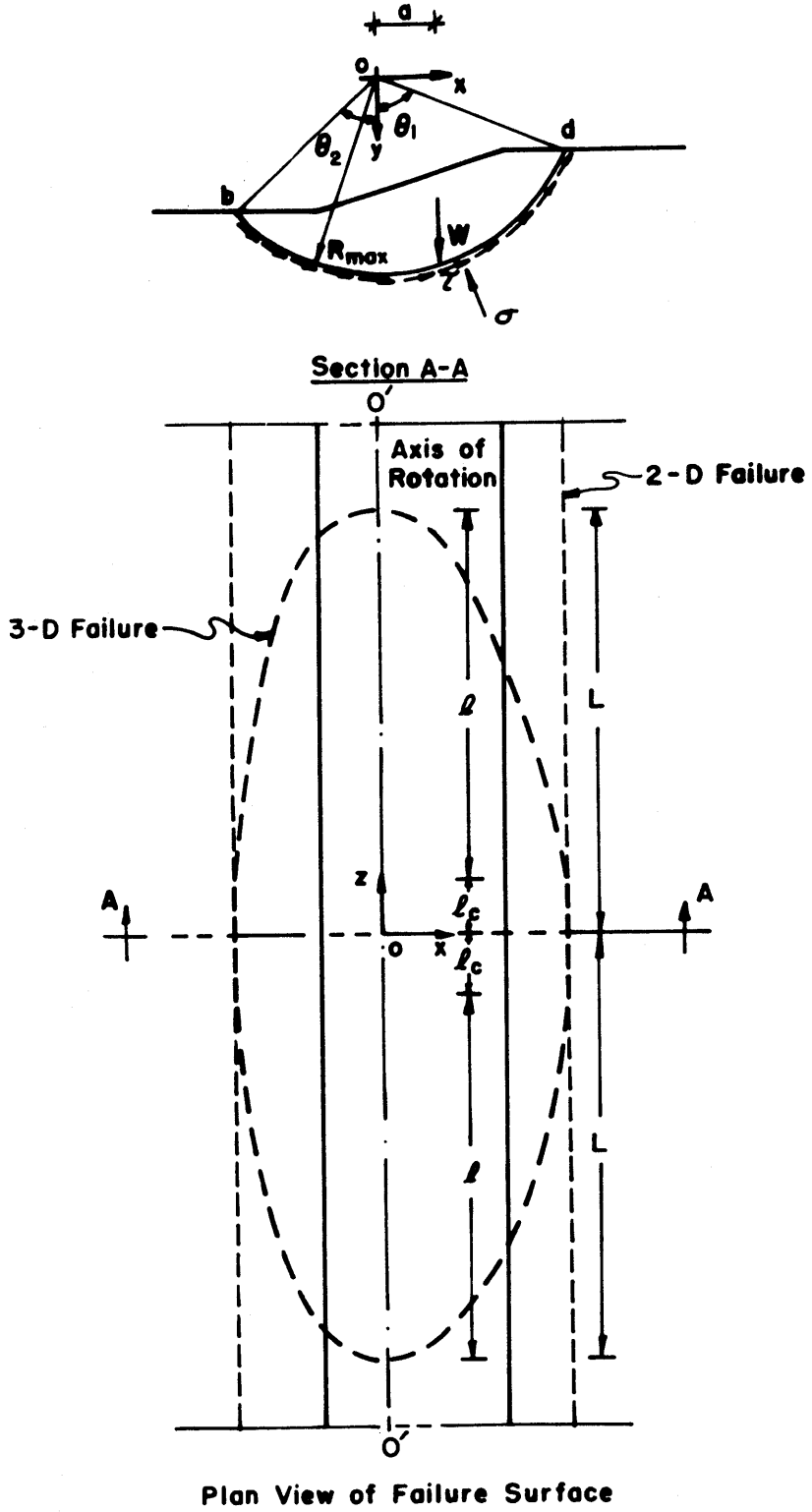


Figure 2.1 Typical Slope Failure

$$\tau_f = [\bar{c} + (\sigma_f - u_f) \tan \bar{\phi}] \qquad (2.3)$$

where,

$\bar{c}$ = the cohesion intercept in terms of effective stresses

σ_f = the total normal stress on the failure plane at failure

u_f = pore pressure at failure

$\bar{\phi}$ = angle of internal friction in terms of effective stresses

Hence, T is given by:

$$T = \int_{-\theta_1}^{\theta_2} [\bar{c} + (\sigma_f - u_f) \tan \bar{\phi}] \cdot R_{max} \cdot d\theta \qquad (2.4)$$

Substituting into Eq. (2.2), one obtains the following expression for the plane strain resisting moment:

$$M_r^0 = \int_{-\theta_1}^{\theta_2} [\bar{c} + (\sigma_f - u_f) \tan \bar{\phi}] \cdot R_{max}^2 \cdot d\theta \qquad (2.5)$$

The factor of safety against plane strain failures, F^0, is therefore given by:

$$F^0 = \frac{M_r^0}{M_d^0} = \frac{T \cdot R_{max}}{W \cdot a} \qquad (2.6)$$

Due to the complex geometry and the variety of soils existing in actual problems, the search for F^0_{min} is usually performed numerically by computer programs. Presently, no

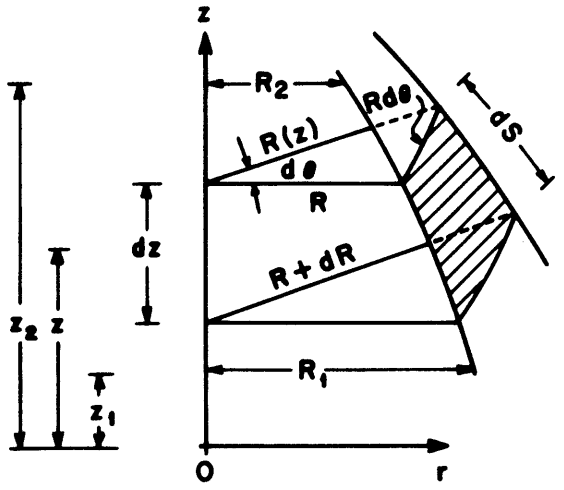
less than 25 to 50 programs for slope stability are in common use (Whitman and Bailey, 1967). Different locations of the z-axis and different values of R_{max} are assumed, and the corresponding values of F^0 are calculated according to Eq. (2.6). Repeated trials ultimately lead to the minimum value of the factor of safety, F^0_{min}, which should exceed unity for the slope to be stable.

2.1.2. Three-Dimensional Problems

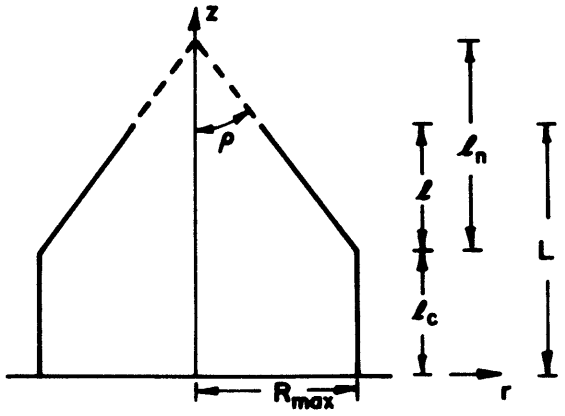
In contrast to the voluminous literature on two-dimensional slope stability, little work has been done in three dimensions (see Chapter 1). Here, we consider the basic class of three-dimensional problems, in which the geometry of a slope and the corresponding soil properties do not vary along the axis. Extensions of the technique to more general conditions can be easily made once the fundamental mechanism has been established.

Three-dimensional analysis is treated herein as an extension of the circular arc method. Whereas the basic assumptions regarding this method are retained, the shear surface is not restricted to an infinitely long cylinder, but is taken as a surface of revolution extending along the ground surface for a finite length, 2L (Fig. 2.1). The rigid body motion at failure still provides an acceptable velocity field which is necessary for obtaining upper-bound solutions.

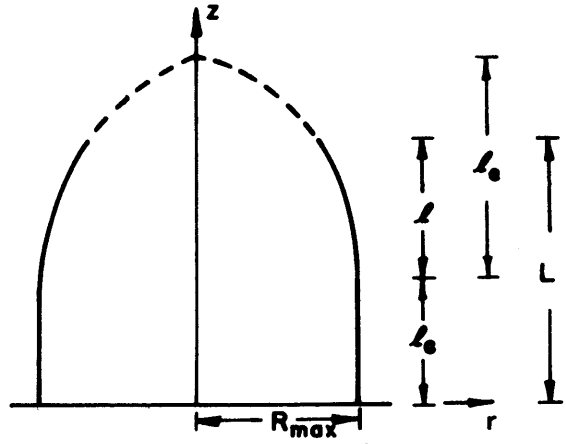
Let us consider the surface of revolution shown in Fig. 2.2a which is symmetric with respect to the plane z = 0, and



a. General Surface of Revolution



b. Cone Attached to a Cylinder



c. Ellipsoid Attached to a Cylinder

Figure 2.2 Failure Surfaces in Three-Dimensional Slope Stability

has a radius, r, varying along the z-axis, i.e.,

$$r = R(z) \tag{2.7}$$

An element of surface area, dA, is given by:

$$dA = R(z) \cdot d\theta \cdot dS \tag{2.8}$$

in which,

$$dS = dz \cdot \sqrt{1 + (dR/dz)^2} \tag{2.9}$$

substituting into Eq. (2.8), we get:

$$dA = R(z) \cdot d\theta \cdot dz \cdot \sqrt{1 + (dR/dz)^2} \tag{2.10}$$

From Eq. (2.3), the shearing force, dF, resulting from the soil resistance along the area dA is:

$$dF = [\bar{c} + (\sigma_f - u_f)\tan\bar{\phi}] \cdot dA \tag{2.11}$$

Substituting for dA from Eq. (2.10), we get:

$$dF = [\bar{c} + (\sigma_f - u_f) \tan \bar{\phi}] \cdot R(z) \cdot \sqrt{1 + (dR/dz)^2} \cdot d\theta \cdot dz \tag{2.12}$$

The resisting moment caused by the force dF is given by:

$$dM_r = [\bar{c} + (\sigma_f - u_f) \tan \bar{\phi}] \cdot R^2(z) \cdot \sqrt{1 + (dR/dz)^2} \cdot d\theta \cdot dz \tag{2.13}$$

and the total resisting moment for the segment of the shear surface between z_1 and z_2 is thus obtained by the double integral:

$$M_r = \int_{z_1}^{z_2} \int_{-\theta_1}^{\theta_2} \{\bar{c} + (\sigma_f - u_f) \tan \bar{\phi}\} \cdot R^2(z) \cdot d\theta \cdot \sqrt{1 + (dR/dz)^2} \cdot dz \qquad (2.14)$$

but, according to Eq. (2.5),

$$\int_{-\theta_1}^{\theta_2} \{\bar{c} + (\sigma_f - u_f) \tan \bar{\phi}\} \cdot R^2(z) \cdot d\theta = M_r^0(z) \qquad (2.15)$$

Hence,

$$M_r = \int_{z_1}^{z_2} M_r^0(z) \cdot \sqrt{1 + (dR/dz)^2} \cdot dz \qquad (2.16)$$

A similar treatment for the driving moment shows that:

$$M_d = \int_{z_1}^{z_2} M_d^0(z) \cdot dz \qquad (2.17)$$

Note here that $M_r^0(z)$ and $M_d^0(z)$ are functions of the coordinate z. The three-dimensional factor of safety, F, is thus given by:

$$F = \frac{M_r}{M_d} \qquad (2.18)$$

The problem is now reduced to determining:

1. The location of the axis of rotation with respect to the slope, and

2. The function R(z) which minimizes the factor of of safety given by Eq. (2.18).

The conventional two-dimensional analysis provides a good estimate of the difficulty of obtaining exact solutions to this problem. In plane strain solutions, where R_{max}, M_r^0 and M_d^0 are independent of z, the surface of revolution becomes a cylinder and Eq. (2.18) reduces to Eq. (2.6). Even under such simple conditions, the complexity of actual problems implies the use of numerical techniques rather than obtaining exact solutions. Furthermore, three-dimensional problems present the additional difficulty that the function R(z) is unknown and, to find it, the factor of safety, F, expressed by Eq. (2.18) has to be minimized. Therefore, no analytic solution will be attempted herein and instead, solutions will be obtained by the computer program STAB3D. (A complete description of STAB3D is given in Appendix A of this thesis.)

2.2 SHEAR SURFACES OF REVOLUTION

The search for the minimum factor of safety is carried out in STAB3D along the same lines of the conventional two-dimensional analysis. The location of the z-axis and the function R(z) are assumed, F is computed and the process is repeated until F_{min} is reached. Arbitrary values of the function R(z) cannot be treated in numerical computations. Instead, two classes of surfaces of revolution are considered.

2.2.1 Cone Attached to a Cylinder

The first type of shear surfaces considered herein consists of a cone attached to a cylinder (Fig. 2.2b). The cylinder has a radius, R_{max} and a length, $2\ell_c$. The cone has a height, ℓ_n, and the total failure length is equal to 2L.

The resisting and driving moments for this shear surface are the sum of the contributions of the cylinder and the cone. The cylinder resisting moment is the plane strain resisting moment (for a unit length along the axis) multiplied by the cylinder length, i.e.,

$$M_r(\text{cylinder}) = 2 \cdot M_r^0(@\ z = 0) \cdot \ell_c \qquad (2.19)$$

Similarly,

$$M_d(\text{cylinder}) = 2 \cdot M_d^0(@\ z = 0) \cdot \ell_c \qquad (2.20)$$

Fig. 2.2b illustrates the geometry of the conical surface, where the radius R along the z-axis is given by:

$$R(z) = (\ell_c + \ell_n - z) \cdot \tan \rho \text{ for } \ell_c < z \leq \ell_n + \ell_c \quad (2.21)$$

where ρ is the cone angle. Differentiating Eq. (2.21) with respect to z, one obtains:

$$\frac{dR}{dz} = - \tan \rho \quad (2.22)$$

Substituting into Eqs. (2.16) and (2.17), and noting the symmetry about the plane z = 0, one obtains the following expressions for the cone resisting and driving moments:

$$M_r(\text{cone}) = 2 \cdot \int_{z=\ell_c}^{z=\ell_c+\ell_n} M_r^0(z) \cdot \frac{dz}{\cos \rho} \quad (2.23),$$

and

$$M_d(\text{cone}) = 2 \cdot \int_{z=\ell_c}^{z=\ell_c+\ell_n} M_d^0(z) \cdot dz \quad (2.24),$$

respectively. The total resisting and driving moments are expressed by:

$$M_r = 2 \cdot \ell_c \cdot M_r^0(@\ z = 0) + 2 \cdot \int_{\ell_c}^{\ell_c+\ell_n} M_r^0(z) \cdot \frac{dz}{\cos \rho} \quad (2.25),$$

and

$$M_d = 2 \cdot \ell_c \cdot M_d^0(@\ z = 0) + 2 \cdot \int_{\ell_c}^{\ell_c+\ell_n} M_d^0(z) \cdot dz \quad (2.26)$$

respectively, and therefore, the three-dimensional factor of safety is the ratio of Eq. (2.25) to Eq. (2.26).

In order to minimize F for a conical-type shear surface, the parameters to be varied are: the z-axis location; R_{max}; ℓ_c and ℓ_n (or ρ).

2.2.2. Ellipsoid Attached to a Cylinder

The second shear surface considered consists of an ellipsoid attached to a cylinder (Fig. 2.2c). The cylinder has a radius, R_{max}, length, $2\ell_c$. The ellipsoid has a semiaxis, ℓ_e and the total failure length is 2L. An ellipsoidal-type shear surface is basically the same as the conical one. The variation of its radius along the z-axis is given by:

$$\left(\frac{z - \ell_c}{\ell_e}\right)^2 + \left(\frac{R}{R_{max}}\right)^2 = 1 \text{ for } \ell_c < z \leq \ell_e + \ell_c \tag{2.27}$$

or,

$$R = R_{max} \cdot \left[1 - \left(\frac{z - \ell_c}{\ell_e}\right)^2\right]^{\frac{1}{2}} \tag{2.28}$$

and,

$$\frac{dR}{dZ} = - \frac{R_{max}}{(\ell_e)^2} \cdot \frac{z - \ell_c}{\left[1 - \left(\frac{z - \ell_c}{\ell_e}\right)^2\right]^{\frac{1}{2}}} \tag{2.29}$$

Substituting into Eq. (2.16), the resisting moment resulting from the ellipsoidal part of the shear surface is expressed by:

$$M_r(\text{ellipse}) = 2 \cdot \int_{\ell_c}^{\ell_c+\ell_e} M_r^0(z) \cdot \left[1 + \frac{R_{max}^2 \cdot (z - \ell_c)^2}{\ell_e^4 - \left[\ell_e^2 \cdot (z - \ell_c)^2\right]}\right]^{\frac{1}{2}} \cdot dz \tag{2.30}$$

and hence, the total resisting moment is given by:

$$M_r = 2 \cdot \ell_c \cdot M_r^0(@\ z = 0) + 2 \cdot \int_{\ell_c}^{\ell_c+\ell_e} M_r^0(z) \cdot \left[1 + \frac{R_{max}^2 \cdot (z - \ell_c)^2}{\ell_e^4 - [\ell_e^2 \cdot (z - \ell_c)^2]}\right]^{\frac{1}{2}} \cdot dz \qquad (2.31)$$

whereas the total driving moment is given by Eq. (2.26).

As can be seen from Eqs. (2.26) and (2.31), the three-dimensional analysis introduces the two parameters ℓ_c and ℓ_e (ℓ_n or ρ) in addition to the ones used in the conventional two-dimensional analysis.

The following parts of this thesis will employ the models described above in solving several problems where three-dimensional effects on stability are significant.

CHAPTER 3

UNDRAINED STABILITY OF HOMOGENEOUS SLOPES

To illustrate the three-dimensional (or end) effects on the undrained stability of cohesive slopes ($\phi = 0$ and $c = s_u$) due to failure along a finite length, concepts presented earlier are applied to:

1. The toe failure of a vertical cut where typical end effects are encountered. Numerical solutions are obtained by means of the program STAB3D and checked analytically.
2. The failure of a slope with angle β where a finite length of failure 2L is imposed.

3.1 UNDRAINED STABILITY OF A VERTICAL CUT

Let us consider the case of a vertical cut of height H in clay as shown in Fig. 3.1. The z-axis is taken at the crest of the cut and the cylinder to pass through the toe, i.e., $R_{max} = H$. Although not providing the minimum factor of safety, these conditions illustrate the fundamental three-dimensional effects and lead to results that could be checked analytically. The cylindrical shear surface assumed in two-dimensional analysis is shown in Fig. 3.1a where ℓ_c is large compared to the height H. Furthermore, Figs. 3.1b and 3.1c show the two classes of three-dimensional shear surfaces considered. We note here that the symmetry with respect to the plane z = 0 is assumed and the particular choice of the location of the z-axis makes $\ell = \ell_e$ and $\ell = \ell_n$ in the cases of the ellipsoidal and conical shear surfaces, respectively.

3.1.1 Closed-Form Solutions

For the vertical cut shown in Fig. 3.1, the plane strain resisting and driving moments are given by:

$$M_r^0 = \frac{\pi}{2} \cdot R_{max}^2 \cdot c \qquad (3.1),$$

and,

$$M_d^0 = \frac{\gamma}{3} \cdot R_{max}^3 \qquad (3.2),$$

respectively. Therefore, the plane strain factor of safety, F^0 is:

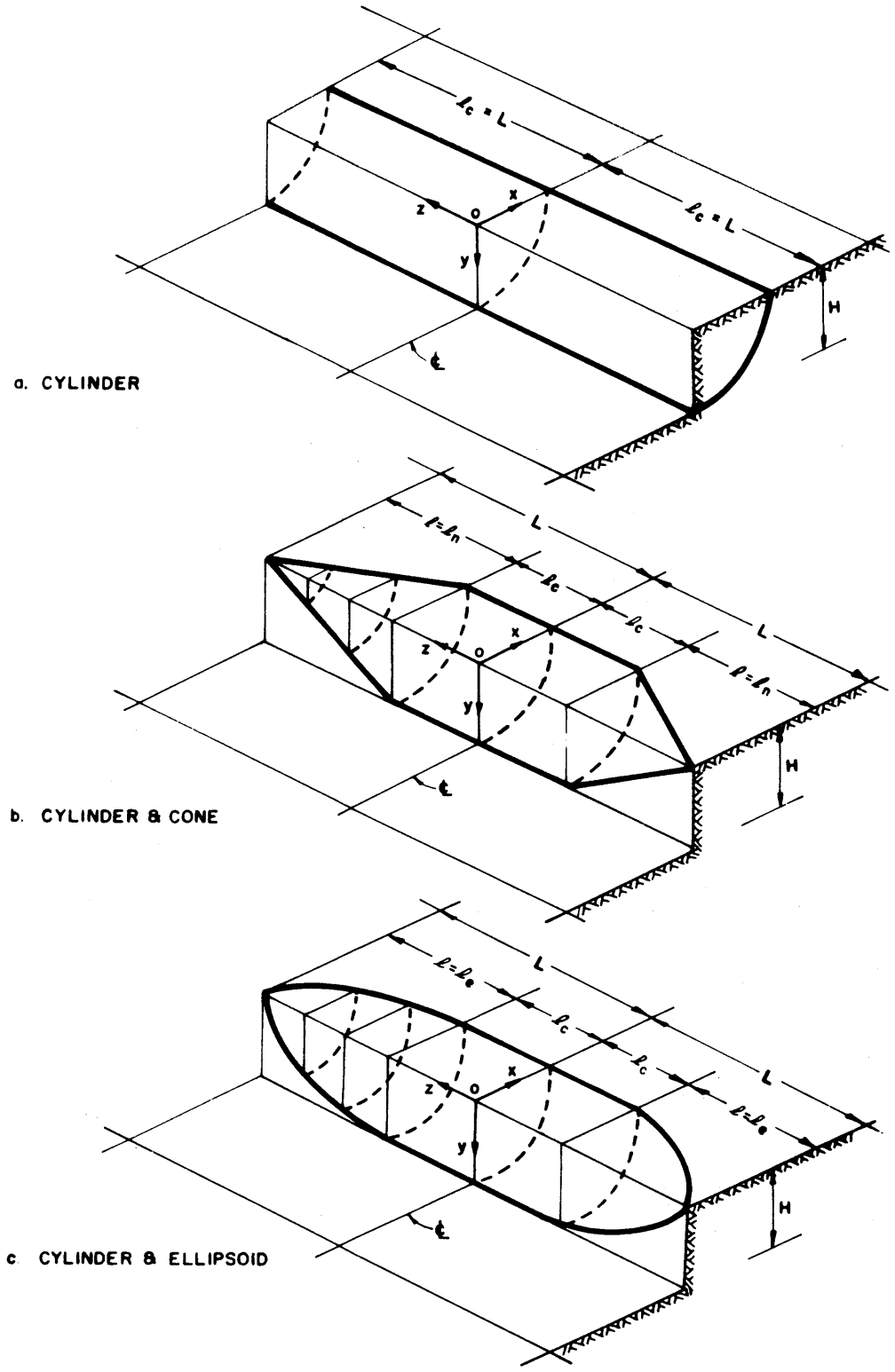


Figure 3.1 Stability of a Vertical Cut

$$F^0 = \frac{3\pi}{2} \cdot \frac{c}{\gamma H} \tag{3.3}$$

Let us consider the case of a shear surface consisting of a cone attached to a cylinder (Fig. 3.1b). The resisting and driving moments resulting from the cylindrical portion of the shear surface are given by (see Eqs. 2.19 and 2.20):

$$M_r(\text{cylinder}) = \pi \cdot R_{max}^2 \cdot c \cdot \ell_c \tag{3.4},$$

and

$$M_d(\text{cylinder}) = \frac{2\gamma}{3} \cdot R_{max}^3 \cdot \ell_c \tag{3.5},$$

respectively.

As for the conical portion, the resisting moment is given by (see Eq. 2.23):

$$M_r(\text{cone}) = 2 \cdot \int_{\ell_c}^{\ell_c+\ell} M_r^0(z) \cdot \frac{dz}{\cos \rho} \tag{3.6}$$

where, ρ is the cone angle. $M_r^0(z)$ is the plane strain resisting moment at a distance z along the embankment axis.

$$M_r^0(z) = \frac{\pi}{2} \cdot R^2(z) \cdot c \tag{3.7}$$

$$R(z) = (\ell_c + \ell - z) \cdot \tan \rho \tag{3.8}$$

Substituting from Eqs. (3.7) and (3.8) into Eq.(3.6), we obtain:

$$M_r(\text{cone}) = \pi \cdot c \cdot \frac{\tan^2 \rho}{\cos^2 \rho} \cdot \int_{\ell_c}^{\ell_c+\ell} (\ell_c + \ell - z)^2 \cdot dz \qquad (3.9)$$

Upon integration and using the following relationships:

$$R_{max} = \ell \cdot \tan \rho \qquad (3.10),$$

$$\cos \rho = \frac{\ell}{\sqrt{\ell^2 + R_{max}^2}} \qquad (3.11)$$

and

$$H = R_{max} \qquad (3.12),$$

the following is obtained:

$$M_r(\text{cone}) = \pi \cdot c \cdot R_{max}^2 \cdot \frac{1}{3}\sqrt{\ell^2 + H^2} \qquad (3.13)$$

The total resisting moment is, therefore, given by

$$M_r = \pi \cdot R_{max}^2 \cdot c \cdot [\ell_c + \frac{1}{3}\sqrt{\ell^2 + H^2}] \qquad (3.14)$$

According to Eq. (2.24) the driving moment resulting from the conical portion of the shear surface is given by:

$$M_d(\text{cone}) = 2 \cdot \int_{\ell_c}^{\ell+\ell_c} M_d^0(z) \cdot dz \qquad (3.15)$$

where,

$$M_d^0(z) = \frac{2\gamma}{3} \cdot R^3(z) \tag{3.16}$$

Substituting from Eq. (3.16) into Eq. (3.15) and integrating, we obtain:

$$M_d(\text{cone}) = \frac{2\gamma}{3} \cdot \frac{\ell^4}{4} \tan^3 \rho \tag{3.17}$$

Using Eq. (3.10),Eq. (3.17) reduces to:

$$M_d(\text{cone}) = \frac{2\gamma}{3} \cdot R_{max}^3 \cdot \frac{\ell}{4} \tag{3.18},$$

and the total driving moment is thus given by:

$$M_d = \frac{2\gamma}{3} \cdot R_{max}^3 \cdot (\ell_c + \ell/4) \tag{3.19}$$

Therefore, the three-dimensional safety factor, F, is given by:

$$F = \frac{3\pi}{2} \frac{c}{\gamma H} \frac{\ell_c + 1/3\sqrt{\ell^2 + H^2}}{\ell_c + \ell/4} \tag{3.20}$$

and the ratio of the three-dimensional to the plane strain safety factors, F/F^0,is given by:

$$F/F^0 = \frac{\ell_c + 1/3\sqrt{\ell^2 + H^2}}{\ell_c + \ell/4} \tag{3.21}$$

Dividing by H, we get:

$$F/F^0 = \frac{\ell_c/H + 1/3\sqrt{(\ell/H)^2 + 1}}{\ell_c/H + 1/4(\ell/H)} \tag{3.22}$$

Figure 3.2 shows a plot of F/F^0 vs ℓ/H for different values of ℓ_c/H as obtained from Eq. (3.22) (dotted lines).

3.1.2 Numerical Solutions

The undrained stability of the vertical cut shown in Fig. 3.1 was then studied using the program STAB3D. The analysis was carried out employing the ordinary method of slices (Fellenius, 1936). The central cross section of the shear surface (at z = 0) was divided into twenty slices. Similarly, and in order to estimate the resisting and driving moments for the conical (or ellipsoidal) surface, the length of the cone (or ellipsoid) was divided into twenty segments. The integration of Eqs. (3.9) and (3.15) was performed numerically using the trapezoidal rule of integration (Crandall, 1956). Appendix A of this thesis gives a detailed description of the computer program STAB3D.

The ratio F/F^0 is plotted against ℓ/H for different values of ℓ_c/H in Fig. 3.2a for the case of a cone attached to a cylinder, and in Fig. 3.2b for the case of an ellipsoid attached to a cylinder.

The three-dimensional effects can be seen in Fig. 3.2 where we note that:

1. Since F/F^0 exceeds unity, three-dimensional effects tend to increase the factor of safety. Slopes would therefore tend to fail for long distances provided the soil properties and the cross section of the embankment are independent of z.

2. As ℓ_c/H increases, the value of F/F^0 decreases. Failures having ℓ_c/H in excess of four can be considered close enough to plane strain ($\ell_c/H = \infty$ and $F = F^0$).

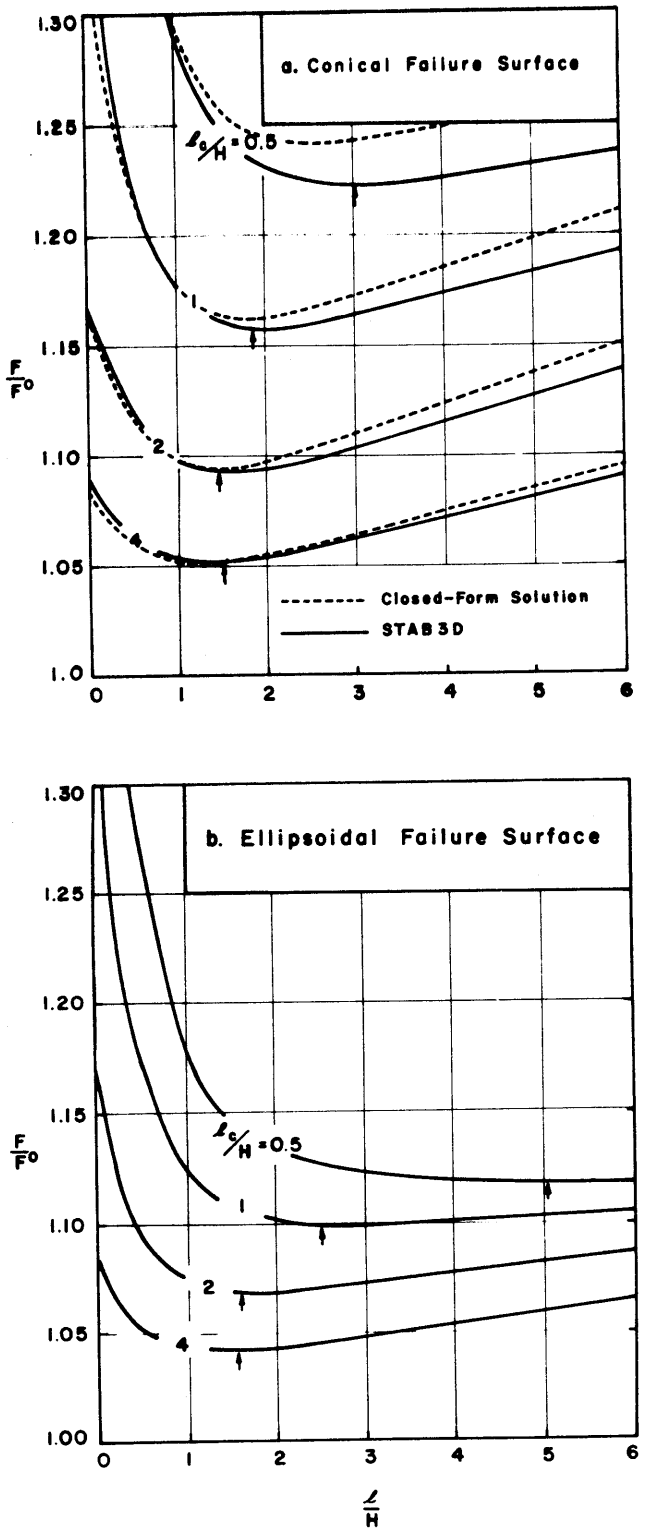


Figure 3.2 End Effects on the Stability of a Vertical Cut

3. For a fixed value of ℓ_c/H, the factor of safety reaches a minimum at the critical value of ℓ/H which determines the most likely length of failure. The curves are, however, quite flat, especially for small values of ℓ_c/H. This means that even though the factor of safety F can be predicted with reasonable accuracy, the length of failure 2L is more difficult to predict.

4. When ℓ equals zero, the values of F are the same in both plots (Fig. 3.2) and correspond to a cylindrical shear surface when the edge effects are taken into consideration. This solution is relatively easy to obtain and can be used to determine if a particular problem needs a three-dimensional analysis.

5. Comparing the solid and dotted lines in Fig. 3.2a, one sees that the solutions obtained by STAB3D are in good agreement with those based on the closed-form solution given by Eq. (3.22). The maximum deviation between the two solutions is about 3.5%. However, the maximum difference between the minimum values of F/F^0 obtained from the two solutions is only about 1.5%.

Finally, a comparison between conical and ellipsoidal shear surfaces is made in Fig. 3.3 where plan views of these surfaces giving the minimum factor of safety at different ℓ_c/H ratios are given. For this problem of a vertical cut in clay, ellipsoidal failure surfaces gave consistently lower values of

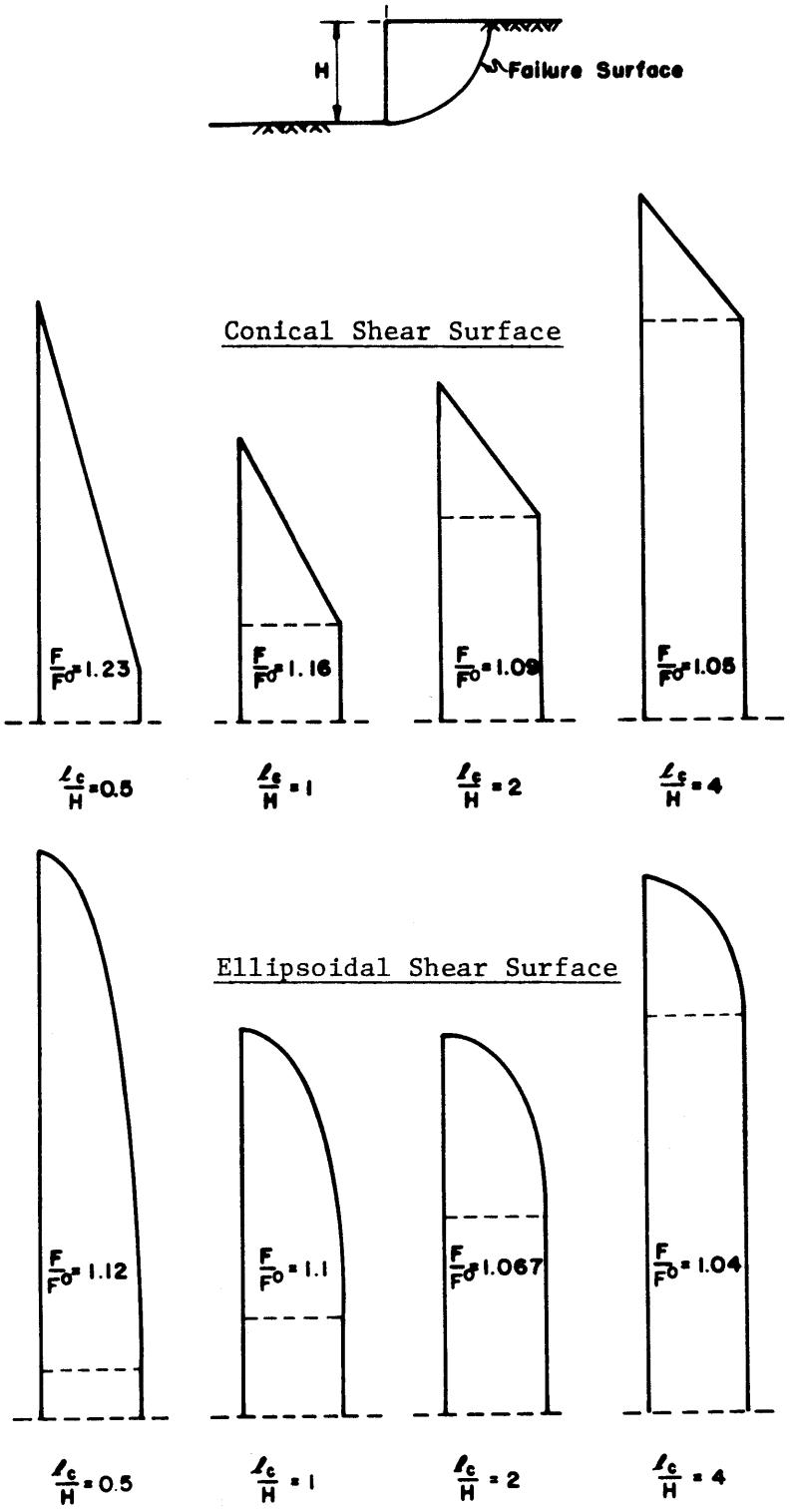


Figure 3.3 Plan View of the Failure Surfaces for a Vertical Cut

F and are therefore more likely to represent actual failures. Moreover, by comparing the plan views of ellipsoidal failures corresponding to $\ell_c/H = 1$ to that of $\ell_c/H = 2$, we note that they are quite close to one another. It would therefore be difficult to decide which of the two has taken place by observing the actual failure of a slope. The same applies to $\ell_c/H = 0.5$ and $\ell_c/H = 4$ in spite of the fact that they have different factors of safety.

3.2 UNDRAINED STABILITY OF HOMOGENEOUS SLOPES

The concepts introduced in Chapter 2 will now be employed to study the undrained stability ($\phi = 0$, and $c = s_u$) of homogeneous slopes restricted to fail along a finite length 2L. These slopes are assumed to have cross sections and soil properties that do not vary along the slopes' axis.

To determine the critical shear surface and the corresponding factor of safety, F_{min} of a slope of height H, making an angle β with the horizontal and restricted to fail along a finite length 2L by numerical techniques, the following steps are needed:

1. Choose a class of admissible shear surfaces. Here we consider a conical surface attached to a cylinder and an ellipsoid attached to a cylinder as previously described.

2. Assume the location of the z-axis. This is equivalent to assuming the location of the center of the circle in two-dimensional analysis.

3. Assume the radius of the cylinder R_{max}. This is equivalent to assuming the radius of the circle in two-dimensional analysis.

4. Assume the length of the cylinder $2\ell_c$ ($0 \leq 2\ell_c \leq 2L$), Fig. 2.2.

5. Obtain the factor of safety F against a shear surface failure defined by steps 1, 2, 3, and 4 above.

6. Repeat steps 2, 3, 4 and 5 to get another factor of safety and, after a sufficient number of trials, choose the minimum value, F_{min}, obtained. This will represent an upper bound on the actual factor of safety of the slope.

Taylor (1937) studied the same problem in two-dimensions (infinite failure length, i.e., plane strain conditions), and concluded that for slopes with angle, β, equal to or greater than 53°, the failure circle passes through the toe of the slope. On the other hand, for $\beta < 53°$, a deep-seated failure is more critical and extends to a depth which depends on the bedrock location, as described by the parameter n in Fig. 3.4.

The end effects imposed by a limited length of failure, 2L, of the slope are illustrated by the results shown in Fig. 3.4 where F/F^0 is plotted against $2L/DR^*$ for slope angles β equal to 10° and 90°, and for n values of 1 (toe failures), 1.25, 1.5 and 2. The results show that:

1. When the length of failure 2L is large, a plane strain failure is approached (F/F^0 approaches unity).

2. For a certain value of 2L/DR, the slope angle β has little influence on F/F^0, i.e., on the increase of factor of safety due to end effects. The case of $\beta = 40°$ was also considered and results were found to lie within the narrow band provided by $\beta = 10°$ and $\beta = 90°$ shown in Fig. 3.4. The same result was also found in case of base failures.

---

*$DR = R_{max} - R_{min}$

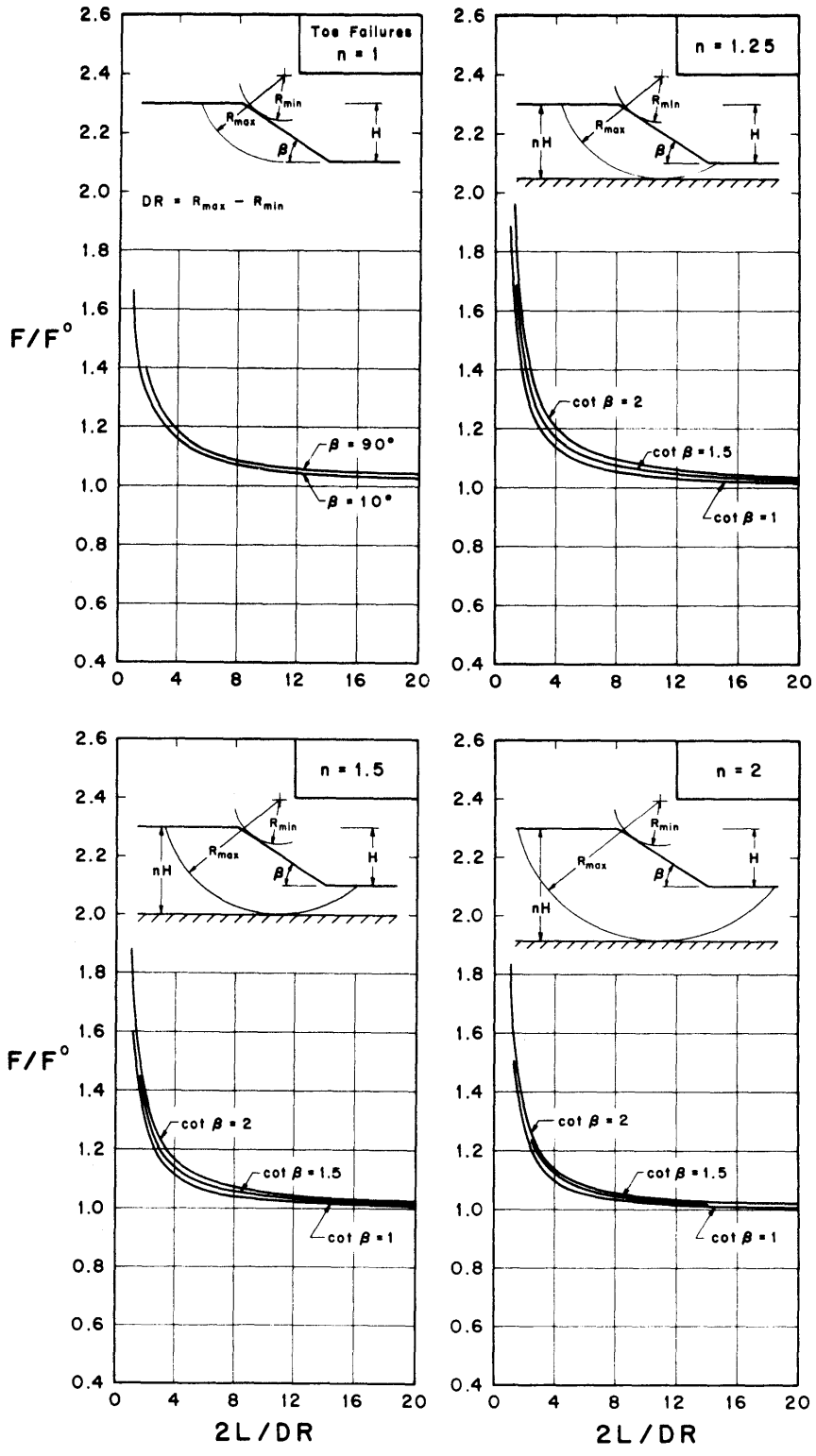


Figure 3.4 End Effects on the Stability of Homogeneous Isotropic Slopes

3. The ratio 2L/DR determines whether end effects in a particular problem are important and whether a thorough three-dimensional analysis is justifiable. Given the slope cross section and the length of failure, 2L, it is therefore important to determine DR. This can be achieved by performing a conventional two-dimensional slope stability analysis to obtain the minimum factor of safety F^0_{min}, the location of the center of the slip circle (the z-axis) and its radius R_{max}. For the simple case of homogeneous cohesive slopes as treated herein, the z-axis and R_{max} and F^0_{min} are given by Taylor (1937). The value of R_{min} is the radius of the circle with the same origin as the slip circle and touching the slope. The value of DR is then computed as the difference between R_{max} and R_{min} (Fig. 3.4). For values of $2L/DR \geq 6$, the increase in the factor of safety due to end effects is less than 10% and a three-dimensional analysis would not, in many cases, be warranted. However, for $2L/DR \leq 6$, a three-dimensional analysis including edge effects might be considered if the savings resulting from a more accurate treatment justify this effort.

4. Strictly speaking, Fig. 3.4 should only be used for homogeneous cohesive slopes. However, Fig. 3.4 provides a rough estimate of the end effects for more general slope conditions after the conventional two-dimensional analysis has been performed.

5. The results of computations showed that elliptic shear surfaces consistently gave a lower factor of safety

than conical ones and are thus more likely to simulate the geometry of actual slope failures of the type considered.

3.3 SUMMARY AND CONCLUSIONS

The end effects on the stability of cohesive slopes are investigated by extending the circular arc method to three-dimensional problems. Results are obtained numerically by means of the computer program STAB3D, and checked analytically for the case of the undrained stability ($\phi = 0$ and $c = s_u$) of a vertical cut. From this investigation the following conclusions can be advanced:

1. The end effects increase the factor of safety obtained by means of a conventional two-dimensional solution. When the geometry of the slope and the soil properties do not change along the slope axis, this increase depends on the ratio between the length of failure, 2L, and the depth of failure, DR. Figs. 3.2 and 3.4 show that for long shallow failures where 2L/DR exceeds eight, the increase in the factor of safety is less than 5% and can therefore be neglected. On the other hand, for short deep failures where 2L/DR is less than two, the increase in the factor of safety can exceed 20% and the use of a three-dimensional analysis is thus recommended.

2. Slopes having a variable cross-section or having variable soil properties along their axis are subjected to more pronounced end effects than uniform slopes. A three-dimensional analysis in such cases is needed for a wider range of 2L/DR than mentioned above.

3. The end effects on the factor of safety can be predicted with reasonable accuracy. However, the length of failure is very sensitive to the parameters defining the problem and is thus difficult to predict.

4. For a certain ratio of 2L/DR, the slope angle β has little influence on the increase in the factor of safety due to end effects. For a value of 2L/DR equal to six, the increase in the factor of safety due to end effects is about 8% for $\beta = 10°$, whereas the corresponding increase for $\beta = 90°$ is about 12% (Fig. 3.4).

5. For flat slopes, the three-dimensional effects (the ratio F/F^0) are influenced by the bedrock location expressed by the parameter n in Fig. 3.4. In case of $\beta = 45°$ ($\cot \beta = 1$), when n increases from 1 (toe failures) to 2, the F/F^0 value at 2L/DR = 4 decreases by about 7%. A similar result for plane strain analysis (a decrease in F^0 with an increase in n) was reported by Taylor (1937) for flat slopes with $\beta < 53°$.

6. Elliptic shear surfaces consistently gave lower factors of safety than conical ones.

7. Figure 3.2a shows that the results obtained by the program STAB3D are confirmed by closed-form solutions derived for a vertical cut in a cohesive soil.

CHAPTER 4

UNDRAINED STABILITY OF HOMOGENEOUS SLOPES SUBJECTED TO SURCHARGE LOADS

4.1 INTRODUCTION

This chapter considers the undrained stability of cohesive slopes ($c = s_u$ and $\phi = 0$) subjected to surcharge loads. Heavy equipment (e.g., draglines and railways) and structures "rapidly" built near the crest of cohesive slopes produce such loadings.

Existing methods of analysis for cohesive slopes subjected to surcharge loads are mostly based on two-dimensional (plane strain) modes of failure where the surcharge load is of infinite extent (Janbu, 1954; Meyerhof, 1957; Brinch Hansen, 1966; Bowles, 1975 and 1977). In cases where the loaded area and/or the failure zone are not "long enough", three-dimensional effects become important, and plane strain analyses are no longer justified. Brinch Hansen (1966) outlined an approximate procedure to account for end effects. Giger and Krizek (1976) studied the stability of a vertical corner cut subjected to a concentrated surcharge load.

The problems considered in this chapter are shown in Fig. 4.1 and are divided into two classes:

I. Plane strain problems which are treated in Section 4.3 as an extension of Taylor's work (1937) using the classical circular arc method of analysis. Fig. 4.1a shows problems I-1 where the slope is subjected to a line load of infinite extent. Problem I-2 is similar to that of I-1 except that the load is applied on a finite width, i.e., along a strip of infinite extent (Fig. 4.1b).

II. Three-dimensional problems which are treated in Section 4.4 as an extension of the work presented in Chapter 2 using conical and ellipsoidal shear surfaces. This class of problems considers the stability of a slope first subjected to a line load of finite length (Problem II-1 in Fig. 4.1c) and then to a rectangular loaded area (Problem II-2 in Fig. 4.1d). Results of the class I problems, Problems II-1 and II-2, for the case of square loaded areas, are presented in charts suitable for performing undrained stability analyses.

Section 4.5 compares predictions based on existing methods with the results in Sections 4.3 and 4.4. Finally, the major findings of this study are summarized in Section 4.6.

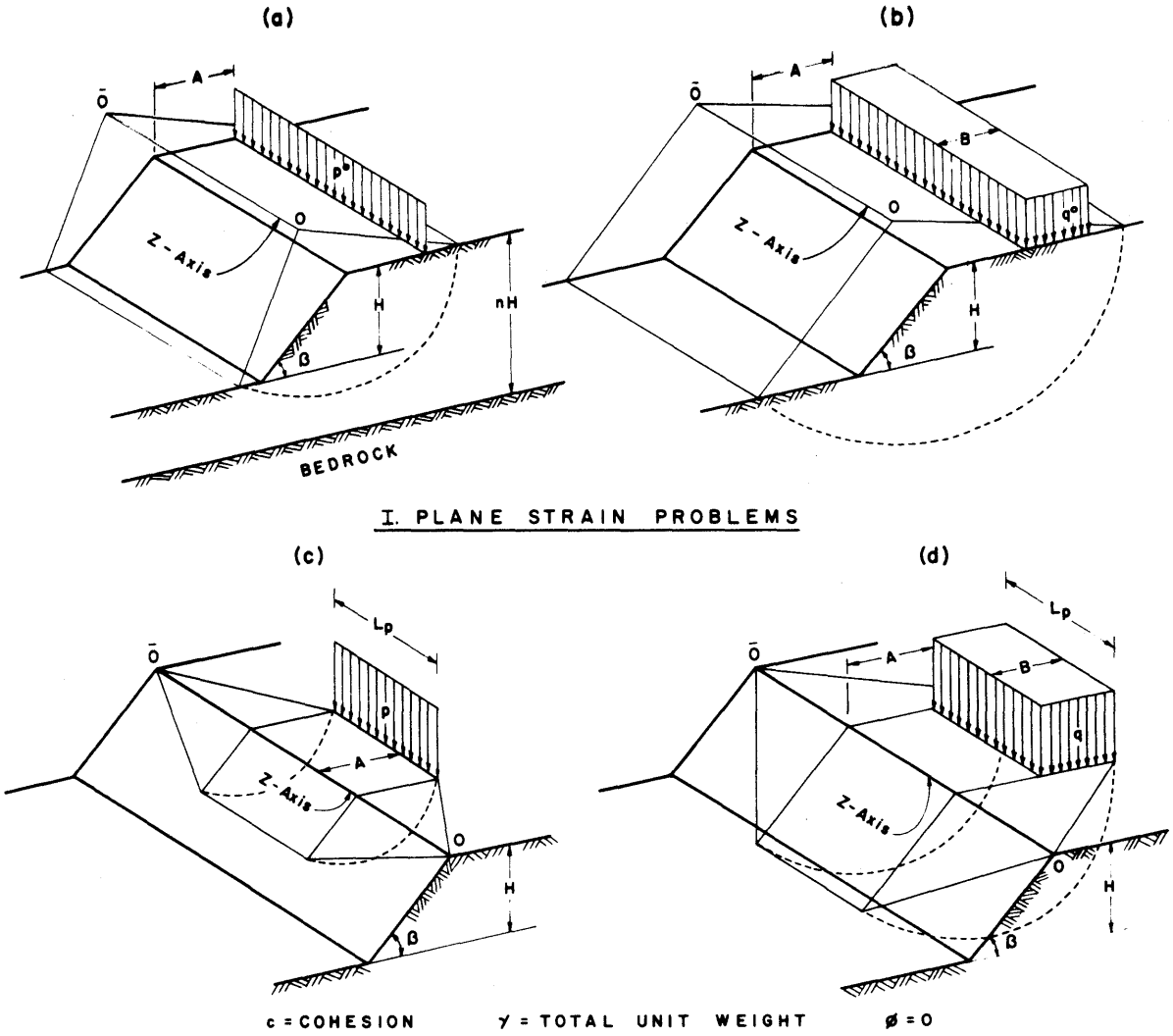


Figure 4.1 Problems Description

4.2 BACKGROUND OF RELATED WORK

Several investigators have considered the stability of cohesive slopes subjected to surcharge loads. Until recently, most existing solutions applied to two-dimensional conditions where the length of the loaded area is reasonably larger than its width. Such solutions include the work of Janbu (1954), Meyerhof (1957), Brinch Hansen (1966), and Bowles (1975, 1977). In contrast to the voluminous literature on two-dimensional stability problems, little work has been done in three-dimensions. Brinch Hansen (1966) presented an approximate procedure to take into consideration the three-dimensional nature of the problem. Giger and Krizek (1976) considered the problem of a vertical cut, with a variable corner angle, subjected to a concentrated surcharge load.

This section presents a summary of the existing methods of analyses and, whenever needed, provides examples to illustrate their use. Comments on the different methods and comparisons between their results are given in Section 4.5.

4.2.1 Two-Dimensional Solutions

Janbu's Analysis. For slope stability problems, Janbu (1954) developed general solutions based on dimensionless parameters and suitable for performing undrained as well as drained stability analyses. The potential sliding surface is cylindrical and the factor of safety is defined as the ratio between the shear strength and the shear stress necessary

for equilibrium along the critical sliding surface. Janbu's analyses considered the influence of several factors such as drawdown conditions, water-filled tension cracks and surcharge loads.

Of particular interest herein is the case of a slope subjected to surcharge loads. Fig. 4.2a shows a profile of a slope in homogeneous, purely cohesive soil which is subjected to a surcharge of constant intensity, q^0 . Assuming that this surcharge is of infinite extent in the horizontal direction, stability considerations for the $\phi = 0$ case yield:

$$F^0 = \mu_{q^0} N_s \frac{c}{\gamma H + q^0} \tag{4.1}$$

in which,

F^0 = plane strain factor of safety

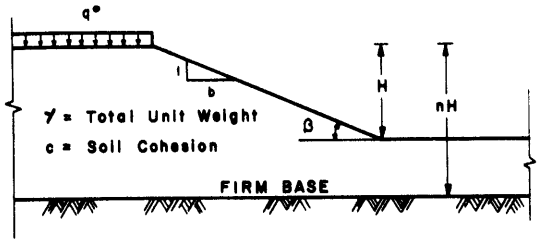
c = soil cohesion (undrained shear strength, s_u)

γ = total unit weight

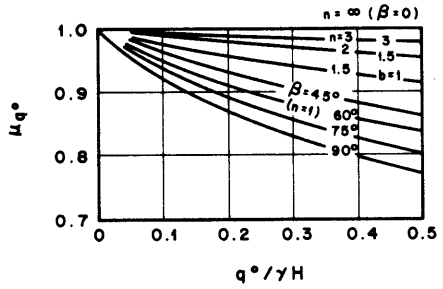
μ_{q^0} = dimensionless reduction factor which is plotted versus the ratio $q^0/\gamma H$ and the slope characteristics β and n in Fig. 4.2b

N_s = stability number for simple slopes under the effect of gravity alone, and is plotted versus the slope angle β and depth factor n in Fig. 4.2c.

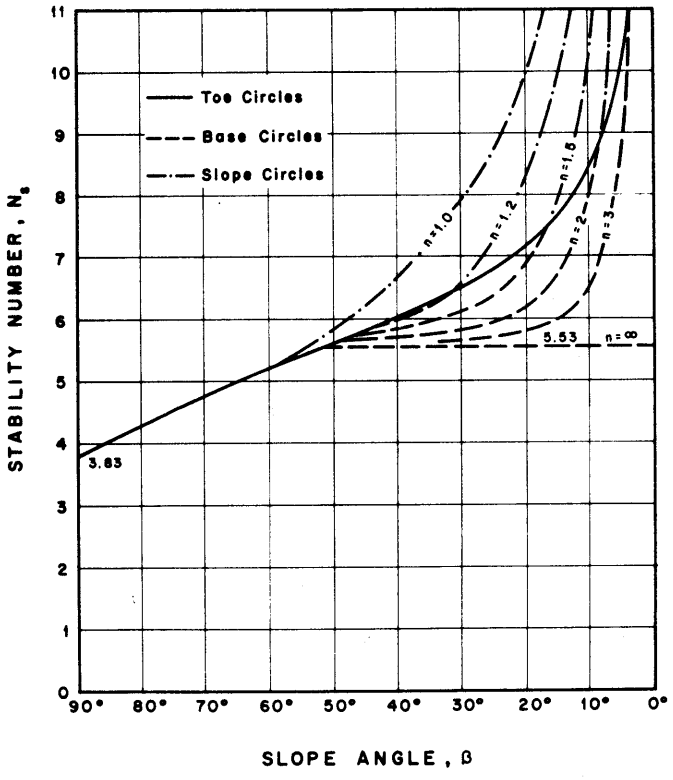
The following example illustrates the use of Janbu's charts: a slope of height 13 ft, rising at an angle of 42°



(a)



(b)



(c)

Figure 4.2 Janbu's Analysis

to the horizontal is subjected to a vertical surcharge load of intensity q^0 = 220 psf. The soil has an undrained shear strength of 410 psf and a total unit weight of 120 pcf. The bedrock is 7 ft below the toe of the slope. What is the factor of safety of this slope? In solving this example, consider two modes of failure: a base failure and a toe failure. For a base circle tangent to bedrock one finds:

N_s = 5.75 for β = 42° and n = 20/13 = 1.54, Fig. 4.2c.

μ_{q^0} = 0.97 for $q^0/\gamma H$ = 0.141 and n = 1.54, Fig. 4.2b.

Hence, Eq. (4.1) yields:

$$F^0 = 0.97 \times 5.75 \frac{410}{1560 + 220} = 1.28$$

For a toe circle analysis one finds:

N_s = 5.90 for β = 42° (independent of n), Fig. 4.2c

μ_{q^0} = 0.95 for $q^0/\gamma H$ = 0.141 and β = 42°., Fig. 4.2b

Therefore, Eq. (4.1) yields:

$$F^0 = 0.95 \times 5.90 \times \frac{410}{1780} = 1.29$$

Both analyses led to practically the same value of the factor of safety.

Meyerhof's Analysis. Meyerhof (1957) indicated that for a slope subjected to a surcharge load, failure can take place according to one of two modes: (1) Foundation failure, where the shear surface intersects the slope in a position higher

than its toe; and (2) Slope failure, where the critical shear surface passes through or below the toe of the slope. Whether one mode or the other will occur is determined primarily by the stability number, N_s, defined as:

$$N_s = \gamma H/c \tag{4.2}$$

Slopes with small N_s values encounter foundation failures, whereas slopes having high N_s values tend to fail through the toe or the base of the slope.

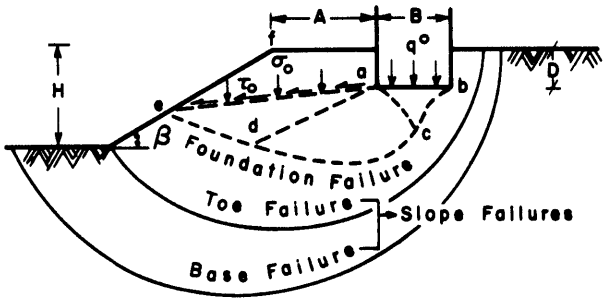
Meyerhof's analysis of foundation failures is based on an approximate bearing capacity theory. Figure 4.3 depicts three zones for such a failure mode: a central rigid zone abc, a radial shear zone acd, and a mixed shear zone adef. Stresses in the zones of plastic equilibrium are obtained, as for the case of a horizontal ground surface, by replacing the weight of the soil wedge aef by the equivalent stresses σ_0 and τ_0 in the normal and tangential directions to plane ae, respectively. The ultimate pressure can then be expressed by:

$$q^0_{cr} = c\ N_c + \tfrac{1}{2}\gamma B\ N_\gamma \tag{4.3}$$

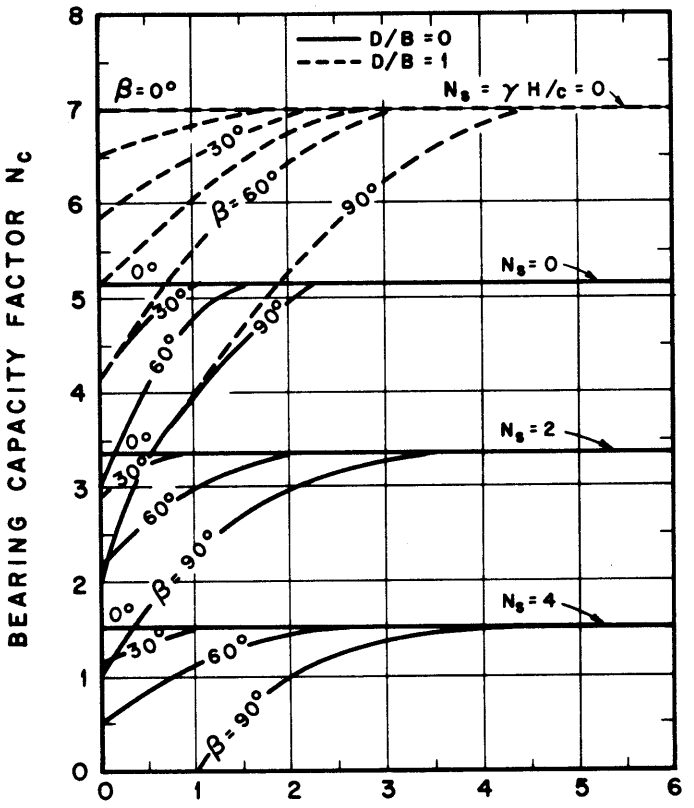
in which,

B = foundation width

N_c and N_γ = dimensionless coefficients which depend on the edge distance, A; foundation width, B; the slope angle β; the angle of internal friction, ϕ;



a) ASSUMED FAILURE SURFACES



b) BEARING CAPACITY FACTORS FOR STRIP FOUNDATION ON TOP OF SLOPE OF PURELY COHESIVE MATERIAL

Figure 4.3 Meyerhof's Analysis

and the depth, D, of the foundation below the ground surface.

The undrained ultimate pressure ($\phi = 0$) is given by:

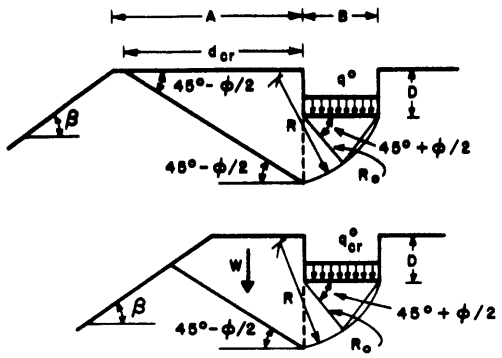
$$q^0_{cr} = s_u N_c \tag{4.4}$$

in which s_u is the undrained shear strength of the soil. Coefficient N_c, given in the upper part ($N_s = 0$) of Fig. 4.3b, decreases with greater inclination of the slope and increases rapidly with greater foundation distance from the edge of the slope.

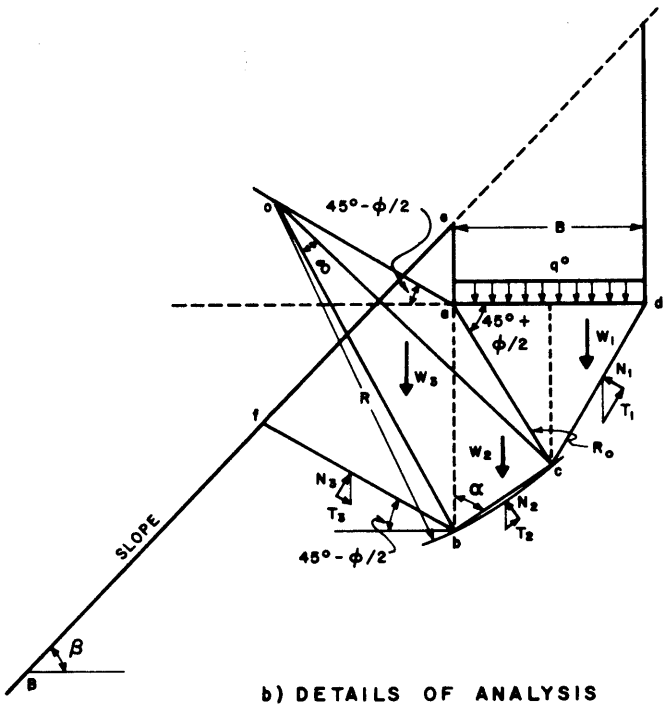
Slope failures are analyzed by means of the classical circular arc method using Janbu's work. Figure 4.3 presents the values of the coefficient N_c (lower part of Fig. 4.3b) for a wide foundation ($B/H = \infty$) located at a distance A from the crest of the slope. N_c increases with A/H, decreases considerably with greater N_s values and, to a smaller extent, with the slope inclination β.

Bowles' Analysis. Bowles (1975) considers the case of a footing located near the top of a slope. When the failure surface (Fig. 4.4a) does not intersect the slope, Bowles recommends no reduction in the footing's bearing capacity and that conventional bearing capacity theories for a horizontal surface be used. For a surface footing, this corresponds to a critical A/B ratio of 0.7 for the case of $\phi = 0$.

When the failure surface intersects the slope, Bowles considers a failure mechanism which consists of three wedges



a) PROBLEM DESCRIPTION



ϕ	R/R_o
0°	1.00
10°	1.18
20°	1.48
30°	2.00
40°	3.09

b) DETAILS OF ANALYSIS

Solution Steps:

1. Draw system to scale and compute R_0.
2. Lay off line ao of indefinite length.
3. Find R, and with center at o draw arc through point c to b.
4. Compute weights w_1, w_2 and w_3.
5. Compute friction resistance to sliding along slip surfaces due to $\bar{N}\tan\phi$ and cohesion.
6. Ultimate pressure q^0_{cr} is found by satisfying the vertical equilibrium of each wedge and the overall horizontal equilibrium of the entire sliding mass.

Figure 4.4 Bowles' Analysis

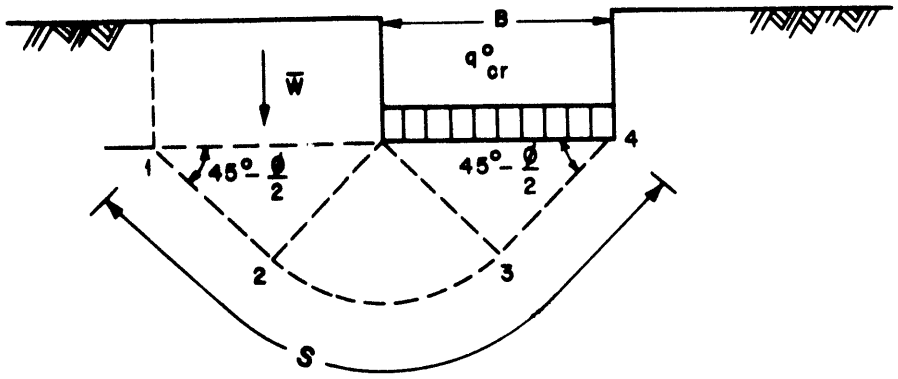
(Fig. 4.4b). Table 4.1 presents a list of the unknown forces along with the available equilibrium equations associated with this failure mode. The number of unknowns is 16 and the number of equations is 12. However, if one neglects to satisfy the moment equilibrium, the corresponding number of unknowns and equations are reduced to 11 and 9, respectively. This means that the problem is twice statically indeterminate, and two simplifying assumptions are needed in order to achieve statical determinancy. Bowles assumes that the interwedge forces are horizontal, and by satisfying the vertical equilibrium of each wedge, the force along the base can be expressed in terms of the ultimate pressure and the soil weight in the three wedges. Considering the overall horizontal equilibrium of the entire sliding mass, we obtained the following expression for q^0_{cr} for the $\phi = 0$ case:

$$q^0_{cr}/c = 2.243 + \frac{2(\cos\beta + \sqrt{2}\ A/B \sin\beta)}{\sin\beta + \cos\beta} - \frac{\gamma H}{c} \times \frac{B}{H} \times \frac{\sqrt{2}}{4}(1 - \sqrt{2}\ A/B)^2 \frac{\sin\beta}{\sin\beta + \cos\beta} \qquad (4.5)$$

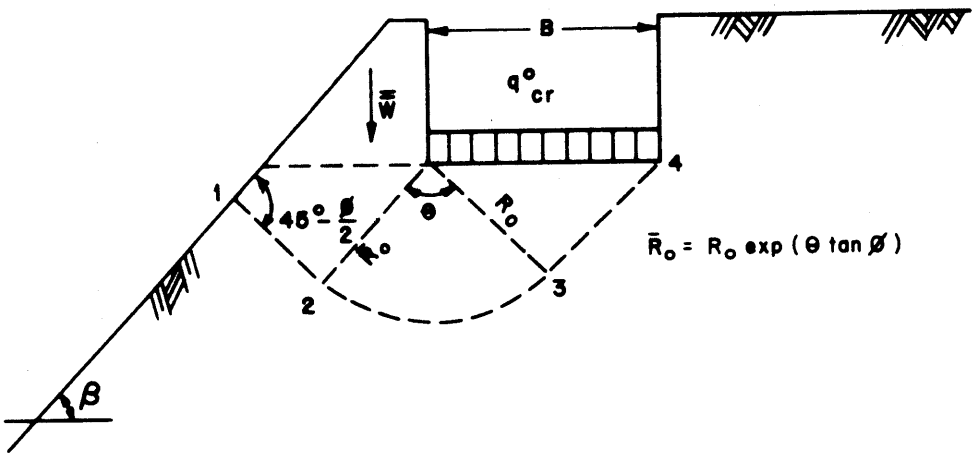
The Modified Bowles' Analysis. Bowles (1977) recommends another alternative for the computation of the ultimate pressure. This alternative is based on modifying the shear surface in Prandtl's solution (1920) for a strip footing on a horizontal surface to account for the existance of the slope. Assuming the shear surface geometry in Fig. 4.5, the adjusted bearing capacity coefficients $\bar{N}_c$ and $\bar{N}_q$ for frictionless

Table 4.1 Equations and Unknowns Associated with Bowles' Analysis (1975)

Unknowns	Satisfying all equilibrium equations	Satisfying force equilibrium only (Neglect moment equilibrium)
Ultimate bearing pressure	1	1
Normal components ($\overline{N}$) of forces on the base of each wedge	3	3
Tangential components (T) of forces on the base of each wedge	3	3
Point of application of forces on the base of each wedge	3	--
Resultant interwedge forces	2	2
Inclination of interwedge forces	2	2
Point of application of interwedge forces	2	--
Total unknowns	16	11
Equations		
Vertical force equilibrium for each wedge	3	3
Horizontal force equilibrium for each wedge	3	3
Moment equilibrium for each wedge	3	--
Mohr-Coulomb yield criterion ($T = \overline{N} \tan \overline{\phi} + \overline{c}$) at the base of each wedge	3	3
Total Equations	12	9



NO SLOPE



ACTUAL CASE

$$\bar{N}_c = \frac{S_{1,2,3,4}}{(S_{1,2,3,4})\ \text{no slope}} \times N_c$$

$$\bar{N}_q = \frac{\bar{\bar{W}}}{\bar{W}} \times N_q$$

Figure 4.5 The Modified Bowles' Analysis

materials ($\phi = 0$) are given by:

$$\bar{N}_c = \frac{S_{1,2,3,4}}{(S_{1,2,3,4})_{\text{no slope}}} N_c \tag{4.6}$$

$$\bar{N}_c = \frac{\bar{\bar{W}}}{\bar{W}} N_q \tag{4.7}$$

where $S_{1,2,3,4}$ is the length along the shear surface. For a surface footing ($D = 0$) resting on a cohesive soil ($\phi = 0$) we get:

$$\bar{N}_c = [2 + (90 - \beta)\frac{\pi}{180} + 2A/B \sin\beta]\frac{N_c}{3.57} \tag{4.8}$$

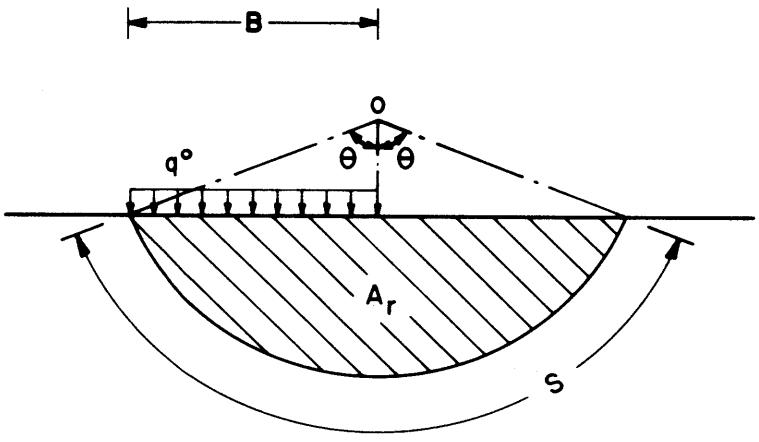
The ultimate bearing pressure is thus given by:

$$q^0_{cr} = s_u \bar{N}_c \tag{4.9}$$

As should be evident, this method is approximate, and is valid only for the case of a footing resting on a weightless soil, i.e., $\gamma H/c = 0$.

4.2.2 Three-Dimensional Solutions

Brinch Hansen's Analysis. Brinch Hansen (1966) considers the undrained bearing capacity ($\phi = 0$, $c = s_u$) of a rectangular footing of dimensions $B \times L_p$ resting on the surface of a saturated clay layer (Fig. 4.6). For the plane strain case ($L_p/B = \infty$), Hansen uses the circular arc method of analysis and evaluates the ultimate footing pressure by equating the resisting moment, due to the shear resistance along the circu-



$\theta_{cr} = 66.8°$

$q^{\circ}_{cr/c} = 5.52$

Figure 4.6 Brinch Hansen's Analysis

lar arc, to the disturbing moment due to gravity and surcharge loads. The critical center lies above the edge of the footing, the half central angle of the slip circle is 66.8° (Fig. 4.6), and the critical load ratio, $q^0_{cr}/c = 5.52$.

When the length of the loaded area, L_p, is not much larger than its width B, Hansen recommends the use of a three-dimensional analysis based on a shear surface consisting of a circular cylinder with plane end surfaces. By equating the resisting and disturbing moments, he obtains the following expression for the three-dimensional load ratio, q_{cr}/c:

$$q_{cr}/c = 5.52\ (1 + 0.57\ B/L_p) \tag{4.10}$$

According to Hansen, this value of q_{cr}/c must be an upper limit, because the considered failure surface is kinematically admissible and does not necessarily satisfy equilibrium at all points within the soil medium.

Hansen also suggests another approximate method to account for the end effects for the case of $\phi = 0$. The safety factor, F , is determined by multiplying the plane strain factor of safety, F^0, by a correction factor, f_r, i.e.,

$$F = f_r\ F^0 \tag{4.11}$$

where,

$$f_r = 1 + \frac{A_r}{kSL_p} \tag{4.12}$$

in which,

k = a constant

S = arc length of the failure surface

A_r = area of the soil mass above the critical failure surface (Fig. 4.6)

L_p = length of the loaded area

In order to determine the constant k, Hansen uses Skempton's expression (1951), for a footing on a horizontal ground surface:

$$f_s = 1 + 0.2\ B/L_p \tag{4.13}$$

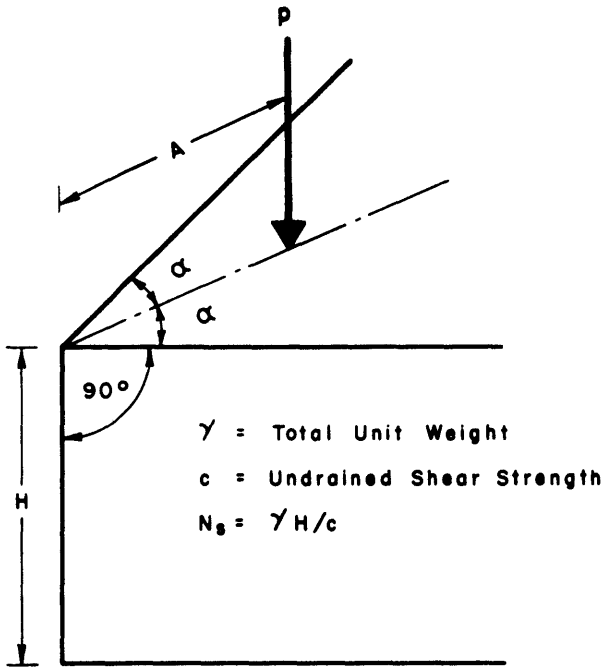
By equating Eqs. 4.12 and 4.13, one obtains $k \simeq 2$ and hence,

$$f_r = 1 + \frac{A_r}{2\ SL_p} \tag{4.14}$$

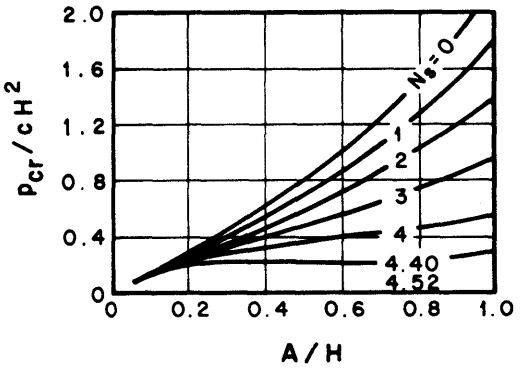
For the case of nonhomogeneous soils, $\Sigma\ c\Delta A_r$ and $\Sigma\ c\Delta S$ should be used instead of A_r and S.

Giger and Krizek's Analysis. Giger and Krizek (1976) present a solution for the stability of a vertical cut with a variable corner angle. The loading consists of the soil's own weight plus a vertical concentrated surcharge load acting in the vertical plane of symmetry at some variable distance from the corner of the cut (Fig. 4.7a).

The solution is based on the "upper bound theorem of the generalized theory of perfect plasticity" where the soil is



a) PROBLEM DESCRIPTION



b) UNDRAINED STABILITY CHARTS FOR A CORNER ANGLE OF 180°

Figure 4.7 Giger's and Krizek's Analysis

assumed to be perfectly plastic, and to obey the Coulomb yield criterion and its associated flow rule (Chen, 1975).

Figure 4.7b presents the results for the case of a vertical cut having a corner angle of 180° and $\phi = 0$. The critical load ratio, p_{cr}/cH^2 is plotted versus the normalized edge distance, A/H for different values of the stability number, N_s.

Table 4.2 summarizes all of the previously mentioned methods, and Section 4.5 presents quantitative comparisons of these methods.

Table 4.2 Methods for Estimating the Undrained Ultimate Pressure of Footings on Slopes

Method	Assumptions and Regions of Applicability	Method of Analysis	Summary of Method
1. Janbu (1954)	1. Two-dimensional solution 2. Soil is homogeneous with an isotropic shear strength 3. The surcharge load is uniform, covers the whole top of the slope, and of infinite extent in the horizontal direction i.e., A/H = 0 and B/H = ∞. 4. Applicable for all slope angles, β and all values of the stability number N_s. Solutions are also provided for cohesive slopes underlain by a rigid firm base.	Circular arc analysis with the factor of safety defined as the ratio between the shear strength and the shear stress necessary for equilibrium along the critical sliding surface.	$F^0 = \mu_q^0 N_s \frac{c}{\gamma H + q^w}$ (Eq. 4.1) μ_q^0, N_s are given in Fig. 4.2
2. Meyerhof (1957)	1. Two-dimensional solution. 2. Soil is homogeneous with isotropic shear strength. 3. Uniform surcharge load. 4. Foundation failure solutions are valid for small values of γH/c (γH/c ≃ 0) 5. Slope failure solutions through the toe or the base of the slope are valid for large values of the stability number γH/c and for wide foundations i.e., B/H = ∞ 6. Solutions are provided for all β values	1. Solutions for small γH/c values (foundation failures) are obtained employing an approximate bearing capacity theory based on plasticity solutions. 2. Solutions for the case of large γH/c and B/H = ∞ (slope failures) are obtained by extending Janbu's solutions presented above.	$q_{cr}^0/c = N_c$ (Eq. 4.4) N_c values for both failure modes are given in Fig. 4.3
3. Bowles (1975)	1. Two-dimensional solution 2. Interwedge forces are horizontal 3. Valid for all β, γH/c, A/H and B/H values 4. Can take into account irregular slope geometries, non-homogeneous soils and any loading conditions	Sliding wedge analysis. Failure surface is divided into 3 wedges (see Fig. 4.4). Solution is achieved by satisfying the vertical equilibrium of each wedge and the overall horizontal equilibrium of the entire sliding mass.	$q_{cr}^0/c = 2.243 + \frac{2(\cos\beta + \sqrt{2}\, A/B \sin\beta)}{\sin\beta + \cos\beta} \frac{\gamma H}{c} \times \frac{B}{H} \times \frac{\sqrt{2}}{4} \times (1 - \sqrt{2}\, A/B)^2 \times \frac{\sin\beta}{\sin\beta + \cos\beta}$ (Eq. 4.5)
4. Modified Bowles (1977)	1. Two-dimensional solution 2. Soil is homogeneous with an isotropic shear strength 3. Valid for a footing on a weightless soil i.e., γH/c = 0 4. Valid for all β, A/H and B/H values	Approximate bearing capacity theory based on plasticity solutions. Comparing failure surface geometries for the case of no slope to that for the actual case, one can obtain adjusted bearing capacity coefficients, $\bar{N}_c$ and $\bar{N}_q$.	$\bar{N}_c = \{2 + (90 - \beta)\frac{\pi}{180} + 2A/B \sin\beta\} \frac{N_c}{3.57}$ (Eq. 4.8)
5. Brinch Hansen (1966)	1. Two-dimensional solution 2. Soil is homogeneous with an isotropic shear strength 3. Uniform surcharge 4. Valid for β = 0 (i.e., a bearing capacity problem). Hence, A, H, γ are irrevelevant.	Circular arc analysis. The factor of safety is defined as the ratio of the resisting moment to the disturbing moment due to gravity and surcharge loads	$q_{cr}^0/c = 5.52$
6. ———	1. Three-dimensional solution. (Everything else is the same as for the two-dimensional solution.)	Circular arc analysis. Failure surface is cylindrical with plane end surfaces. An additional resisting moment is thus created by the end surfaces.	$q_{cr}/c = 5.52\ (1 + 0.57\ B/L_p)$ (Eq. 4.10) or in general $F = F^0(1 + A_r/2\ SL_p)$ (Eq. 4.14)
7. Giger and Krizek (1976)	1. Three-dimensional solution. 2. Valid for a concentrated surcharge load. 3. Valid for β = 90°, B/H = 0, all values of A/H and γH/c. 4. The soil is assumed to be perfectly plastic with a mechanical behavior that is completely specified by the Coulomb yield criteria and its associated flow rule.	Limit analysis (Chen, 1975). The solution is based on the "upper bound theorem of the generalized theory of perfect plasticity."	See charts in Fig. 4.7.

4.3 PLANE STRAIN PROBLEMS

4.3.1 Vertical Line Loads of Infinite Extent

Fig. 4.1 shows a cohesive slope of height H making an angle β with the horizontal. The clay possesses a total unit weight γ and a cohesion c. In addition to gravity forces, the slope is subjected to an infinite line load of intensity p^0 which acts at an edge distance A from the crest of the slope.

Using the circular arc method, Taylor (1937) analyzed the stability of this slope due to gravity only, i.e., with no surcharge. He assumed that the shear surface is a cylinder of infinite length and that the mechanism of failure consists of a rigid body rotation of the cylinder about its axis $\bar{o}$-o (z-axis, Fig. 4.1). For a unit length along the z-axis, the driving moment, M_d^0, and the resisting moment, M_r^0, are given by:

$$M_d^0 = f_0(g)\ \gamma H^3 \tag{4.15}$$

$$M_r^0 = f_2(g)\ cH^2 \tag{4.16}$$

where $f_1(g)$ and $f_2(g)$ are dimensionless functions of the geometry of the slope and the shear surface. For a slope on the verge of failure (a factor of safety equalling unity), the resisting and driving moments are equal, and hence:

$$(\gamma H/c)_{cr} = F(g) \tag{4.17}$$

Taylor obtained values of the function F(g) for different slope angles β and concluded that for β equal to or greater than 53°, the failure circle passes through the toe of the slope. On the other hand, for $\beta < 53°$, a deep-seated failure is more critical and extends to a depth which depends on the bedrock location, as described by the parameter n in Fig. 4.1. Table 4.3 summarizes Taylor's results.

For a slope subjected to a surcharge load, failure can take place according to either of two modes: a) Bearing capacity, where the shear surface does not intersect the slope and, therefore, is limited to the neighborhood of the load (Bearing capacity theories for horizontal ground surfaces are applicable to such modes of failure); and, b) Slope failure, where the critical shear surface extends beyond the crest and hence involves part of the slope. Note that these two classifications are different from those used by Meyerhof (Section 4.2). In the case of a line load, bearing capacity considerations are meaningless because they lead to a zero value of the load. Hence, following treatment of line loads only considers slope failures.

The effect of a surcharge line load p^0 on the overall stability of a slope was treated by the circular arc method, as in the case of gravity alone. From consideration of equilibrium of a unit length, along the z-axis, the resisting moment, M_r^0, is given by Eq. 4.16. whereas the driving moment, M_d^0, is now given by:

Table 4.3 Critical Values of Stability Number, $(\gamma H/C)_{cr}$, After Taylor (1937)

Slope Angle, β	90°	75°	60°	45°		30°				15°		
Bedrock Location, n* (see Fig. 4.1)	--	--	--	∞	1	∞	1.5	1.25	1	∞	2	1
$(\frac{\gamma H}{c})_{cr}$	3.83	4.57	5.24	5.53	6.10	5.53	6.20	6.60	7.50	5.53	6.67	11.50

* for $\beta \gtrsim 60°$, bedrock location is irrelevant, as most critical failure mode is a toe failure (see Fig. 4.2).

$$M_d^0 = f_1(g) \cdot \gamma H^3 + f_3(g) \cdot p^0 \cdot A \qquad (4.18)$$

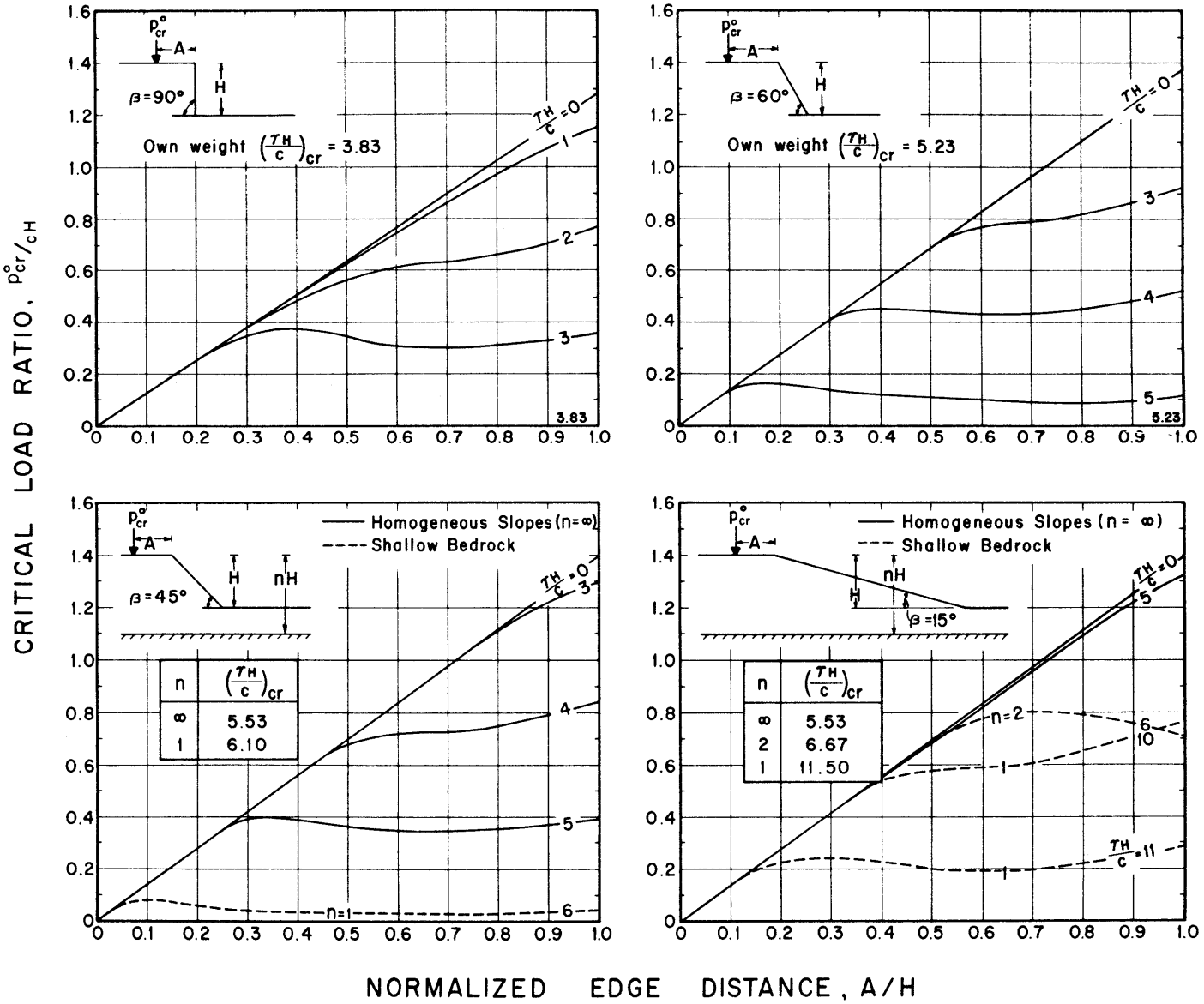
where $f_3(g)$ is a dimensionless function of the geometry of the slope and the shear surface. The critical load p_{cr}^0 required to cause failure ($M_r^0 = M_d^0$) is thus given by:

$$\frac{p_{cr}^0}{cH} = \frac{f_2(g) - (\gamma H/c)\, f_1(g)}{f_3(g) \cdot (A/H)} \qquad (4.19)$$

Since the rigid body rotation is a kinematically acceptable mechanism of failure, one seeks a minimum upper-bound solution. Contrary to the case of gravity only, which was considered by Taylor, no analytic solutions were attempted and we obtained a minimum value of p_{cr}^0/cH by employing the two dimensional option of the program STAB3D. We assumed different locations of the z-axis and different radii of the shear circle and in each case computed the functions f_1, f_2 and f_3 in order to determine the minimum value of the load p_{cr}^0/cH.

Figure 4.8 presents the dependence of the critical load ratio, p_{cr}^0/cH, on the normalized edge distance A/H for different values of $\gamma H/c$ and for slope angles between 90 and 15 degrees. It also gives the values of $(\gamma H/c)_{cr}$ which correspond to Taylor's solution for slope failure due to its own weight alone. The results for steep slopes ($\beta \geq 45°$) show that:

1. For small values of $\gamma H/c$ compared to $(\gamma H/c)_{cr}$, p_{cr}^0/cH increases linearly with A/H. This linearity basically means that for given values of β, γ, c, and A, the critical



n	$\left(\frac{\gamma H}{c}\right)_{cr}$
∞	5.53
1	6.10

n	$\left(\frac{\gamma H}{c}\right)_{cr}$
∞	5.53
2	6.67
1	11.50

Figure 4.8 Stability Charts for Line Loads of Infinite Extent

load is independent of H if the slope has a high factor of safety for self-weight only.

2. For large values of $\gamma H/c$, the surcharge load is small. In the limit, when $\gamma H/c$ equals $(\gamma H/c)_{cr}$, p^0_{cr}/cH equals zero.

3. For intermediate values of $\gamma H/c$, three distinct types of behavior can be depicted: a) when the load is near the crest, i.e., A/H is small ($\leq$ 0.3), the effect of gravity is negligible and p^0_{cr} is very close to the case of $\gamma H/c = 0$; b) for values of A/H between 0.3 and 0.8 to 0.9, gravity becomes important and decreases p^0_{cr}/cH from the value given by the $\gamma H/c = 0$ envelope; and c) when the edge distance is large ($A/H > 0.8 - 0.9$), p^0_{cr}/cH increases with A/H because of a greater increase in the resisting moment. This is a result of considering slope failures only, as discussed earlier. A more complete treatment where bearing capacity is also considered, as in the following problem of a strip load, will show that for large values of A/H, bearing capacity failures become more critical than slope failures.

4. The effect of the slope inclination β can be seen by comparing the results obtained for different values of β. For given values of $\gamma H/c$ and A/H, p^0_{cr}/cH decreases as β increases, i.e., the steeper the slope, the more important the gravity effects, and, hence, the smaller the surcharge load p^0_{cr} that can be supported by the slope. This decrease in

p^0_{cr}/cH with β is also more pronounced for large values of $\gamma H/c$.

For a flat slope (e.g., $\beta \leq 30°$), p^0_{cr}/cH is significantly affected by the location of the bedrock, as expressed by the parameter, n. For $\beta = 30°$ and $\gamma H/c = 6$, Fig. 4.9 shows that increasing the bedrock depth factor from n = 1 to n = 1.5 reduces the value of p^0_{cr}/cH significantly (especially for values of A/H greater than about 0.2). Furthermore, for the same value of n (e.g. n = 1), an increase of $\gamma H/c$ reduces the corresponding value of p^0_{cr}/cH.

The location of the z-axis (center of the slip circle) leading to the minimum value of p^0_{cr}/cH depends on β , $\gamma H/c$ and A/H. For steep slopes ($\beta \geq 45°$) and large values of A/H (≥ 0.3), the shear surface passes under the load and through the toe, resulting in a slope failure. This is also true for flatter slopes, except that in flatter slopes the z-axis falls close to the vertical line passing through the mid point of the slope, resulting in a deep-seated failure. As for smaller values of A/H (< 0.3), the z-axis falls close to the load location, indicating that a bearing capacity mode of failure is more likely than a slope failure. We emphasize, however, that only slope failures were considered, and hence centers falling to the left of the line dividing the edge distance between the load and the crest of the slope were not considered. We found no significant dependence of the location of the z-axis on the stability number $\gamma H/c$.

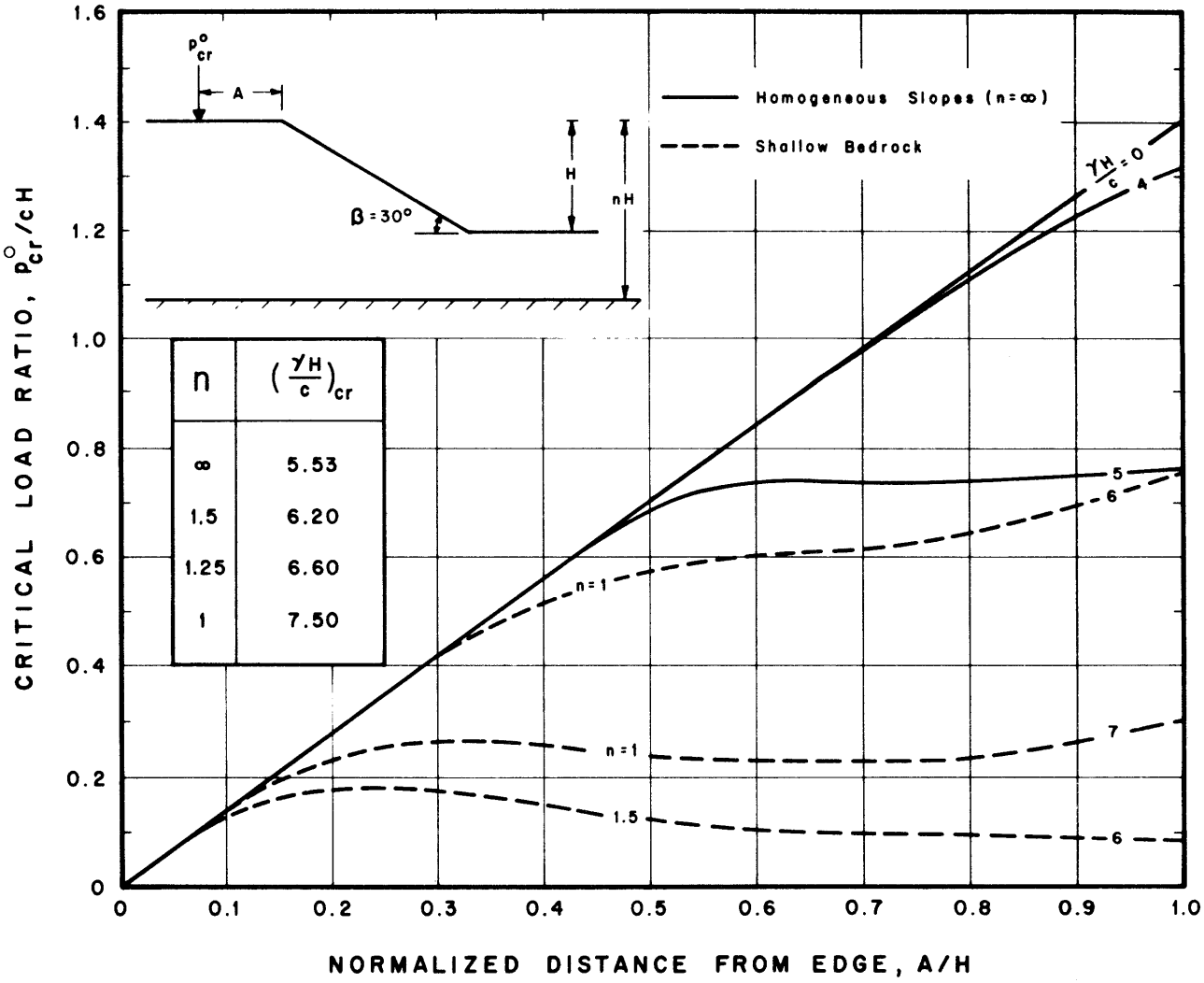


Figure 4.9 Effect of Bedrock Location for Line Loads of Infinite Extent

4.3.2 Uniform Vertical Strip Loads

The case of a strip load is similar to that of the line load treated above, except that the pressure q^0 is now applied over a finite width, B (Fig. 4.1). This problem has more practical applications because it includes both bearing capacity and slope failures, and its results can be compared with those available in the literature and presented in Section 4.2.

Using the circular arc method of analysis, the moment equilibrium of the sliding mass shows that Eq. 4.19 is valid if we use:

$$q^0_{cr} = p^0_{cr}/B \tag{4.20}$$

Combining Eqs. 4.19 and 4.20, the normalized ultimate pressure, q^0_{cr}/c is thus given by:

$$q^0_{cr}/c = \frac{H}{B} \frac{f_2(g) - \frac{\gamma H}{c} f_1(g)}{(A/H) \quad f_3(g)} \tag{4.21}$$

In order to present the results of q^0_{cr}/c obtained by the program STAB3D in a comprehensive manner, we introduce the incremental stability number, $\Delta\gamma H/c$, defined as:

$$\Delta\gamma H/c = (\gamma H/c)_{cr} - \gamma H/c \tag{4.22}$$

where the values of $(\gamma H/c)_{cr}$ are given in Table 4.3. Small values of $\Delta\gamma H/c$ correspond to slopes which are close to failure due to own weight only.

Figure 4.10 gives values of q^0_{cr}/c as a function of the slope angle, β; the normalized edge distance A/H, normalized width ratios, B/H of 0.25, 0.5 and 1; and values of $\Delta\gamma H/c$ of 1 and 3. Based on this figure, we advance the following:

1. As in the case of an infinite line load, small values of $\Delta\gamma H/c$ (corresponding to large $\gamma H/c$ values) result in small ultimate pressures, q^0_{cr}. In the limit, when $\Delta\gamma H/c = 0$, q^0_{cr}/c is also equal to zero.

2. For larger values of $\Delta\gamma H/c$ (e.g. 3), and fixed values of β and B/H, the variation of q^0_{cr}/c with A/H exhibits two types of behavior. For small values of A/H, a slope failure takes place and q^0_{cr}/c increases with A/H. Beyond a certain edge distance, which depends on $\Delta\gamma H/c$, β and B/H, bearing capacity becomes more critical and q^0_{cr}/c equals 5.52 irrespective of $\Delta\gamma H/c$ and A/H. This type of behavior was also reported by Meyerhof (Fig. 4.3b). Note here that the curves for B/H = 1, shown in Fig. 4.10, are still exhibiting the first type of variation (an increase in q^0_{cr}/c with A/H), up to the value of A/H = 1 considered. The 5.52 value, obtained by the circular arc method and reported by Brinch Hansen, is 7% higher than the more accurate bearing capacity factor 5.14 derived from plasticity theory (Prandtl, 1920).

3. For steep slopes and small values of $\Delta\gamma H/c$ (e.g. $\beta = 90°$ and $\Delta\gamma H/c = 1$), q^0_{cr}/c first increases with A/H as in the case of large values of $\Delta\gamma H/c$ described above. However, when A/H is between 0.3 and 0.5 to 0.6, the gravity effects

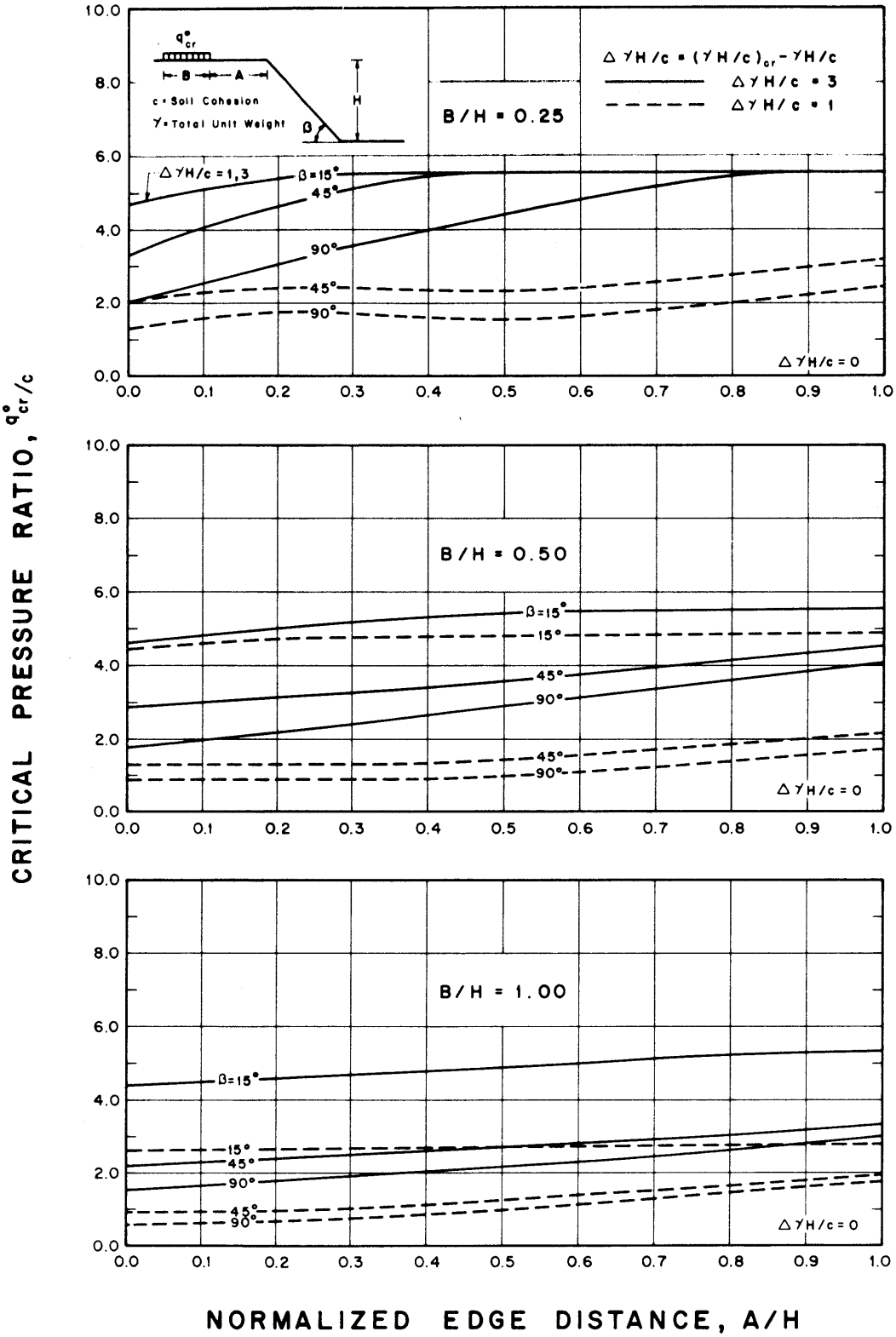


Figure 4.10 Stability Charts for a Uniform Strip Load

become important and the dependence of the surcharge load on A/H becomes similar to that observed in the case of a line load (see Fig. 4.8), i.e., decreases with A/H. For higher values of A/H, the ratio of q^0_{cr}/c increases with A/H and approaches the 5.52 limit.

4. For flat slopes ($\beta \leq 15°$), the dependence of q^0_{cr}/c on $\Delta\gamma H/c$, is not significant. On the other hand, the q^0_{cr}/c values are greatly affected by the bedrock location expressed by the parameter n (not shown in Fig. 4.10).

5. The ultimate pressures in case of narrow strip loads ($B/H < 0.25$) can be obtained by interpolation between the values in Fig. 4.10 for $B/H = 0.25$ and the results for the line loads ($B/H = 0$) in Figs. 4.8 and 4.9.

6. Similarly, for wide strip loads ($B/H > 1$), the ultimate pressures can be obtained by interpolation between the values in Fig. 4.10 for $B/H = 1$ and the results for the case of a surcharge load of infinite width ($B/H = \infty$) given by Janbu in Fig. 4.2.

7. Values of q^0_{cr}/c in Fig. 4.10 are obtained on the basis of the circular arc method of analysis. These results represent upper bound solutions and are, therefore, expected to overestimate q^0_{cr}. In the case of a footing on a horizontal surface, the circular arc method gives $q^0_{cr}/c = 5.52$ instead of the correct value of $q^0_{cr}/c = 5.14$ obtained from plasticity theory (Prandtl, 1920), the error is 7%. In order to achieve safe designs, we recommend that q^0_{cr}/c obtained from Fig. 4.10

be reduced by 7% to compensate for the error introduced by the circular arc method.

The location of the z-axis (center of the slip circle) leading to the minimum value of q^0_{cr}/c depends on β, $\Delta\gamma H/c$ (or $\gamma H/c$), and A/H (as in the case of a line load), as well as B/H. For fixed values of β, $\Delta\gamma H/c$ and A/H, the value of B/H will determine whether a bearing capacity, or a slope failure will be encountered. For any values of $\Delta\gamma H/c$ and β, large values of A/H and small values of B/H lead to bearing capacity types of failures. The corresponding z-axis is located above the right hand edge of the footing, and gives $q^0_{cr}/c = 5.52$. This result was also reported by Hansen (1966). By increasing B/H, slope failures take place and q^0_{cr}/c is reduced from 5.52 to the values shown in Fig. 4.10. In reference to the z-axis' location for slope failures, when B/H increases from zero (line load) to unity, the center of the slip circle moves to the right in an upward direction.

Finally, for the case of surcharge load located at small distances ($A/H \simeq 0$) from the crest of a steep slope ($\beta \geq 45°$), the critical failure surface tends to approach a plane with the z-axis going to infinity. This plane has an inclination of 45° and passes through the left hand edge of the strip load.

4.4 THREE-DIMENSIONAL PROBLEMS

The stability of slopes subjected to loads of finite length requires a three-dimensional analysis. Using the shear surfaces and the formulation presented in Chapter 2, we consider herein slopes with constant geometry and constant soil properties along their axis. However, in this case, the cylinder length is taken equal to that of the loaded area ($2\ell_c = L_p$, Fig. 4.11). The cone has a height, ℓ_n, the ellipsoid has a semiaxis, ℓ_e, and the total length of failure is equal to 2L.

The search for the critical shear surface is performed along the same lines as in the plane strain analysis. We assume the location of the z-axis, the value of R_{max}, and the height of the cone ℓ_n (or the ellipsoid, ℓ_e) and compute the load required to cause failure. After several trials, where all of these parameters are changed, the minimum value of the load is obtained.

4.4.1 Line Loads of Finite Length

In the case of a line load of finite length, three-dimensional end effects are expressed by the influence ratio f_L defined by the expression:

$$p_{cr} = f_L \, p^0_{cr} \tag{4.23}$$

Given β, $\gamma H/c$ and A/H, one can obtain the value of the critical line load p^0_{cr} acting along a length L_p by first deter-

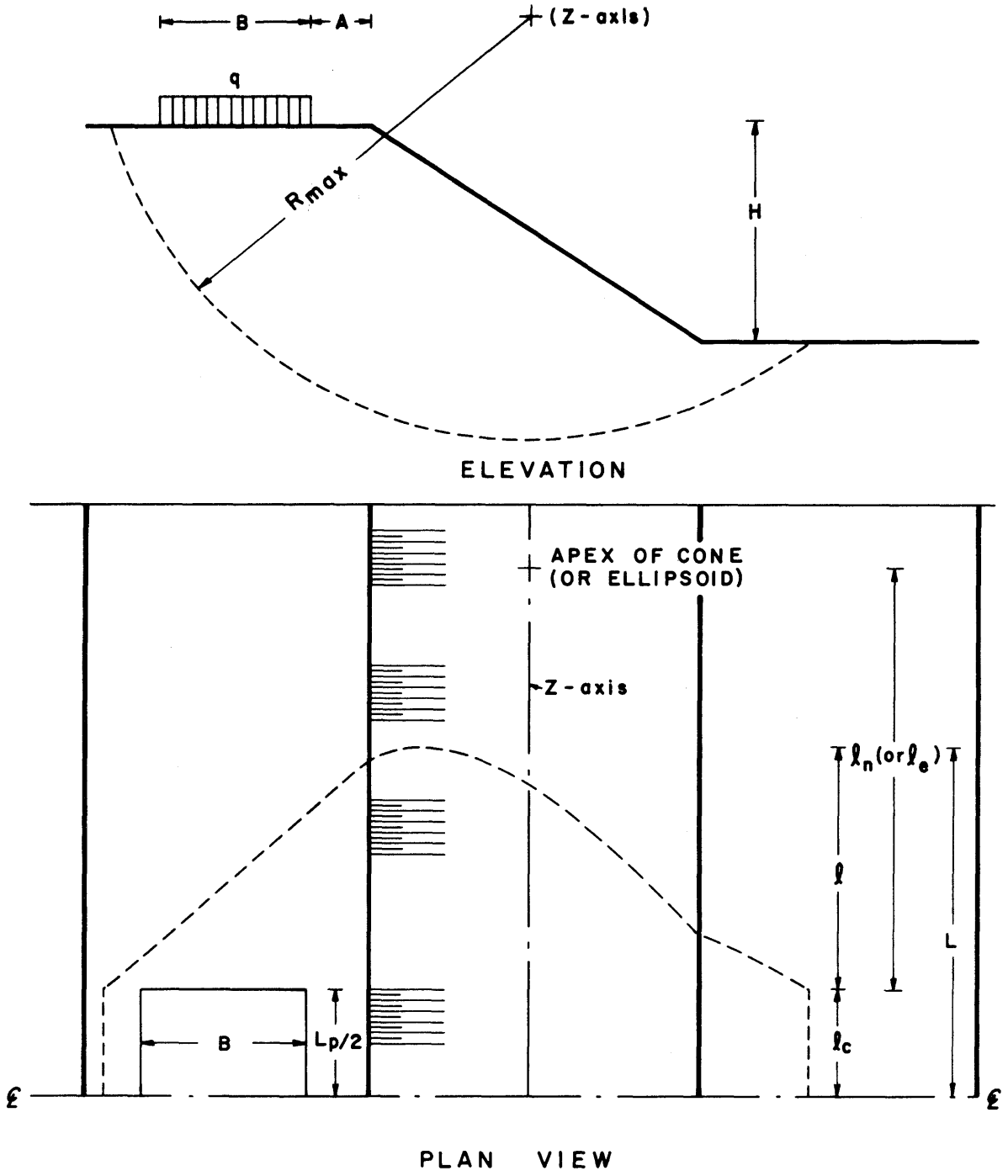


Figure 4.11 Three-Dimensional Failure Surfaces

mining p^0_{cr}/cH from Fig. 4.8 and then evaluating f_L from the plots presented in Fig. 4.12 for $0.5 \leq A/H \leq 1.1$ and in Fig. 4.13 for $0.05 \leq A/H \leq 0.5$. The results show that:

1. The magnitude of f_L decreases with increasing L_p/H for fixed values of β, $\gamma H/c$ and A/H. When L_p/H is very large, f_L equals unity (plane strain conditions).

2. Three-dimensional effects can be significant. This is illustrated by f_L values in excess of 20. Moreover, the largest f_L values for a given geometry are associated with slopes which are close to failure due to gravity alone, i.e., where $\gamma H/c$ is close to the critical value $(\gamma H/c)_{cr}$ (see Table 4.3).

3. The case of a concentrated load, corresponding to very small values of L_p/H, provides meaningless results. The most critical condition for this case was found to correspond to a failure surface having zero area, i.e., a bearing capacity type of failure with zero load.

4. For intermediate values of L_p/H, the magnitude of f_L is generally affected by β, $\gamma H/c$ and A/H. For a given slope angle β, the value of f_L increases with $\gamma H/c$ and A/H. However, f_L is not significantly dependent on the slope angle β for slopes having high factors of safety under gravity forces, e.g., when $\gamma H/c$ is small compared to $(\gamma H/c)_{cr}$. Furthermore, for values of A/H smaller than 0.5, f_L is essentially independent of both $\gamma H/c$ and β (Fig. 4.13).

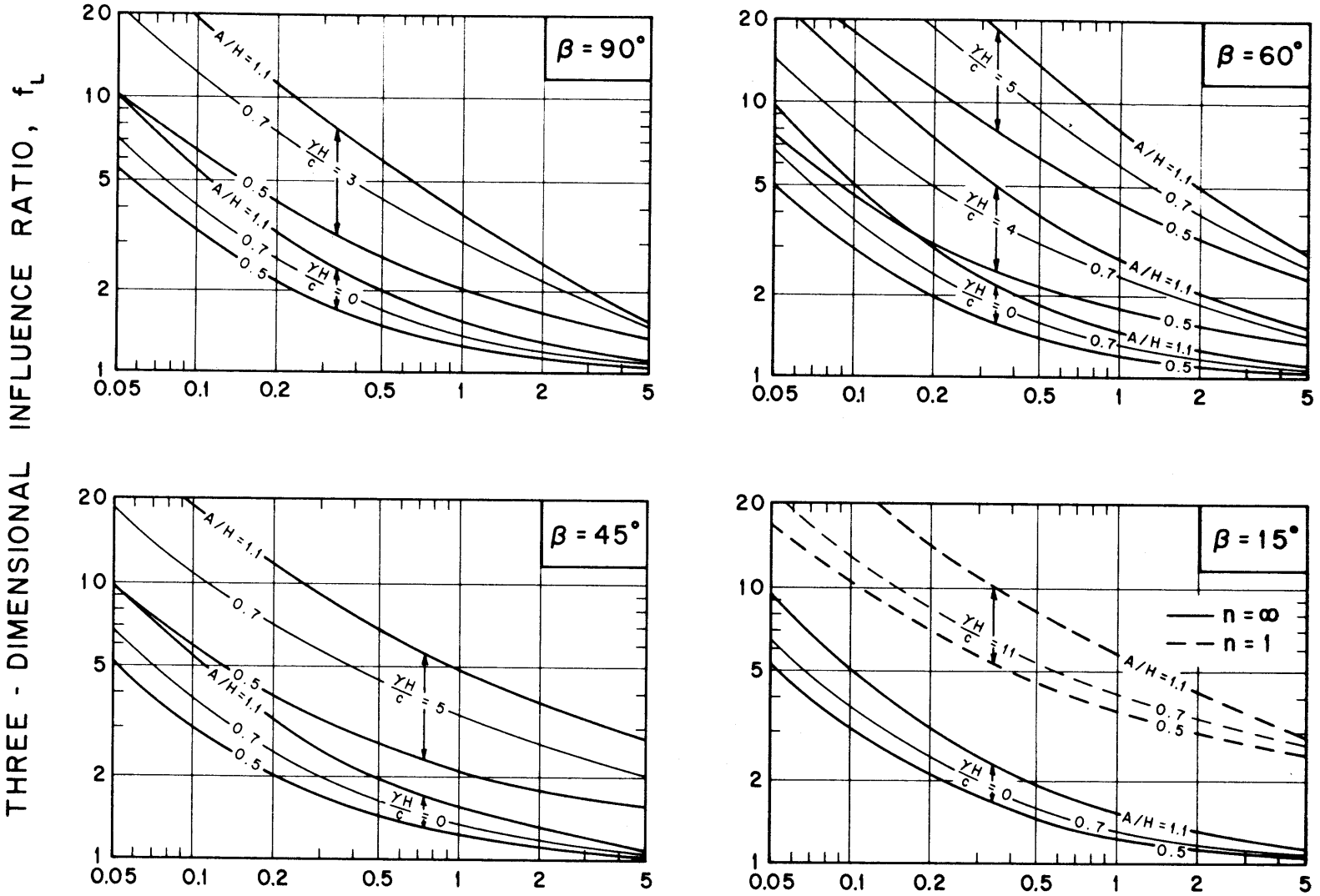


Figure 4.12 End Effects for Line Loads of Finite Length (A/H $\geq$ 0.5)

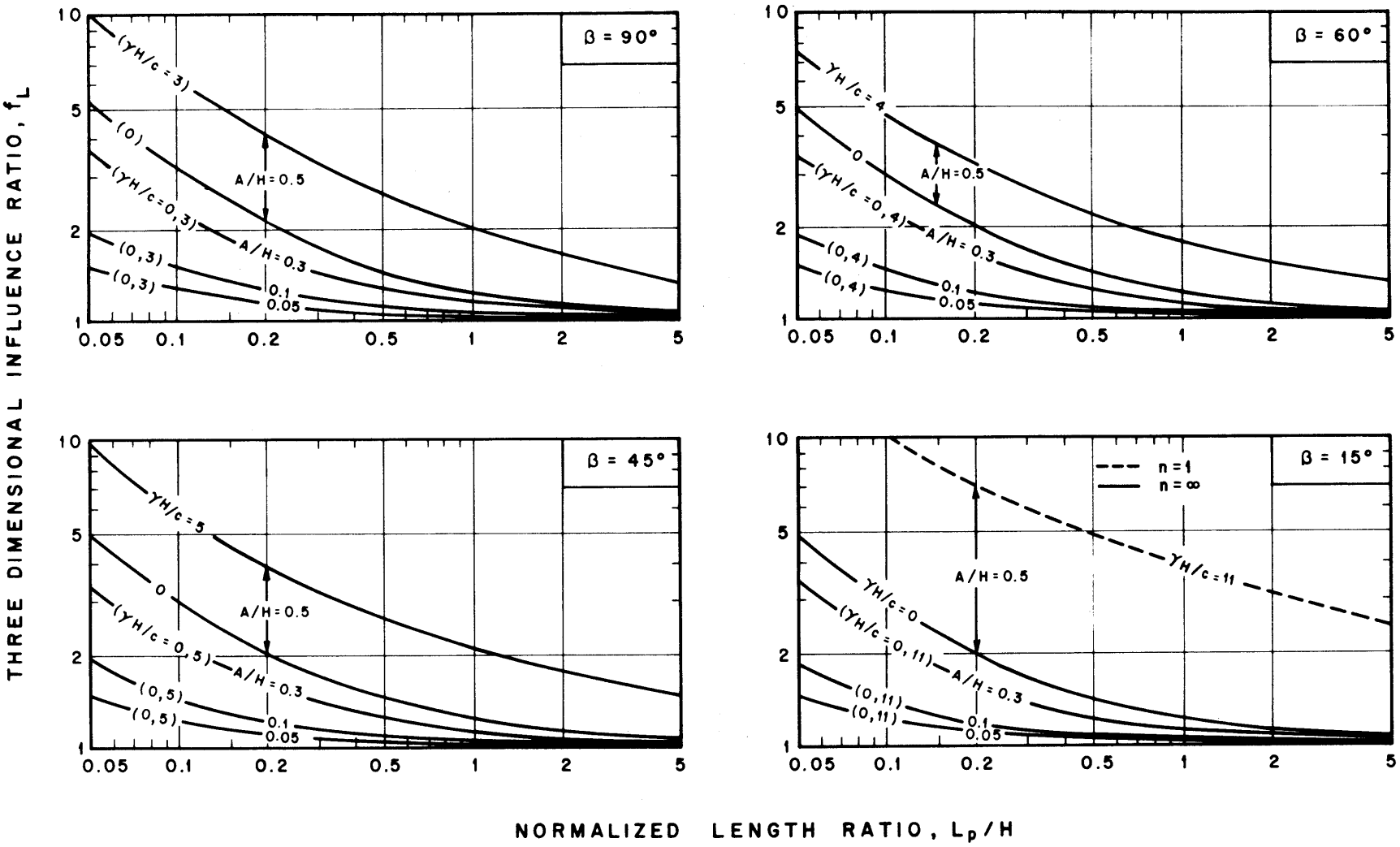


Figure 4.13 End Effects for Line Loads of Finite Length ($A/H \leq 0.5$)

5. As in plane strain solutions, the location of bedrock, as expressed by the depth factor, n, affects the value of the critical load causing failure of shallow slopes.

The shape of the shear surface (conical vs. ellipsoidal) depends on the stability number, N_s, and on the normalized edge distance A/H. For small values of N_s (e.g. ≤ 2) and values of A/H smaller than 0.5, we found the most critical shear surfaces to be conical. Ellipsoidal shear surfaces are more critical for larger values of N_s and A/H. However, the critical load ratio is not significantly different for ellipsoidal and conical shear surfaces (no more than 5 to 10%).

Three-dimensional effects influence the location of the z-axis by moving the two-dimensional centers downward and in the direction of the load. The amount of center displacement depends mainly on the normalized length ratio, L_p/H.

4.4.2 Square Loaded Areas

Finally, we considered the problem of a loaded area of length L_p and width B which is often encountered in practice. In general, we can express the ultimate pressure, q_{cr}, of a footing located on the top of a slope as follows:

$$q_{cr}/c = f(\gamma H/c, \beta, A/H, B/H, L_p/H, n) \qquad (4.24)$$

The uniform strip load problem (Section 4.3) corresponding to one value of L_p/H ($L_p/H = \infty$), gives an indication of the effort and cost that would be required to develop stability charts for all values of L_p/H. Therefore, we decided to treat only the

case of square loaded areas ($L_p/B = 1$). This ratio has special significance because it can closely approximate the case of circular loaded areas frequently encountered.

Figure 4.14 presents the values of q_{cr}/c for different values of β, B/H, A/H and $\Delta\gamma H/c$. The results show that:

1. Small values of $\Delta\gamma H/c$ results in small surcharge loads q_{cr}/c. In the limit when $\Delta\gamma H/c$ equals zero, the surcharge load also equals zero.

2. As in the case of a uniform strip load, the curves in Fig. 4.14 exhibit two types of behavior. For small values of A/H, q_{cr}/c increases with increasing A/H, and failure includes part of the slope. However, beyond a critical value of A/H, which depends on β, B/H, $\Delta\gamma H/c$, bearing capacity becomes more critical, and q_{cr}/c reaches a constant value of 8.64. This corresponds to a shear surface consisting of a cylinder with plane end surfaces as reported by Brinch Hansen (1966). The end effects increase the bearing capacity by about 57% (8.64/5.52).

3. Three-dimensional effects can be significant, especially in slopes which are close to failure due to gravity alone, i.e., where $\Delta\gamma H/c$ is close to zero. As an illustration of end effects, let us consider a vertical cut ($\beta = 90°$) with $\gamma H/c = 2.83$ ($\Delta\gamma H/c = 1$) which supports a square loaded area with a width ratio B/H = 0.5 located at an edge distance ratio A/H = 0.5. A conventional plane strain analysis of this slope ($L_p/H = \infty$) gives $q^0_{cr}/c = 0.9$ (see Fig. 4.10). Introducing end effects with $L_p/H = B/H = 0.5$, Fig. 4.14 gives

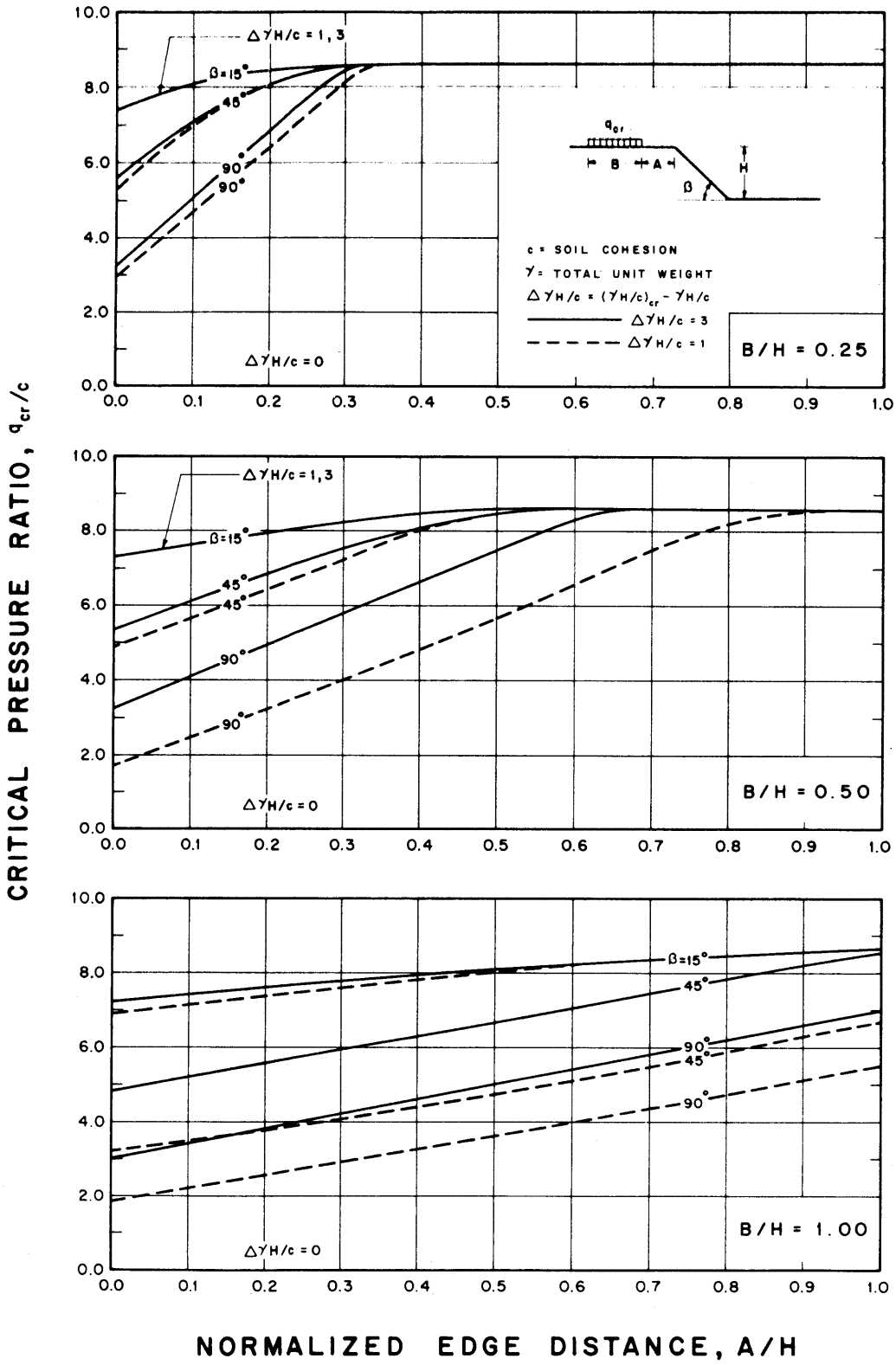


Figure 4.14 End Effects for Square Loaded Areas

$q_{cr}/c = 5.60$, i.e., three-dimensional effects increase the critical pressure about 6 times.

4. For small values of A/H, q_{cr}/c is significantly dependent on the slope angle β. When $B/H = A/H = 0.5$, and $\Delta\gamma H/c = 1$, the effect of increasing β from 15° to 90° causes a decrease in q_{cr}/c from 8.64 to 5.60.

5. In flat slopes ($\beta \leq 15°$), q_{cr}/c is not significantly affected by $\gamma H/c$. However, q_{cr}/c is considerably influenced by the location of bedrock, as described by the parameter n (not shown in figure 4.14).

6. Values of q_{cr} for narrow footings ($B/H < 0.25$) can be estimated from p_{cr}/B, where p_{cr} is given by the line load solutions in Fig. 4.8 and 4.12 (or 4.13). In such cases, bearing capacity failures need to be checked separately.

7. Values of q_{cr} determined herein are based on shear surfaces of revolution (cylinders, cones and ellipsoids). These results represent upper bound solutions and are, therefore, expected to overestimate q_{cr}. In the case of a square footing on a horizontal surface, we get $q_{cr}/c = 8.64$. On the basis of empirical observations, Skempton (1951) recommends $q_{cr}/c = 6.2$ for a square footing. Plasticity solutions for a circular footing derived by Shield (1955) give $q_{cr}/c = 5.69$. Upper bound solutions for a square footing obtained by Shield and Drucker (1953) give $q_{cr}/c = 5.71$.

Hence, in order to achieve safe designs, we recommend

that q_{cr}/c obtained from Fig. 4.14 be reduced 30% to compensate for the error introduced by using simple shear surfaces of revolution.

As with the two-dimensional case, footings located at small distances from the crest of steep slopes ($\beta \geq 45°$) produce planar failure surfaces. These planes are inclined at 45° and pass through the left hand edge of the loaded areas.

Finally, the comments mentioned earlier about the shapes of the most critical failure surfaces (Section 4.4.1) and the locations of the corresponding axes (z-axes) are also valid here. For slopes with small N_s values subjected to loads located at edge distances < 0.5 H, conical failure surfaces are more critical than ellipsoidal. The inverse is true for larger N_s and A/H values.

4.5 METHODOLOGY EVALUATION

This section presents evaluations of the prediction techniques mentioned in previous sections. We will look at the advantages and disadvantages of each prediction method, and pay particular attention to the assumptions used, the regions of applicability, and the accuracy of predictions.

4.5.1 Evaluation of Two-Dimensional Methods

Janbu's method (1954) considers the case of a slope subjected to a surcharge load of infinite extent in the horizontal direction -- an assumption rarely encountered in actual problems. Furthermore, the method is based on the circular arc method of analysis, which, in case of a drained analysis ($\phi \neq 0$), requires simplifying assumptions regarding the effective normal stress on the failure plane at failure in order to achieve statical determinancy. Janbu adopts the assumption of the ordinary method of slices (Fellenius, 1936). This method was shown (Wright, 1969) to yield unreasonable values of the factor of safety, which may in turn lead to inaccurate estimates of the ultimate pressure p^0_{cr}. Therefore, one should be cautious when using Janbu's method to compute the ultimate drained pressure of footings on slopes. On the other hand, Janbu's method is very simple to apply, and is capable of taking the effect of a rigid layer at a certain depth below the toe of the slope into consideration.

Meyerhof (1957) indicated in his analysis that the sta-

bility number, $\gamma H/c$, governs the type of the failure mode of foundations on slopes. Slopes with small $\gamma H/c$ values tend to have a foundation failure, whereas slopes with large $\gamma H/c$ values have an overall failure through the toe or the base of the slope (see Fig. 4.3). Meyerhof solved the case of slope failures for wide foundations ($B/H = \infty$) located at a distance, A, from the crest of the slope. He achieved that by extending Janbu's solutions presented in Fig. 4.2. Observing the bottom part of Fig. 4.3, one finds that a vertical cut with $N_s = 4$ is capable of carrying an additional surcharge load. However, as Table 4.3 indicates, the most critical N_s value for a 90° slope is 3.83, beyond which the slope fails due to gravity alone. Let us consider the following example: a vertical cut of height H = 20 ft, a total unit weight, γ = 100 pcf and an undrained shear strength, s_u = 500 psf. Find the ultimate uniform load that can be placed at a distance of 30 ft from the edge of the slope. The input parameters needed for Meyerhof's charts (Fig. 4.3) are:

$$N_s = \gamma H/c = \frac{100 \times 20}{500} = 4$$

$$A/H = \frac{30}{20} = 1.5$$

Figure 4.3 shows that for $N_s = 4$, $A/H = 1.5$ and $\beta = 90°$, the ultimate pressure $q^0_{cr} = 0.6 \times 500 = 300$ psf. Let us then check the stability of this slope due to gravity alone, i.e., without the surcharge load. Using Fig. 4.2c of Janbu's charts

one finds for a $\beta = 90°$ that $N_s = 3.83$. Hence, the factor of safety, F^0 , is equal to $3.83/4 = 0.96$ and the slope is unsafe due to gravity forces alone, i.e., no surcharge loads can be added. Therefore, Meyerhof's curve for $\beta = 90°$ and $\gamma H/c$ of 4 should not be used. Furthermore, Meyerhof's charts do not provide solutions for foundations with $B/H \leq 1$ resting on slopes with large values of $\gamma H/c$, i.e., near failure due to gravity. Finally, Meyerhof does not detail how he extended Janbu's solutions.

Bowles' method of analysis (1975) allows one to consider such factors as irregular geometries, non-homogeneous soil conditions, and nonuniform surcharge loads. Bowles achieves statical determinancy by assuming that the interwedge forces are horizontal, and determines an expression for the ultimate pressure by satisfying the vertical equilibrium of each wedge and the overall horizontal equilibrium of the entire sliding mass. This assumption neglects the shear resistance along the vertical boundaries between wedges, which may lead to unreasonable estimates of the ultimate surcharge pressure. An improved technique would consider inclined interwedge forces. The modified Bowles' method (1977) offers simplicity and can therefore be used to indicate the ultimate pressure.

Brinch Hansen's solutions (1966) are approximate and, difficult to assess and will not be used in the following discussions or comparisons.

In order to compare the different methods of analysis,

we consider the following three examples which were chosen to portray three different failure modes. The first represents a slope with a small value of $\gamma H/c$ supporting a narrow footing located at a small edge distance, A. The shear surface in such a case intersects the slope in a position higher than its toe. The second example is the same as the first, but the edge distance A is large enough to cause a bearing capacity failure. The ultimate pressure in this case is independent of the slope angle, β, and the stability number, $\gamma H/c$. The third example considers a failure through the toe or the base of the slope because $\gamma H/c$ is large and the footing is wide.

Table 4.4 shows the predictions obtained according to different methods. It indicates that the method proposed herein generally agrees with the other methods in their range of applicability. However, as was mentioned in Section 4.3, a 7% reduction should be applied to all the results to compensate for the error introduced by the circular arc method of analysis.

To summarize, the method we propose in this thesis complements the existing design charts. For example, it provides solutions for the case of a foundation with $B/H \leq 1$ resting on a slope with a large $\gamma H/c$ value -- a condition one is very likely to encounter, and one that Meyerhof's charts fail to include.

4.5.2 Evaluation of Three-Dimensional Methods

Giger and Krizek (1976) attempted to solve the problem at

Table 4.4 Comparison of Predictions According to Different Methods

Case	Geometry characteristics			Load Characteristics		Ultimate bearing pressure according to			
	β°	γH/c	ΔγH/c	A/H	B/H	Figure 4.10(1)	Bowles (1975)	Janbu (1954)	Meyerhof(3) (1957)
1	90	0.83	3	0.1	0.25	2.5	3.36	N.A.(2)	3.20
	45	2.53	3	0.1	0.25	4.0	3.79	N.A.	2.20
2	90	0.83	3	1.00	0.25	5.52	5.14	N.A.	3.00
	45	2.53	3	1.00	0.25	5.52	5.14	N.A.	2.65
3	90	2.83	1	0	1.00	0.60	1.24	0.50	0.55
	60	4.24	1	0	1.00	0.70	2.03	0.63	0.35

(1) Before the 7% reduction recommended for design

(2) Method not applicable

(3) Method is not clearly applicable to the author

hand in three dimensions. They considered the problem of a vertical cut, with variable corner angle, subjected to a concentrated surcharge load. However, the following remarks are in order regarding their method of analysis:

1. We found the case of a concentrated load treated in their work (line load solutions with very small values of L_p/H) to yield meaningless results. The most critical condition for this case corresponds to a failure surface having zero area, i.e., a bearing capacity type of failure with zero load.

2. Observing the results in Fig. 4.7b for the case of a vertical cut with a corner angle of 180°, one finds that, for the $\phi = 0$ case, the maximum stability number on the design chart is 4.52. Since the slope extends infinitely in the longitudinal direction, and soil properties along the axis of the slope are constant, one would expect a plane strain failure due to gravity alone to take place at an N_s value of 3.83; hence, the 4.52 value will never be reached.

3. More importantly, Giger and Krizek's method significantly overestimates the values of the critical load needed to cause undrained failures of vertical slopes. Figure 4.15 reproduces their results for $\gamma H/c = 0$ and 3. Figure 4.15 also shows the results obtained by assuming a conical failure surface with its axis at the crest of the slope and passing under the load. This mode of failure is simple enough to have the analytic solution presented in Fig. 4.16 but <u>does not</u>

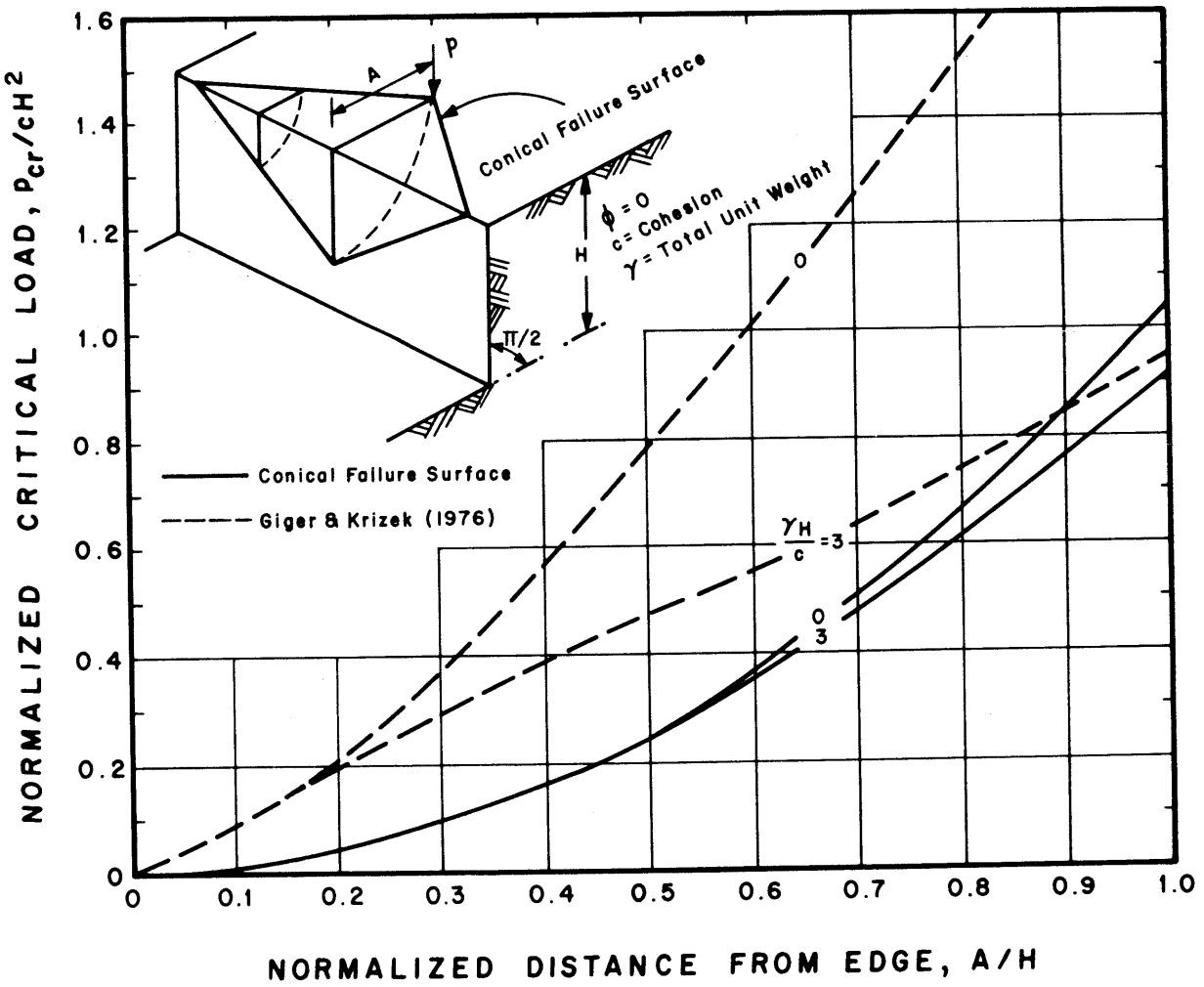


Figure 4.15 Critical Concentrated Load Causing Failure Along a Conical Surface

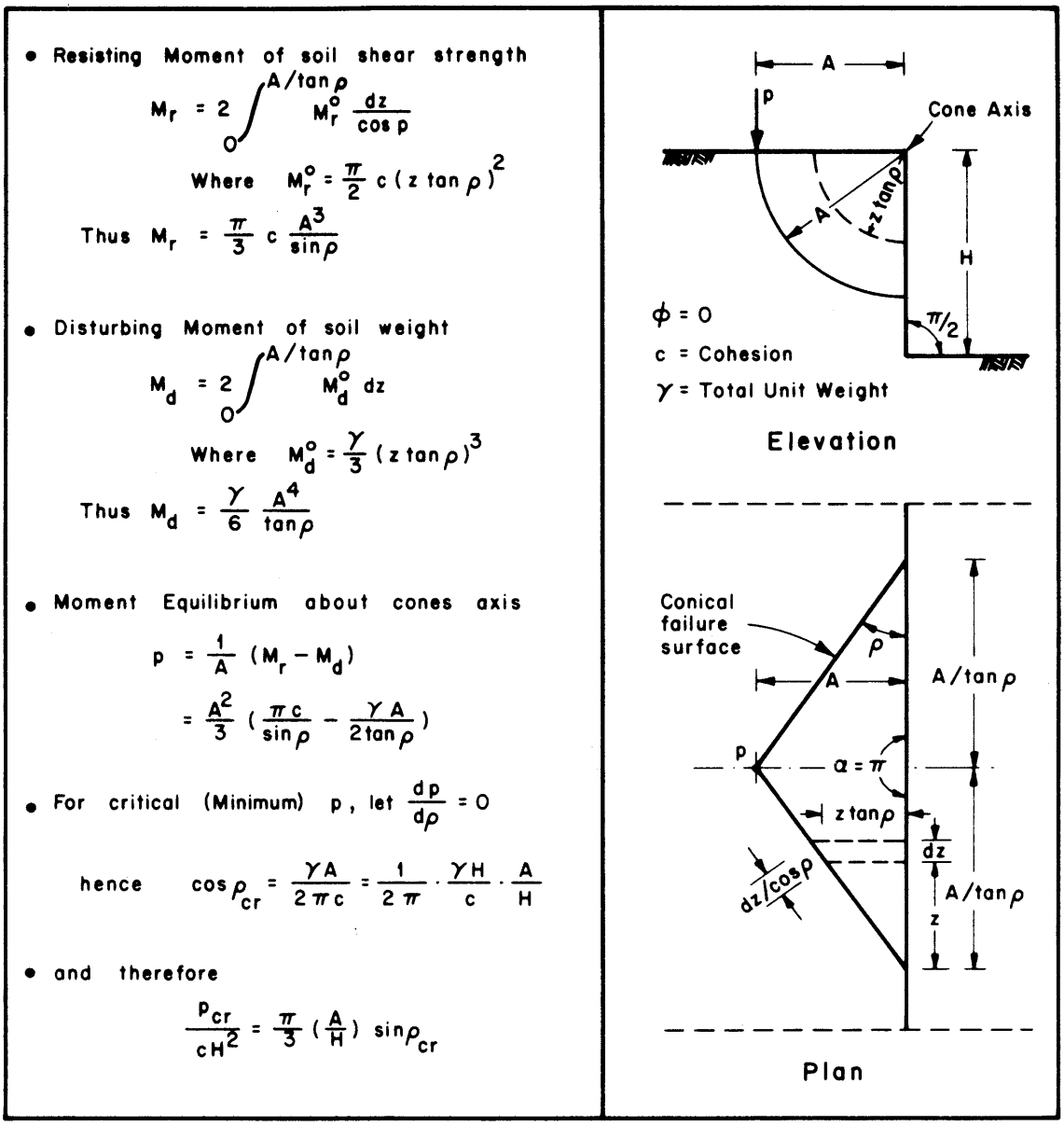


Figure 4.16 Concentrated Load Causing Failure of a Vertical Cut in Frictionless Soil

represent the most critical mode which gives the minimum value of the concentrated load. Nevertheless, Fig. 4.15 shows that the load p_{cr} predicted on the basis of this simple solution is much lower that that obtained by the complicated mechanism used by Giger and Krizek, especially for small values of $\gamma H/c$ and A/H.

As an illustration, they predict that for a vertical cut of height H = 50 ft, in a clay having an undrained shear strength, $c = s_u = 1$ tsf, and a total unit weight $\gamma = 110$ pcf, a drag line weight, $p_{cr} = 500$ tons can be located as close as A = 10 ft (A/H = 0.2) from the crest of the slope. On the other hand, the simple analysis presented herein shows that p_{cr} in excess of 105 tons acting at A/H = 0.2 would cause failure of the slope. Hence, Giger and Krizek's design charts should be used with extreme caution.

4.6 SUMMARY AND CONCLUSIONS

This chapter considers the undrained stability ($\phi = 0$, $c = s_u$) of homogeneous slopes subjected to infinitely long line and strip loads, as well as line loads of finite length and square loaded areas.

Two-dimensional analysis is treated by means of the classical circular arc method. Slopes subjected to three-dimensional loadings, are analyzed by the shear surfaces presented in Chapter 2 and shown in Fig. 4.11. The factor of safety is defined as the ratio of the resisting moment, due to the soil resistance along the shear surface, to the disturbing moment due to gravity and surcharge loads. The critical surcharge load, leading to a value of the factor of safety equal to unity, is found numerically by means of the program STAB3D. Results are presented in the form of charts suitable for performing undrained stability analyses. The major conclusions advanced from this study are as follows:

1. The critical surcharge load to cause failure of a cohesive slope of height H possessing a uniform strength, c, and a unit weight, γ (Fig. 4.1) depends on six dimensionless parameters grouped into two categories. The first describes the slope and consists of the stability number, $\gamma H/c$, the slope angle β, and the bedrock location expressed by the parameter

n. The second set of parameters describes the load by means of the width ratio, B/H, length ratio, L_p/H, and the normalized edge distance from the edge of the slope, A/H.

2. For a slope subjected to a surcharge load, failure can take place according to one of two modes: a) Bearing capacity, where the failure surface does not intersect the slope (bearing capacity theories for horizontal ground surfaces are applicable to such modes of failure); and, b) slope failure, where the critical shear surface extends beyond the crest and hence involves part of the slope.

This can be illustrated by observing Figs. 4.10 and 4.14. For fixed values of β and B/H, the variation of the critical load with the normalized edge distance exhibits two types of behavior. For small values of A/H, a slope failure takes place and the critical load increases with A/H. Beyond a certain edge distance, which depends on $\gamma H/c$, β and B/H, bearing capacity becomes more important and the critical load reaches a constant value irrespective of all other parameters influencing the problem.

3. The stability number, $\gamma H/c$, is a measure of the importance of gravity. Failure of a certain slope due to gravity alone takes place when its $\gamma H/c$ is equal to the critical value $(\gamma H/c)_{cr}$ given in Table 4.3. The incremental stability number, $\Delta\gamma H/c$ (= $(\gamma H/c)_{cr} - \gamma H/c$), which vanishes for a slope on the verge of failure due to gravity alone is, in some cases, a more convenient indication of the gravity effects. In

general, small values of $\Delta\gamma H/c$ lead to small values of the critical surcharge load (Figs. 4.10 and 4.14). This is particularly true for long loaded areas (L_p/H large) acting on steep slopes ($\beta \geq 45°$).

4. The slope angle β is important in two aspects -- an increase in β will decrease the value of $(\gamma H/c)_{cr}$ and hence decreases the critical surcharge pressure. However, the use of $\Delta\gamma H/c$ instead of $\gamma H/c$ tend to reduce the importance of β in this respect. Furthermore, as β increases, the failure mode changes from base to toe failure. This reduces the arc length of the shear surface leading to smaller surcharge loads.

5. The bedrock location as described by the parameter n affects the surcharge load on flat slopes which are close to failure due to gravity alone ($\Delta\gamma H/c$ is small). A shallow bedrock (n small) prevents deep-seated failures from taking place and thus increases the critical load.

6. The dimensions of the load are important in determining the failure mode: a - Large B/A values indicate that slope, rather than bearing capacity failure is likely to take place. If $\Delta\gamma H/c$ is small and B/H is large, deep-seated failures (base or toe failures) occur. However, if $\Delta\gamma H/c$ is large and B/H is small, a shallow slope failure is more probable. b - When B/A is small, bearing capacity failure takes place irrespective of the slope characteristics. The critical value of B/A beyond which bearing capacity failure occurs

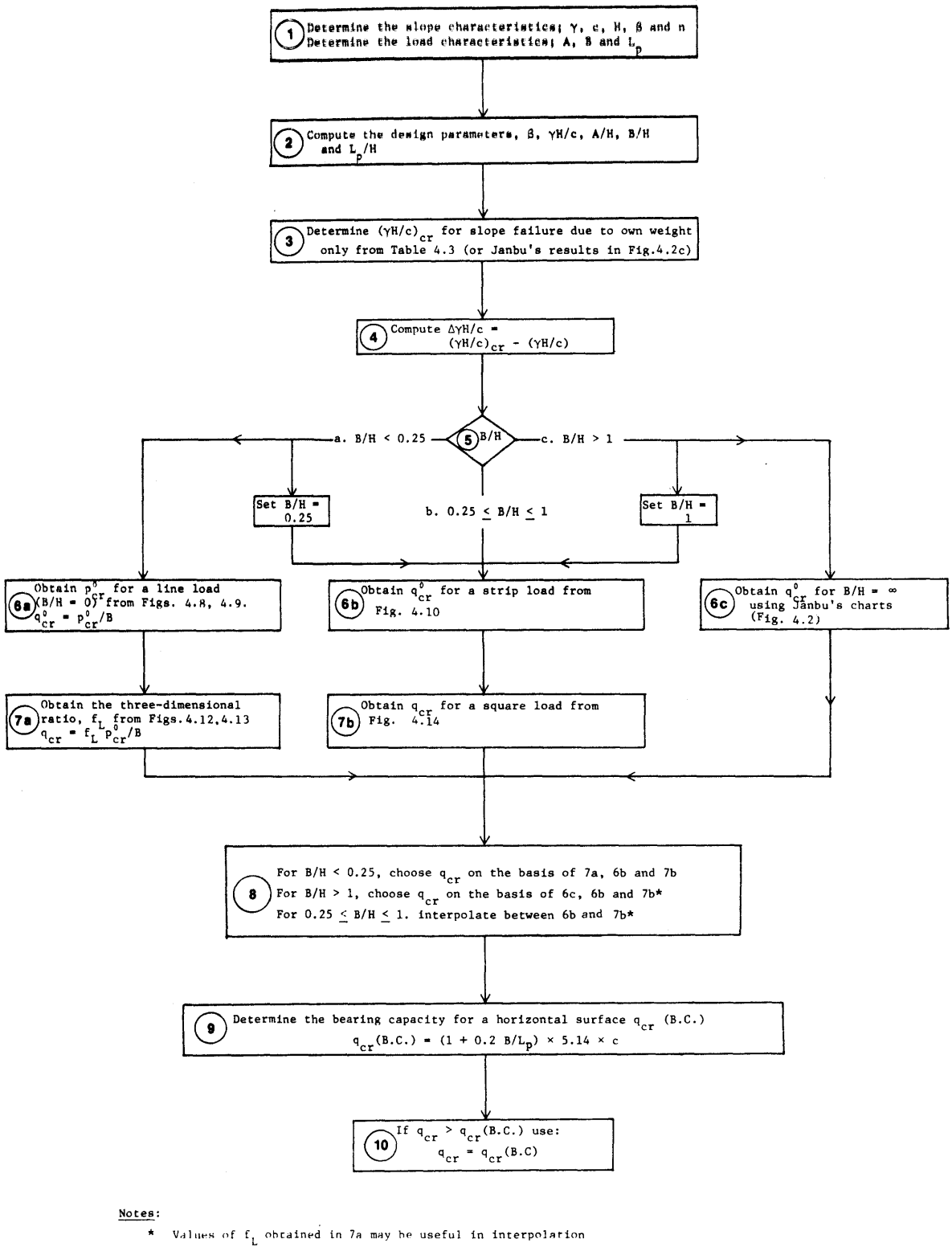
depends on β, $\Delta\gamma H/c$ and L_p/H.

7. Results for lines loads show that three-dimensional effects become significant whenever L_p/H is less than unity and are especially important when the factor of safety of the slope due to own weight only is close to unity ($\Delta\gamma H/c \simeq 0$). For many practical situations, three-dimensional effects would increase the plane strain critical load by a factor of 5 to 10.

8. The shape of the three-dimensional failure surface (conical vs. ellipsoidal) depends on $\gamma H/c$ and A/H. For small values of $\gamma H/c$ ($\leq$ 2) and values of A/H smaller than 0.5, we found the most critical shear surfaces to be conical. Ellipsoidal shear surfaces are more critical for larger values of $\gamma H/c$ and A/H. However, the critical load is not significantly different for ellipoidal and conical shear surfaces (no more than 5 to 10%).

9. Values of the critical load determined herein are based on shear surfaces of revolution (cylinders, cones and ellipses). These results represent upper bound solutions and are, therefore, expected to overestimate the critical load. Hence, in order to achieve safe designs, we recommend that critical load values obtained from Fig. 4.10 be reduced 7% and those obtained from Fig. 4.14 be reduced 30%.

Finally, a flow chart, showing the use of the design charts presented in this chapter to predict the ultimate load causing failure of a cohesive slope, is presented in Fig. 4.17.



Notes:

* Values of f_L obtained in 7a may be useful in interpolation

Figure 4.17 Prediction Method for the Ultimate Surcharge Load

CHAPTER 5

UNDRAINED STABILITY OF HOMOGENEOUS SLOPES WITH ANISOTROPIC STRENGTH

Anisotropy of the undrained shear strength denotes the dependence of s_u on the principal directions at failure, Fig. 5.1. When a sample is tested with the major principal stress at failure, σ_{1f}, is either in the vertical or horizontal directions, the measured shear strength is designated by $s_u(V)$ or $s_u(H)$, respectively. When the major principal stress at failure makes an angle i with the vertical, the strength is denoted by $s_u(i)$.

Ladd et al. (1977) interpret the undrained shear strength anisotropy, in terms of:

(1) Inherent Anisotropy - This component of strength anisotropy is a direct result of the in situ soil structure. During one-dimensional deposition and subsequent loading, particles tend to become oriented in the horizontal direction. This preferred particle orientation causes an inherent anisotropy in the undrained shear strength as well as other soil properties. Inherent anisotropy also occurs if the material is layered (non-homogeneous). One example of this type of anisotropy is with varved clays consisting of alternating layers of "silt" and "clay."

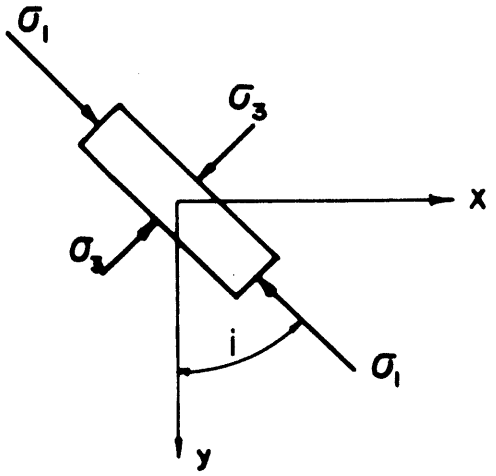


Figure 5.1 A Soil Sample Loaded with σ_1 Making an angle i with the Vertical

(2) Stress System Induced Anisotropy - Soils can exhibit a stress system induced anisotropy whenever the coefficient of earth pressure at rest, K_o, is not equal to unity. This results from the fact that different increments of shear stress are required to produce failure as the major principal stress at failure, σ_{1f}, varies between the vertical and horizontal directions.

(3) Combined Anisotropy - Combined anisotropy includes the total effects of inherent and stress system induced anisotropy.

Sambhandharaksa (1977) presented an excellent review of different means of measuring the undrained shear strength anisotropy. According to Sambhandharaksa, two approaches are used to measure strength anisotropy of clays in the laboratory. The first consists of testing samples at different orientation (with respect to the in situ vertical axis) using the unconsolidated-undrained triaxial compression test, UUC. However, sample disturbance tends to mask the anisotropic effects measured in the UUC tests for nonlayered (homogeneous) clays, and may increase them for layered soils. Furthermore, in the UUC tests, shear starts from an isotropic state of stress, and hence, the measured anisotropy does not include the stress system effect. Therefore, UUC tests give, at best, a crude estimate of strength anisotropy.

The second approach uses consolidated-undrained tests, CU.

In order to reduce the effect of sample disturbance, and include the stress system effect, the sample is reconsolidated before shearing under a system of stresses simulating the field conditions. With the current testing capabilities, $s_u(i)$ can be measured for i = 0° (plane strain or triaxial compression), i = 90° (plane strain or triaxial extension) and i = 30°-45° (direct simple shear). However, it should be noted that triaxial compression, direct simple shear and triaxial extension tests have different values of the intermediate principal stress (in triaxial compression, $\sigma_2 = \sigma_3$; in direct simple shear, $\sigma_1 > \sigma_2 > \sigma_3$; and, in triaxial extension, $\sigma_2 = \sigma_1$). Therefore, results of these tests cannot be used directly to obtain the in situ directional variation of s_u unless the data are corrected for the estimated effect of this factor.

The variation of the undrained shear strength with loading direction of several normally consolidated clays is presented in Table 5.1. The data were obtained from K_o - consolidated-undrained plane strain compression, direct simple shear and plane strain extension tests, $\overline{CK_oU}$PSC, $\overline{CK_oU}$DSS and $\overline{CK_oU}$PSE, respectively (Ladd et al., 1977). The data show that, for the first five soils, s_u decreases progressively as σ_{1f} moves from the vertical to the horizontal direction with the reduction being largest with lean sensitive clays. For example, $s_u(V)/\bar{\sigma}_{vc}$ for Portsmouth Clay is more than twice the value of $s_u(H)/\bar{\sigma}_{vc}$. For varved clay (soil No. 6 in Table 5.1), $s_u(DSS)/\bar{\sigma}_{vc}$ is significantly lower than both $s_u(V)/\bar{\sigma}_{vc}$ and $s_u(H)/\bar{\sigma}_{vc}$. In sum-

Table 5.1 Undrained Strength Anisotropy of Normally Consolidated Clays*
(from Ladd et al., 1977)

Type of Soil	Index Properties			$s_u/\bar{\sigma}_{vc}$ (1)			$K_s = \frac{(5)}{(3)}$	$b/a = \frac{(4)}{\sqrt{(3) \times (5)}}$
	w_ℓ (%)	P.I. (%)	(2) L.I.	(3) PSC	**(4) DSS	(5) PSE		
Portsmouth Clay	35	15	1.8	0.350	0.200	0.155	0.44	0.86
Haney Sensitive Clay	44	18	0.75	0.296	———	0.211	0.71	———
Boston Blue Clay	41	21	0.81	0.340	0.200	0.190	0.56	0.79
AGS CH Clay	71	40	——	0.370	0.250	0.220	0.59	0.88
San Francisco Bay Mud	88	45	1.04	0.370	0.250	0.280	0.76	0.78
Connecticut Valley Varved Clay	35-65	12-39	1.00	0.280	0.165	0.255	0.91	0.62

* From $\overline{CK_oU}$ plane strain tests with $\bar{\sigma}_{vc}$ > (1.5 to 2) × $\bar{\sigma}_{vm}$

(1) $s_u = q_f = 0.5(\sigma_1 - \sigma_3)_f$ except for DSS where $s_u = (\tau_h)_{max}$ (2) L.I. $= \frac{w_n - w_p}{w_\ell - w_p}$

(3) plane strain compression (4) direct simple shear (5) plane strain extension

** Assuming $s_u(DSS) = s_u(45°)$

mary, Table 5.1 shows that undrained shear strength of clays is highly dependent on the direction of loading.

In slope stability problems, the state of stress varies significantly along potential failure surfaces. Near the top of the slope, the direction of the major principal stress, σ_1, is nearly vertical (Fig. 5.2), whereas near the toe, σ_1 acts in an almost horizontal direction. Hence, the use of $s_u(V)$ in the design of slopes in anisotropic soils will, undoubtedly, lead to unsafe designs. This chapter reviews existing models of undrained strength anisotropy for clays and, based on the model proposed by Davis and Christian (1971), evaluates the effect of anisotropy on the two- and three-dimensional undrained stability of homogeneous slopes.

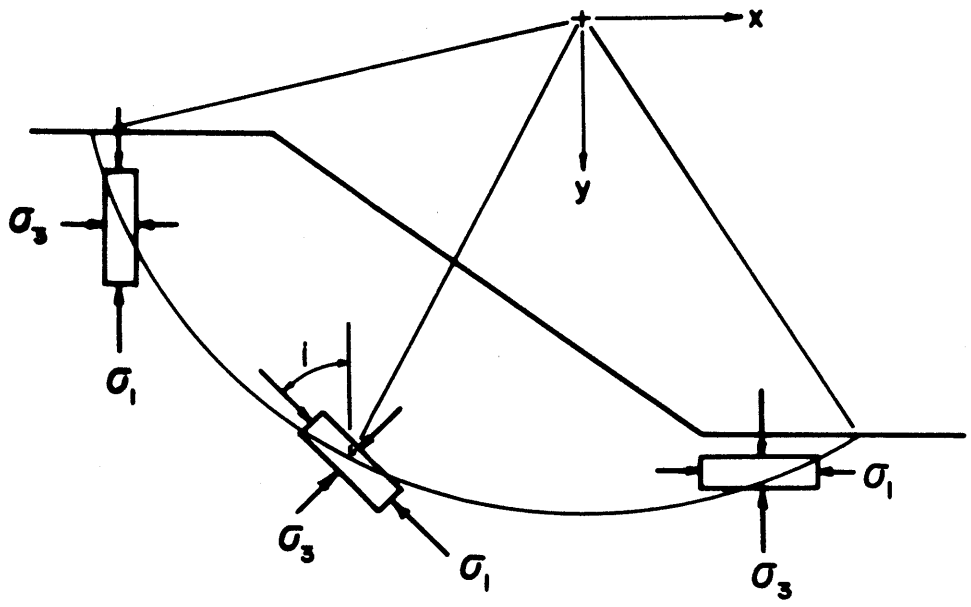


Figure 5.2 State of Stress Along a Typical Failure Circle

5.1 STRENGTH ANISOTROPY MODELS

Mathematical models describing the undrained shear strength anisotropy of clays were proposed by a number of investigators.

Casagrande and Carillo (1944) suggested the expression

$$s_u(i) = s_u(H) + [s_u(V) - s_u(H)] \cos^2 i \qquad (5.1)$$

without experimental justification. Most of the subsequent work on the stability of slopes with anisotropic strength (e.g. Lo, 1965 and Chen et al., 1975) is based on Eq. 5.1.

Bishop (1966) proposed a modification of the Casagrande-Carillo equation:

$$s_u(i) = s_u(V)(1 - t_1 \sin^2 i)(1 - t_2 \sin^2 2i) \qquad (5.2)$$

to fit UUC test data on London clay. The parameters $s_u(V)$, t_1 and t_2 are determined experimentally. Bishop suggested the use of $s_u(V)$, $s_u(H)$ and $s_u(45^\circ)$ for establishing these parameters.

Ranganatham and Matthai (1967) expressed the shear strength along a plane inclined at an angle θ to the horizontal, $s_{u\theta}$, in terms of the shear strengths on horizontal and vertical failure planes, s_{uh} and s_{uv}, respectively. This relationship is given by

$$s_{u\theta} = s_{uh}(\cos^2\theta + r_1 \sin^2\theta) \qquad (5.3)$$

where $$r_1 = \frac{s_{uv}}{s_{uh}} \qquad (5.4)$$

Since Eq. 5.3 involves shear strengths on predetermined failure planes, Ranganatham and Matthai (1967) recommended the use of the direct shear test to determine s_{uv} and s_{uh}. In a subsequent article, Ranganatham et al. (1969) present experimental data from direct shear tests on one soil (clay concentrated black cotton soil with w_ℓ = 224% and w_p = 70%), which agree with Eq. 5.3. However, direct shear tests may not give a true measure of strength anisotropy due to the problem of partial drainage encountered in these tests* (see Ladd, 1971 for details). According to Ladd (1971), partial drainage will reduce the undrained shear strength, s_u, for overconsolidated clays and increase it for normally consolidated clays. This may, in turn, have an effect on the directional variation of s_u.

Scott (1963) recommended the criterion initially proposed by Hill (1950) for anisotropic yielding of metals to be used for clays:

$$\left(\frac{\sigma_y - \sigma_x}{2}\right)^2 + \frac{a^2}{b^2}\tau_{xy} = a^2 \qquad (5.5)$$

where,

σ_y, σ_x and τ_{xy} = total stress components in the (x,y) plane

a and b = material constants to be measured by means of laboratory tests.

---

* The most common way to prevent drainage is to vary the normal load to keep a constant height of the sample, and thus maintain a constant volume.

According to Eq. 5.5, the value of $q_f = s_u = 0.5\ (\sigma_1 - \sigma_3)$ at yielding is given by:

$$s_u(i) = a\left[1 - \left(1 - \frac{a^2}{b^2}\right) \sin^2 2i\right]^{-1/2} \qquad (5.6)$$

Equation 5.6 describes an ellipse when plotted in polar coordinates (r, Ω), with $r = s_u$ and $\Omega = 2i$ (Fig. 5.3). Furthermore, Eq. 5.6 shows that a and b are the values of s_u for i=0 and 45 degrees, respectively, and that for i=0 and 90 degrees, s_u is the same. This means that Eq. 5.6 predicts that $s_u(V) = s_u(H)$ and thus contradicts the experimental results given in Table 5.1.

To introduce differences between $s_u(V)$ and $s_u(H)$, Davis and Christian (1971) modified Hill's yield criterion and proposed the more general expression:

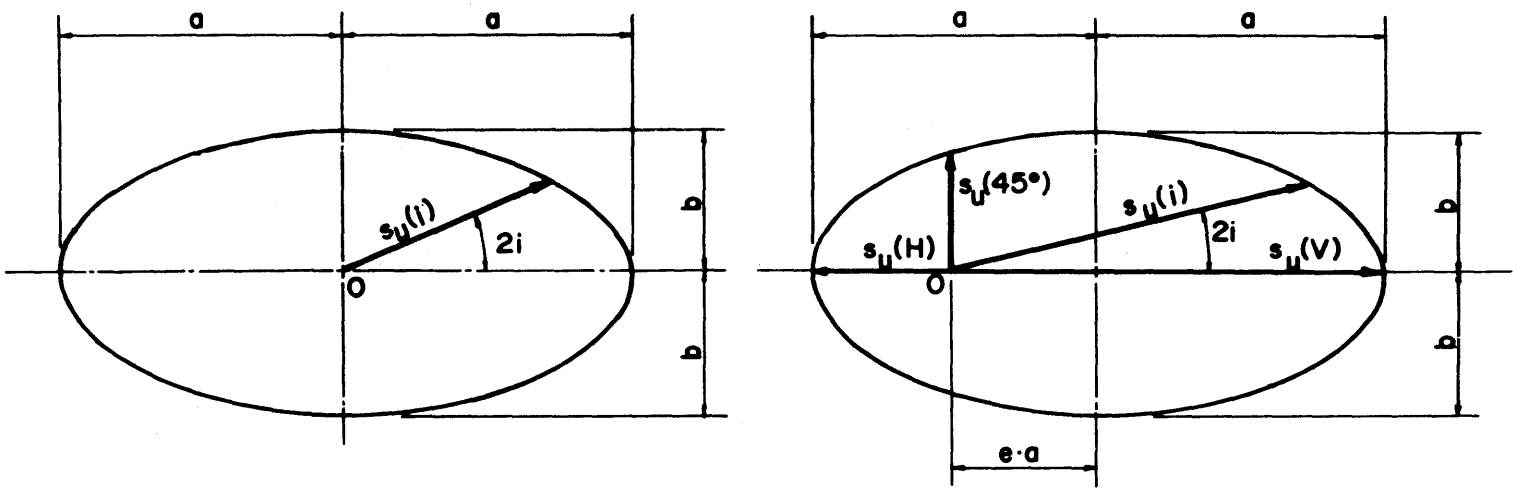
$$\left[\frac{\sigma_y - s_u(V)}{2} - \frac{\sigma_x - s_u(H)}{2}\right]^2 + \frac{a^2}{b^2}\tau_{xy}^2 = a^2 \qquad (5.7)$$

in which:

$s_u(V)$ and $s_u(H)$ = the undrained shear strength in compression in the vertical and horizontal directions, respectively,

a and b = constants to be determined experimentally.

Equation (5.7) reduces to Eq. (5.5) when $s_u(V) = s_u(H)$, and predicts that the value of $s_u = 0.5(\sigma_1 - \sigma_3)_f$ is given by



$$a = s_u(V) = s_u(H)$$

$$b = s_u(45°)$$

$$s_u(i) = a\left[1-(1-a^2/b^2)\sin^2 2i\right]^{-1/2}$$

Hill's Model

$$a = 0.50\left[s_u(V) + s_u(H)\right]$$

$$b/a = \frac{s_u(45°)}{\sqrt{s_u(V)\cdot s_u(H)}} \qquad d = 1-(b/a)^2$$

$$e = \frac{1-K_s}{1+K_s} \qquad K_s = \frac{s_u(H)}{s_u(V)}$$

$$s_u(i) = \frac{a(1-d)\,e\cdot\cos 2i + a\sqrt{1-d}\sqrt{1-d\cdot\cos^2 2i - e^2\cdot\sin^2 2i}}{(1-d\cdot\cos^2 2i)}$$

Davis and Christian's Model

Figure 5.3 Elliptic Strength Plots

$$s_u(i) = [a(1-d)\ e \cdot \cos 2i + a\sqrt{1-d}\ \sqrt{1-d\cos^2 2i - e^2 \sin^2 2i}]/[1-d\cos^2 2i] \quad (5.8)$$

where $$d = 1 - b^2/a^2 \quad (5.9)$$

$$e = \frac{s_u(V) - s_u(H)}{s_u(V) + s_u(H)} = \frac{1 - K_s}{1 + K_s} \quad (5.10)$$

$$K_s = \frac{s_u(H)}{s_u(V)} \quad (5.11)$$

In polar coordinates ($r = s_u$ and $\Omega = 2i$), Eq. 5.8 describes an ellipse with principal axes equal to a and b (Fig. 5.3). This ellipse is similar to the one in Fig. 5.3, which is based on Hill's criterion, except that the origin for s_u is now shifted horizontally a distance "e.a". From the geometry of the ellipse, the following relationships can be obtained:

$$b/a = \frac{s_u(45^\circ)}{\sqrt{s_u(V) \cdot s_u(H)}} \quad (5.12)$$

and $$a = 0.5[s_u(V) + s_u(H)] \quad (5.13)$$

Davis and Christian (1971) presented an extensive amount of UUC test results on several soils where s_u was measured for at least four values of i. These data indicated that:

1. The Casagrande-Carillo model is reasonably good when b nearly equals a. However, for soils in which b and a are different, this model introduces significant errors.

2. The two models proposed by Bishop and by Davis and Christian provide equally acceptable predictions. Since the two models require the same experimental data to determine the necessary soil parameters, and since the Davis and Christian model offers the added advantage of allowing simple plasticity solutions to be obtained, slope stability analysis in anisotropic soils were performed on the basis of this model. Figure 5.4 shows the variation of $s_u(i)$ vs i, according to the models described above, for the Portsmouth Clay and the Connecticut Valley Varved Clay in Table 5.1.

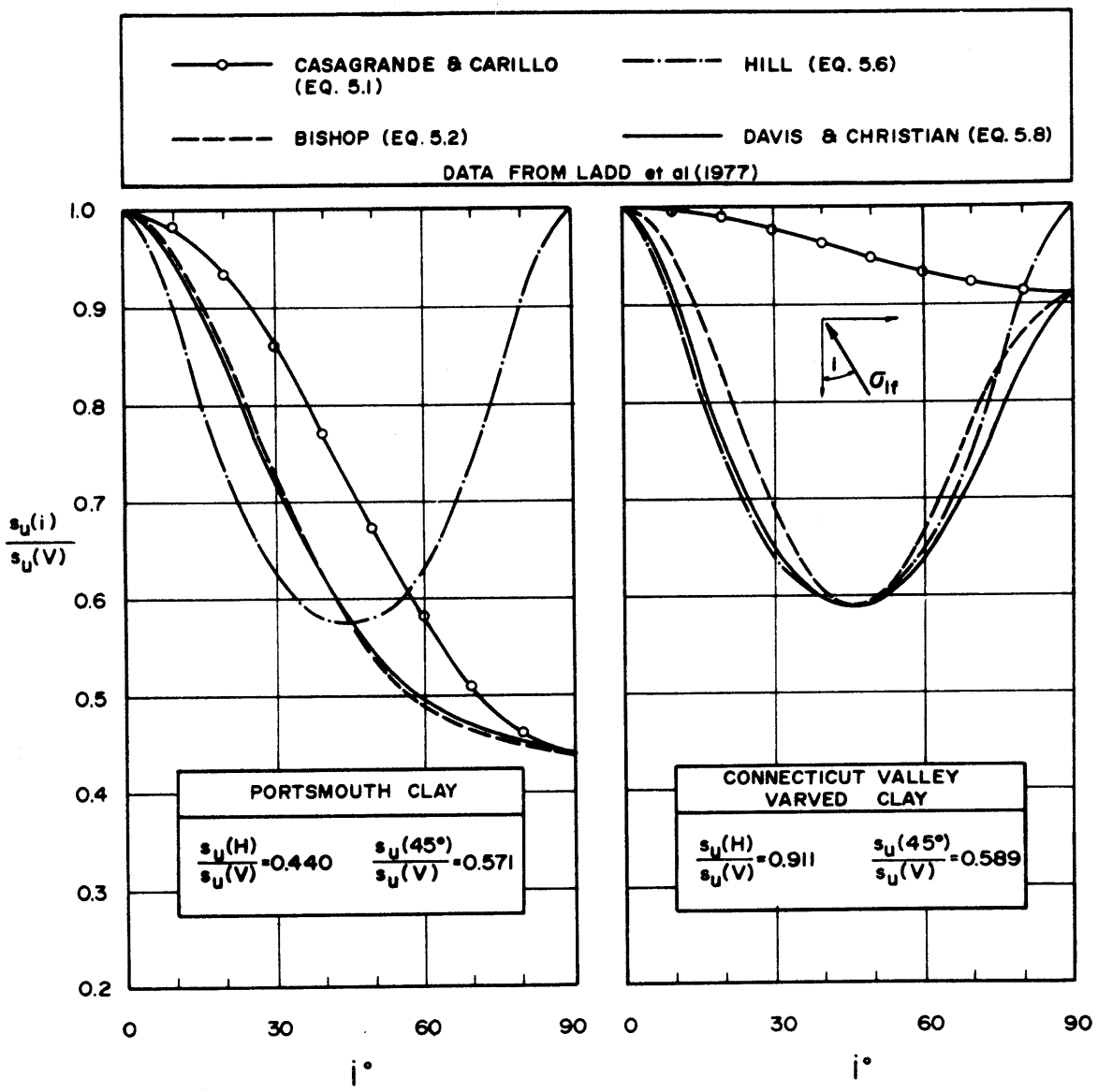


Figure 5.4 Strength as a Function of Orientation for Two Normally Consolidated Clays

5.2 TWO-DIMENSIONAL ANALYSIS OF HOMOGENEOUS SLOPES

Lo (1965) and Chen et al. (1975) presented design charts for performing stability analyses of slopes in anisotropic soils. Their solutions are based on the Casagrande-Carillo strength anisotropy model (Eq. 5.1) and were obtained for homogeneous as well as nonhomogeneous (strength increasing linearly with depth) soils. The charts developed by Chen et al. (1975) are based on the "upper bound theorem of the generalized theory of perfect plasticity" where the soil is assumed to be perfectly plastic, and to obey the Coulomb yield criterion and its associated flow rule (Chen, 1975). Charts by Lo (1965) are based on the conventional limit equilibrium method of slope stability analysis where the factor of safety against a slope failure is defined as the ratio of the resisting to the disturbing moment. The solutions presented herein are based on limit equilibrium methods and apply to the toe failure of homogeneous slopes with an anisotropic strength described by the Davis and Christian model (Eq. 5.8).

Figure 5.5 shows a cohesive slope of height H making an angle β with the horizontal and fails along the circular arc LM. The clay possesses a total unit weight, γ, and its strength characteristics are described by $s_u(V)$, K_s and b/a. At any point along the arc LM, the outward normal is $\underset{\sim}{n}$, the major principal stress is σ_{1f}, the angle between $\underset{\sim}{n}$ and the vertical is θ, the angle between the direction of σ_{1f} and the

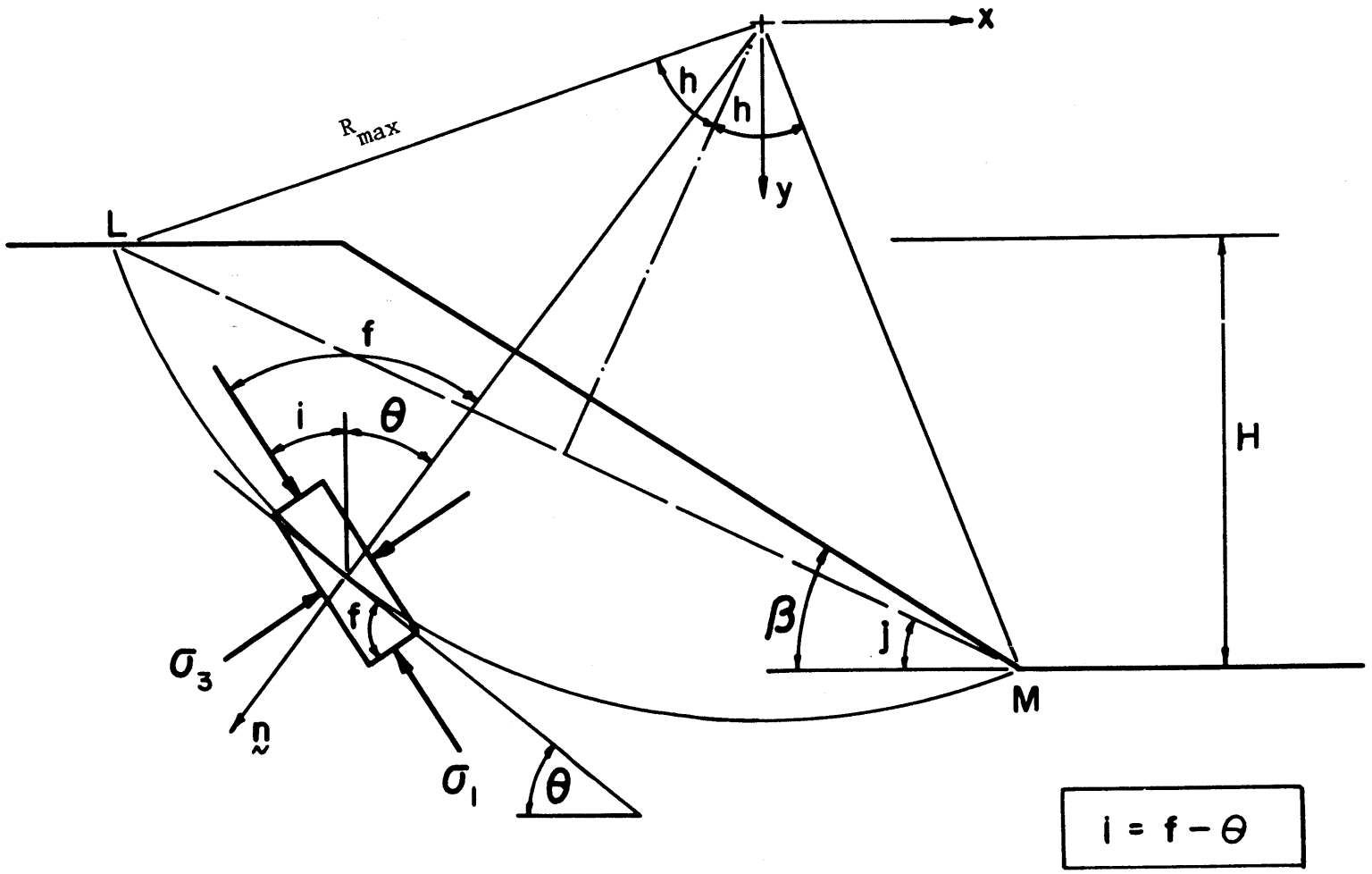


Figure 5.5 Definition of Geometric Parameters of a Typical Failure Circle

vertical is i, and the angle between $\underset{\sim}{n}$ and the direction of σ_{1f} is f, i.e.,

$$i = f - \theta \tag{5.14}$$

Based on the results of about 170 and 500 unconfined compression tests on London and Welland Clay, respectively, Lo (1965) concluded that the angle f is independent of the orientation of σ_{1f} and has an average value of about 56° for the two soils mentioned above. Using Eq. 5.14 and, based on Lo's results, the angle i at any point along the circular arc can thus be computed. The undrained shear strength, $s_u(i)$, can then be estimated from Eq. 5.8.

For the case of a toe failure, the plane strain disturbing moment, M_d^0, is given by (see Taylor, 1937):

$$M_d^0 = \frac{\gamma H^3}{12} [1 - 2 \cot^3\beta + 3 \cot j \cot\beta + 3 \cot h \cot j - 3 \cot h \cot \beta] \tag{5.15}$$

where the angles j and h are given in Fig. 5.5.

Writing that

$$Y = 1 - 2 \cot^3\beta + 3 \cot j \cot \beta + 3 \cot h \cot j - 3 \cot h \cot \beta \tag{5.16}$$

Then,

$$M_d^0 = \frac{\gamma H^3}{12} Y \tag{5.17}$$

The plane strain resisting moment, M_r^0, is given by:

$$M_r^0 = \int_L^M R_{max}^2 \, c(\theta) \, d\theta \tag{5.18}$$

Combining Eqs. 5.8, 5.11, 5.13, 5.14 and 5.18 and noting that

$$R_{max} = \frac{H}{2 \sin j \sin h} \qquad (5.19),$$

M_r^0 can be written as follows:

$$M_r^0 = \frac{H^2 s_u(V)(1 + K_s)}{8 \sin^2 j \sin^2 h} \int_L^M \frac{c(\theta)\, d\theta}{a} \qquad (5.20)$$

Writing that

$$Z = \frac{\int_L^M \frac{c(\theta) d\theta}{a}}{\sin^2 j \sin^2 h} \qquad (5.21)$$

Then:

$$M_r^0 = \frac{H^2 s_u(V)(1 + K_s)}{8} Z \qquad (5.22)$$

Hence, the plane strain factor of safety is given by:

$$F^0 = \frac{M_r^0}{M_d^0} \qquad (5.23)$$

$$= \frac{s_u(V)}{\gamma H} X \qquad (5.24)$$

where,

$$X = \frac{3}{2} (1 + K_s) \frac{Z}{Y} \qquad (5.25)$$

The minimum factor of safety can be obtained by minimizing X with respect to j and h such that:

$$\frac{\partial X}{\partial j} = 0 \qquad \frac{\partial X}{\partial h} = 0 \qquad (5.26)$$

Hence, the minimum value of X is a function of β, f, K_s and b/a. Given values of f, K_s and b/a, X is thus a function of β only. Calculations were carried out for f = 55° and different values of b/a, K_s and β.

The dependence of X on the slope angle β for three values of b/a (1, 0.75 and 0.5) and three values of K_s (1, 0.75 and 0.5) is shown in Fig. 5.6 where we note that:

1. The case of slopes with isotropic strength is given by the curve with b/a = K_s = 1. This curve is identical to the one given by Taylor (1937) for toe failures of slopes with homogeneous isotropic strength.

2. For the same value of $s_u(V)/\gamma H$, the plane strain factor of safety, F^0, is greatly affected by strength anisotropy. This can be illustrated by the decrease in F^0 due to a decrease in the anisotropy parameters, b/a and K_s. This reduction becomes very significant as the slope angle, β, decreases.

3. When b/a = 1, the results in Fig. 5.6 agree reasonably well with results obtained by Lo (1965) for toe failures of homogeneous slopes with an anisotropic strength described by the Casagrande-Carillo model (Eq. 5.1). With lower values of b/a, the results in Fig. 5.6 are totally different from Lo's results. This result was expected, since the two strength models (Eqs. 5.1 and 5.8) predict similar anisotropic strengths when b nearly equals a, but widely different strengths when b is different from a.

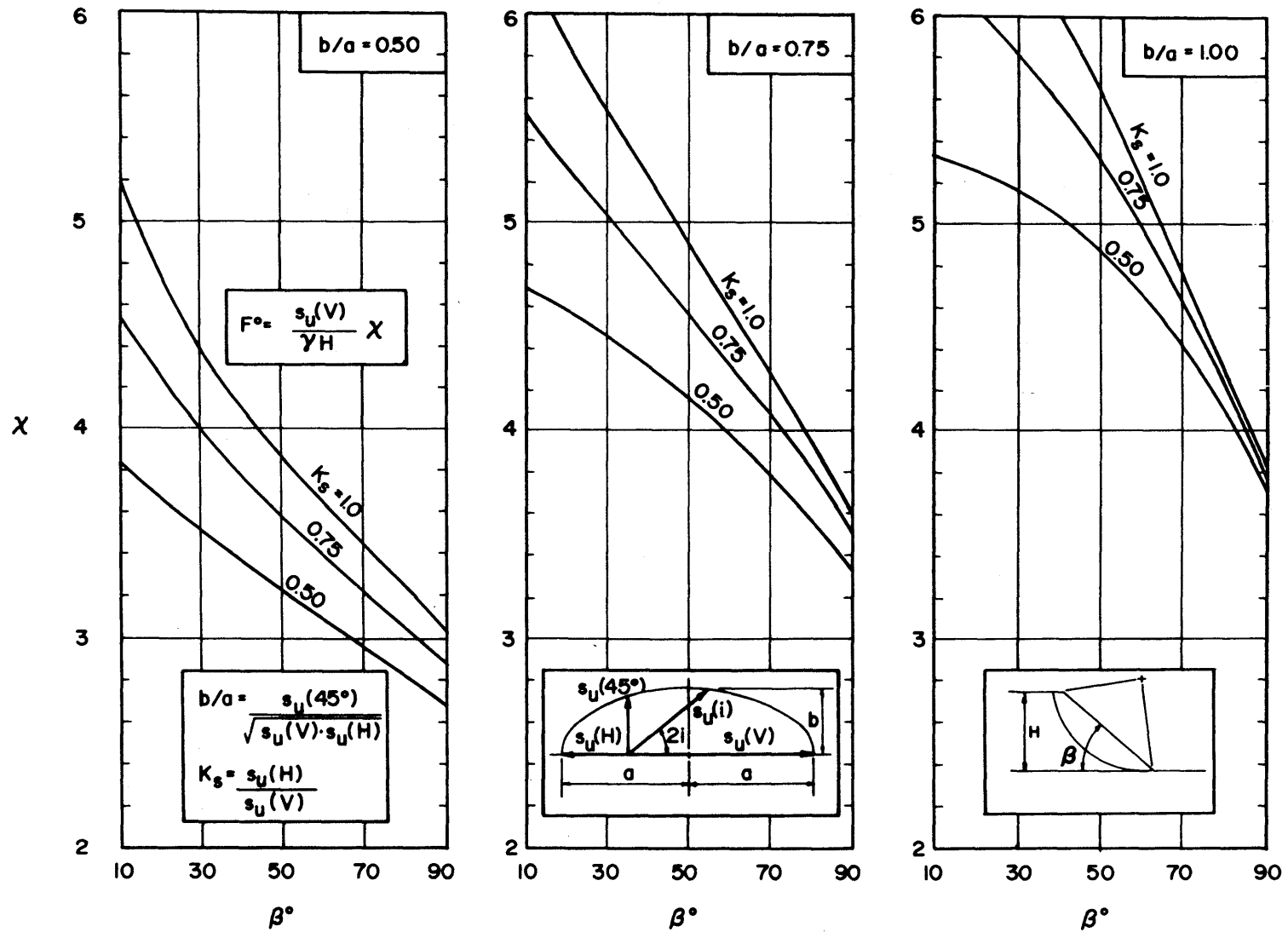


Figure 5.6 Effect of Strength Anisotropy on the Toe Failure of Homogeneous Slopes

Chen et al. (1975) provide solutions, based on the limit analysis method, for the stability of slopes in c and ϕ soils, where the cohesion c can be nonhomogeneous (linearly increasing with depth) and anisotropic. The directional variation of c is described by the Casagrande-Carillo model (Eq. 5.1) and the angle f (Eq. 5.14) was taken equal to:

$$f = 45^{\circ} + \frac{\phi}{2} \tag{5.27}$$

According to Chen et al. (1975), a good agreement exists between their solutions and Lo's results if f is taken equal to 55° and ϕ is set equal to zero.

5.3 THREE-DIMENSIONAL ANALYSIS OF HOMOGENEOUS SLOPES

In order to evaluate the effects of the strength anisotropy on the three-dimensional stability of slopes, the following two assumptions are made:

1. The clay is transversely isotropic where s_u depends only on the inclination i of σ_{1f} to the vertical direction. This is illustrated in Fig. 5.7, which shows a surface of revolution describing the directional variation of s_u. The vector joining the origin to any point on this surface is in the direction of σ_{1f} (and, therefore, is inclined by an angle i to the vertical) and its magnitude is s_u. For example, the two samples A and B in Fig. 5.7 will have the same shear strength even though they are differently inclined with respect to the x and z axes.*

This assumption is considered reasonable in view of the method of deposition, erosion, ... etc. of most clays where the only preferred direction is vertical. Furthermore, it allows the anisotropic strength models discussed earlier to be applied to three-dimensional states of stress.

2. The direction of σ_{1f} at any point on the shear surface lies in the plane described by the outward normal, $\underset{\sim}{n}$, and the vertical direction. This implies that:

$$i = f - \overline{\theta} \qquad (5.28)$$

---

* This model does not take into consideration the orientation of the minor principal stress at failure, nor the magnitude of the intermediate principal stress at failure.

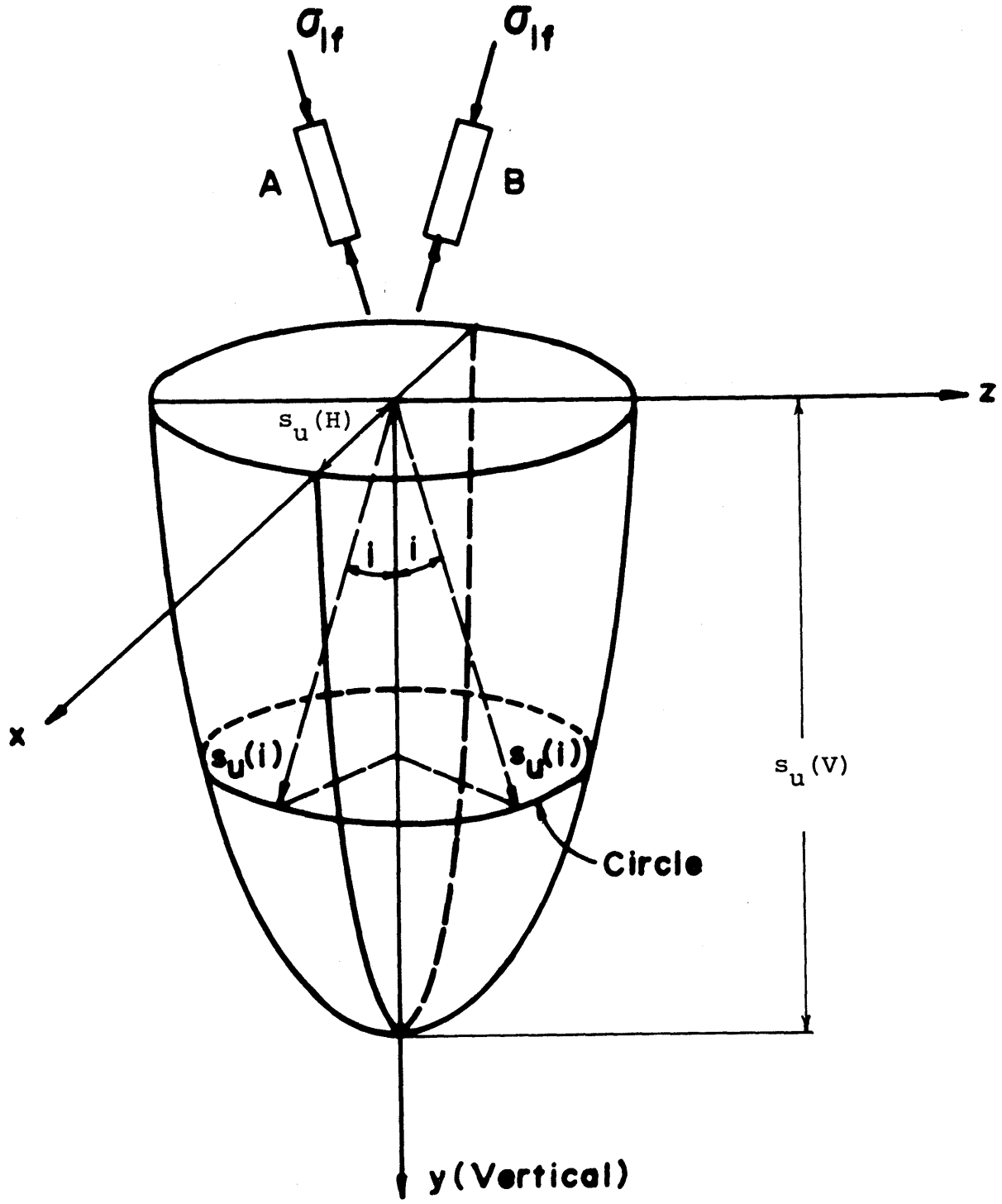


Figure 5.7 Definition of Strength Variation with Direction in Three-Dimensional Problems

where: f = angle between outward normal and the direction of σ_{1f}. As discussed earlier, f is relatively constant and equal to 55°.

$\bar{\theta}$ = angle between the outward normal and the vertical direction.

For fixed values of f and $\bar{\theta}$, this assumption yields a minimum value of i. The validity of this assumption is difficult to evaluate, but its importance on the three-dimensional effects can be estimated by means of parametric studies.

In order to estimate $\bar{\theta}$, consider the shear surface shown in Fig. 5.8. The outward normal, $\underset{\sim}{n}$, at any point is given by :

$$\underset{\sim}{n} = \begin{Bmatrix} \cos\rho \sin\theta \\ \cos\rho \cos\theta \\ \sin\rho \end{Bmatrix} \tag{5.29}$$

where ρ is the angle between the plane tangent to the shear surface and the z-axis. Hence, $\bar{\theta}$ is given by:

$$\bar{\theta} = \cos^{-1}(\cos\theta \cos\rho) \tag{5.30}$$

When $\rho = 0$, the problem becomes two-dimensional, Eq. 5.30 gives $\bar{\theta} = \theta$, and Eq. 5.30 reduces to Eq. 5.14. Knowing i, the corresponding value of s_u can then be obtained from Eq. 5.8.

The effect of the strength anisotropy on the three-dimensional factor of safety, F, was evaluated for the vertical cut in Fig. 3.1. The z-axis is taken at the crest of the cut and the cylinder passes through the toe, i.e., $R_{max} = H$. Analysis

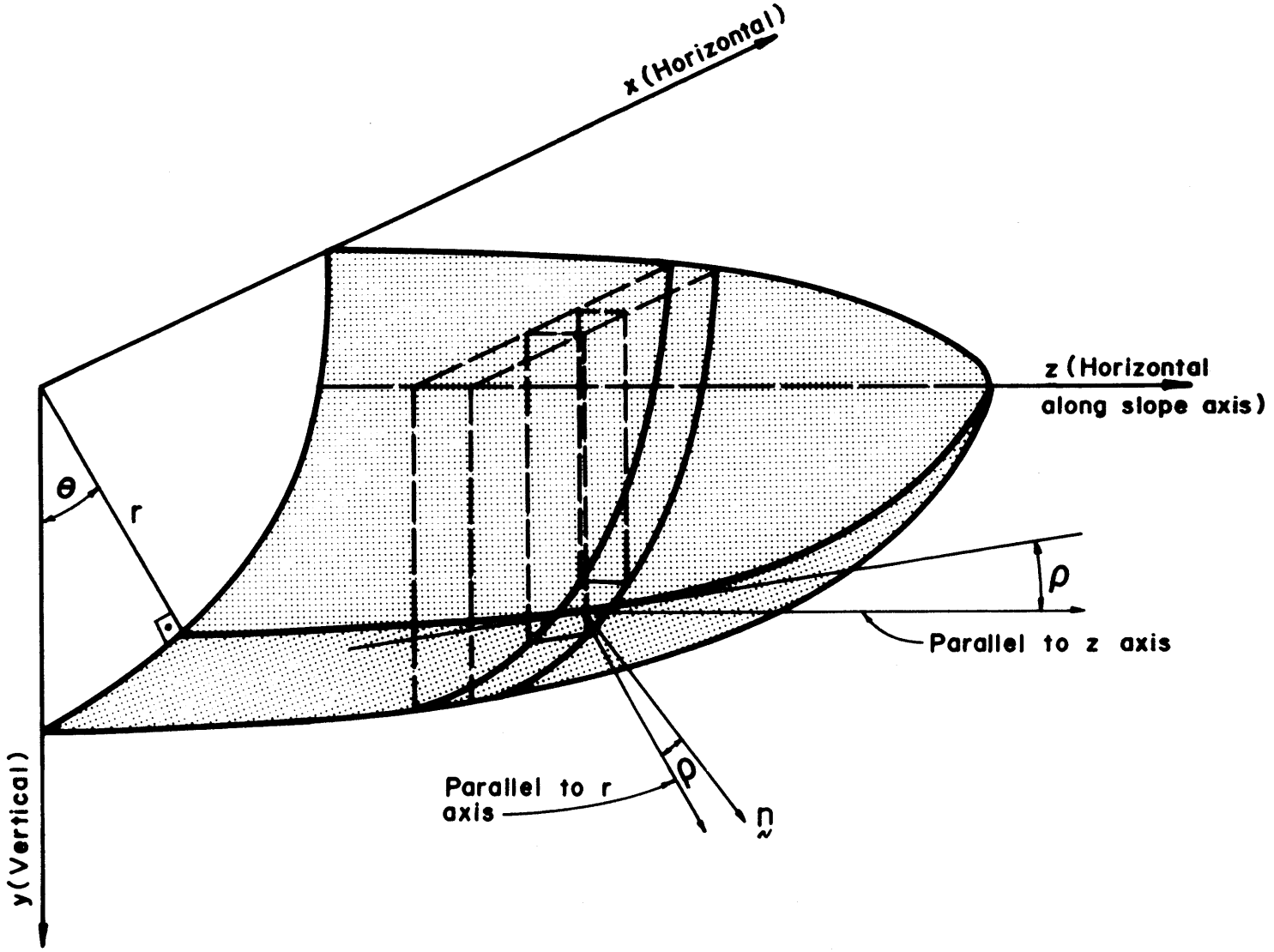


Figure 5.8 Definition of Geometric Parameters of a Typical Three-Dimensional Failure Surface

was performed for the shear surfaces consisting of cones attached to cylinders by means of the computer program STAB3D. The results are shown in Fig. 5.9 where the end effects, expressed by the ratio F/F^0, are plotted versus the normalized failure length 2L/H for different values of the strength anisotropy parameters K_s and b/a. From this figure, it can be seen that the end effects (F/F^0 ratio) are not significantly affected by the anisotropy of the shear strength. F/F^0 vs. 2L/H curve for the isotropic soil (dotted curve) is very close to the one for anisotropic soil given by $b/a = K_s = 0.5$. But, as was shown in Fig. 5.6, the plane strain factor of safety is greatly affected by the anisotropic behavior of the soil.

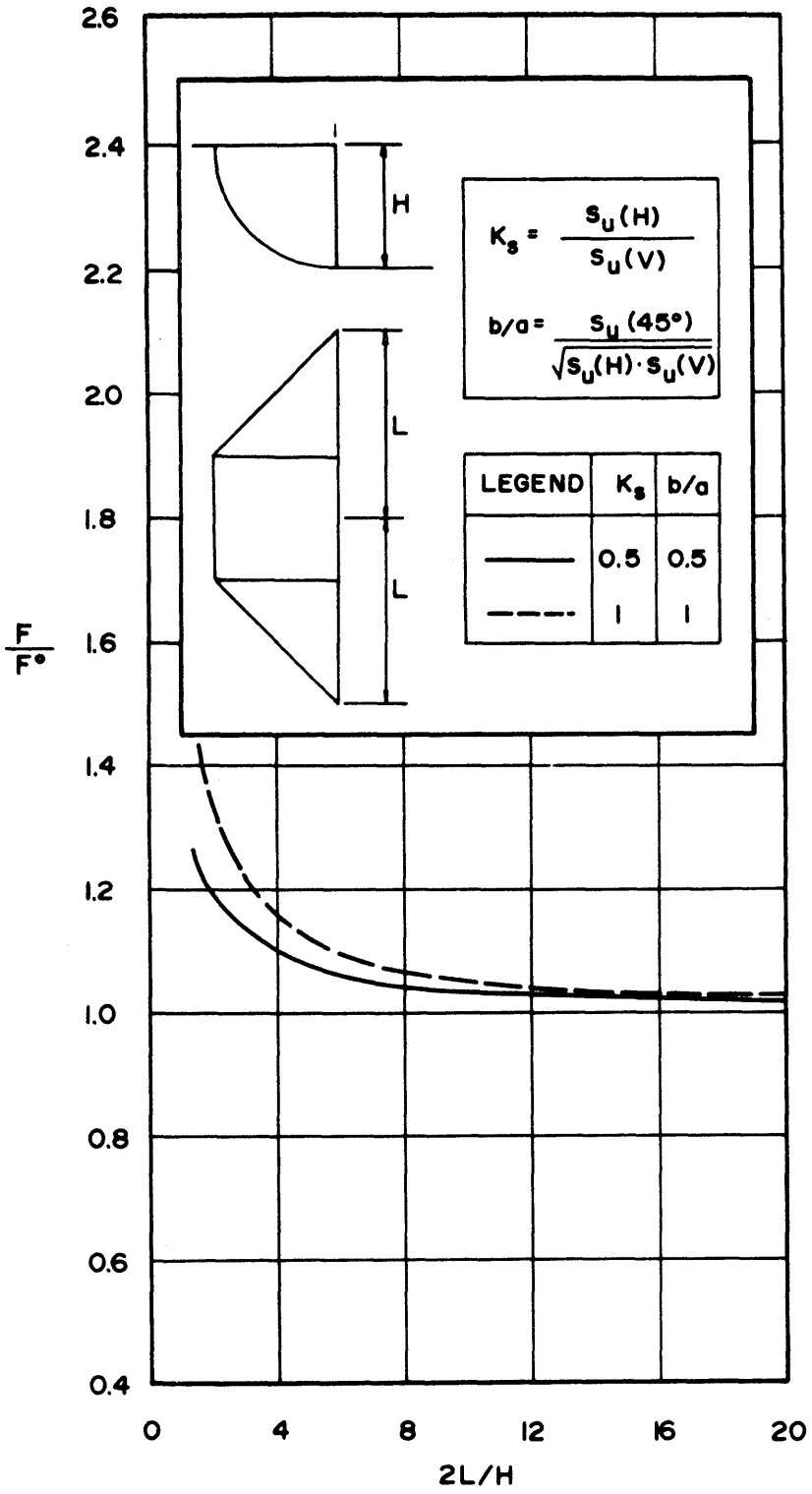


Figure 5.9 End Effects on the Stability of a Vertical Cut with Anisotropic Strength

5.4 SUMMARY AND CONCLUSIONS

Clays often exhibit a significant anisotropy in their undrained shear strength, Ladd et al. (1977). Results of slope stability analyses based on the Davis and Christian (1971) model for strength anisotropy show that:

1. The plane strain factor of safety, F^0, can be significantly affected by the strength anisotropy. This effect becomes more pronounced when the anisotropy parameters b/a and K_s, as well as the slope angle β decrease. For the case of a vertical cut in an anisotropic soil with K_s = b/a = 0.5, Fig. 5.6 shows that analysis based on $s_u(V)$ will overestimate the factor of safety by about 45%. However, this error can be reduced to 8% when the average strength, $(0.5[s_u(V) + s_u(H)])$ is used.

2. End effects (F/F^0) are not significantly affected by strength anisotropy. The curves of F/F^0 vs 2L/DR for slopes with isotropic (K_s = b/a = 1) and anisotropic (K_s = b/a = 0.5) strengths are very similar.

CHAPTER 6

DRAINED STABILITY OF HOMOGENEOUS SLOPES

The total stress undrained ($\phi = 0$ and $c = s_u$) stability analysis of slopes discussed in previous chapters applies when the shear strength of the soil is independent of the normal stress along the failure surface. This chapter considers the drained stability of slopes where the shear strength is related to the normal effective stress by the Mohr-Coulomb criterion in Eq. 2.3. In such cases, the stability problem is statically indeterminate and the normal effective stresses along the shear surface must be assumed in order to estimate the safety factor of a slope by means of limiting equilibrium techniques.

Methods of slope stability analyses for frictional soils in common use divide the slope into slices and assume the effective normal stress, $\bar{\sigma}_N$, at the base of each slice. Most of these methods assume $\bar{\sigma}_N$ in terms of the vertical overburden stress, σ_v, and the pore pressures. Various workers assume different relationships between $\bar{\sigma}_N$ and σ_v which lead to different estimates of the factor of safety.

In two-dimensional slope stability analysis, it can be shown that, when n slices are used, (5n - 2) unknowns must be determined from (3n) equilibrium conditions and the problem is, therefore, (2n - 2) statically indeterminate, i.e.,

(2n - 2) assumptions are required. A general extension of the method of slices to three dimensions requires additional simplifying assumptions tc achieve statical determinancy. This is illustrated in Fig. 6.1 by a prismatic slope where the sliding soil mass is divided by vertical planes into m segments along the slope (the z-axis), and n segments in the transverse direction (the x-axis). When the soil mass consists of m × n slices*, Steiner (1977) showed that [1 + 11 mn - 6(m + n)] assumptions are needed. Simplifying assumptions represent the source of disagreement between existing methods of plane strain analysis, and will, undoubtedly, be more controversial in three dimensions. Therefore, three dimensional extensions of the general method of slices was avoided herein in favor of simplified procedures which are aimed at estimating "reasonable" bounds for the normal effective stress, $\bar{\sigma}_N$, on the shear surface.

In this chapter, we consider two methods for the drained analysis of slopes. The assumptions used by each method to estimate the normal stress on the shear surface (in two and three dimensions) are emphasized. The effect of these assumptions on the two and three-dimensional factors of safety are then evaluated by means of solutions obtained for homogeneous slopes.

---

* The actual number of slices depends on the geometry of the shear surface, and is generally less than m × n.

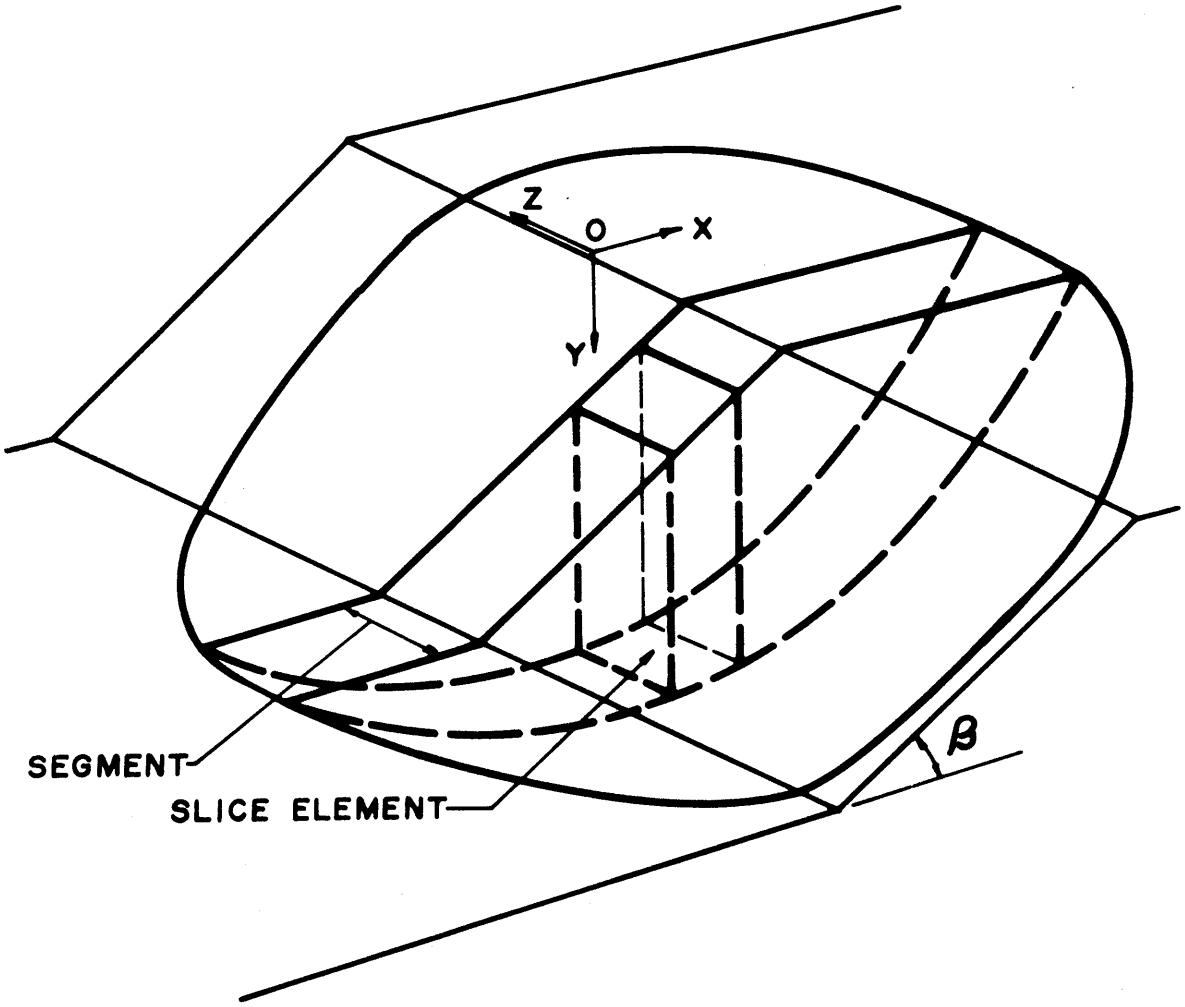


Figure 6.1 Three-Dimensional Failure of a Prismatic Slope

6.1 THE ORDINARY METHOD OF SLICES

The Ordinary Method of Slices (OMS), introduced by Fellenius in 1936, represents one of the earliest methods of two-dimensional slope stability analyses. The method basically assumes no interslice forces.* The effective normal force at the base of each slice, $\overline{N}$, is obtained from the equilibrium condition in the normal direction to the base of the slice, i.e.,

$$\overline{N} = W \cos \theta - u d\ell \tag{6.1}$$

where

W = total weight of slice per unit thickness along the z-axis

θ = inclination of the base of the slice

u = pore pressure at the base of the slice

$d\ell$ = base length of the slice

The effective normal stress acting on the base of the slice, $\overline{\sigma}_N$, is thus given by:

$$\overline{\sigma}_N = \frac{\overline{N}}{d\ell} \tag{6.2}$$

and the total vertical stress resulting from the weight of the slice is equal to:

---

*An equivalent assumption is to consider the interslice resultant force parallel to the base of the slice, Bishop, 1955.

$$\sigma_v = \frac{W}{dx} \tag{6.3}$$

Substituting from Eqs. 6.2 and 6.3 into 6.1, and noting that:

$$dx = d\ell \cos \theta \tag{6.4}$$

the relationship between $\bar{\sigma}_N$ and σ_v can be established:

$$\bar{\sigma}_N = \sigma_v \cos^2 \theta - u \tag{6.5}$$

Introducing the pore pressure ratio (Bishop and Morgenstern, 1961)

$$r_u = \frac{u}{\sigma_v} \tag{6.6},$$

Eq. 6.5 can be rewritten in the form:

$$\bar{\sigma}_N = \sigma_v(\cos^2 \theta - r_u) \tag{6.7}$$

At failure, the shear force at the base of each slice, dF, can be found by combining the Mohr-Coulomb criterion in Eq. 2.3 with Eqs. 6.3, 6.4 and 6.7:

$$dF = \bar{c}d\ell + \frac{W}{\cos \theta} (\cos^2 \theta - r_u) \tan \bar{\phi} \tag{6.8}$$

Hence, the resisting moment in a circular arc plane strain analysis is given by:

$$M_r^0 = \sum_1^n [\bar{c}d\ell + \frac{W}{\cos \theta} (\cos^2 \theta - r_u) \tan \bar{\phi}] \cdot R_{max} \tag{6.9}$$

where R_{max} is the radius of the cylindrical shear surface.

Since the plane strain disturbing moment is:

$$M_d^0 = \sum_1^n W \cdot \sin\theta \cdot R_{max} \tag{6.10}$$

The plane strain factor of safety, F^0 , in a circular arc analysis is thus given by:

$$F^0 = \frac{\sum_1^n [\bar{c}d\ell + \frac{W}{\cos\theta}(\cos^2\theta - r_u)\tan\bar{\phi}]}{\sum_1^n W \sin\theta} \tag{6.11}$$

In extending the OMS to three dimensions, we assume that the interslice forces acting on the x - y faces are also equal to zero, Fig. 6.1. Hence, equilibrium in the normal direction to the base of the slice requires:

$$\bar{N} = W \cdot dz \cdot \cos\theta \cdot \cos\rho - u \cdot dA \tag{6.12}$$

where:

ρ = angle between the tangent plane to the base of the slice and the z-axis (see Fig. 5.8)

dz = thickness of the slice in the z direction

dA = area of the base of the slice

$= d\ell \cdot dS$ (see Eq. 2.8)

$$= d\ell \cdot \frac{dS}{dz} \cdot dz \tag{6.13}$$

The three-dimensional factor of safety, F, is thus given by:

$$F = \sum_1^m \sum_1^n [\bar{c}d\ell \cdot \frac{dS}{dz} \cdot dz + \frac{W}{\cos\theta}(\cos^2\theta \cdot \cos\rho - r_u \frac{ds}{dz}) \times dz \tan\bar{\phi}] / \sum_1^m \sum_1^n W \cdot dz \cdot \sin\theta \tag{6.14}$$

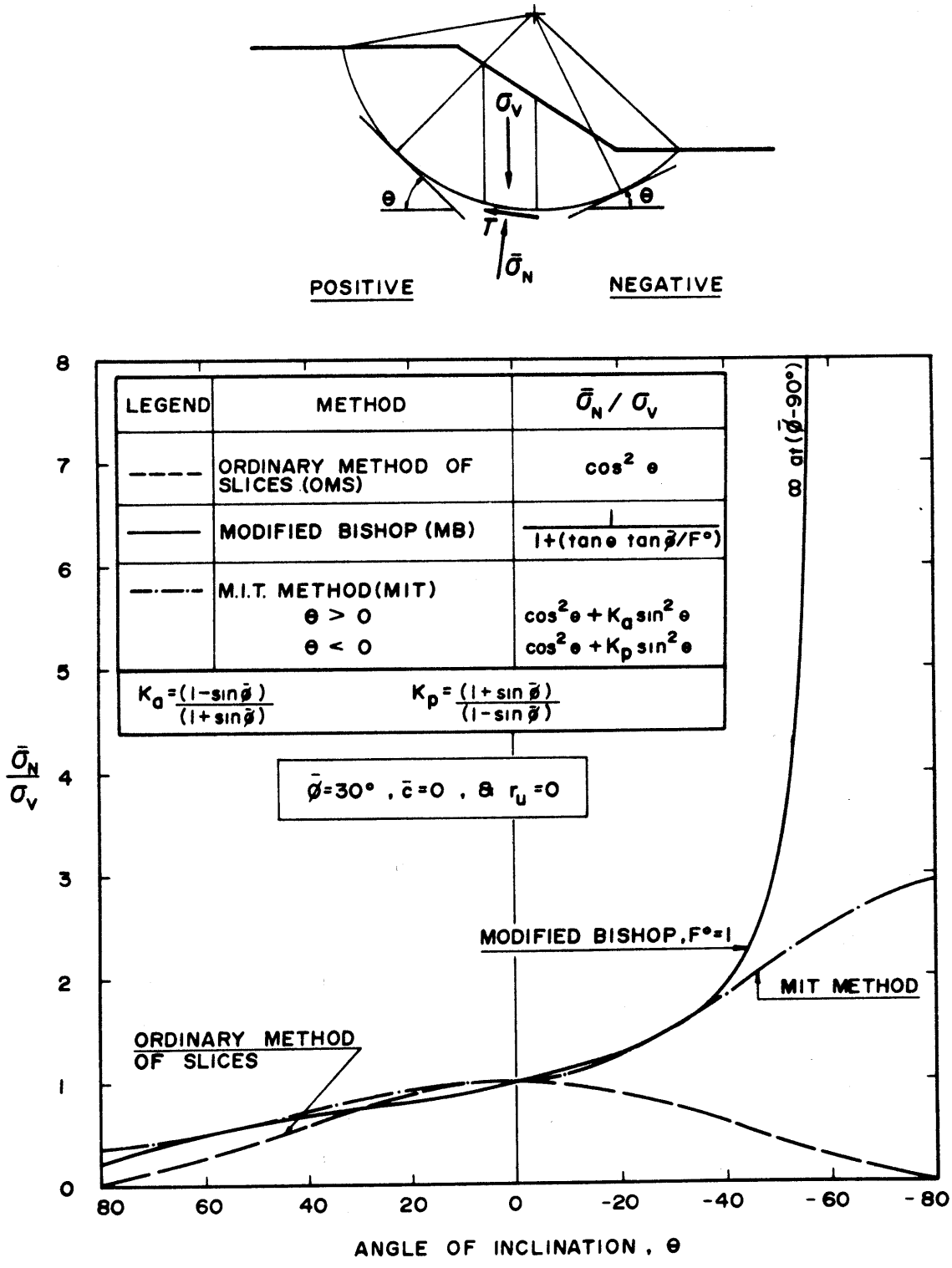


Figure 6.2 Influence of Base Inclination of Slices in Two-Dimensional Slope Stability Analysis

6.2 THE M.I.T. METHOD

In 1957, the Maine State Highway Commission developed a method for the plane strain analysis of slopes. The method assumes that the overburden stress, σ_v, equals the major principal stress at failure, σ_{1f}, i.e., the soil is in an active state. The effective stress normal to the base of a slice making an angle θ with the horizontal (Fig. 6.2) is thus given by:

$$\bar{\sigma}_N = (\sigma_v - u)(\cos^2 \theta + \frac{\sin^2 \theta}{N_\phi}) - \frac{2\bar{c}}{\sqrt{N_\phi}} \cdot \sin^2 \theta \qquad (6.15)$$

where

$$N_\phi = \frac{1 + \sin \bar{\phi}}{1 - \sin \bar{\phi}} = \tan^2(45 + \bar{\phi}/2) \qquad (6.16)$$

At M.I.T., Ladd (1970) modified the Maine State Highway method by using Eq. 6.15 only when $\theta > 0$, Fig. 6.2, and by assuming that σ_v equals the minor principal stress at failure, σ_{3f}, when $\theta < 0$. Therefore, the MIT method assumes that the soil is in an active state when $\theta > 0$ and in a passive state when $\theta < 0$, i.e.,

$$\bar{\sigma}_N = (\sigma_v - u)(\cos^2 \theta + N_\phi \cdot \sin^2 \theta) + 2\bar{c} \cdot \sqrt{N_\phi} \cdot \sin^2 \theta$$

$$\text{for } \theta < 0 \qquad (6.17)$$

Equation 6.15 predicts negative (tensile) normal stresses for large positive values of θ and $\bar{c}$. Since this result appears un-

reasonable, especially in drained analyses, we modified the MIT method further by taking the minimum values of $\bar{\sigma}_N$ to be equal to zero.

From Eqs. 6.15 and 6.17, and according to the Mohr-Coulomb yield criterion in Eq. 2.3, the MIT method estimates the shear force at the base of a slice, dF, to be:

$$dF = \bar{c}d\ell + \left[\frac{W}{\cos\theta}(1 - r_u)\ \chi_a - \frac{2\bar{c}}{\sqrt{N_\phi}} \cdot d\ell \cdot \sin^2\theta\right] \tan\bar{\phi}$$

$$\text{for } \theta > 0 \qquad (6.18)$$

and

$$dF = \bar{c}d\ell + \left[\frac{W}{\cos\theta}(1 - r_u)\ \chi_p + 2\bar{c}\sqrt{N_\phi} \cdot d\ell \cdot \sin^2\theta\right] \tan\bar{\phi}$$

$$\text{for } \theta < 0 \qquad (6.19)$$

where :

$$\chi_a = \cos^2\theta + \frac{\sin^2\theta}{N_\phi} \qquad (6.20),$$

and

$$\chi_p = \cos^2\theta + N_\phi \cdot \sin^2\theta \qquad (6.21)$$

The plane strain factor of safety is thus given by:

$$F^0 = \sum_1^n dF / \sum_1^n W \cdot \sin\theta \qquad (6.22)$$

It is important to note that, by assuming the principal direction at failure to be vertical, the MIT method over-estimates the shear strength on the base of the slice compared

to that implied by the assumed state of stress*. However, the MIT method is not believed to derive its potential from completeness but, instead, from its simplicity and capability to predict reasonable factors of safety, as shown later.

In order to extend the MIT method to three dimensional stability problems, we maintain the plane strain assumptions (that the vertical stress is a major, or minor principal stress at failure depending on whether $\theta > 0$, or $\theta < 0$, respectively) and, in addition, we assume that the longitudinal (out-of-plane) stress, σ_ℓ is also a principal stress and given by:

$$\sigma_\ell = K \bar{\sigma}_v + u \tag{6.23}$$

Eq. 6.23 is a simplifying assumption that achieves the necessary statical determinancy in three-dimensional stability problems involving frictional materials. Solutions obtained for different values of K (between the active and passive earth pressure coefficients, say) will determine a range of possible values for the factor of safety and hence evaluate the importance of the longitudinal stress on stability. Based on these assumptions, the effective stress tensor, $\bar{\sigma}_{ij}$, at any point on the shear surface is thus given by:

---

*Unless $\theta = 45 + \bar{\phi}/2$ or $-(45 - \bar{\phi}/2)$ when the MIT method is correct for the assumed state of stress.

$$\bar{\sigma}_{ij} = \begin{bmatrix} \bar{\sigma}_x & 0 & 0 \\ 0 & \bar{\sigma}_y & 0 \\ 0 & 0 & \bar{\sigma}_z \end{bmatrix} \tag{6.24}$$

where:

$$\bar{\sigma}_y = \sigma_v - u \tag{6.25}$$

$$\begin{aligned} \bar{\sigma}_x &= (\sigma_v - u) \cdot \frac{1}{N_\phi} - \frac{2\bar{c}}{\sqrt{N_\phi}} && \text{for } \theta > 0 \\ &= (\sigma_v - u) \cdot N_\phi + 2\bar{c}\sqrt{N_\phi} && \text{for } \theta < 0 \end{aligned} \tag{6.26}$$

$$\bar{\sigma}_z = \bar{\sigma}_\ell = K\,\bar{\sigma}_y = K(\sigma_v - u) \tag{6.27}$$

Noting that the outward normal vector to the base of the slice, $\underset{\sim}{n}$, is given by (see Fig. 5.8):

$$\underset{\sim}{n} = \begin{Bmatrix} \cos\rho \cdot \sin\theta \\ \cos\rho \cdot \cos\theta \\ \sin\rho \end{Bmatrix} \tag{6.28}$$

and the normal stress on the failure plane at failure is:

$$\bar{\sigma}_N = \sum_{i=1}^{3} \sum_{j=1}^{3} \bar{\sigma}_{ij} \cdot n_i n_j \tag{6.29},$$

we thus get:

$$\bar{\sigma}_N = \bar{\sigma}_x \cos^2\rho \sin^2\theta + \bar{\sigma}_y \cos^2\rho \cos^2\theta + \bar{\sigma}_z \sin^2\rho \tag{6.30}$$

Utilizing the Mohr-Coulomb criterion in Eq. 2.3 together with Eqs. 6.25 through 6.27, the shear force at the base of any slice is given by:

$$dF = \bar{c}\,d\ell\,\frac{dS}{dz}\,dz + \left\{\frac{W}{\cos\theta}(1 - r_u)\,\chi_a\cos^2\rho\,\frac{dS}{dz} - \frac{2\bar{c}}{\sqrt{N_\phi}}\sin^2\theta\cos^2\rho\,d\ell\,\frac{dS}{dz} + K\,\frac{W}{\cos\theta}(1 - r_u)\sin^2\rho\,\frac{dS}{dz}\right\}dz\tan\bar{\phi}$$

$$\text{for } \theta > 0 \qquad (6.31)$$

and

$$dF = \bar{c}\,d\ell\,\frac{dS}{dz}\,dz + \left\{\frac{W}{\cos\theta}(1 - r_u)\,\chi_p\cos^2\rho\,\frac{dS}{dz} + 2\bar{c}\sqrt{N_\phi}\sin^2\theta\cos^2\rho\,d\ell\,\frac{dS}{dz} + K\,\frac{W}{\cos\theta}(1 - r_u)\sin^2\rho\,\frac{dS}{dz}\right\}dz\tan\bar{\phi}$$

$$\text{for } \theta < 0 \qquad (6.32)$$

χ_a and χ_p are given by Eqs. 6.20 and 6.21, respectively. The three-dimensional factor of safety, F, is:

$$F = \frac{\sum_1^m \sum_1^n dF}{\sum_1^m \sum_1^n W\,dz\sin\theta} \qquad (6.33)$$

6.3 DRAINED STABILITY OF HOMOGENEOUS SLOPES

In order to perform parameteric studies for the drained stability of homogeneous slopes, the use of the frictional strength parameters $\lambda_{c\phi}$ (Janbu, 1954) is convenient:

$$\lambda_{c\phi} = \frac{\gamma H}{\bar{c}} \tan \bar{\phi} \tag{6.34}$$

where:

H = slope height

γ = total unit weight of soil

$\lambda_{c\phi}$ is a measure of the frictional strength of the slope. When $\lambda_{c\phi} = 0$, the soil is frictionless ($\bar{\phi} = 0$) and when $\lambda_{c\phi}$ tends to ∞, the soil is purely frictional ($\bar{c} = 0$).

For homogeneous slopes, it can be easily shown (Janbu, 1954) that the plane strain factor of safety, F^0, can be written in the form:

$$F^0 = N_{sf} \frac{\bar{c}}{\gamma H} \tag{6.35}$$

where the stability number N_{sf} depends on $\lambda_{c\phi}$, the slope angle β, and the pore pressure ratio, r_u. Hence, the results of different methods of analysis can be evaluated by comparing N_{sf} for fixed values of $\lambda_{c\phi}$, β, and r_u. Alternatively, this can be done by comparing F^0 for fixed values of $\lambda_{c\phi}$, β, r_u and $\bar{c}/\gamma H$. In this study we consider three slope angles β

(cot β = 2, 1.5, and 1), four values of $\lambda_{c\phi}$ (0, 4, 20 and 100) and r_u = 0.

6.3.1 Two-Dimensional Analysis

Two-dimensional analyses were performed by means of the program STAB3D to check the accuracy of the MIT method. This was achieved by analyzing slopes with three different angles β, and four values of $\lambda_{c\phi}$, utilizing three methods of analysis: 1) The Ordinary Method of Slices (OMS); 2) the Modified Bishop method (MB), and, 3) the MIT method. The results of these analyses show that:

1. In frictionless slopes ($\lambda_{c\phi}$ = 0), the three methods (OMS, MB and MIT) give identical results. Since this case corresponds to a total stress analysis (ϕ = 0), no assumption is required to achieve statical determinancy, and this result was therefore expected.

2. In all the cases investigated, the three methods of analysis (OMS, MB and MIT) showed that toe failures were more critical than base failures. This result was expected from the work of Janbu (1954) and Wright (1969).

3. Table 6.1 presents the coordinates x/H and y/H of the critical toe circles in each of the cases considered. For a particular slope, the critical centers obtained by different methods lie on a straight line through the midpoint of the slope. The inclination of this line approaches the normal to the slope as $\lambda_{c\phi}$ increases. The critical center according to the MIT method lies below that for the MB method and above the

Table 6.1 Results of Two-Dimensional Drained Stability Analysis

cot β	$\lambda_{c\phi}$	$\bar{c}/\gamma H$	$\bar{\phi}°$	Ordinary Method of Slices (OMS)		Modified Bishop Method (MB)		M.I.T. Method (MIT)		$\frac{F^0_{MIT}}{F^0_{OMS}}$	$\frac{F^0_{MIT}}{F^0_{Bishop}}$
				F^0	x/H* y/H*	F^0	x/H y/H	F^0	x/H y/H		
1					-0.10		0.10		0.10		
	4	0.10	24.2	1.277	1.20	1.326	1.50	1.342	1.50	1.051	1.012
					0.30		0.50		0.50		
	20	0.05	45	1.664	1.50	1.750	1.70	1.734	1.70	1.042	0.991
					0.80		1.20		1.20		
	100	0.01	45	1.216	1.90	1.257	2.30	1.369	2.30	1.126	1.089
1.5					-0.40		-0.20		-0.30		
	4	0.10	24.2	1.542	1.40	1.625	1.80	1.603	1.60	1.040	0.986
					0.00		0.20		0.10		
	20	0.05	45	2.202	1.80	2.315	2.20	2.342	2.00	1.064	1.012
					0.50		0.90		0.80		
	100	0.01	45	1.720	2.50	1.768	3.10	1.848	2.90	1.074	1.045
2.0					-0.60		-0.50		-0.50		
	4	0.10	24.2	1.783	1.70	1.891	2.00	1.874	2.00	1.051	0.991
					-0.20		0.00		-0.10		
	20	0.05	45	2.751	2.30	2.882	2.80	2.922	2.60	1.062	1.014
					0.30		0.60		0.50		
	100	0.01	45	2.236	3.20	2.292	3.80	2.395	3.60	1.071	1.045

*x/H and y/H are the coordinates of the critical toe circle when the origin is located at the toe of the slope.

critical OMS center.

4. The results obtained by the OMS and MB methods in case of cot β = 1 and $\lambda_{c\phi}$ = 20 agree very well with solutions reported by Wright (1969) for the same problem. This provides a check on the two methods as performed by the program STAB3D.

5. A comparison between the factor of safety, F^0, obtained by the three methods of analysis shows that:

   a. F^0 (MB) is consistently higher than F^0(OMS)

   b. F^0(MIT) is consistently higher than F^0(OMS)

   c. The agreement between F^0(MIT) and F^0(MB) is good for the more cohesive slopes. When $\lambda_{c\phi} \leq 20$, the difference between the two methods is less than 1.5%.

   d. In more frictional slopes ($\lambda_{c\phi}$ = 100), the difference between F^0(MIT) and F^0(MB) is about 4.5% when β is relatively small (cot β = 1.5 and 2). For steeper slopes (cot β = 1) the difference between F^0(MIT) and F^0(MB) is 9%. However, the failure surface in this case is very shallow, and therefore, this case is not considered to be of major practical importance.

The Modified Bishop method (MB) is one of the most widely used methods in circular arc slope stability analyses. Wright (1969) shows that the MB method predicts factors of safety F^0, which are within 1% of those predicted by the more exact method of Spencer* (1967) for homogeneous slopes with

---

*which satisfies all equilibrium conditions for each slice.

$0 \leq \lambda_{c\phi} \leq 50$, $1.5 \leq \cot \beta \leq 3.5$, and $r_u = 0$. Since the results in Table 6.1 show that, for these slopes, the MIT method is expected to predict F^0 to within 5% of the MB method, we thus conclude that the MIT method provides a reasonable degree of accuracy.

However, Whitman and Bailey (1967) and Turnbull and Hvorslev (1967) show that the Modified Bishop (MB) method is likely to yield questionable results when "deep" circles are encountered. This is illustrated in Fig. 6.2 by the distribution of $\bar{\sigma}_N/\sigma_v$ along the shear surface in case of a homogeneous slope with $\bar{\phi} = 30°$, $\bar{c} = 0$ and $r_u = 0$. For large negative values of θ, the MB method predicts very large values of $\bar{\sigma}_N/\sigma_v$ and hence an infinite passive resistance, when $\theta \leq \bar{\phi} - 90°$. Furthermore, Fig. 6.2 shows that the Ordinary Method of Slices (OMS) predicts very small values of $\bar{\sigma}_N/\sigma_v$ for large negative values of θ thus leading to small passive resistances. On the other hand, the distribution of $\bar{\sigma}_N/\sigma_v$ according to the MIT method appears reasonable for all values of θ.

Finally, the MIT method provides an explicit expression for the factor of safety, F^0, and thus avoids the iterations needed in the MB method. This reduces the required computer time by a factor of two, and offers a method which can easily be extended to three dimensional and/or probabilistic analyses.

6.3.2 Three-Dimensional Analyses

Three-dimensional analyses were performed for three slope angles (cot β = 1, 1.5 and 2), four values of $\lambda_{c\phi}$ (0, 4, 20 and

100) and $r_u = 0$. The analyses were conducted according to the extended OMS and MIT methods using the shear surfaces introduced in Chapter 2 which consist of a cone attached to a cylinder and an ellipsoid attached to a cylinder.

Analysis According to the Extended Ordinary Method of Slices. The results obtained according to the extended OMS by means of the computer program STAB3D are shown in Fig. 6.3. The ratio of the three-dimensional to the two-dimensional factor of safety F/F^0, is plotted versus the total normalized failure length, 2L/DR for cot $\beta = 1$ (dotted lines) and cot $\beta = 2$ (solid lines). We note in Fig. 6.3 that:

1. For the more cohesive slopes ($\lambda_{c\phi} = 0$ or 4), increasing the failure length reduces the end effects expressed by the ratio F/F^0. In the limit, when 2L/DR approaches infinity, $F/F^0 = 1$, and a plane strain mode of failure is, therefore, more likely to take place. For 2L/DR > 8, the end effects are smaller than 10%, and, in many cases, a two-dimensional analysis would be satisfactory. However, for 2L/DR < 8, the end effects may be significant enough to justify a three-dimensional analysis.

2. An increase in the frictional component of the shear strength reduces the end effects, i.e., F/F^0 decreases as $\lambda_{c\phi}$ increases, Fig. 6.3. For $\lambda_{c\phi} = 100$, F/F^0 is less than unity and the critical failure length is very short (2L/DR = 0.6 for cot $\beta = 2$). The extended OMS thus predicts that the failure of frictional slopes takes place along very short and

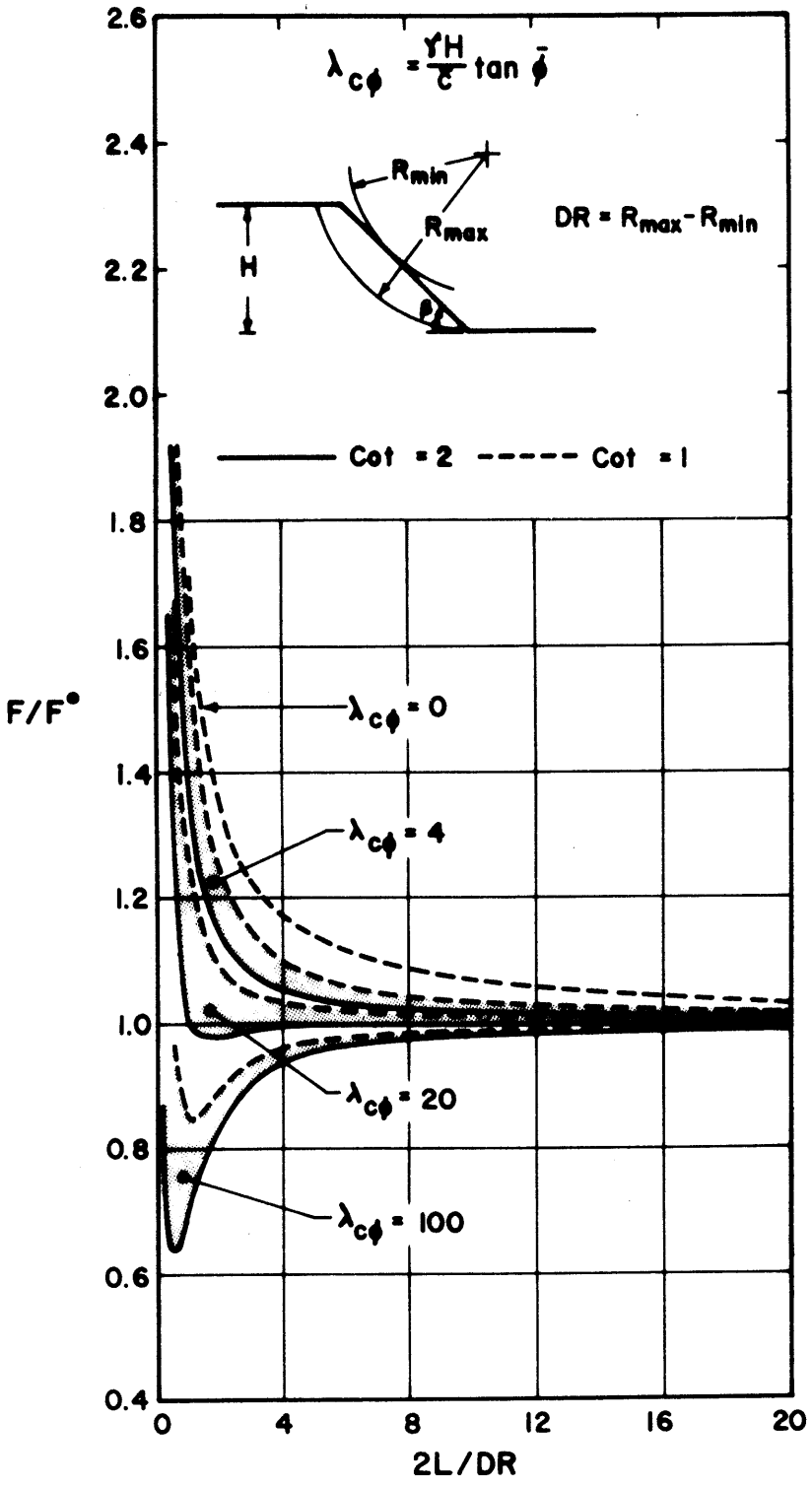


Figure 6.3 Results of the Drained Stability Analysis of Homogeneous Slopes According to the Ordinary Method of Slices

deep failures contrary to typical observed failure modes. This discrepancy arises because the extended OMS assumes that the effective longitudinal stress, $\bar{\sigma}_\ell$, is equal to zero. This assumption underestimates the fricitonal resistance on vertical planes and, therefore, becomes significant when $\lambda_{c\phi}$ increases.

3. The results in case of cot β = 1.5 fall between those for cot β = 1 and 2, in Fig. 6.3.

In conclusion, results obtained by the extended ordinary method of slices are not satisfactory, and a method which takes the longitudinal stress into consideration is needed.

Analysis According to the MIT Method. Three-dimensional analyses were performed according to the MIT method for the same slopes described earlier in the method of slices. The ratio, K, between the longitudinal effective stress to the vertical effective stress, ($K = \bar{\sigma}_\ell/\bar{\sigma}_v$) varied between 0.3 to 2 for $\lambda_{c\phi}$ = 4 and 20, and between 0 to 2 for $\lambda_{c\phi}$ = 100. The results are shown in Fig. 6.4 a, b and c for $\lambda_{c\phi}$ = 4, 20 and 100, respectively. From this figure we note that:

1. For $\lambda_{c\phi}$ = 100, the MIT method with K = 0 gives very similar results to the extended OMS: F/F^0 is less than unity, and the critical failure length is very short. These results were previously considered unsatisfactory in discussing the OMS because the longitudinal stresses, $\bar{\sigma}_\ell$, are neglected.

2. For most practical situations where K is expected to exceed 0.3 ($K \geq 0.3$), F/F^0 decreases as 2L/DR increases.

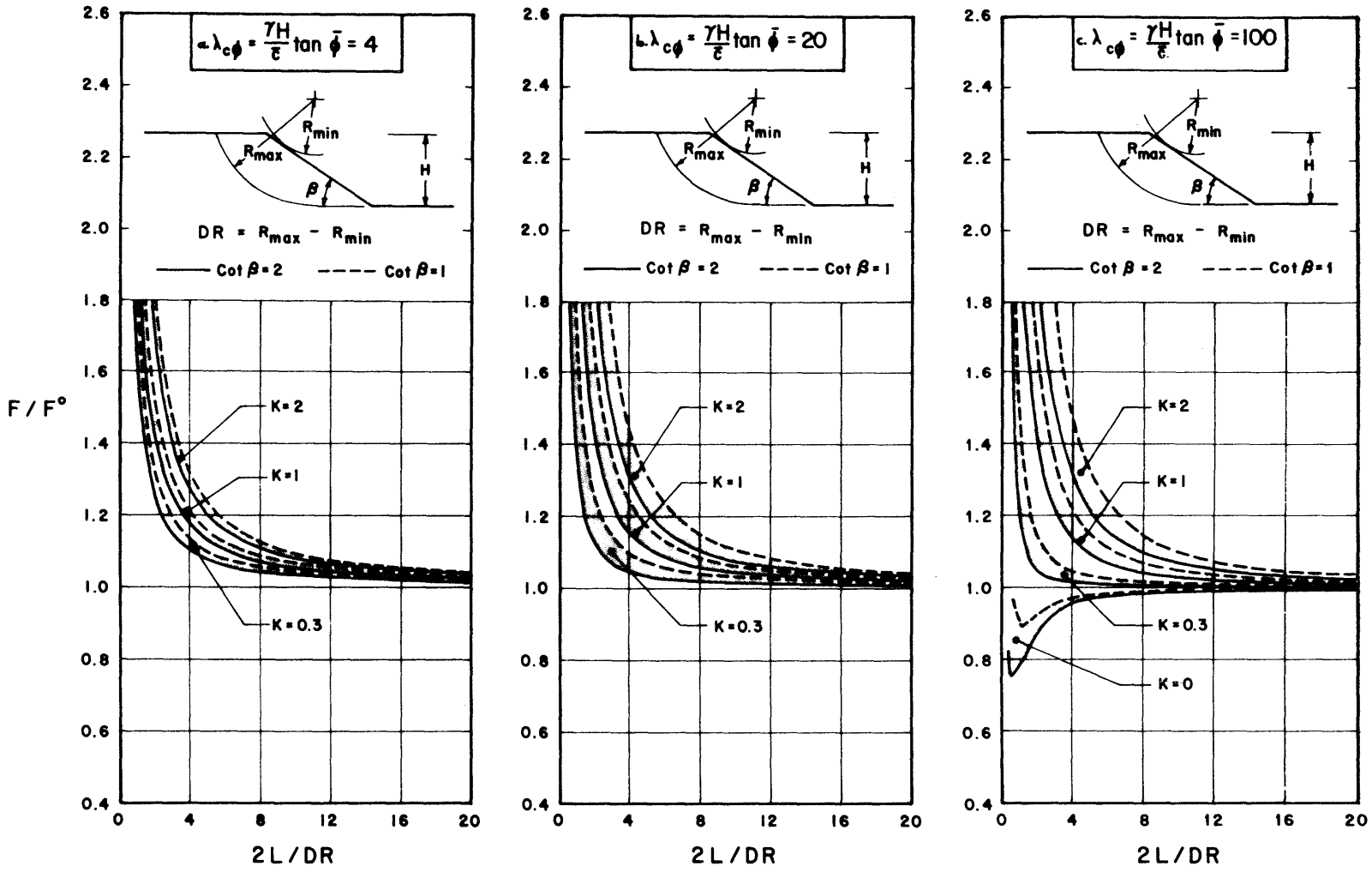


Figure 6.4 Results of the Drained Stability Analysis of Homogeneous Slopes According to the MIT Method

3. For $2L/DR \geq 10$, the end effects are not significant (i.e., F/F^0 approaches unity) for all values of $\lambda_{c\phi}$, cot β and K considered in the analyses.

4. An increase in the longitudinal effective stress, $\bar{\sigma}_\ell$, increases the end effects, i.e., F/F^0 increases when K increases. Furthermore, this effect of $\bar{\sigma}_\ell$ increases as the frictional strength parameter $\lambda_{c\phi}$ increases, and vanishes for frictionless slopes ($\lambda_{c\phi} = 0$). As an illustration, for $2L/DR = 4$ and cot $\beta = 1$, an increase in K from 0.3 to 2.0 increases F/F^0 by 16% (from 1.14 to 1.32) when $\lambda_{c\phi} = 4$ and by 40% (from 1.05 to 1.475) when $\lambda_{c\phi} = 100$.

5. In the case of $K = 0.3$ and $\lambda_{c\phi} = 100$, which corresponds to highly frictional slopes near the active state in the longitudinal direction, Fig. 6.4c shows no significant change in F/F^0 for $2L/DR \geq 2$.

6. The end effects are slightly increased by the slope angle β. The results obtained for cot $\beta = 1.5$ fall between the ones corresponding to cot $\beta = 1$ (dotted lines) and cot $\beta = 2$ (solid lines) in Fig. 6.4.

7. For all cases considered, the factor of safety obtained from ellipsoidal shear surfaces is lower than that from conical surfaces.

6.4 SUMMARY AND CONCLUSIONS

This chapter investigates the drained stability of slopes where the shear strength depends on the normal effective stress according to the Mohr-Coulomb criterion. In such cases, the stability problem is statically indeterminate and the normal effective stresses, $\bar{\sigma}_N$, along the shear surface must be assumed in order to estimate the factor of safety. This was achieved by adopting simplified procedures which are aimed at estimating "reasonable" bounds on $\bar{\sigma}_N$.

Two methods of analysis were used to estimate $\bar{\sigma}_N$: The Ordinary Method of Slices (OMS), and the MIT method (MIT). In the OMS, all interslice forces are neglected and $\bar{\sigma}_N$ is obtained from equilibrium in a direction normal to the base of the slice.

In two dimensions, the MIT method assumes that the vertical overburden stress is a major, or minor, principal stress at failure depending on whether the inclination of the base angle, θ, is positive or negative, respectively. In three dimensions, the longitudinal (out-of-plane) effective stress, $\bar{\sigma}_\ell$, is also assumed to be a principal stress and given by the ratio K ($= \bar{\sigma}_\ell/\bar{\sigma}_v$). Knowing the principal stress tensor, $\bar{\sigma}_N$ can then be easily computed.

In order to evaluate the effect of these assumptions on the two and three-dimensional factors of safety, the drained stability of homogeneous slopes was considered for three

slope angles (cot β = 1, 1.5 and 2), four values of the frictional strength parameter $\lambda_{c\phi}$, ($\lambda_{c\phi}$ = 0, 4, 20 and 100) and no pore water pressures (r_u = 0). In two-dimensional analyses, the Modified Bishop (MB) procedure (1955) was also used. The results of the stability analyses showed that:

In Two Dimensions

1. Similar to the ordinary method of slices (OMS), the MIT method provides an explicit expression for the plane strain factor of safety, F^0, and thus avoids the iteration required by the Modified Bishop (MB) method. This reduces the computer time significantly and enables extensions of the method to three dimensions to be easily performed. However, the MIT method predicts factors of safety that are in close agreement with those predicted by the MB method (for $\lambda_{c\phi} \leq 20$, the maximum difference between F^0 (MIT) and F^0 (MB) is about 1.5%).

2. The distribution of $\bar{\sigma}_N$ along the shear surface according to the MIT method appears reasonable for all values of θ even for "deep" circles (large negative values of θ). For this case, the MB method predicts infinite passive resistance for $\theta \leq \bar{\phi} - 90°$, and the OMS predicts a very small passive resistance which tends to zero at $\theta = -90°$.

In Three Dimensions

1. The results obtained by the extended OMS to three dimensions are shown in Fig. 6.3 where F/F^0 is plotted vs 2L/DR. The method predicts that failure of frictional slopes

($\lambda_{c\phi}$ = 100) takes place along very short and deep shear surfaces contrary to typical observed failure modes. This arises because the extended OMS assumes the effective longitudinal stress, $\bar{\sigma}_{\ell}$, to be equal to zero. This assumption underestimates the frictional resistance on vertical planes, becomes significant when $\lambda_{c\phi}$ increases, and, therefore, is not considered satisfactory.

2. The results obtained by the MIT method are shown in Fig. 6.4 for K = 0.3, 1 and 2 for $\lambda_{c\phi}$ = 4 and 20 and K = 0, 0.3, 1 and 2 for $\lambda_{c\phi}$ = 100.

In case K = 0, the MIT method, gives very similar results to the extended OMS: F/F^0 is less than unity, and the critical failure length is very short. This confirms the earlier conclusions that the extended OMS yields unrealistic results because the longitudinal stresses are neglected.

3. An increase in the longitudinal effective stress, $\bar{\sigma}_{\ell}$, increases the end effects, i.e., F/F^0 increases when K increases. Furthermore, this effect of $\bar{\sigma}_{\ell}$ increases as the frictional strength parameter, $\lambda_{c\phi}$, increases, and vanishes for frictionless slopes ($\lambda_{c\phi}$ = 0).

4. An increase in the frictional component of the shear strength reduces the end effects, i.e., F/F^0 decreases as $\lambda_{c\phi}$ increases (Fig. 6.3). In the case of K = 0.3 and $\lambda_{c\phi}$ = 100, which corresponds to highly frictional slopes near the active state in the longitudinal direction, end effects (F/F^0) are not significant when $2L/DR \geq 3$.

5. For $2L/DR \geq 10$, the end effects are not significant

for all values of $\lambda_{c\phi}$, cot β and K considered in the analyses (Fig. 6.4).

6. The end effects are slightly increased by the slope angle β. The results obtained for cot β = 1.5 fall between the ones corresponding to cot β = 1 (dotted lines) and cot β = 2 (solid lines) in Figs. 6.3 and 6.4.

7. Ellipsoidal shear surfaces gave consistently lower values of the factor of safety than conical surfaces.

CHAPTER 7

LENGTH OF FAILURE

The importance and consequences of a slope failure often depend on the length of failure along the slope. A short failure length can easily be repaired without severe financial losses, whereas a long failure might have disastrous consequences. Existing methods of slope stability analysis which rely on a plane strain formulation assume an infinite failure length and, therefore, are not suitable for predicting the failure length of a slope. Instead, a three-dimensional analysis is required.

Chapter 2 of this thesis presents the fundamental approach to three-dimensional slope stability for slopes with homogeneous cross sections, where the shear strength is constant along their axis. For such slopes, three-dimensional effects increase the factor of safety. The most critical failure length is thus infinite and corresponds to the plane strain solution (Chapters 3 and 6).

In order to better simulate the field conditions, where actual failures are three-dimensional, the variation of the shear strength along the slope axis is taken into consideration in this chapter. Models for such a variability are presented and evaluated both deterministically and prob-

abilistically. The results are then compared with the case of a uniform shear strength described in Chapter 3.

7.1 MODELS FOR STRENGTH VARIABILITY

In this chapter, we consider the undrained stability of cohesive slopes ($\phi = 0$, $c = s_u$) using two models for the variation of the cohesion, c, along the z-axis:

1. Sinusoidal Model:

$$c(z) = c^*[1 - m \cdot \cos \frac{\pi z}{\delta}] \qquad (7.1)$$

and

2. Saw-Tooth Model:

$$c(z) = c^*[1 - (-1)^i \cdot m\{(1 + 2i) - \frac{2|z|}{\delta}\}] \qquad (7.2)$$

where,

c^* = average cohesion along the length of the embankment. This is the value of the cohesion used to obtain the plane strain factor of safety, F^0,

m = amplitude of variation,

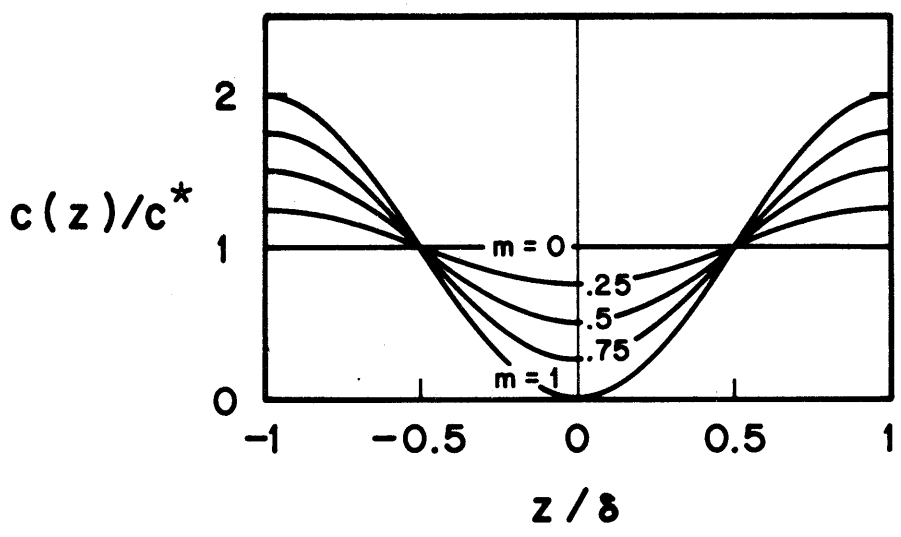
δ = half the wave length,

z = distance along the slope axis,

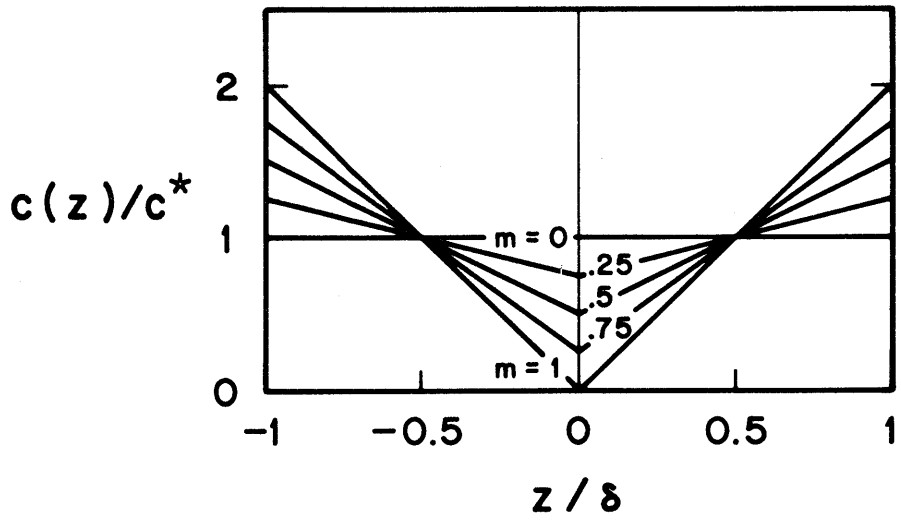
$|z|$ = absolute value of z, and

i = integer part of $(|z|/\delta)$

Equations (7.1) and (7.2) are illustrated in Fig. 7.1. We note that when $m = 0$, both models reduce to the case of a slope with a uniform shear strength along its axis.



SINUSOIDAL MODEL



SAW-TOOTH MODEL

Figure 7.1 Models for the Variation of Shear Strength Along the Longitudinal Axis of Embankments

7.2 UNDRAINED STABILITY OF A VERTICAL CUT

Let us consider the undrained stability of the vertical cut shown in Fig. 3.1 in Chapter 3. The z-axis is taken at the crest of the cut and the cylinder passes through the toe, i.e., $R_{max} = H$.

7.2.1 Closed-Form Solutions

For simplicity, analytical solutions are only obtained for the case of a conical shear surface attached to a cylinder (Fig. 3.1b) using the sinusoidal model described by Eq. (7.1).

The plane strain resisting and driving moments are given by:

$$M_r^0 = \frac{\pi}{2} \cdot R_{max}^2 \cdot c \qquad (7.3),$$

and

$$M_d^0 = \frac{\gamma}{3} \cdot R_{max}^3 \qquad (7.4),$$

respectively. The plane strain factor of safety is thus given by:

$$F^0 = \frac{3\pi}{2} \cdot \frac{c}{\gamma H} \qquad (7.5)$$

The resisting moment resulting from the cylindrical portion of the shear surface is expressed as follows:

$$M_r(\text{cylinder}) = \pi \cdot R_{max}^2 \int_{z=0}^{z=\ell_c} c(z) \cdot dz \qquad (7.6)$$

Substituting for c(z) from Eq. (7.1), we get:

$$M_r(\text{cylinder}) = \pi \cdot R_{max}^2 \cdot c^* \int_0^{\ell_c} (1 - m \cdot \cos \frac{\pi z}{\delta}) \cdot dz \qquad (7.7)$$

Upon integration and rearranging of terms, one obtains:

$$M_r(\text{cylinder}) = \pi \cdot c^* \cdot R_{max}^3 \cdot$$

$$[\frac{\ell_c}{R_{max}} - \frac{m}{\pi} \cdot \frac{\delta}{R_{max}} \cdot \sin \frac{\pi \ell_c}{\delta}] \qquad (7.8)$$

The driving moment of the cylindrical shear surface is given by Eq. (3.5), or,

$$M_d(\text{cylinder}) = \frac{2\gamma}{3} \cdot R_{max}^3 \cdot \ell_c \qquad (7.9)$$

For the conical shear surface, the resisting moment is given by: (see Eq. 2.23)

$$M_r(\text{cone}) = 2 \cdot \int_{\ell_c}^{\ell_c + \ell} M_r^0(z) \cdot \frac{dz}{\cos \rho} \qquad (7.10)$$

where,

ρ = cone angle

$$M_r^0(z) = \frac{\pi}{2} \cdot R^2(z) \cdot c^*(1 - m \cdot \cos \frac{\pi z}{\delta}) \qquad (7.11)$$

but, for the conical shear surface,

$$R(z) = (\ell_c + \ell - z) \tan \rho \qquad (7.12)$$

Hence,

$$M_r(\text{cone}) = \pi \cdot c^* \cdot \frac{\tan^2 \rho}{\cos \rho} \cdot \int_{\ell_c}^{\ell_c+\ell} (\ell + \ell_c - z)^2 \cdot$$

$$(1 - m \cdot \cos \frac{\pi z}{\delta}) \cdot dz \qquad (7.13)$$

Upon integration, simplification, and using the following relationships:

$$R_{max} = \ell \cdot \tan \rho \qquad (7.14)$$

$$\cos \rho = \frac{\ell}{\sqrt{\ell^2 + R_{max}^2}} \qquad (7.15)$$

$$DR = R_{max} = H \qquad (7.16)$$

and,

$$\lambda = \delta/DR \qquad (7.17),$$

the total (cylinder + cone) resisting moment is given by:

$$M_r = \pi \cdot c^* \cdot R_{max}^3 \left[\frac{\ell_c}{H} - \frac{m}{\pi} \cdot \lambda \cdot \sin(\frac{\pi \ell_c}{\lambda H}) + \right.$$

$$\sqrt{1 + (\ell/H)^2} \left\{ 1/3 - m[\frac{2}{\pi^3}(H/\ell)^3 \cdot \lambda^3 \cdot \sin(\frac{\pi \ell_c}{\lambda H}) - \right.$$

$$\frac{2}{\pi^3}(H/\ell)^3 \cdot \lambda^3 \cdot \sin(\frac{\pi \ell_c}{\lambda H} + \frac{\pi \ell}{\lambda H}) +$$

$$\left. \left. \frac{2}{\pi^2}(H/\ell)^2 \cdot \lambda^2 \cdot \cos(\frac{\pi \ell_c}{\lambda H}) - \frac{1}{\pi}(H/\ell) \cdot \lambda \cdot \sin(\frac{\pi \ell_c}{\lambda H})] \right\} \right] \qquad (7.18)$$

For the case of m = 0, Eq. (7.18) reduces to:

$$M_r = \pi \cdot c^* \cdot R_{max}^3 \left[\ell_c/H + 1/3\sqrt{1 + (\ell/H)^2}\right] \qquad (7.19)$$

which is identical to Eq. (3.14) obtained for the case of uniform shear strength (Chapter 3). The total driving moment is given by:

$$M_d = \frac{2\gamma}{3} \cdot R_{max}^4 \left(\ell_c/H + 1/4 \cdot \ell/H\right) \qquad (7.20)$$

and hence, the three-dimensional factor of safety is the ratio of M_r (Eq. 7.18) to M_d (Eq. 7.20). Figure 7.2 shows a plot of F/F^0 vs 2L/H for different values of λ and m.

7.2.2 Numerical Solutions

The effect of the shear strength variability on the undrained stability of the vertical cut shown in Fig. 3.1 was then studied using the program STAB3D. The analysis was carried out employing the ordinary method of slices (Fellenius, 1936). Results, shown in Fig. 7.3, were obtained for the two strength variability models expressed by Eqs. (7.1) and (7.2), using the shear surfaces described in Chapter 2.

From Figs. 7.2 and 7.3, the following can be advanced:

1. The results for the case of a uniform shear strength along the slope axis (considered in Chapter 3) are given by the curve for m = 0. The minimum value of F/F^0, $(F/F^0)_{min}$, is equal to unity and occurs at a critical failure length, $(2L/H)_{cr}$ equal to infinity. This means that a plane strain failure will take place.

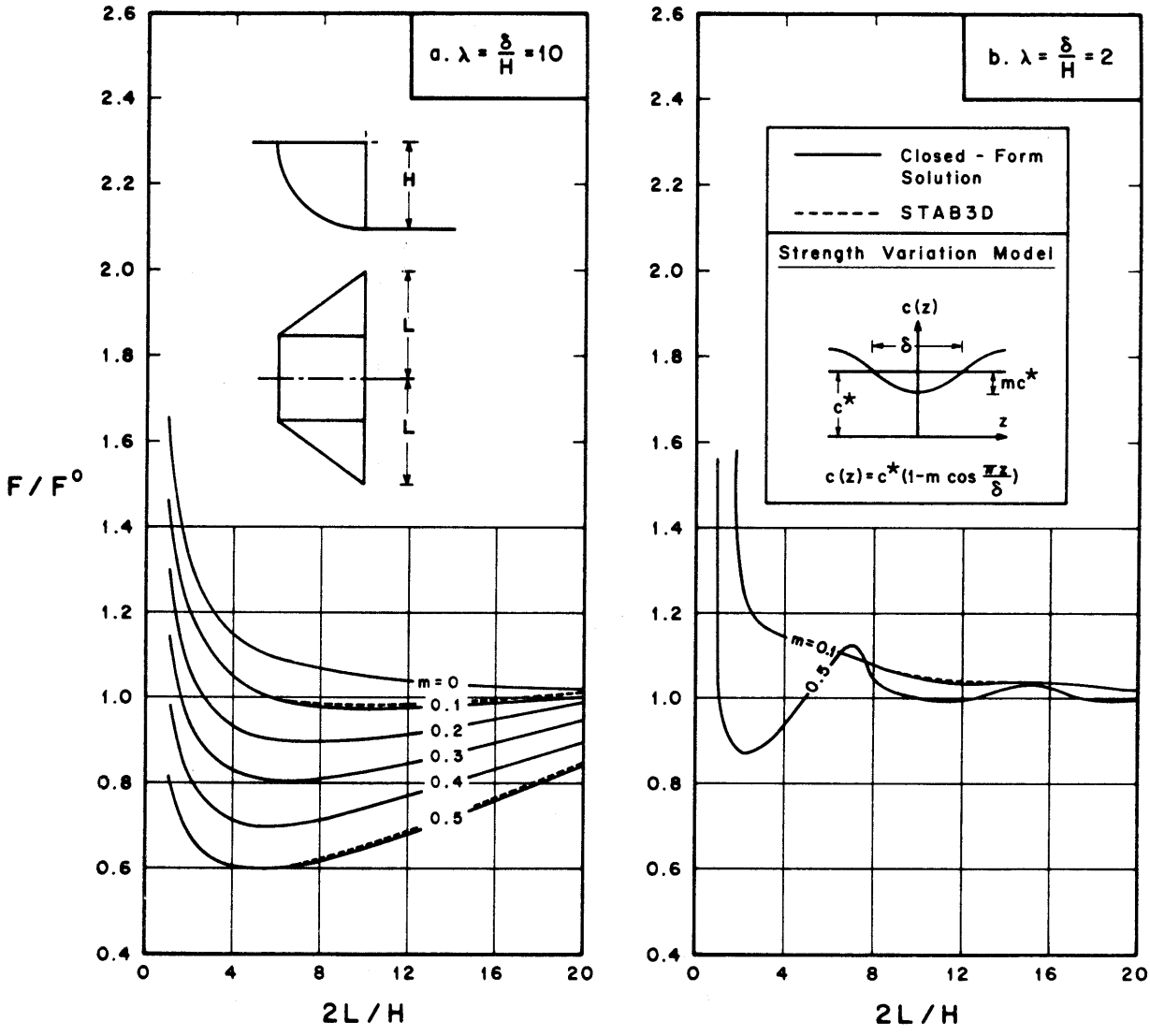


Fig. 7.2 End Effects on the Stability of a Vertical Cut with Non-Uniform Shear Strength Along the Longitudinal Axis (Conical Shear Surface)

2. Depending on the two parameters λ and m, the variability of the shear strength along the slope axis may cause a failure of finite length. For example, when the normalized half wave length $\lambda = \delta/H = 10$, and the wave amplitude factor $m = 0.5$ (solid line in Fig. 7.2a), the minimum factor of safety corresponds to a length of failure $2L \simeq 5.5H$ and is given by $F \simeq 0.6F^0$, i.e., three-dimensional effects reduce the plane strain factor of safety and, if neglected, can lead to unsafe designs.

On the other hand, in the case of $\lambda = 2$ and $m = 0.1$ in Fig. 7.2b, F/F^0 oscillates above unity. The minima for this curve decrease in amplitude as 2L/H increases and reach an absolute minimum equal to unity when 2L goes to infinity. This indicates that, for this case, a plane strain failure is more critical.

3. For a vertical cut, the critical finite failure length 2L is shorter than half the wave length δ of the strength variability, i.e., $(2L/H)_{cr} < \lambda$.

4. For the case of finite failures, an increase in m or in λ reduces the minimum factor of safety.

5. For the same values of m and λ , the sinusoidal and saw-tooth models give practically identical results (See Fig. 7.3). Therefore, only the sinusoidal model will be used in the remaining of this chapter.

6. Comparing the solid and dotted lines in Fig. 7.2, the solutions obtained by the computer program STAB3D show

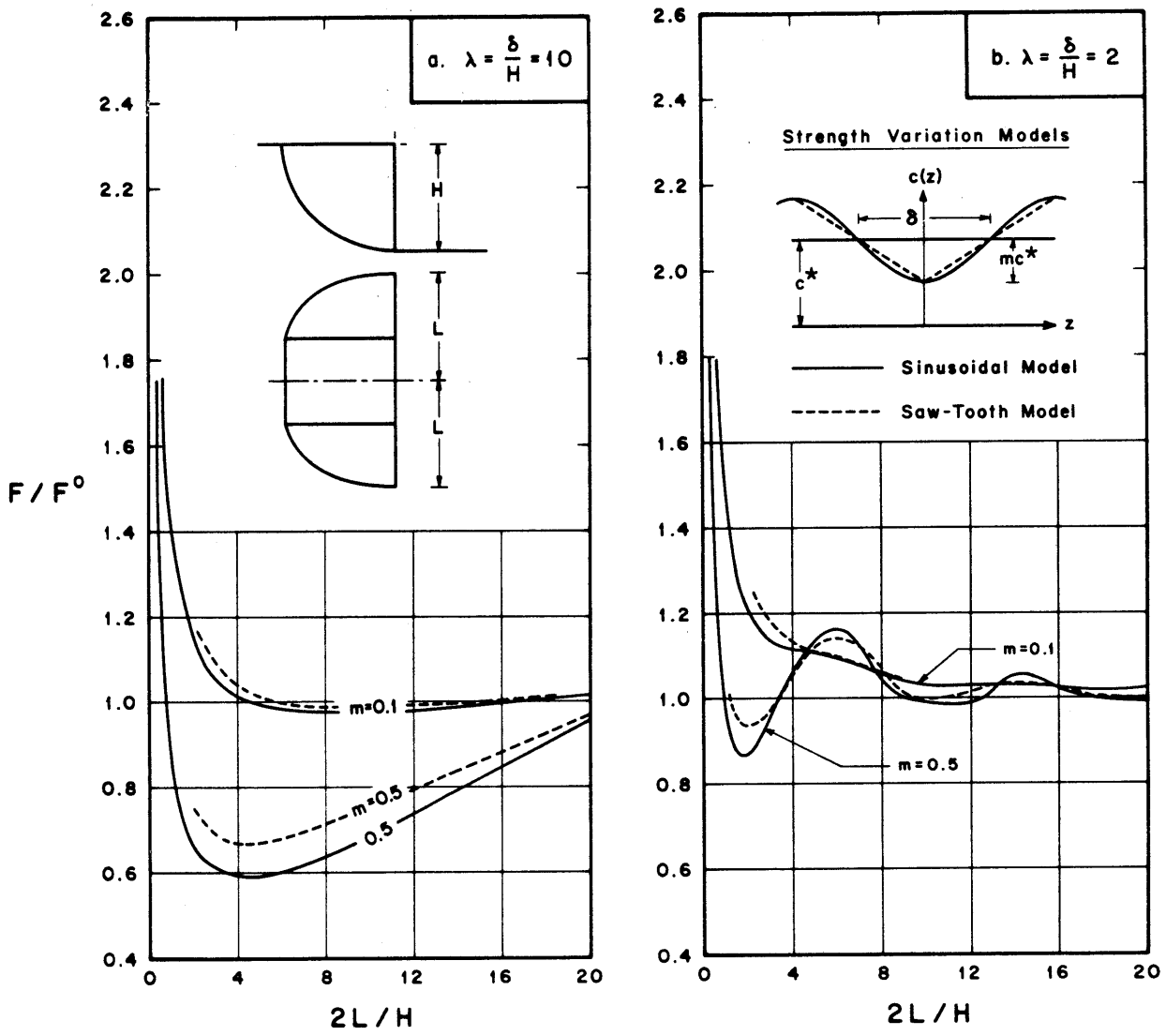


Figure 7.3 End Effects on the Stability of a Vertical Cut with Non-uniform Shear Strength Along the Longitudinal Axis (Ellipsoidal Shear Surface)

excellent agreement with the closed-form solutions presented in Section 7.2.1.

7. For a vertical cut, ellipsoidal failure surfaces gave consistently lower values of the factor of safety than conical surfaces and are, therefore, more likely to represent actual failures.

7.3 UNDRAINED STABILITY OF HOMOGENEOUS SLOPES

The effect of strength variation along the axis of slopes with homogeneous cross sections was evaluated numerically using the program STAB3D. Figure 7.4 shows a slope of height H, making an angle β with the horizontal, where the failure length is 2L.

The steps used in determining the minimum safety factors and the associated critical shear surfaces are the same as those described in Section 3.2 of Chapter 3. We assume the location of the z-axis, values of R_{max} and ℓ_c, the shape of the shear surface (cone or ellipsoid attached to a cylinder), and the mode of strength variation. The corresponding value of the safety factor, F, is obtained. The process is repeated until the minimum value of F is obtained.

Figure 7.4 shows a plot of F/F^0 against 2L/DR for the toe failure of slopes with $\beta = 10°$ and $\beta = 90°$, and for the shear strength variation described by the sinusoidal model in Eq. (7.1). The results show that:

1. The two parameters m and λ, which describe the strength variation along the slope axis, determine the mode of failure. This is illustrated by the curves corresponding to $\lambda = 10$ and $\lambda = 2$ when $m = 0.25$. For the short wave length $\lambda = 2$, the curve of F/F^0 vs 2L/DR oscillates above unity resulting in an infinite failure length with an $(F/F^0)_{min} = 1$. On

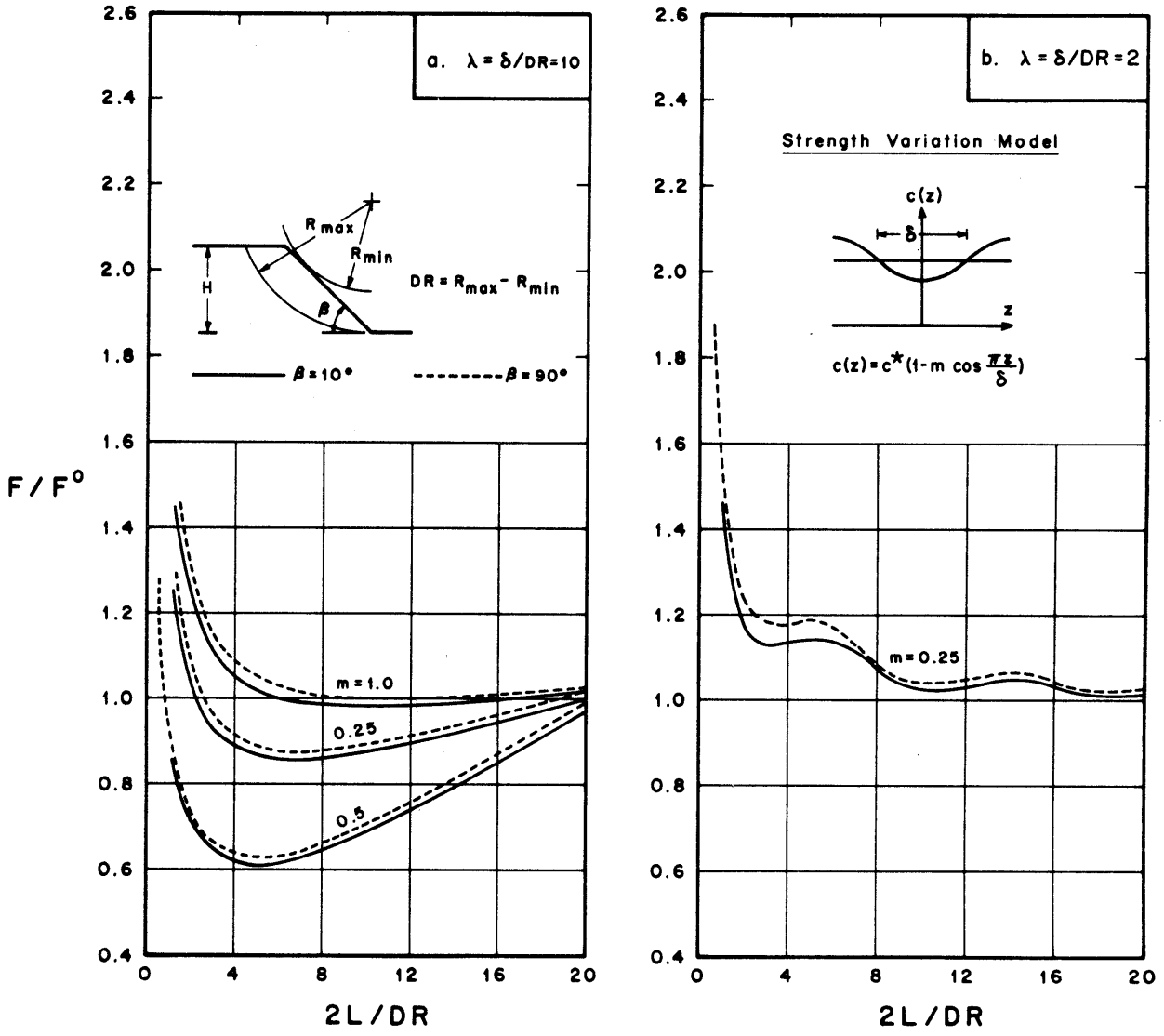


Figure 7.4 End Effects on the Stability of Slopes with Homogeneous Cross Sections and Non-uniform Shear Strength Along Their Axis

the other hand, for the longer wave length $\lambda = 10$, F/F^0 has a minimum which is less than unity and, therefore, corresponds to a finite failure length.

2. For finite failure lengths, the factor of safety decreases when m increases or when λ increases.

3. For slopes with homogeneous cross sections considered herein, finite failure lengths, 2L, are shorter than the half wave length, δ, of the strength variation.

4. For a given ratio of 2L/DR, the slope angle β has little influence on the values of F/F^0 , $(F/F^0)_{min}$ and $(2L/DR)_{cr}$.

5. Ellipsoidal shear surfaces gave consistently lower values of $(F/F^0)_{min}$ than conical shear surfaces and, therefore, they are more likely to simulate actual field conditions.

7.4 LENGTH OF FAILURE -- APPROXIMATE ANALYSIS

Considering the sinusoidal strength variation model described by Eq. (7.1), let us define the average cohesion, $\bar{c}$, along a length 2L by the expression (see Fig. 7.5):

$$\bar{c} = \frac{1}{2L} \cdot \int_{-L}^{L} c(x) \cdot dx \tag{7.21}$$

From Eqs. (7.1) and (7.21) and using the fact that c(x) is an even function, we get:

$$\bar{c} = \frac{2c^*}{L} \cdot \int_{0}^{L} (1 - m \cdot \cos \frac{\pi x}{\delta}) \cdot dx \tag{7.22}$$

Integrating we get:

$$\bar{c} = c^*[1 - \frac{2m}{\pi} \cdot \frac{\delta}{2L} \cdot \sin \frac{2\pi L}{2\delta}] \tag{7.23}$$

Eq. (7.23) may be also written as:

$$\frac{\bar{c}}{c^*} = 1 - \frac{2m}{\pi} \cdot \frac{\delta}{DR} \cdot \frac{DR}{2L} \cdot \sin(\frac{\pi}{2} \cdot \frac{2L}{DR} \cdot \frac{DR}{\delta}) \tag{7.24}$$

Using $\lambda = \delta/DR$, Eq. (7.24) can be written as:

$$\frac{\bar{c}}{c^*} = 1 - \frac{2m}{\pi} \cdot \lambda \cdot \frac{DR}{2L} \cdot \sin(\frac{\pi}{2} \cdot \frac{2L}{DR} \cdot \frac{1}{\lambda}) \tag{7.25}$$

7.4.1 Factor of Safety and Critical Failure Length

For slopes with uniform shear strength along their axis (m = 0), the dependence of F/F^0 on 2L/DR (see Fig. 3.4) can

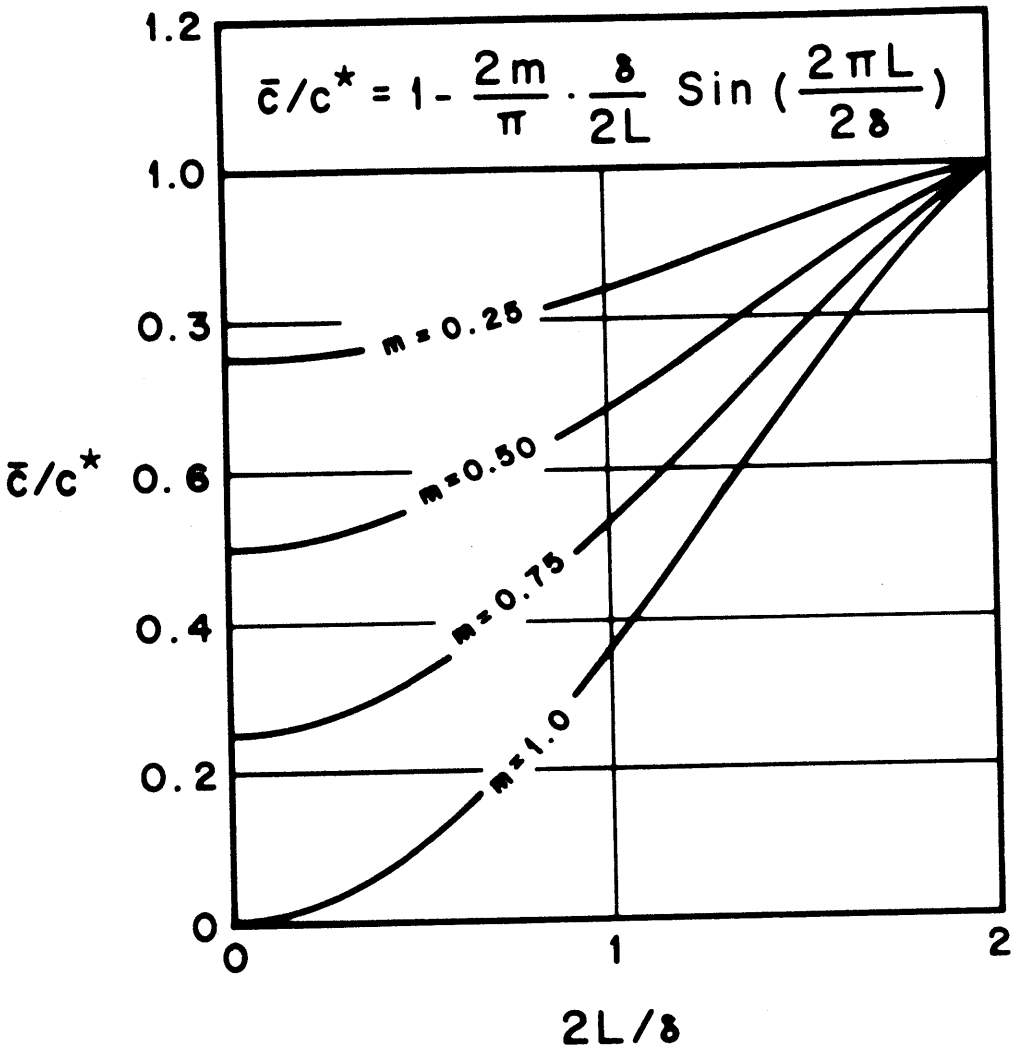


Figure 7.5 Average Strength Along Length 2L of an Embankment (Centered at z = 0)

be approximated by the expression:

$$F = [1 + \alpha(\frac{2L}{DR})^{\gamma}] \cdot F^0 \qquad (7.26)$$

where α and γ are constants that depend on the slope geometry as well as the soil properties, and F^0 is the plane strain factor of safety based on $c = c^*$. Knowing that F is proportional to the value of $\bar{c}$, we use Eq. (7.25) to write the factor of safety F for a slope, where the strength varies along its axis, in the form:

$$F = \left\{1 - \frac{2m}{\pi} \cdot \lambda \cdot \frac{DR}{2L} \cdot \sin(\frac{\pi}{2} \cdot \frac{2L}{DR} \cdot \frac{1}{\lambda})\right\} \left\{1 + \alpha(\frac{2L}{DR})^{\gamma}\right\} \cdot F^0 \qquad (7.27)$$

This is an approximate expression for F which will be shown to be of reasonable accuracy for practical applications.

7.4.2 Constants α and γ

In order to determine the constants α and γ in Eq. (7.26) for the curves in Fig. 3.4 of Chapter 3, the least squares approach was used (Crandall, 1956). Table 7.1 gives these values for different slope geometries. The dependence of α and γ on the slope angle β and the depth to bedrock n, (in case of base failures), is not significant. The following analysis was, therefore, performed using $\alpha = 0.7$ and $\gamma = -1$ for toe failures, and $\alpha = 0.8$ and $\gamma = -1.25$ for base failures.

7.4.3 Results

Figure 7.6 shows a plot of F/F^0 against 2L/DR, according

Table 7.1 Constants α and γ in the Equation

$$F = [1 + \alpha(\frac{2L}{DR})^{\gamma}]\ F^{0}$$

Case			α	γ	Correlation Coefficient r
Base Failures	cot β = 1	n = 1.25	0.792	-1.276	0.993
		1.5	0.673	-1.306	0.991
		2	0.566	-1.269	0.984
	cot β = 1.5	n = 1.25	1.011	-1.274	0.998
		1.5	0.801	-1.241	0.992
		2	0.742	-1.340	0.997
	cot β = 2	n = 1.25	1.037	-1.160	0.999
		1.5	0.895	-1.191	0.995
		2	0.793	-1.257	0.998
All Base Failures			0.80	-1.25	0.952
Toe Failures	β = 10°		0.674	-1.075	0.999
	β = 90°		0.881	-1.120	0.998
All Toe Failures			0.70	-1.00	0.976

to Eq. (7.27), for the case of toe failures when $\lambda = 10$ and $m = 0$, 0.25 and 0.5. To check the accuracy of this approximate expression, results obtained previously (Fig. 7.4) by means of the computer program STAB3D for the same cases described above are also plotted on the same figure. The agreement between the solid curves (approximate) and the dotted ones (STAB3D) is good and shows that Eq. (7.27) offers adequate accuracy.

Using the approximate expression in Eq. (7.27), the minimum value $(F/F^0)_{min}$ and the corresponding critical failure length $(2L/DR)_{cr}$ at any values of λ and m can be easily obtained by differentiation. The results of this analysis are shown in Fig. 7.7a for toe failures and in Fig. 7.7b for base failures when λ varies between 1 and 100 and m varies between 0.1 and 0.6. Results in Fig. 7.7 show that:

1. The parameters m and λ describing the shear strength variation along the slope axis determine the mode of failure. For example, when $m = 0.2$, Fig. 7.7a shows that $(F/F^0)_{min}$ and $(2L/DR)_{cr}$ in case of $\lambda = 100$ are given by 0.82 and 32, respectively, i.e., a failure with finite length will take place. By decreasing the value of λ, $(F/F^0)_{min}$ increases, and $(2L/DR)_{cr}$ decreases until $\lambda \simeq 5$. For $\lambda < 5$, $(F/F^0)_{min} = 1$ and the failure has an infinite length.

2. For finite failure lengths, the factor of safety decreases when m increases or when λ increases.

3. For the case of slopes with homogeneous cross sec-

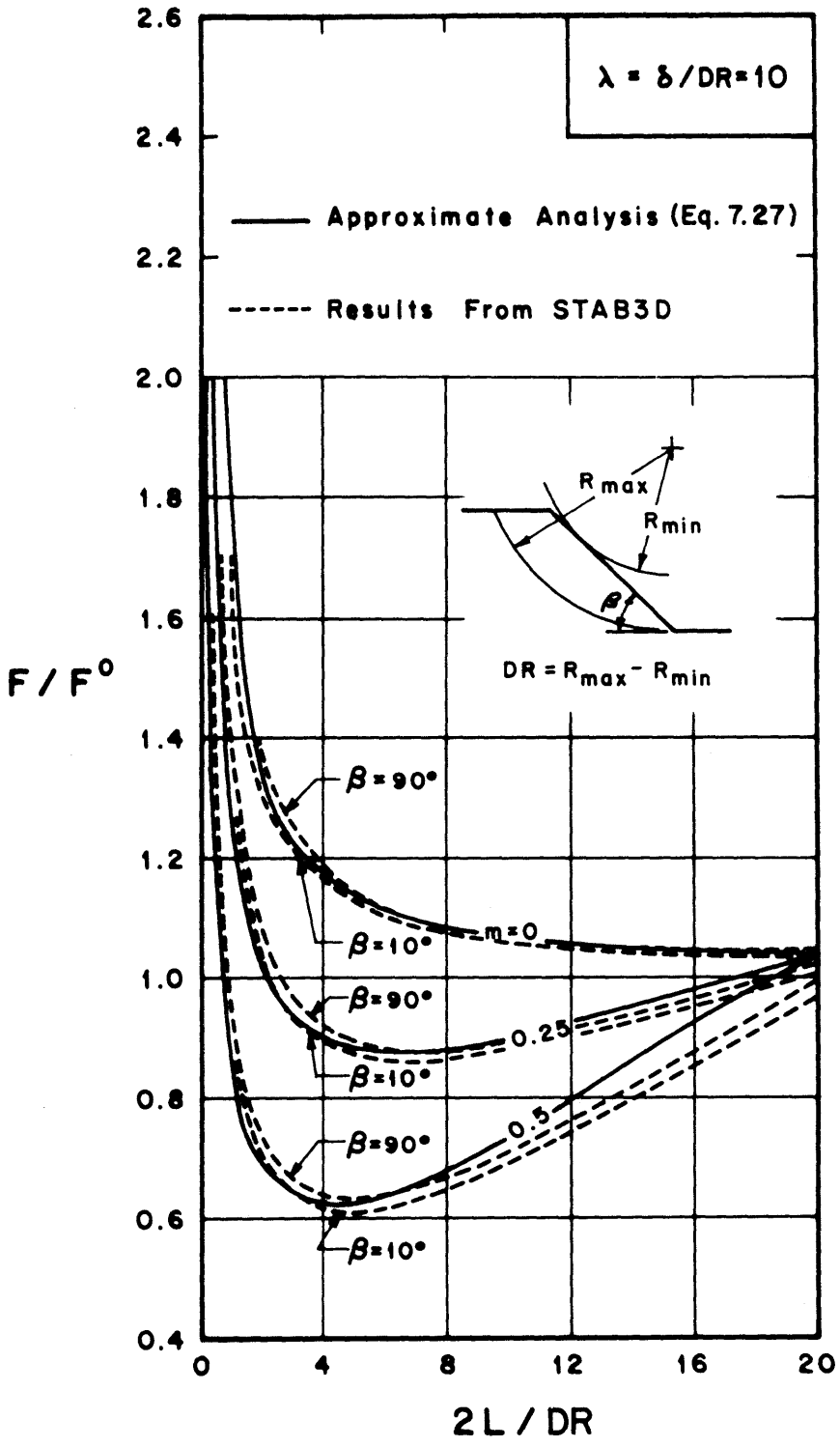


Figure 7.6 A Comparison Between the Results of the Approximate Analysis, Eq. 7.27, and Results from STAB3D

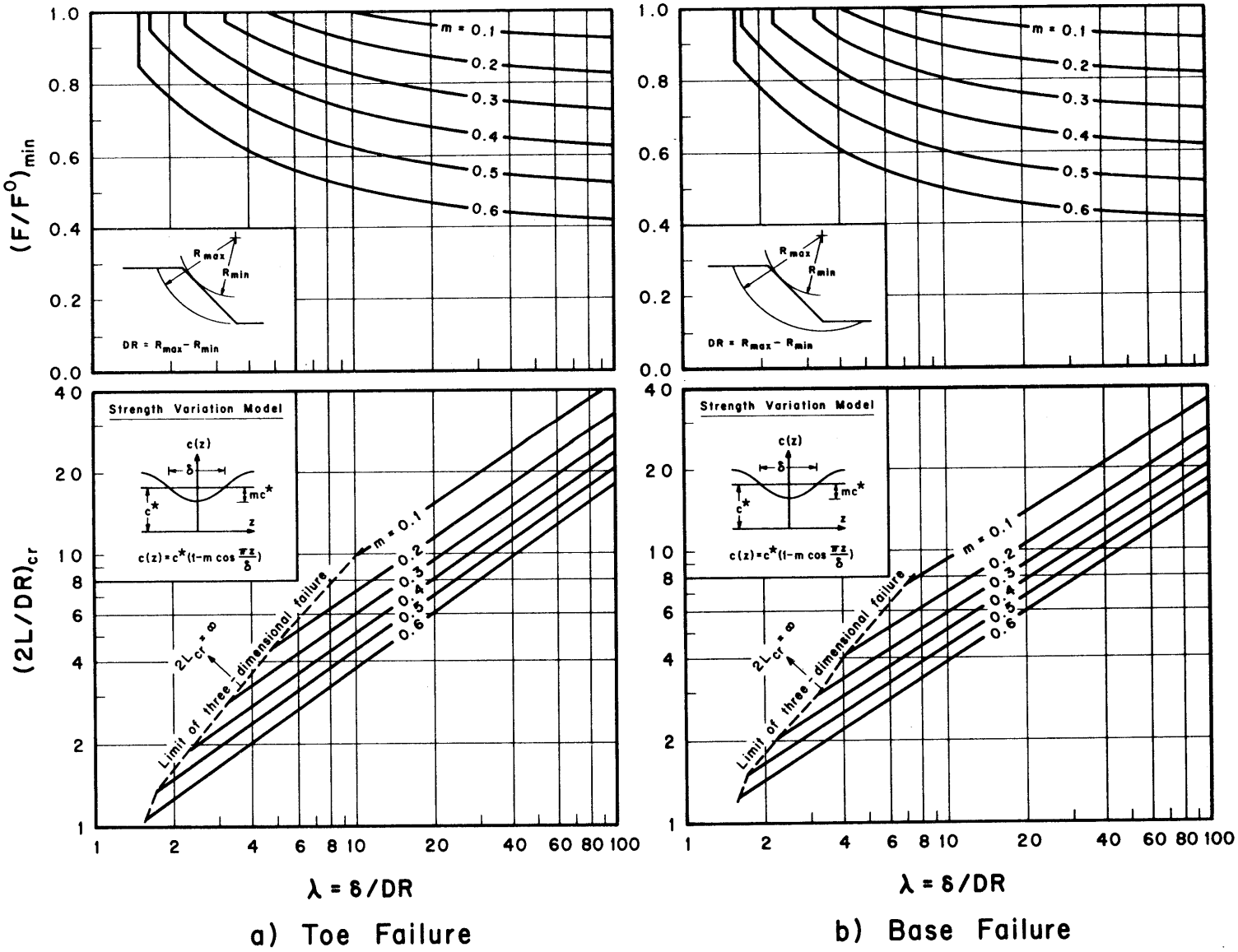


Figure 7.7 Minimum Factors of Safety and Critical Failure Lengths for Slopes with Homogeneous Cross Sections and Non-uniform Shear Strength Along Their Axis

tions considered herein, finite failure lengths are shorter than the half wave length δ of the strength variation.

7.4.4 Design Methodology

In order to design cohesive slopes taking into account the three-dimensional nature of failure and the variability of the shear strength along the slope axis, the following procedure is recommended:

1. Determine the cohesion distribution along the axis of the slope and compute the overall average cohesion c* along the embankment. Obtain the plane strain solution, and evaluate F^0 and DR.

2. Choose an origin for the z-axis (parallel to the slope axis) at a point where the cohesion is low.

3. Estimate the average cohesion $\bar{c}$ along a length 2L between z = -L and z = L, the distance L varies between zero and the closest end of the embankment. Note that when 2L approaches the embankment length, $\bar{c}$ approaches c*.

4. Assume a value of δ and plot $\bar{c}/c^*$ vs $2L/\delta$ on Fig. 7.5. Estimate m such that, for this value of δ, the area under the actual curve of $\bar{c}/c^*$ vs $2L/\delta$ and the idealized cosine curve is the same.

5. Knowing m and δ, obtain F_{min} and $2L_{cr}$ corresponding to this first trial from Fig. 7.7.

6. Repeat steps 4 and 5 to determine for a new set of values of m and λ, a new set of F_{min} and $2L_{cr}$. Note that F_{min} decreases with both m and λ.

7. Repeat steps 2 through 6.

8. The most critical length and its location will correspond to the minimum value of F_{min} of all trials.

7.5 LENGTH OF FAILURE -- A PROBABILISTIC APPROACH

In practice, the safety factor of embankments and slopes is evaluated on the basis of shear strength data obtained at selected elevations and at discrete locations along both the transverse and longitudinal directions. Errors in the factor of safety are introduced by the method of analysis (limit equilibrium, circular arc, partial drainage, ... etc.), systematic sampling errors, and testing techniques, etc. In addition, errors are also introduced because of inherent soil variability.

More recent advances in the analysis of slopes rely on probability, statistics and decision theory to evaluate the effect of the previously mentioned factors on the stability of embankments (Morla Catalan and Cornell, 1976; Gilbert, 1974; Matsuo and Kuroda, 1974, 1971; Yucemen et al, 1973; Barboteu, 1972; and Wu and Kraft, 1970). All of these studies are based on the classical plane strain (two-dimensional) method of analysis.

Vanmarcke (1977b) developed a three-dimensional probabilistic model to predict the reliability of embankments. This model is an extension of the circular arc method where the shear surface is a cylinder of finite length bounded by vertical end sections. Vanmarcke considers only the uncertainties resulting from shear strength variability along the cylindrical shear surface. The resistance of both ends

of the shear surface and the unit weight of the soil are treated as deterministic variables. The model determines the most likely failure length of an embankment and its probability of occurance. It also predicts the probability of a slope failure anywhere along an embankment with a given length.

In the remaining of this chapter, the reliability of slopes is assessed, employing the principles established by Vanmarcke, for more realistic modes of failure. Results are compared with the deterministic solutions presented in Section 7.4.

7.5.1 Probabilistic Model

The plane strain factor of safety can be expressed by (see Eq. 2.6):

$$F^0 = \frac{M_r^0}{M_d^0} = \frac{T \cdot R_{max}}{W \cdot a} \tag{7.28}$$

For the case of cohesive slopes with homogeneous cross sections, T is given by:

$$T = c \cdot S \tag{7.29}$$

Where S is the arc length of the failure surface. Substituting in Eq. (7.28) we get:

$$F^0 = \frac{c \cdot S \cdot R_{max}}{W \cdot a} \tag{7.30}$$

Substituting from Eq. (7.30) into Eq. (7.26), the factor of

safety associated with a failure length 2L is given by:

$$F_{2L} = \frac{c \cdot S \cdot R_{max}}{W \cdot a} [1 + \alpha(2L/DR)^{\gamma}] \qquad (7.31)$$

In the analysis presented herein, the following assumptions are made:

1. Soil is statistically homogeneous, i.e., the shear strength varies randomly about the average throughout the soil. However, these deviations are of a uniform statistical nature.

2. The inherent variability of the shear strength, c, constitutes the major uncertainty in the factor of safety, F_{2L}. Hence, F_{2L} is a function of only one random variable, and, its probability distribution can be easily obtained once the probability distribution of the shear strength is estimated. Ideally, this probability distribution should be determined from a sufficiently large number of tests. However, in view of limited reliable data in this area, more than one distribution is often used. We will consider herein the following two distributions:

1. The Gaussian distribution, where the probability density function of the undrained shear strength, p(c), is given by:

$$p(c) = \frac{1}{\tilde{c}\sqrt{2\pi}} \exp[-1/2(\frac{c - \bar{c}}{\tilde{c}})^2] \qquad -\infty \leq c \leq \infty \qquad (7.32)$$

The cumulative distribution function, P(c), which is the

probability that the undrained shear strength is less or equal to a specific value c is given by :

$$P(c) = \frac{1}{\tilde{c}\sqrt{2\pi}} \int_{-\infty}^{c} \exp[-\tfrac{1}{2}(\frac{\eta - \bar{c}}{\tilde{c}})]d\eta \qquad (7.33)$$

which can be rewritten as:

$$P(c) = \tfrac{1}{2}[1 + \text{erf}(\frac{c - \bar{c}}{\sqrt{2}\tilde{c}})]^{*} \qquad (7.34)$$

in which erf( ) is the error function (Abramowitz and Stegun, 1970).

2. The sinusoidal distribution. The cumulative distribution function of the shear strength whose longitudinal variation is described by Eq. (7.1) is given by (Thomson, 1965):

$$P(c) = \frac{1}{2} + \frac{1}{\pi} \sin^{-1}(\frac{c - c^*}{mc^*}) \quad \text{for}$$

$$c^*(1 - m) \leq c \leq c^*(1 + m)$$

$$P(c) = 0 \text{ for } c < c^*(1 - m) \text{ or } c > c^*(1 + m) \qquad (7.35)$$

The corresponding probability density function is given by:

$$p(c) = \frac{1}{c^*\pi}[m^2 - (\frac{c}{c^*} - 1)^2]^{-\frac{1}{2}} \text{ for}$$

$$c^*(1 - m) \leq c \leq c^*(1 + m) \qquad (7.36)$$

$$p(c) = 0 \text{ for } c < c^*(1 - m) \text{ or } c > c^*(1 + m)$$

Both of these functions are shown in Fig. 7.8.

---

* $\bar{c}$ and $\tilde{c}$ are the mean and the standard deviation of c, respectively.

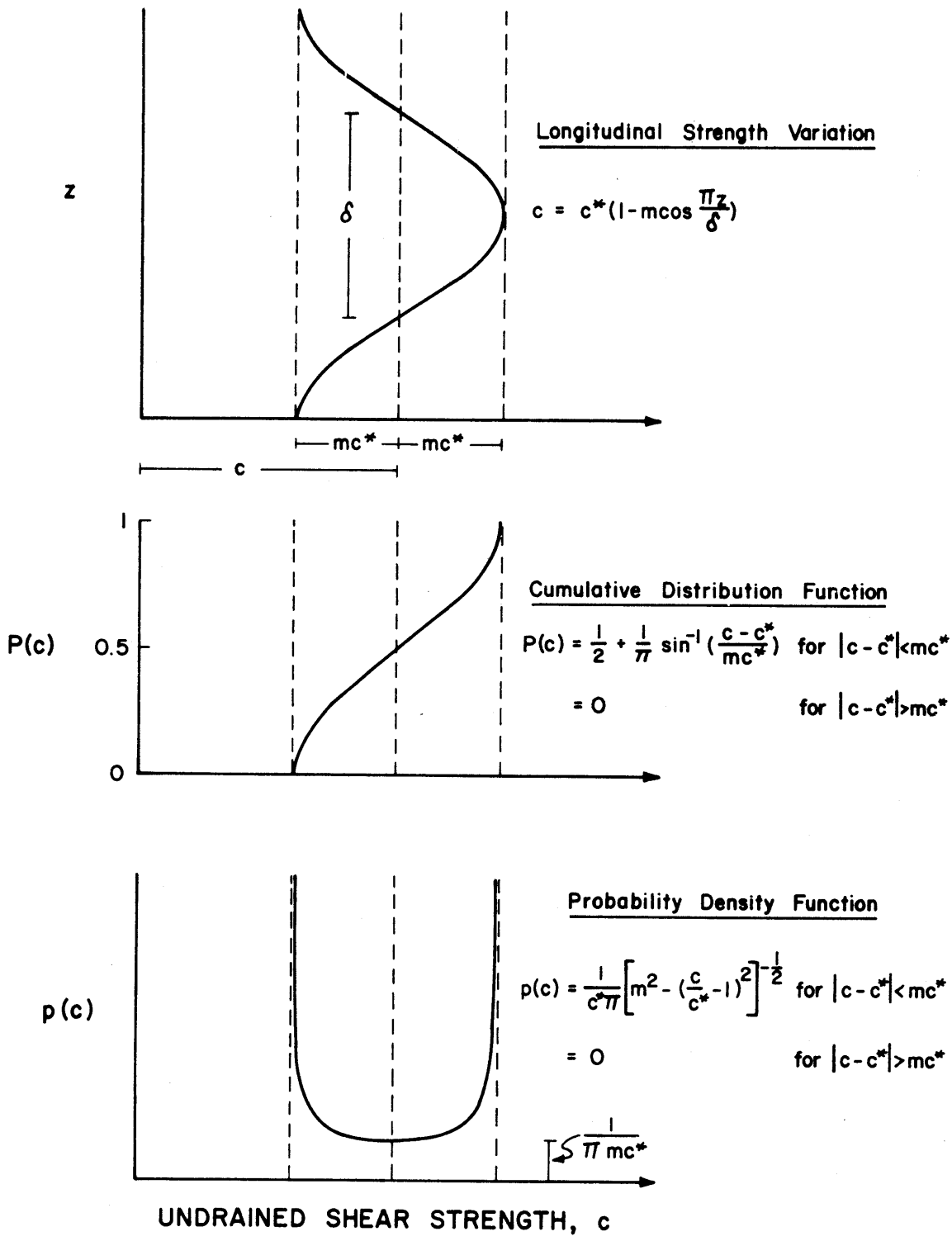


Figure 7.8 Sinusoidal Probability Distribution Models

The probability that the factor of safety associated with a failure length 2L is equal to or less than a specific value, $P(F_{2L})$, can, therefore, be determined by replacing c by F_{2L} in Eqs. (7.34) and (7.35), or

$$P(F_{2L}) = \frac{1}{2}\left[1 + \text{erf}\left(\frac{F_{2L} - \bar{F}_{2L}}{\sqrt{2}\,\tilde{F}_{2L}}\right)\right] \tag{7.37}$$

for the case of Gaussian distribution, and

$$P(F_{2L}) = \frac{1}{2} + \frac{1}{\pi}\sin^{-1}\left(\frac{F_{2L} - \bar{F}_{2L}}{\sqrt{2}\,\tilde{F}_{2L}}\right) \tag{7.38}$$

for the case of sinusoidal distribution, and realizing that

$$mc^* = \sqrt{2}\,\tilde{c} \tag{7.39}$$

The probability of an embankment failure along a length 2L, $p_f(2L)$, corresponding to the probability that $F_{2L} \leq 1$, is obtained by setting $F_{2L} = 1$ in either of the above two equations depending on the probability distribution at hand. In Eqs. (7.37) and (7.38), $\bar{F}_{2L}$ and $\tilde{F}_{2L}$ are the mean and standard deviation of the factor of safety. They are given by (see Eq. 7.31):

$$\bar{F}_{2L} = \frac{\bar{c}_{2L} \cdot S \cdot R_{max}}{W \cdot a}\left[1 + \alpha\left(\frac{2L}{DR}\right)^{\gamma}\right] \tag{7.40}$$

and

$$\tilde{F}_{2L} = \frac{\tilde{c}_{2L} \cdot S \cdot R_{max}}{W \cdot a}\left[1 + \alpha\left(\frac{2L}{DR}\right)^{\gamma}\right] \tag{7.41}$$

respectively, where $\bar{c}_{2L}$ and $\tilde{c}_{2L}$ are the mean and standard deviations of the shear strength of all sections of length = 2L.

Following Vanmarcke (1977a), $\bar{c}_{2L}$ and $\tilde{c}_{2L}$ are related to the point mean $\bar{c}$ and standard deviation $\tilde{c}$ by the expressions:

$$\bar{c}_{2L} = \bar{c} \tag{7.42}$$

and

$$\tilde{c}_{2L} = \Gamma(2L)\ \tilde{c} \tag{7.43},$$

where $\Gamma(2L)$ is a dimensionless reduction factor between 0 and 1 which will be discussed in the following section. Rewriting Eqs. (7.40) and (7.41) and noting that the mean value of the plane strain factor of safety is expressed by:

$$F^0 = \frac{\bar{c} \cdot S \cdot R_{max}}{W \cdot a} \tag{7.44}$$

we get

$$\bar{F}_{2L} = F^0 [1 + \alpha (\frac{2L}{DR})^{\gamma}] \tag{7.45}$$

and

$$\tilde{F}_{2L} = \Gamma(2L)\ \frac{\tilde{c}}{\bar{c}}\ \bar{F}_{2L} \tag{7.46}.$$

Note here that $\tilde{c}/\bar{c}$ is the coefficient of variation of the shear strength.

7.5.2 Reduction Factors

The reduction factor Γ (Eq. 7.43) should be evaluated for the soil deposit under consideration from a large number of tests. Such data is not presently available and, therefore, three expressions for Γ are considered herein. Two of these expressions were used by Vanmarcke (1977a) and are shown in Fig. 7.9.

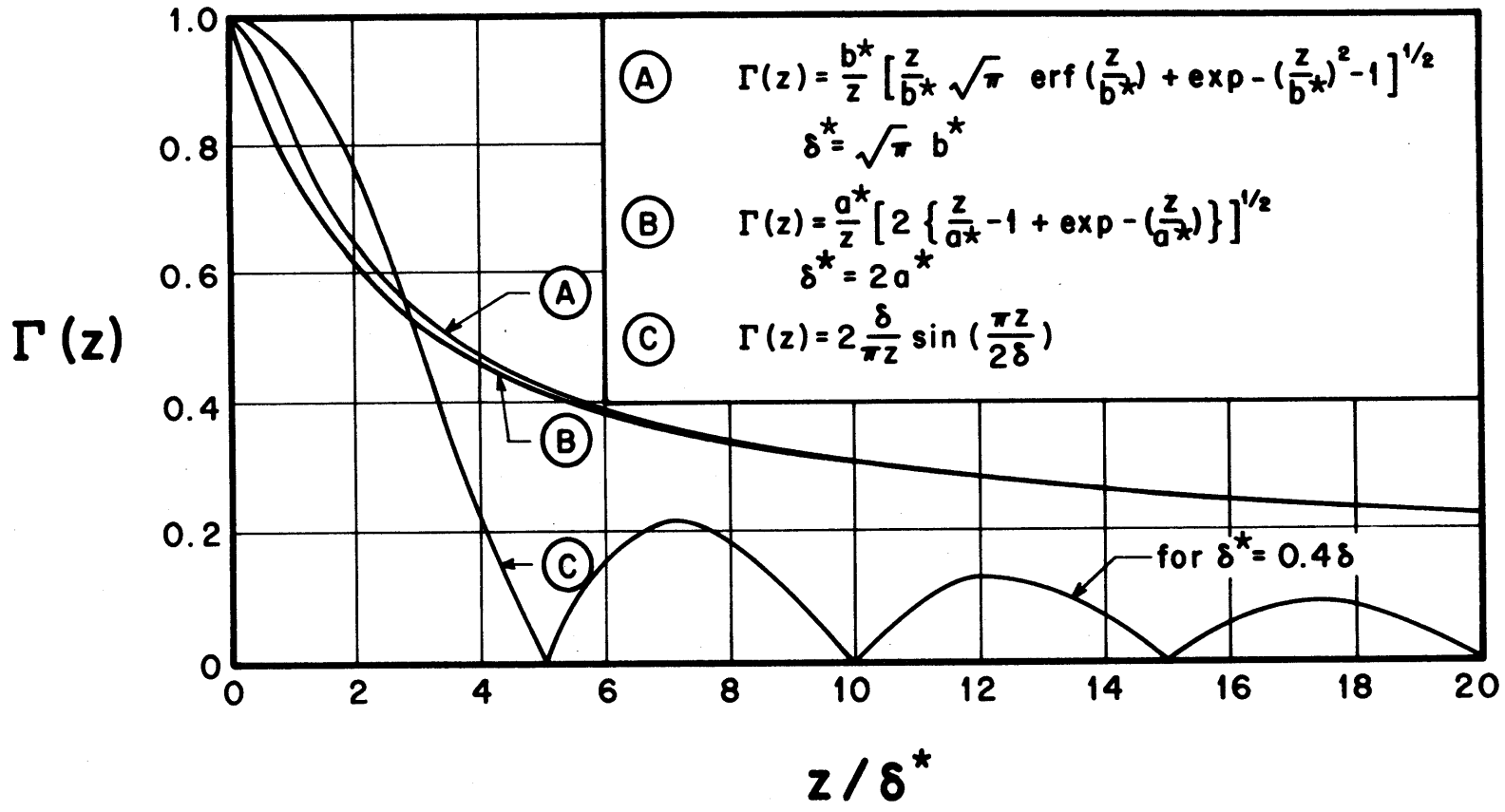


Figure 7.9 Reduction Factors Describing the Strength Variability

$$\Gamma(z) = \left(\frac{a^*}{z}\right) \cdot \left[2\left(\frac{z}{a^*}\right) - 1 + \exp\left(\frac{-z}{a^*}\right)\right]^{\frac{1}{2}} \qquad (7.47)$$

and

$$\Gamma(z) = \left(\frac{b^*}{z}\right) \cdot \left[\frac{z}{b^*}\sqrt{\pi}\ \mathrm{erf}\left(\frac{z}{b^*}\right) + \exp\left(\frac{-z}{b^*}\right)^2 - 1\right]^{\frac{1}{2}} \qquad (7.48)$$

where a* and b* are the decaying parameters and are related to the autocorrelation distance, δ^*, by (Vanmarcke, 1977a):

$$a^* = \frac{\delta^*}{2} \qquad (7.49),$$

and

$$b^* = \delta^*/\sqrt{\pi} \qquad (7.50),$$

respectively.

The third expression for Γ corresponds to the sinusoidal variation of the shear strength expressed by Eq. (7.1). It is given by (see Fig. 7.9):

$$\Gamma(z) = 2\ \delta/z\pi \cdot \sin(\pi z/2\delta) \qquad (7.51)$$

It should be emphasized, however, that the expressions considered in this analysis are not necessarily superior to other existing expressions. The most appropriate reduction factor for the soil at a specific site should be determined based on test data obtained for the soil deposit at this site.

7.5.3 Risk or Probability of Failure

A convenient way of assessing the reliability of embankments consists of using the reliability index, R_i, defined as:

$$R_i = \frac{\bar{F}_{2L} - 1}{\tilde{F}_{2L}} \tag{7.52}$$

R_i measures the difference between the mean value of the factor of safety and the critical value of one in terms of the standard deviation $\tilde{F}_{2L}$.

Given a certain cumulative distribution function, P(u), the probability of failure p_f can be obtained for each potential failure length, 2L (see Eqs. 7.37 and 7.38). The most likely length of failure is, therefore, the length that maximizes p_f (or minimizes the reliability index R_i). This concept was used by Vanmarcke (1977a), Veneziano et al. (1977) and others. Results of this method of analysis are very sensitive to $\bar{F}_{2L}$ (which is actually the deterministic value of the factor of safety) as well as $\tilde{F}_{2L}$ and P(u).

In order to incorporate the inevitable uncertainty in $\bar{F}_{2L}$ (estimated by the deterministic methods) due to the variety of errors mentioned previously, we redefine the reliability index R_i by the more general expression:

$$R_i = \frac{\bar{F}_{2L} - F_{2L}}{\tilde{F}_{2L}} \tag{7.53}$$

For a fixed probability of failure (fixed reliability index), we determine the critical length corresponding to the minimum value of F_{2L}. In the special case when F_{2L} equals unity, Eqs. (7.52) and (7.53) are identical and the two approaches yield the same results.

Figure 7.10 illustrates the difference between the two approaches based on Eqs. (7.52) and (7.53). The first approach (Eq. 7.52) evaluates the maximum probability of failure and the corresponding failure length for $F_{2L} = 1$ (vertical plane in Fig. 7.10). However, in order to use these results, a designer must estimate $\bar{F}_{2L}$, $\tilde{F}_{2L}$ and P(u) reliably. The second approach (Eq. 7.53) determines, for a given probability of failure (or reliability index), the minimum factor of safety and the corresponding critical failure length (horizontal plane in Fig. 7.10). Results of this approach can be compared to deterministic solutions presented earlier and, in spite of the difficulties of estimating $\bar{F}_{2L}$, $\tilde{F}_{2L}$ and P(u), can be easily used in practical designs.

Combining Eqs. (7.53) and (7.37), and noting that:

$$\text{erf}(-x) = -\text{erf}(x) \tag{7.54}$$

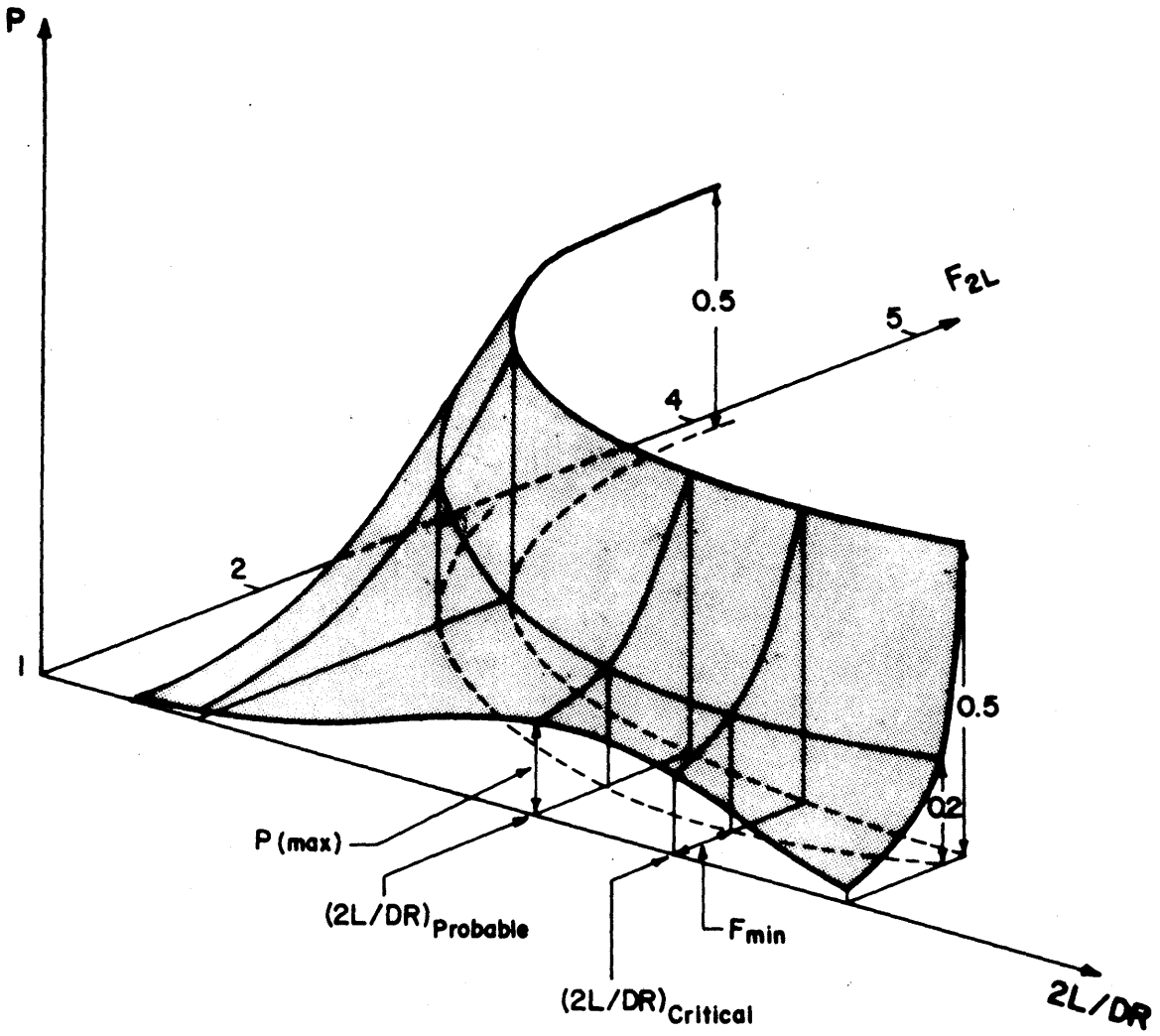
the relationship between the Gaussian cumulative distribution function and the reliability index for the factor of safety is given by:

$$P(F_{2L}) = \frac{1}{2}\left[1 - \text{erf}(R_i/\sqrt{2})\right] \tag{7.55}$$

The corresponding relationship for the case of sinusoidal distribution is given by:

$$P(F_{2L}) = \frac{1}{2} - \frac{1}{\pi}\sin^{-1}\left(\frac{R_i}{\sqrt{2}}\right) \tag{7.56}$$

Figure 7.11 shows a plot of Eqs. (7.55) and (7.56) where



P = Cumulative Probability

F_{2L} = Factor of Safety

2L/DR = Normalized Failure Length

Figure 7.10 Definitions Regarding the Reliability Analysis of Embankments

we note that the two distributions are likely to yield similar results when P is high, but widely different results when P is small. Since actual slopes are designed with significant margins of safety, corresponding to small failure probabilities, the selection of an adequate probability density function at such small failure probabilities is important for assessing the reliability of a slope. This is not only true for the two distributions considered herein, but for more "representative" distributions as well. This emphasizes the need for very well-controlled tests on a wide variety of soils before more reliable distributions can be used.

7.5.4 Results

Substituting Eqs. (7.45) and (7.46) into Eq. (7.53) and rearranging terms, one obtains:

$$F_{2L} = \left[1 - R_i \, \Gamma(2L) \, \frac{\tilde{c}}{\bar{c}}\right] \left[1 + \alpha \left(\frac{2L}{DR}\right)^{\gamma}\right] F^0 \qquad (7.57)$$

For the case of the sinusoidal shear strength variation, the reduction factor $\Gamma(2L)$ is given by Eq. (7.51). Combining Eqs. (7.51) and (7.57), the probabilistic model of the factor of safety is given by:

$$F_{2L} = \left[1 - R_i \cdot \frac{2\delta}{2\pi L} \cdot \frac{\tilde{c}}{\bar{c}} \cdot \sin\left(\frac{2\pi L}{2\delta}\right)\right] \left[1 + \alpha \left(\frac{2L}{DR}\right)^{\gamma}\right] F^0 \qquad (7.58)$$

This expression is identical to that of the approximate deterministic model given by Eq. (7.27) if one sets:

$$m = \bar{m}, \text{ where } \bar{m} = R_i \, \frac{\tilde{c}}{\bar{c}} \qquad (7.59)$$

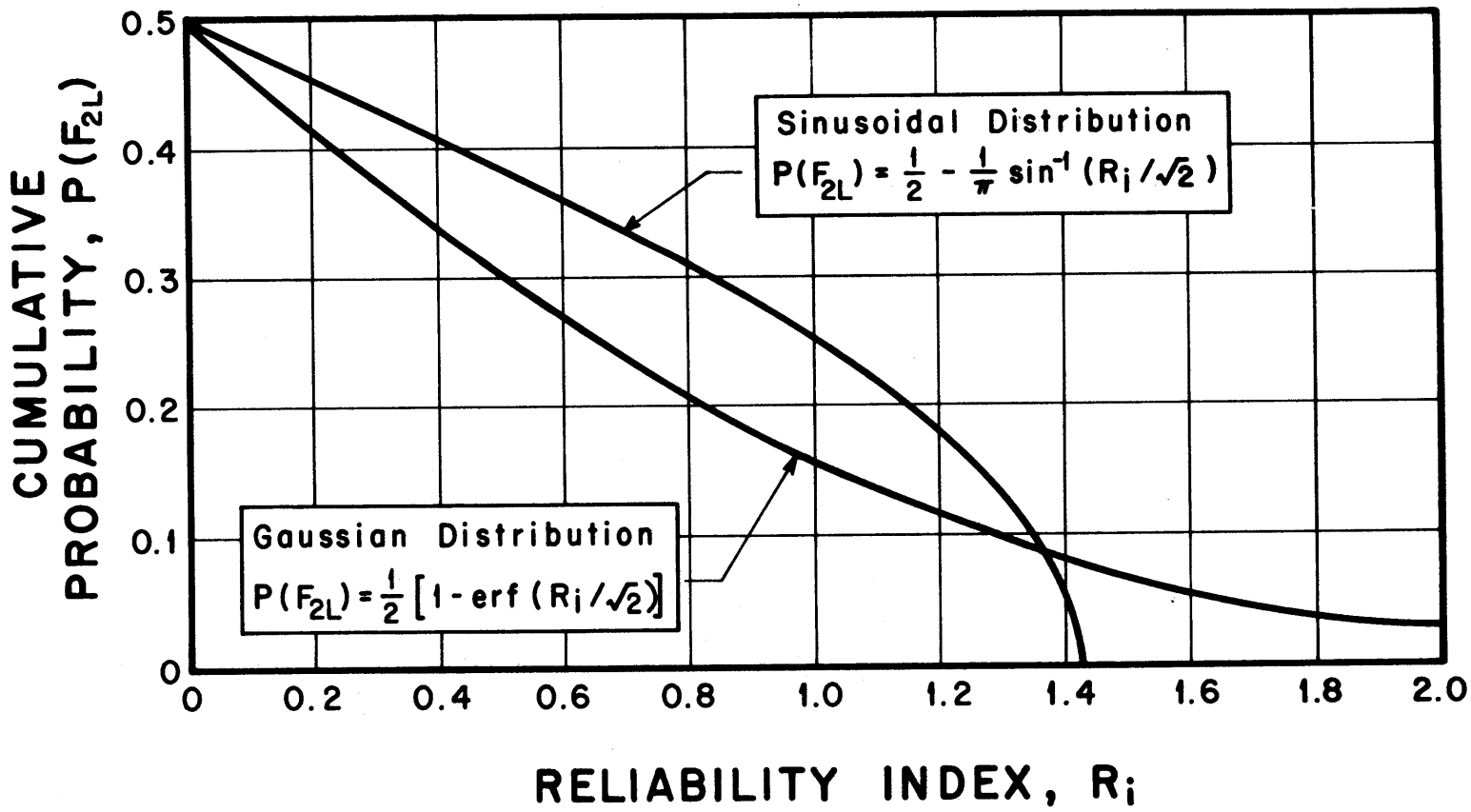


Figure 7.11 Relationship Between the Probability of Failure and the Reliability Index

Equation (7.59) shows that the wave amplitude factor m of the deterministic sinusoidal strength variation model (Fig. 7.1) is equivalent to the reliability index (corresponding to a certain probability of failure) multiplied by the coefficient of variation of the shear strength. Furthermore, Eqs. (7.27) and (7.58) show that, for the case of the sinusoidal strength variation, both the deterministic and probabilistic models give exactly the same results. However, in order to use Fig. 7.7 to predict the results of the probabilistic model, one must enter Fig. 7.7 with the value of $\bar{m}$ instead of m. From Eq. (7.59), $\bar{m}$ depends on the reliability index, R_i, and the coefficient of variation of the shear strength, $\frac{\tilde{c}}{\bar{c}}$. The value of R_i can be estimated from Fig. 7.11 after an acceptable probability of failure is selected and an adequate probability distribution for the shear strength of the slope material is identified. The equivalence between the probabilistic and deterministic approaches for the sinusoidal distribution relies on : (1) the manner in which the reliability index R_i was defined in the probabilistic approach; and (2) the choice of the approximate deterministic expression in Eq. (7.27). This is primarily emphasized herein in order to bridge a gap between deterministic and probabilistic approaches and help elucidate the use of probability in slope stability.

The minimum factor of safety can be obtained by differentiating Eq. (7.57) with respect to 2L. The results obtained for toe failures, assuming the shear strength to have a Gaussian probability distribution are shown in Figs. 7.12a and 7.12b using the reduction factors given by Eqs. (7.47) and (7.48),

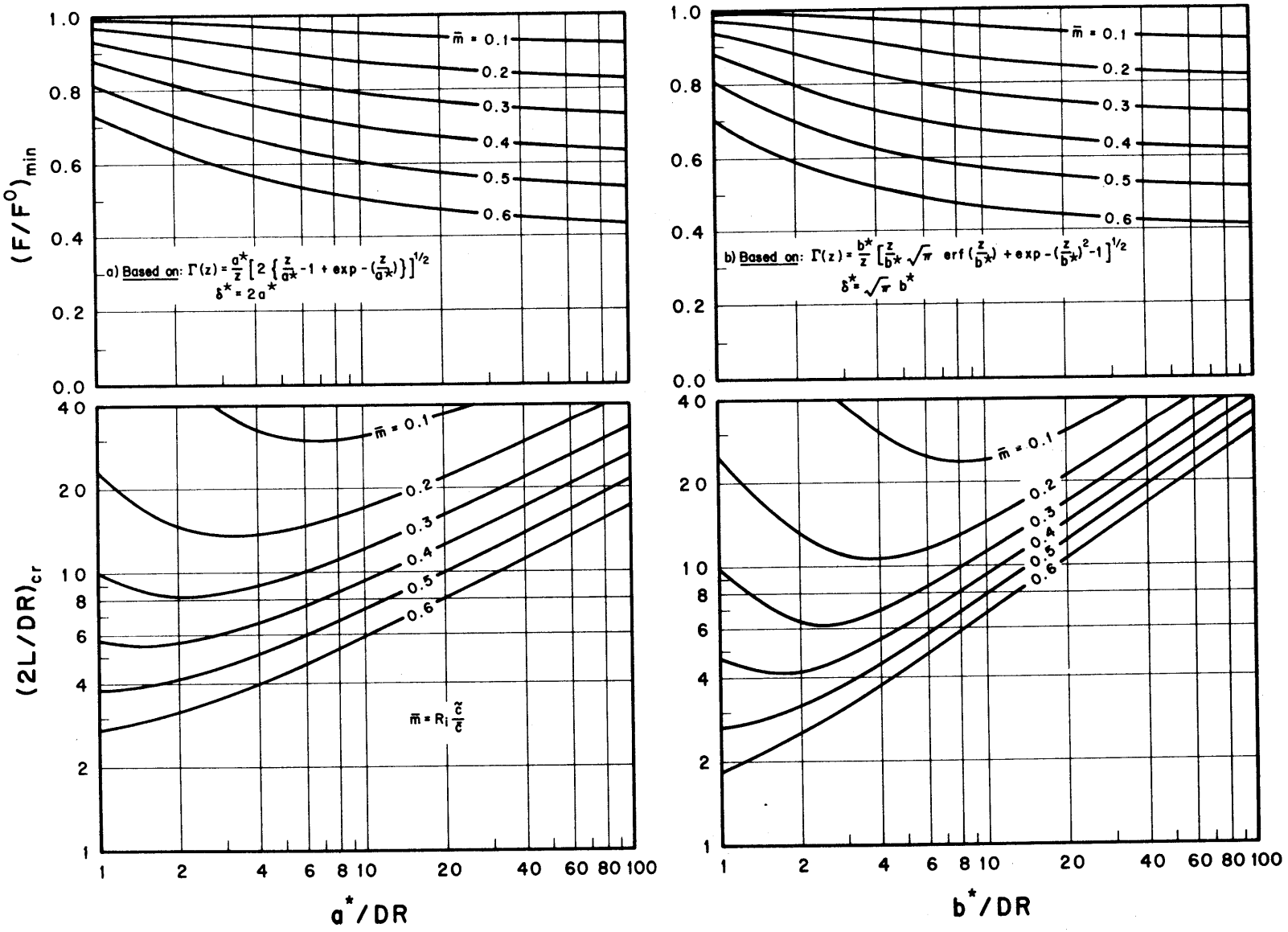


Figure 7.12 Results of the Probabilistic Analysis of Toe Failures of Slopes with Homogeneous Cross Sections

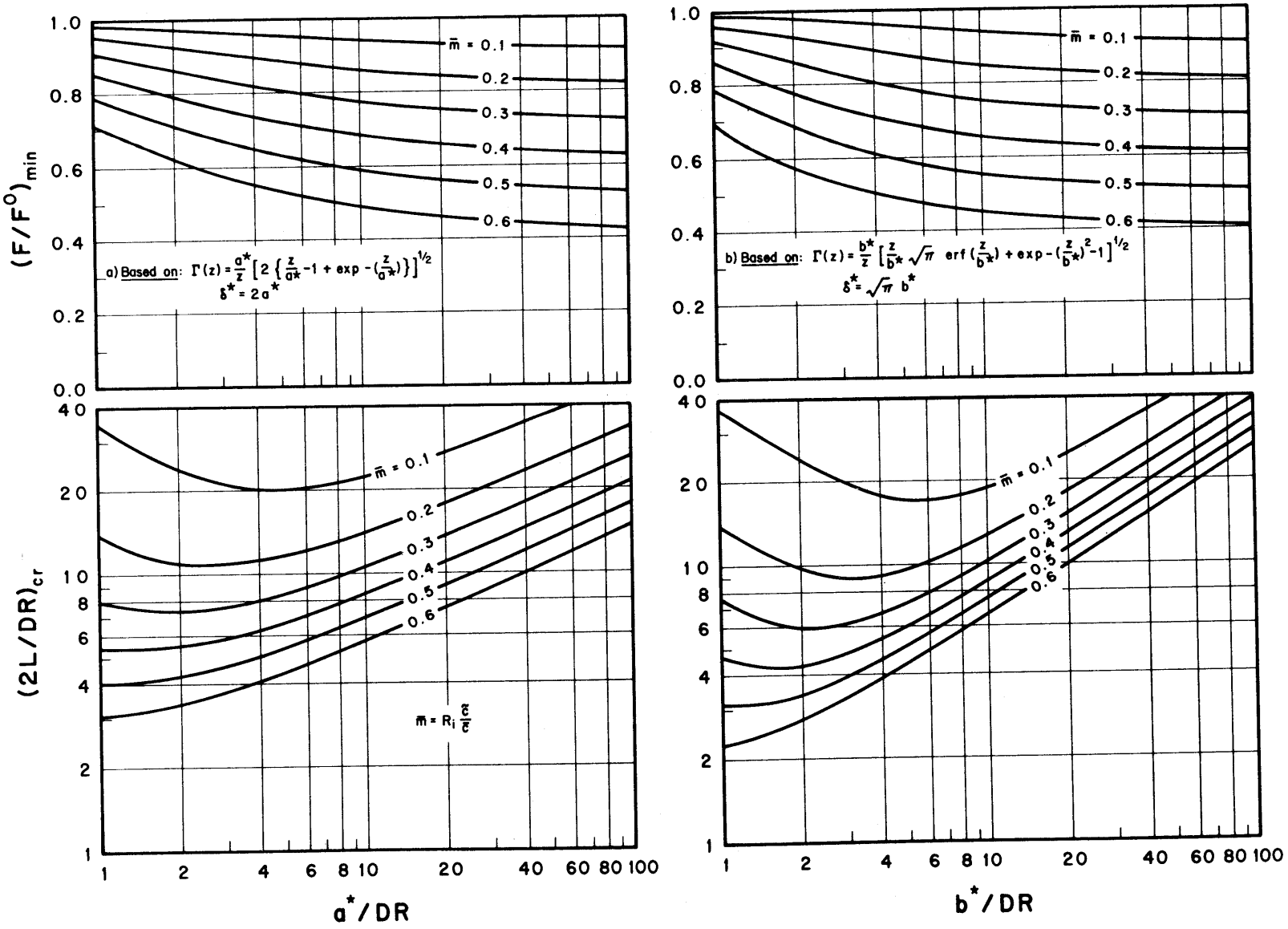


Figure 7.13 Results of the Probabilistic Analysis of Base Failues of Slopes with Homogeneous Cross Sections

respectively. The corresponding results for the case of base failures are given in Fig. 7.13a and 7.13b. From these results we note that:

1. Using Eq. (7.59), the probabilistic results in Figs. 7.12 and 7.13, and the deterministic results in Fig. 7.7 show similar trends: - a decrease in $(F/F^0)_{min}$ with the increase of $\bar{m}$ $(=R_i\frac{\tilde{c}}{\bar{c}})$ or the increase of δ^*/DR.

2. The two parameters, δ^*/DR, and $\bar{m}$ determine the mode of failure. For example, Fig. 7.12a shows that for $\bar{m}$=0.3 and δ^*/DR=100, $(F/F^0)_{min}$ and $(2L/DR)_{cr}$ are given by 0.74 and 34, respectively, i.e., a failure with finite length is likely to take place. By decreasing δ^*/DR (or a^*/DR), $(F/F^0)_{min}$ increases, and $(2L/DR)_{cr}$ decreases until $a^*/DR \simeq 2.5$. A further decrease in a^*/DR beyond 2.5 will increase the critical failure length resulting in plane strain failures with infinite (or very long) failure lengths. This result (the dependence of the mode of failure on δ^*/DR and $\bar{m}$) is similar to that obtained for the deterministic analysis (using the equivalent parameters λ and m). However, in the case of the probabilistic analysis, the transition from finite to plane strain failures is not as abrupt as in the case of deterministic analysis (compare Fig. 7.7 with Figs. 7.12 and 7.13).

3. For fixed values of δ^*/DR and $\bar{m}$, the effect of the spatial variability of the shear strength on the minimum factor of safety is not significant. This can be illustrated by comparing the results in Figs. 7.12a and 7.12b developed based on two different expressions for the reduction factor, $\Gamma(2L)$.

7.6 SUMMARY AND CONCLUSIONS

This chapter investigates the undrained stability (ϕ=0 and $c=s_u$) of slopes with a variable shear strength along their axis. The first part of the chapter uses a deterministic approach while the second part is based on probabilistic approaches.

In the deterministic approach, two models for strength variation are considered (Fig. 7.1): a sinusoidal model (Eq. 7.1); and a saw-tooth model (Eq. 7.2). Both models are described by the two parameters δ and m representing half the wave length and its amplitude, respectively. Three-dimensional stability analyses were performed by means of the program STAB3D using the two strength variability models in conjunction with the shear surfaces described in Chapter 2. The results presented in Figs. 7.2 through 7.4 show that:

1. The two parameters m and δ, which describe the strength variation along the slope axis, determine the mode of failure. This is illustrated by the curves in Fig. 7.4 corresponding to a normalized half wave length, λ, of 10 and 2, and a wave amplitude factor, m=0.25. For the short wave length (λ=2), the curve of F/F^0 vs. 2L/DR oscillates above unity. The minima for this curve decrease in amplitude as 2L/DR increases and reach an absolute minimum equal to unity when 2L goes to infinity. This indicates that, for this case, a plane strain failure is more critical.

On the other hand, for the longer wave length, λ=10, F/F^0

reaches a minimum which is less than unity and, therefore, corresponds to a finite failure length. In this case, three-dimensional effects reduce the plane strain factor of safety and, if neglected, can lead to unsafe designs.

2. For the same values of m and λ, the sinusoidal and saw-tooth models give practically identical results. This is illustrated by Fig. 7.3 obtained for the case of a vertical cut where the z-axis is taken at the crest of the cut and the cylinder passes through the toe (See Fig. 3.1). Although other slope geometries were not considered, we believe that, for given values of m and λ, the two models will also give similar results.

3. For finite failure lengths, the factor of safety decreases when either m or λ increases.

4. For slopes with homogeneous cross sections (as considered herein), finite failure lengths are shorter than half the wave length, δ, of the strength variation.

5. For a given ratio of 2L/DR, the slope angle β has little influence on the values of F/F^0, $(F/F^0)_{min}$ and $(2L/DR)_{cr}$ (See Fig. 7.4).

6. Ellipsoidal shear surfaces gave consistently lower values of $(F/F^0)_{min}$ than conical shear surfaces and, therefore, they are more likely to represent actual failure conditions.

7. In the case of a vertical cut, Fig. 7.2 shows excellent agreement between results obtained by the program STAB3D and the closed-form solutions derived using the sinusoidal strength model.

An approximate expression for the three-dimensional factor of safety, F, is given by Eq. (7.27) in terms of the plane strain factor of safety, F^0, and the parameters m and λ describing the sinusoidal model. Fig. 7.6 shows that Eq. (7.27) gives reasonably accurate results when compared to solutions obtained by the program STAB3D. Using Eq. (7.27), design charts (Fig. 7.7) were then developed for the undrained stability analysis of slopes having homogeneous cross sections and a non-uniform shear strength along their axis. A design methodology taking into account the three-dimensional nature of failure and the variability of the shear strength along the slope axis is then presented.

The second part of this chapter presents a three-dimensional probabilistic approach to estimate the reliability of embankments. The soil model considered is statistically homogeneous and the inherent variability of the shear strength constitutes the major uncertainty in the factor of safety. Analyses were carried out assuming two types of probability distributions (the Gaussian and sinusoidal distributions) and three models for the spatial variability of the shear strength. In an actual design problem, the probability distribution and the spatial variability of the undrained shear strength at the site should be determined from a sufficiently large number of tests. The results of the probabilistic analysis show that:

1. For the case of the sinusoidal strength variation, both the deterministic and probabilistic models give exactly the same results. The wave amplitude factor, m, of the deterministic model is equivalent to $\bar{m}$ in the probabilistic approach. The parameter $\bar{m}$ is the product of the reliability index, R_i (corresponding to a certain probability of failure) and the coefficient of variation of the shear strength, $\frac{\tilde{c}}{\bar{c}}$.

2. The failure length of a slope depends on the autocorrelation distance, δ^*, describing the spatial variability of the shear strength, and $\bar{m}$ $(=R_i\frac{\tilde{c}}{\bar{c}})$. This is similar to the case of the deterministic analysis where the failure mode is affected by δ and m.

3. For fixed values of $\bar{m}$ and δ^*, the effect of different shear strength spatial variability models on the minimum factor of safety is not significant.

CHAPTER 8

CASE STUDIES

This chapter presents four case histories of embankments on saturated clay foundations which were rapidly loaded to failure. A brief description of these cases is given below.

Name	Soil Deposit	Nature of Case Study
I-95 Embankment, Massachusetts	lean, medium to stiff clay of medium sensitivity	granular embankment purposely loaded to failure on partially consolidated Boston Blue Clay
Experimental Test Section, New Hampshire	lean, medium to soft very sensitive clay	granular embankment purposely loaded to failure by designer
New Liskeard Embankment, New Liskeard, Canada	medium to soft varved clay	granular embankment failed during construction
Fore River Test Section, Maine	tidal mudflat deposit of soft, slightly organic clay	granular test embankment failed during construction

In each case, the site is briefly described with emphasis on the selection of soil parameters. Results of two- and three-dimensional total stress ($\phi = 0$, $c = s_u$) stability analyses are then obtained on the basis of two types of shear strength s_u models: 1) the (uncorrected) field vane strength

s_u (FV), and 2) the Stress History and Normalized Soil Engineering Properties Strength (Ladd and Foott, 1974), wherein anisotropy is considered by extending the elliptical model proposed by Davis and Christian to three dimensions (Chapter 5), SHANSEP-$S_u(\theta)$.

In each of the four case studies, the computed three-dimensional factor of safety, F, (which accounts for end effects, strength anisotropy, and strain compatibility) is compared to the actual value of F = 1 at failure. Conclusions regarding adequate estimates of the shear strength of clays for stability computations are then derived.

8.1 I-95 EMBANKMENT, SAUGUS, MASSACHUSETTS

8.1.1 Description of the Site

In 1965, work began on a 3-mile extension of Interstate Highway I-95, north of Boston (Fig. 8.1). The extension required construction of a high embankment on a layer of peat and sand underlain by a thick deposit of a medium to stiff clay commonly known as Boston Blue Clay, BBC. In August 1967, the top 10-foot layer of peat was removed and replaced by sand and gravel. When filling was completed, by July 1969, the embankment crest elevation ranged from +25 to +40 ft. along the 3-mile extension.

In order to resolve the uncertainties involved in choosing the undrained shear strength of BBC for stability analyses, a test fill was rapidly built to failure in 1974 on a 300-foot long section of the embankment at Station 263 (Fig. 8.1).* Considerable lateral movements at Sta 263 had previously required the construction of a stabilizing berm on the west side as shown in Fig. 8.2. To cause the failure, fill was first dumped until the east slope was about 40°. The fill was then placed uniformly over the entire test section in 1-foot lifts at an average of 1 to 2 ft. per day. The geometry for the placement of the additional fill (Fig. 8.2) was

---

* Performed as part of an MIT research contract sponsored by the Massachusetts Department of Public Works, MDPW, entitled "Movement and Stability of Cuts and Fills."

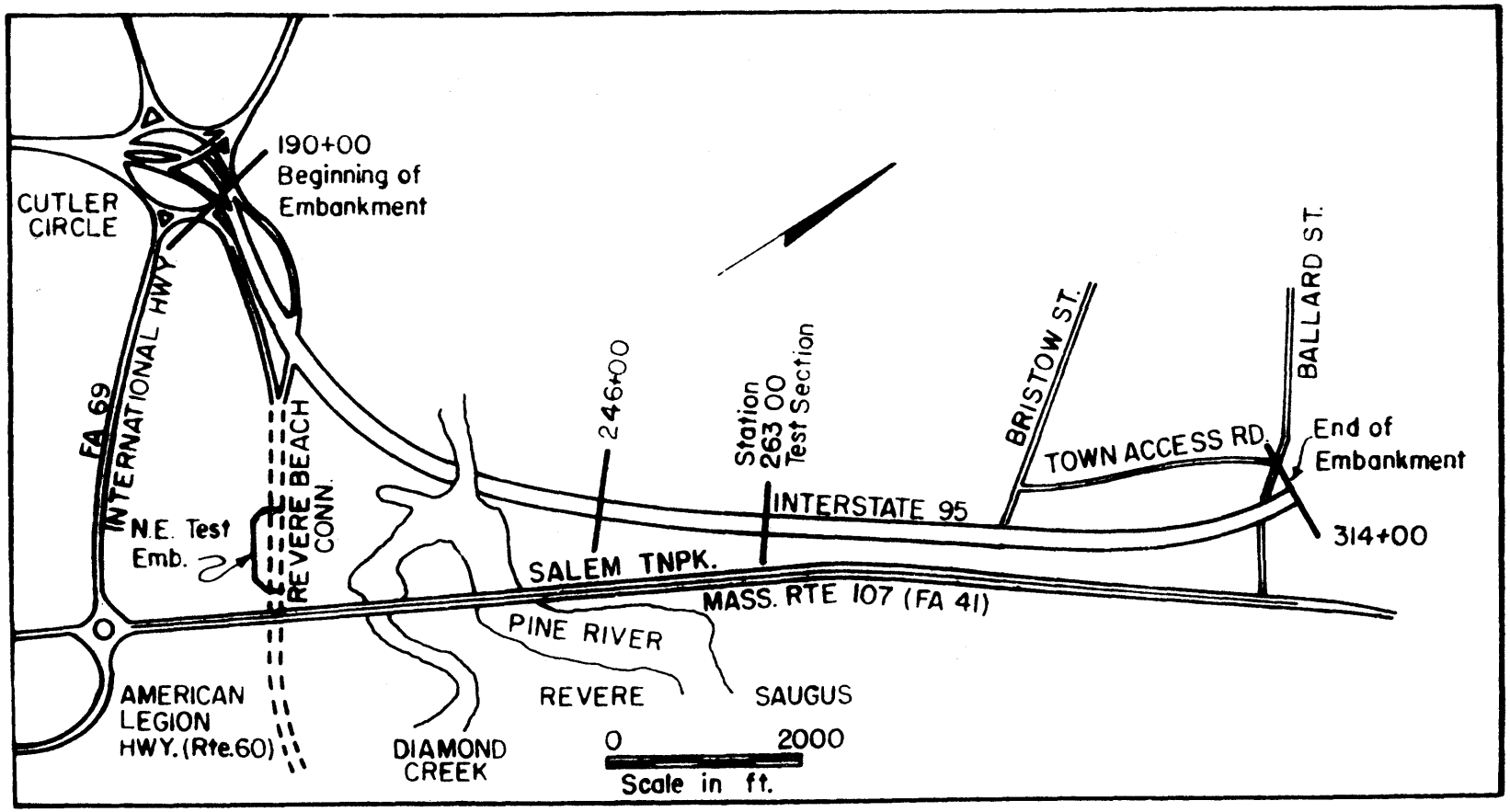


Figure 8.1 Location Map, I-95 (From Silva, 1975)

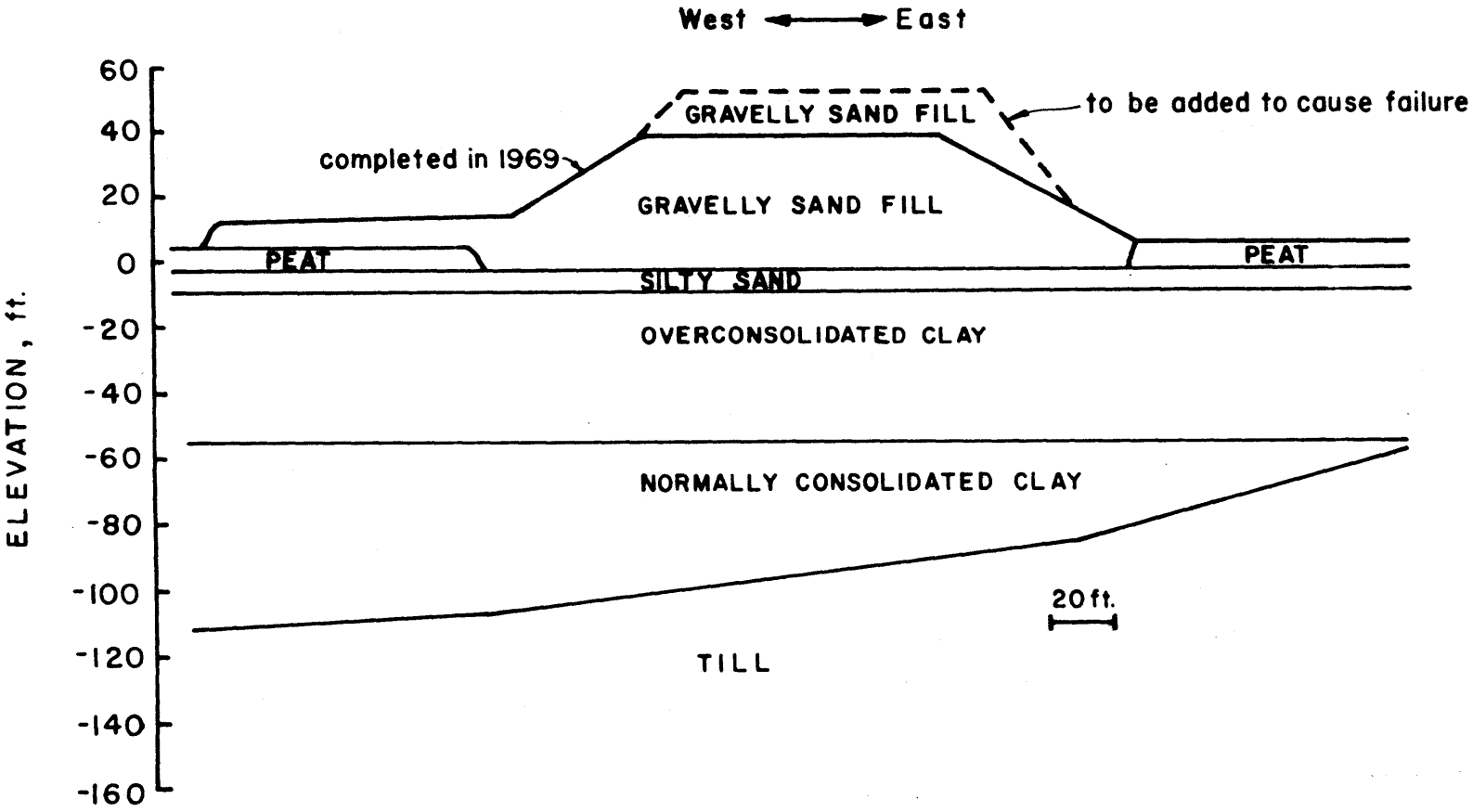


Figure 8.2 Cross Section of the I-95 Embankment at Station 263

designed to cause failure of the east side.

8.1.2 Failure

The failure of the test section occurred when the fill elevation was at 56.5 ft. Both sides of the embankment failed simultaneously, causing the crest to drop about 30 ft. and the sides to heave as much as 14 ft. The failure extended over a distance of 280 ft. on one side of the 300-ft. test section and 450 ft. on the other. The total failure length was, therefore, along 1030 ft., while the loaded length was only 300 ft. More detailed information is given in a special M.I.T. report (1975).

8.1.3 Soil Properties

Embankment Fill - The fill for the embankment consisted of well graded sand which was end dumped up to El +5 and compacted with rubber tired rollers thereafter. For the end-dumped fill, we estimated the unit weight, γ_t = 110 pcf and the friction angle, $\overline{\phi}$ = 30°. For the compacted fill we assumed γ_t = 122 pcf and $\overline{\phi}$ = 40°, respectively. As for the additional fill, γ_t was taken = 122 pcf and $\overline{\phi}$ = 37°.

Foundation Sand - The natural sand overlying the clay is a well graded silty sand with some gravel. An average value of γ_t = 113 pcf and a $\overline{\phi}$ = 35° were assumed for this sand.

Peat - No tests were performed on the peat layer. Based on Ladd (1975b), we estimated the γ_t = 75 pcf and the undrained shear strength, s_u = 300 psf.

Till - The till layer underlying the BBC is very dense, with blow counts, N, in excess of 50. Stability analyses conducted by Silva (1975) showed that all the critical shear surfaces obtained from a variety of methods of analysis were located above this stratum. Hence, no attempts were made to determine the properties of the till or to include it in the analyses.

Boston Blue Clay - The Boston Blue Clay is a sensitive, marine illitic clay with a natural water content, w_n, of 40 $\pm$ 5% and plasticity index, P.I., of 20 $\pm$ 5%.

Figure 8.3 shows Geonor field vane, FV, tests conducted at the site (Sta 263) in June 1973, i.e., 14 months prior to failure. However, Silva (1975) presents field vane measurements at Sta 244, taken in 1967, 1969 and 1972, which indicate very little gain in field vane strength with time. We, therefore, considered the FV strength profile given by the two solid lines in Fig. 8.3 to be adequate for the stability analyses of the 1974 failure.

A critical step in the use of the SHANSEP method is an accurate estimation of the existing vertical effective consolidation stress, $\bar{\sigma}_{vc}$, the maximum past pressure, $\bar{\sigma}_{vm}$, and hence the overconsolidation ratio, OCR, $(= \bar{\sigma}_{vm}/\bar{\sigma}_{vc})$.

Beyond 90 ft. east and 55 ft. west, the clay foundation is virtually unaffected by the embankment and the prefailure vertical stress in the ground is given in Fig. 8.4 by the line labelled "$\bar{\sigma}_{vo}$". In the central portion under the embankment,

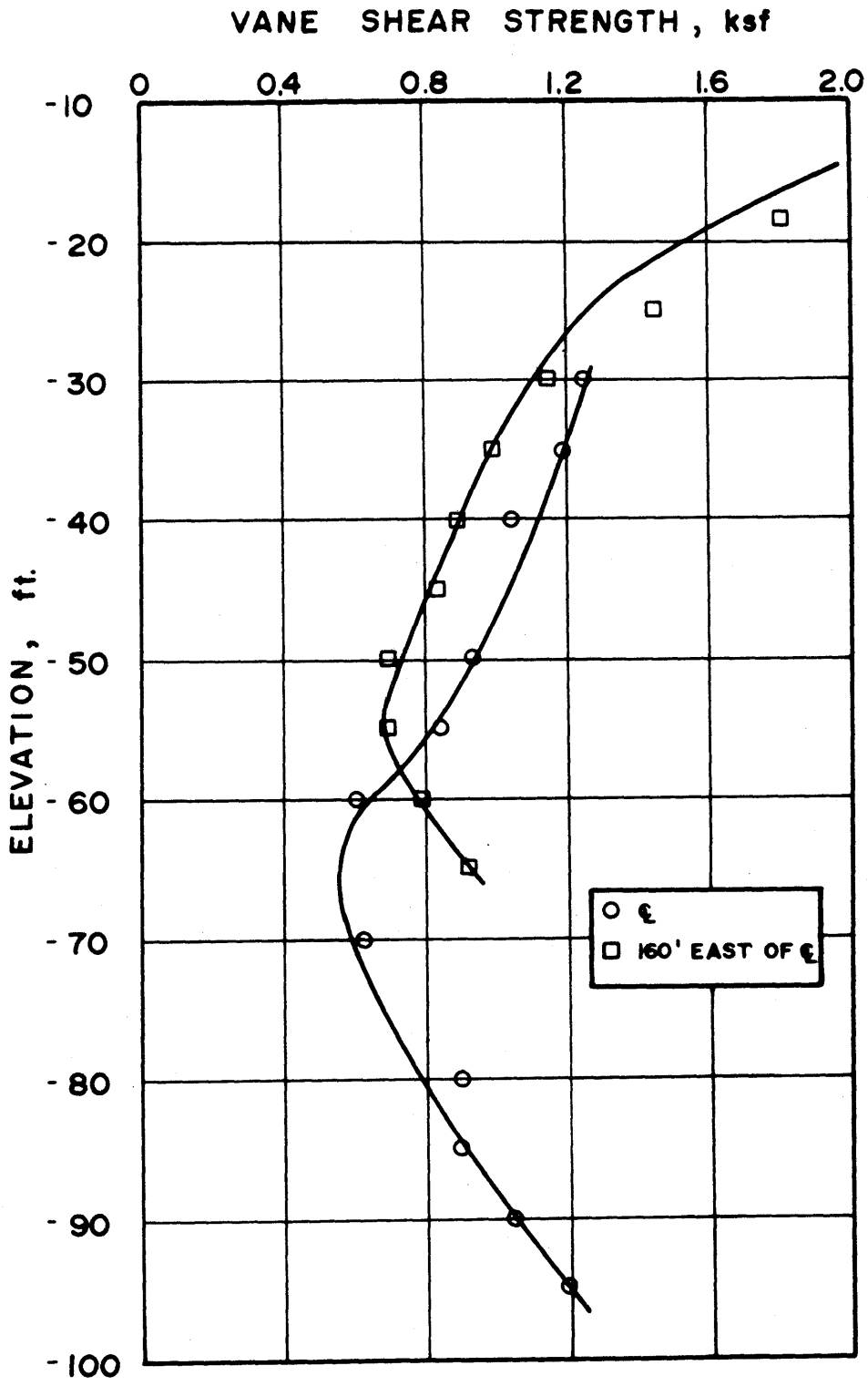


Figure 8.3 Field Vane Strength, I-95 Station 263

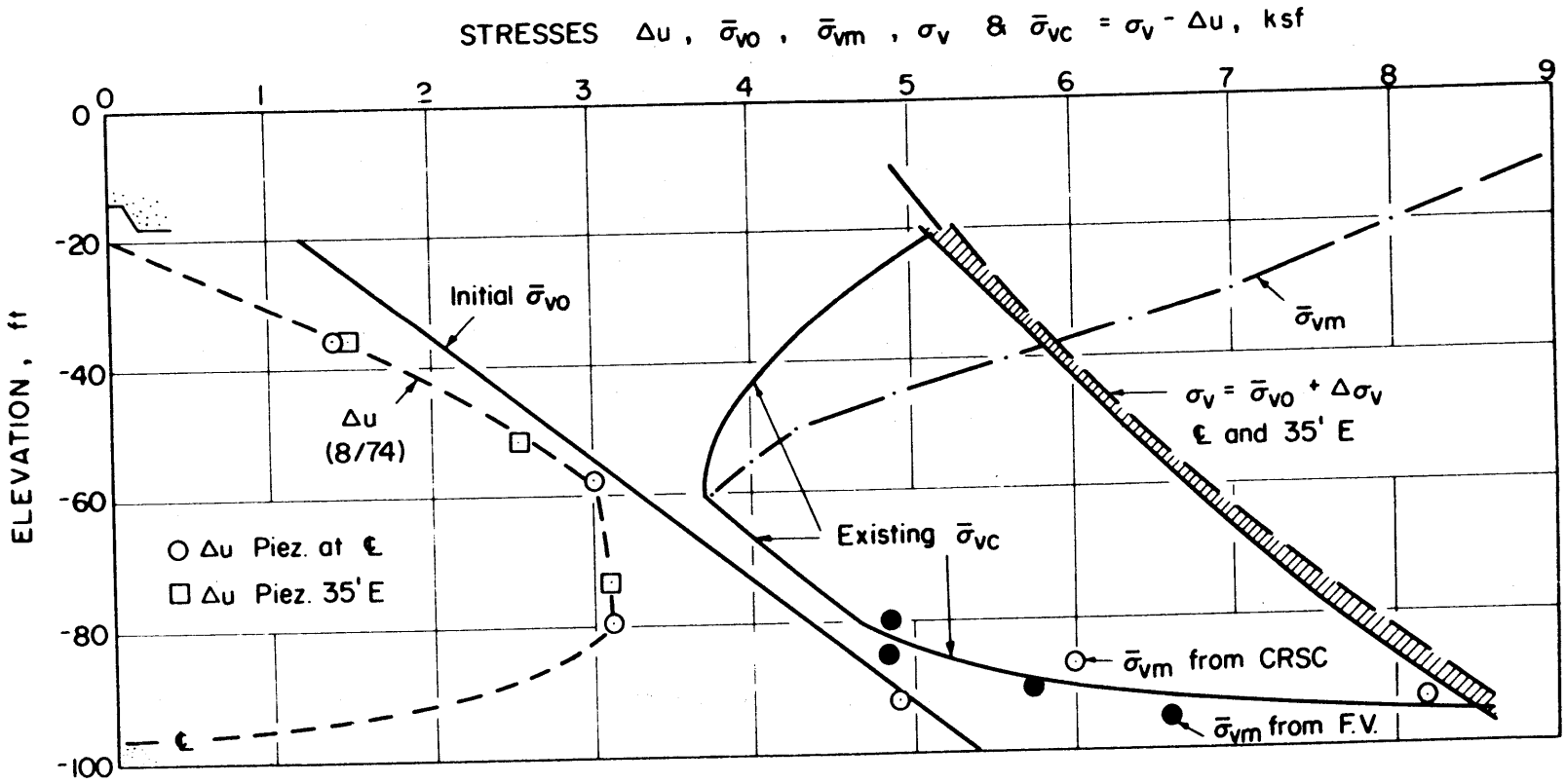


Figure 8.4 Evaluation of Existing Stresses August 1974, I-95 Station 263 Centerline to 35' East (from Ladd, 1975b)

a new stress history based on pore pressure measurements and finite element analyses of total stress increments caused by the fill was established by Ladd (1975b), and is shown in Fig. 8.4 by the line labelled "existing $\bar{\sigma}_{vc}$", i.e., the pre-failure value.

The maximum past pressures, $\bar{\sigma}_{vm}$, were determined from oedometer tests and from constant rate of strain consolidation, CRSC, tests (Wissa et al., 1971). Values of $\bar{\sigma}_{vm}$ were also estimated indirectly from the results of FV tests (Ladd, 1975b) in the following manner: At a given depth, the measured FV strength is divided by the existing vertical effective stress, $\bar{\sigma}_{vo}$ or $\bar{\sigma}_{vc}$, and from the relationship between $s_u(FV)/\bar{\sigma}_{vo}$ vs. OCR established from the extensive data available at Sta 246 , the value of OCR is determined. The maximum past pressure, $\bar{\sigma}_{vm}$, is then obtained by multiplying this OCR value by the existing vertical effective stress. The profiles of $\bar{\sigma}_{vm}$ developed from consolidation and FV data are given in Fig. 8.5.

The input parameters for the analysis based on the SHANSEP-$S_u(\theta)$ strength model rely on results of K_o consolidated-undrained tests sheared under various stress systems: plane strain compression ($\overline{CK_oU}$ PSC), plane strain extension ($\overline{CK_oU}$ PSE) and direct simple shear ($\overline{CK_oU}$ DSS). The data were obtained from Ladd et al. (1971), and Ladd and Edgers (1972). Table 8.1 gives the normalized strength ratios, $s_u/\bar{\sigma}_{vc}$, at different values of OCR for the various stress systems consid-

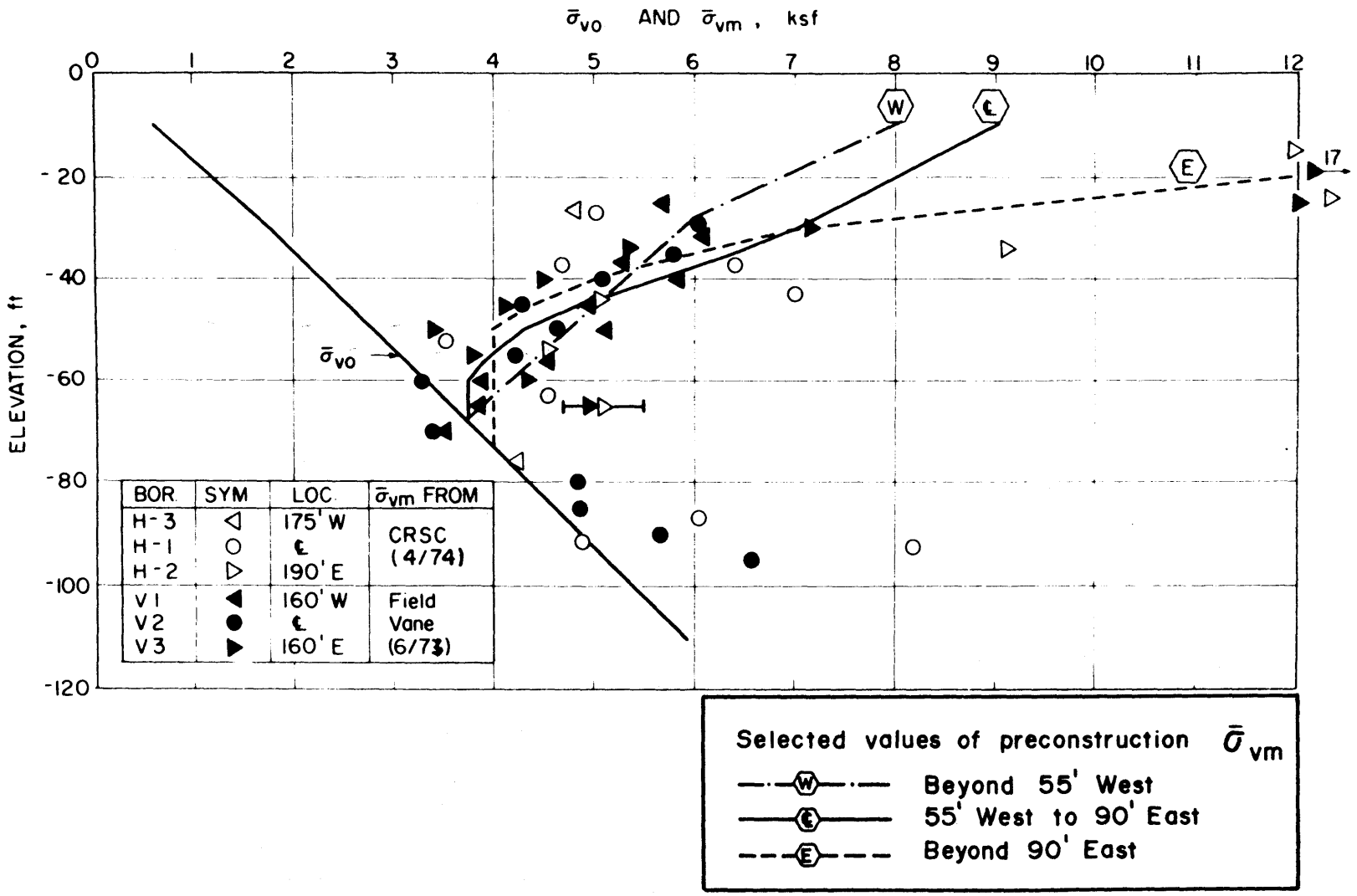


Figure 8.5 Initial Stress History, I-95 Station 263 (From Ladd, 1975b)

Table 8.1 Undrained Strength Ratio vs OCR for Boston Blue Clay[1]

OCR	$\overline{CK_oUPSC}$			$\overline{CK_oUDSS}$		$\overline{CK_oUPSE}$		
	$q_f/\overline{\sigma}_{vc}$	$\overline{\phi}°$	$\tau_{ff}/\overline{\sigma}_{vc}$	$\tau_h/\overline{\sigma}_{vc}$ [2]	$\overline{\phi}°$	$q_f/\overline{\sigma}_{vc}$	$\overline{\phi}°$	$\tau_{ff}/\overline{\sigma}_{vc}$
1	0.34	29	0.30	0.20	30	0.19	37.5	0.15
2	0.57	33	0.48	0.37	33	0.37	37.5	0.29
4	0.95	33	0.80	0.61	33	0.67	37.5	0.53
6	1.25	33	1.05	0.80	33	0.92	37.5	0.73
8	1.50	33	1.26	0.97	33	1.14	37.5	0.90
12	1.90	33	1.59	1.24	33	1.51	37.5	1.20
16	2.19	33	1.84	1.44	33	1.82	37.5	1.44

(1) Data from Ladd et al (1971); and Ladd and Edgers (1972)

(2) $\tau_{ff} \simeq \tau_h$

ered. Beyond OCR of 4, extrapolations were based on a linear relationship between $[(s_u \text{ at } \bar{\sigma}_{vc})/(s_u \text{ at } \bar{\sigma}_{vm})]$ vs. log OCR (Ladd, 1971).

In order to use the shear strength data given in Table 8.1 for stability analyses, two types of corrections are required:

1) The shear strength on the failure plane at failure, τ_{ff}, is of primary interest in stability analyses rather than the maximum shear stress q_f. τ_{ff} is related to q_f by:

$$\tau_{ff} = q_f \cdot \cos \bar{\phi} \qquad .. \qquad .. \qquad (8.1)$$

The values of $\bar{\phi}$ and $\tau_{ff}/\bar{\sigma}_{vc}$ are given in Table 8.1.

2) Strain compatibility. The stress system in a circular arc stability analysis varies considerably along the arc (Chapter 5). For BBC, Figs. 8.6 and 8.7 show a large difference in the shear strain at failure for the different failure modes. Ladd (1975a) presents a simplified methodology to account for strain compatibility by averaging the values of $q/\bar{\sigma}_{vc}$ and $\tau_h/\bar{\sigma}_{vc}$ at the same shear strains for the three stress systems (PSC, PSE AND DSS). Applying this averaging procedure to the BBC (Table 8.2) shows that the maximum mobilized resistance for the normally consolidated BBC, which occurs at a shear strain of 6%, is 7% less than the average of the peak strengths. At this shear strain, the ratios of q/q_f for the compression and extension modes of failure are about 0.88 and 0.94, respectively. At OCR = 4, the maximum mobil-

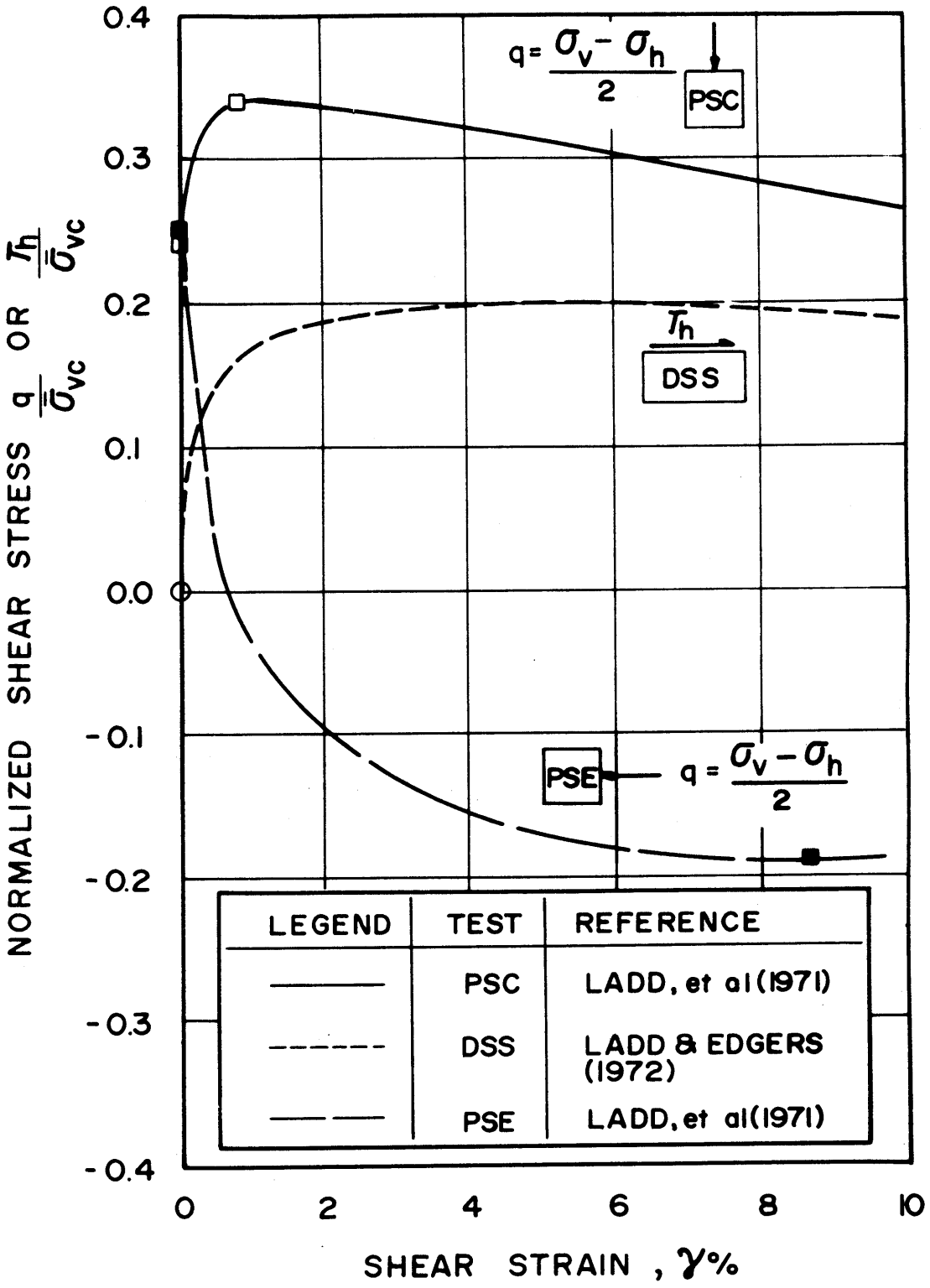


Figure 8.6 Stress-Strain Curves from $\overline{CK_oU}$ Tests on Normally Consolidated Boston Blue Clay

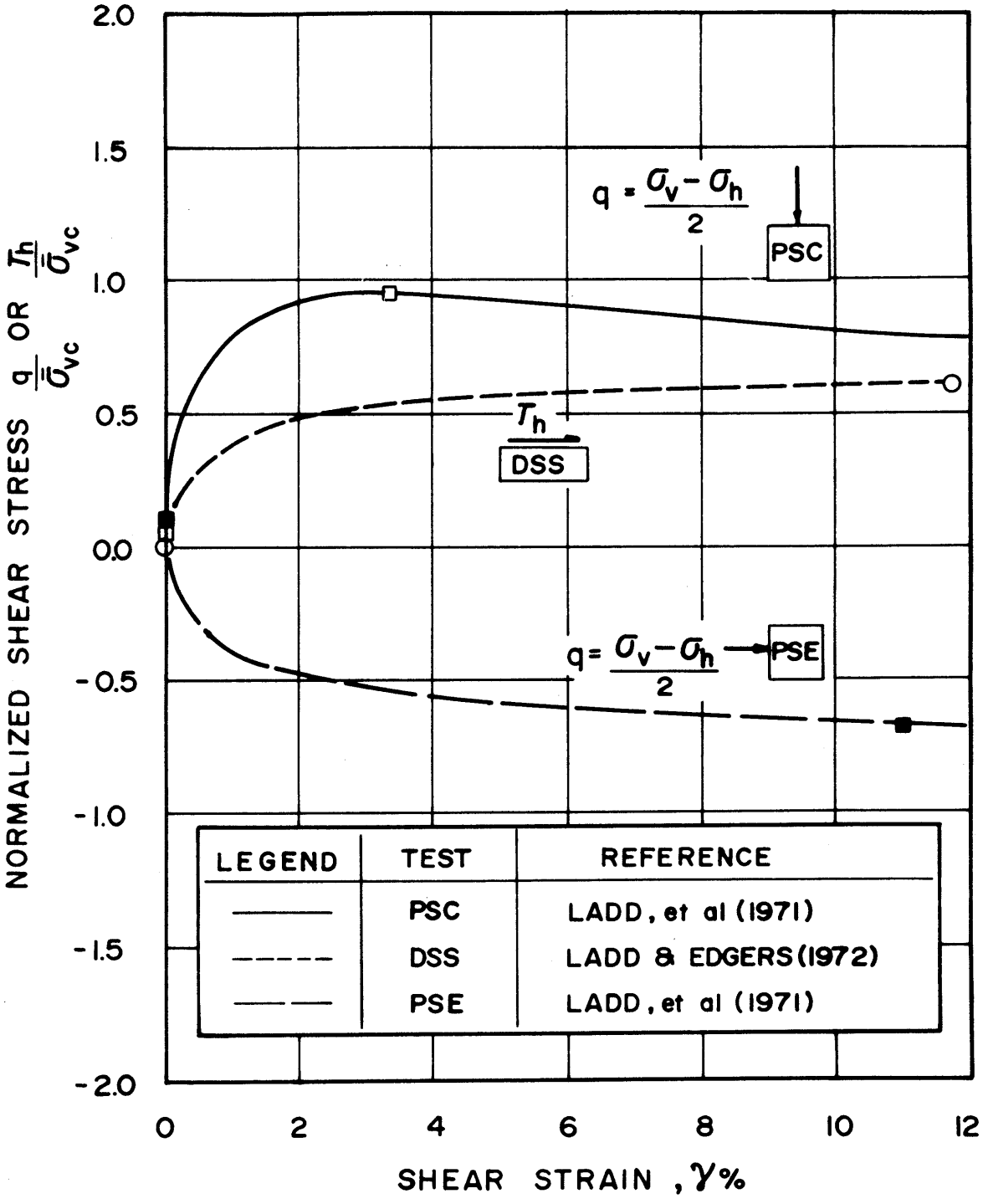


Figure 8.7 Stress-Strain Curves from $\overline{CK_oU}$ Tests on Boston Blue Clay at OCR = 4

Table 8.2 Strain Compatibility Effects for Boston Blue Clay

O C R = 1		
Average Normalized Peak Strength = 1/3(0.34 + 0.20 + 0.19) = 0.243		
Shear Strain, γ (%)	Average Mobilized Strength Ratio	Fraction of Average Peak Strength (%)
2	1/3(0.335 + 0.186 + 0.100) = 0.21	85
4	1/3(0.320 + 0.199 + 0.151) = 0.22	92
6	1/3(0.300 + 0.198 + 0.180) = 0.23	93
8	1/3(0.283 + 0.195 + 0.188) = 0.22	91
10	1/3(0.266 + 0.192 + 0.191) = 0.22	89
Reduction in $s_u(PSC)/\bar{\sigma}_{vc} = 1 - \frac{0.30}{0.34} = 12\%$		
Reduction in $s_u(PSE)/\bar{\sigma}_{vc} = 1 - \frac{0.18}{0.19} = 6\%$		
O C R = 4		
Average Normalized Peak Strength = 1/3(0.95 + 0.67 + 0.61) = 0.74		
Shear Strain, γ (%)	Average Mobilized Strength Ratio	Fraction of Average Peak Strength (%)
2	1/3(0.905 + 0.475 + 0.475) = 0.62	83
4	1/3(0.950 + 0.550 + 0.550) = 0.68	92
6	1/3(0.900 + 0.575 + 0.590) = 0.69	92.6
8	1/3(0.860 + 0.590 + 0.625) = 0.69	93
10	1/3(0.825 + 0.610 + 0.640) = 0.69	93
12	1/3(0.750 + 0.600 + 0.675) = 0.68	91
Reduction in $s_u(PSC)/\bar{\sigma}_{vc} = 1 - \frac{0.86}{0.95} = 9\%$		
Reduction in $s_u(PSE)/\bar{\sigma}_{vc} = 1 - \frac{0.625}{0.670} = 5\%$		

ized resistance occurs at a shear strain of 8%. The corresponding q/q_f ratios are 0.91 and 0.95, respectively.

Based on the above, strain compatibility effects were taken into consideration by reducing $s_u(PSC)/\bar{\sigma}_{vc}$ by 12% at OCR = 1, 9% ot OCR = 4, and 0% for OCR $\geq$ 10. Furthermore, $s_u(PSE)/\bar{\sigma}_{vc}$ were reduced by 6% at OCR = 1, 5% at OCR = 4, and 0% for OCR $\geq$ 10. Reduction factors at intermediate values of OCR were estimated by linear interpolation between OCR = 1, 4 and 10. No reduction factor was applied to the $s_u(DSS)/\bar{\sigma}_{vc}$ ratios. A summary of the strength ratios for the foundation clay is given in Table 8.3.

The variation of the undrained shear strength with the inclination of the failure surface at a given point in the soil deposit can be estimated by means of the ellipsoidal relationship described in Chapter 5. The parameters describing this model, as introduced by Davis and Christian (1971) are based on the peak values of the maximum shear stress q_f, determined for three different stress systems. However, in this thesis, we assume that the parameters for the ellipsoidal model can be expressed in terms of τ_{ff} after adjustments are made for strain compatibility. These parameters, are, therefore, given by:

Table 8.3 Undrained Strength Ratios Corrected for Strain Compatibility vs OCR for Boston Blue Clay

OCR	$\frac{\tau_{ff}(PSC)}{\bar{\sigma}_{vc}}$	$\frac{\tau_{ff}(DSS)}{\bar{\sigma}_{vc}}$	$\frac{\tau_{ff}(PSE)}{\bar{\sigma}_{vc}}$	$\bar{K}_s$	$\bar{b}/\bar{a}$
1	0.263	0.200	0.137	0.52	0.88
2	0.435	0.365	0.275	0.63	0.96
4	0.725	0.605	0.504	0.70	0.93
6	0.956	0.800	0.692	0.72	0.91
8	1.190	0.970	0.864	0.73	0.89
12	1.594	1.236	1.203	0.76	0.83
16	1.830	1.440	1.446	0.79	0.83

$s_u(V) = \tau_{ff}$ for plane strain compression shear

$\bar{K}_s = s_u(H)/s_u(V)$, where $s_u(H) = \tau_{ff}$ for plane strain extension shear*

$$\bar{b}/\bar{a} = \frac{s_u(45^\circ)}{\sqrt{s_u(H) \cdot s_u(V)}}$$, where $s_u(45^\circ) = \tau_{ff}$ for plane strain shear with $i = 45^\circ$*

Hence, the $\bar{K}_s$ values shown in Table 8.3 were obtained by dividing $[\tau_{ff}(PSE)/\bar{\sigma}_{vc}]$ by $[\tau_{ff}(PSC)/\bar{\sigma}_{vc}]$ at each value of OCR.

In order to estimate $\bar{b}/\bar{a}$, we need the angle i between $\bar{\sigma}_{1f}$ and the vertical direction in a DSS test. This requires an assumption regarding the state of stress in a DSS test, since the stresses are known on the horizontal plane only. Several such assumptions were analyzed by Ladd and Edgers (1972), who showed that reasonable results can be obtained by assuming the location of the effective stress Mohr-Coulomb envelope. The state of stress at failure is, therefore, represented by a Mohr circle which is tangent to this envelope and passes through a point representing the state of stress on the horizontal plane. The direction of the major principal stress at failure, $\bar{\sigma}_{1f}$, can then be found and the angle i easily determined.

---

*A bar is added to differentiate between parameters based on τ_{ff} and those based on the peak q_f values.

Applying this hypothesis to BBC (Figs. 8.8 and 8.9), the angle i in DSS tests was found to be in the range of 30° - 35°, depending on OCR. The $\bar{b}/\bar{a}$ values were then computed (Table 8.3) by trial and error from Eq. 5.8 such that τ_{ff} (at i = 30° - 35°) = τ_{ff}(DSS). It should be noted, however, that these values of $\bar{b}/\bar{a}$ are approximate, given the assumptions used. For example, if one assumes $\bar{\phi}$ = 35° instead of 30° in Fig. 8.8, the resulting $\bar{b}/\bar{a}$ is reduced from 0.88 to 0.85. Figure 8.10 presents the shape of the elliptical strength relationship for different values of OCR, and Fig. 8.11 gives the anisotropic undrained strength parameters plotted versus OCR.

8.1.4 Stability Analyses

Two-Dimensional Analysis Based on Field Vane Data. Total stress stability analyses (ϕ = 0, c = s_u)* were first performed utilizing the field vane strength profile shown in Fig. 8.3. Figure 8.12 shows the different layers and soil types used in the analysis and Table 8.4 gives pertinent parameters.

The minimum plane strain factor of safety based on the FV strength model, F^0(FV), as obtained by the program STAB3D is 0.89. In order to check the accuracy of STAB3D, the same problem was analyzed using the program ICES-LEASE II (Dawson, 1972). The critical circle and the factor of safety obtained from both programs are shown in Fig. 8.12. The difference in

*This refers only to the foundation clay. The effective strength parameters ($\bar{c}$ and $\bar{\phi}$) were used for the frictional fill material.

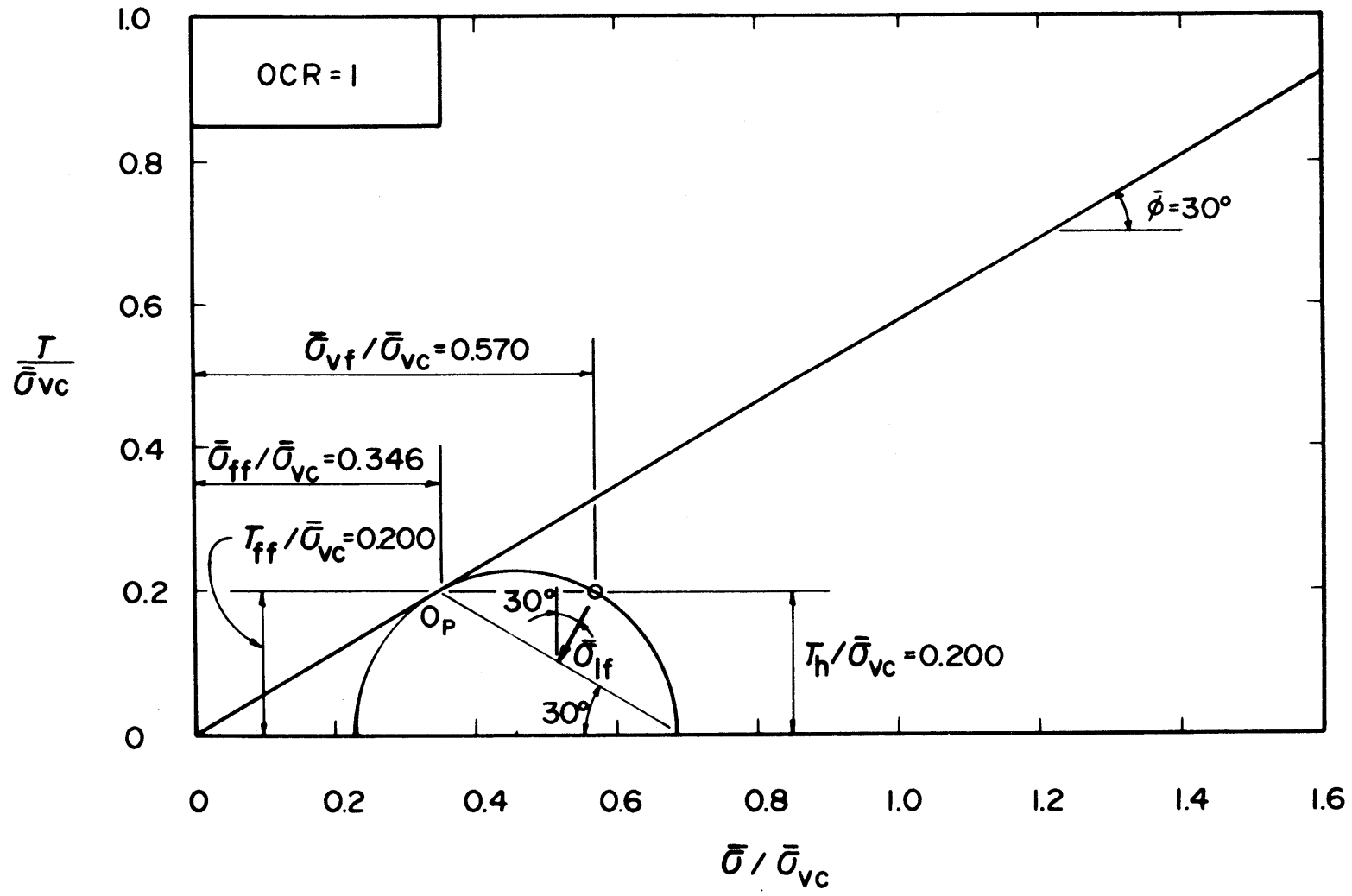


Figure 8.8 Interpretation of the $\overline{CK_oUDSS}$ Test Results for the Normally Consolidated Boston Blue Clay

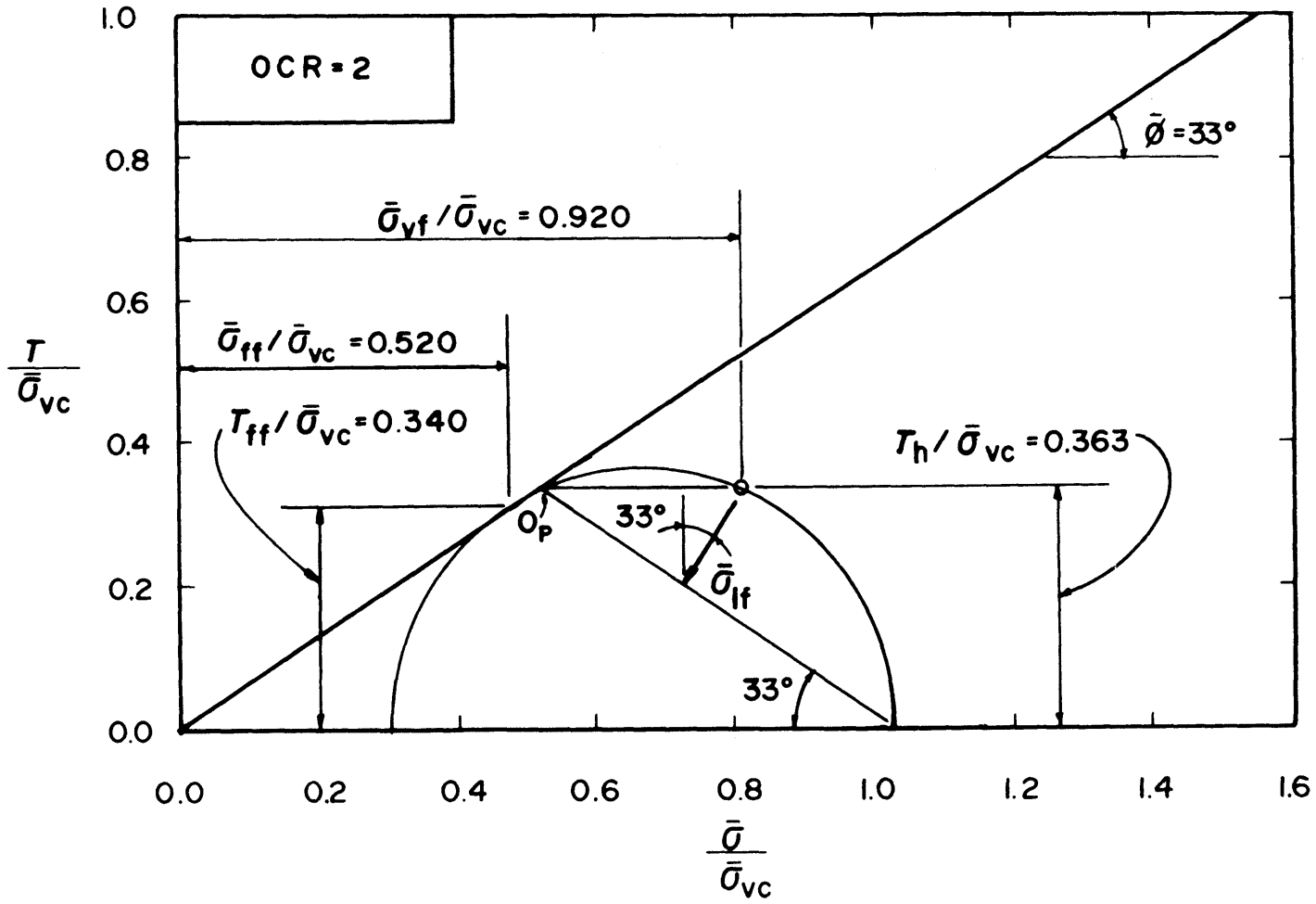


Figure 8.9 Interpretation of the $\overline{CK_oUDSS}$ Test Results for Boston Blue Clay at OCR = 2

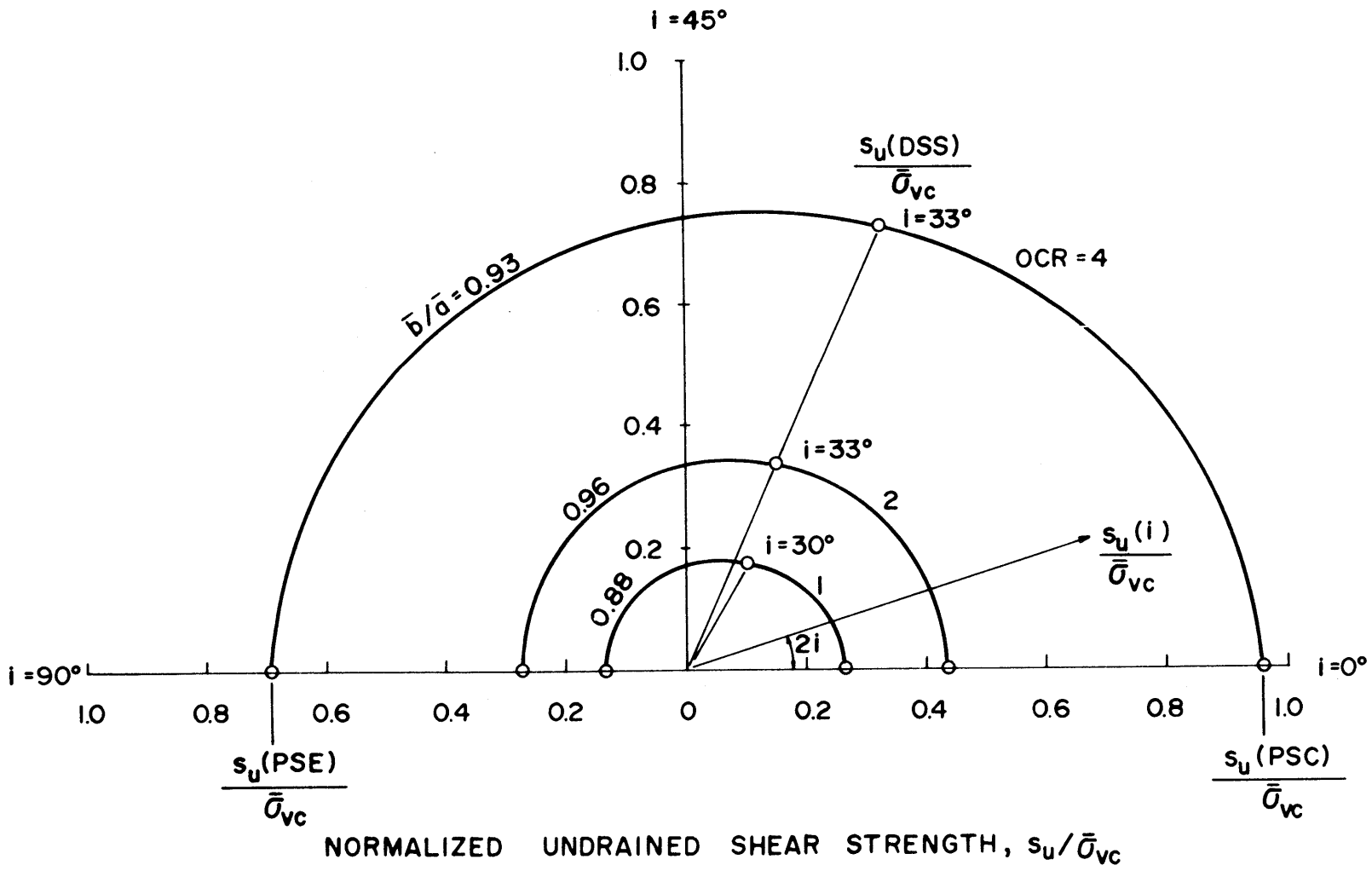


Figure 8.10 Normalized Polar Plots for Boston Blue Clay

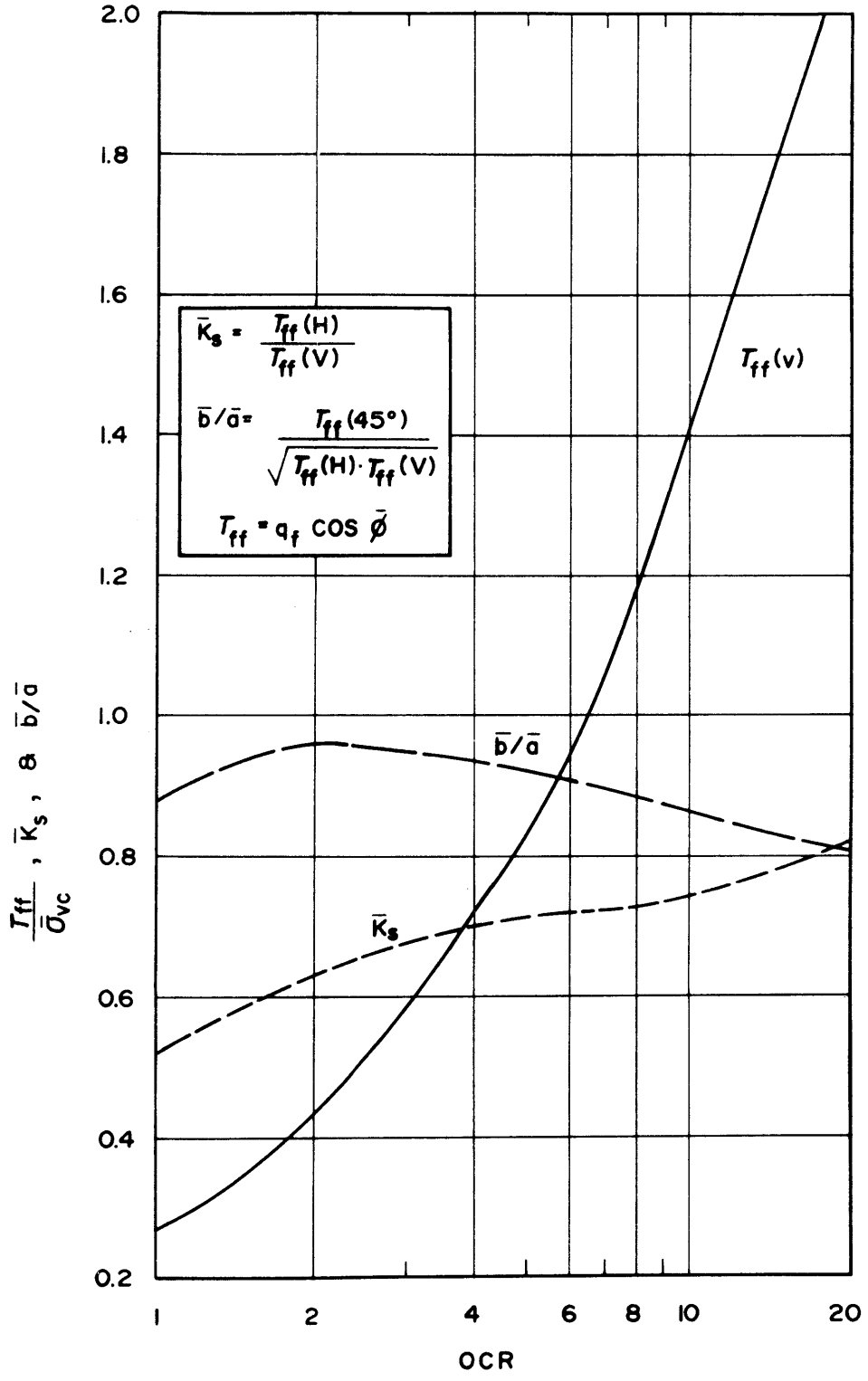


Figure 8.11 Anisotropic Undrained Strength Parameters for Boston Blue Clay

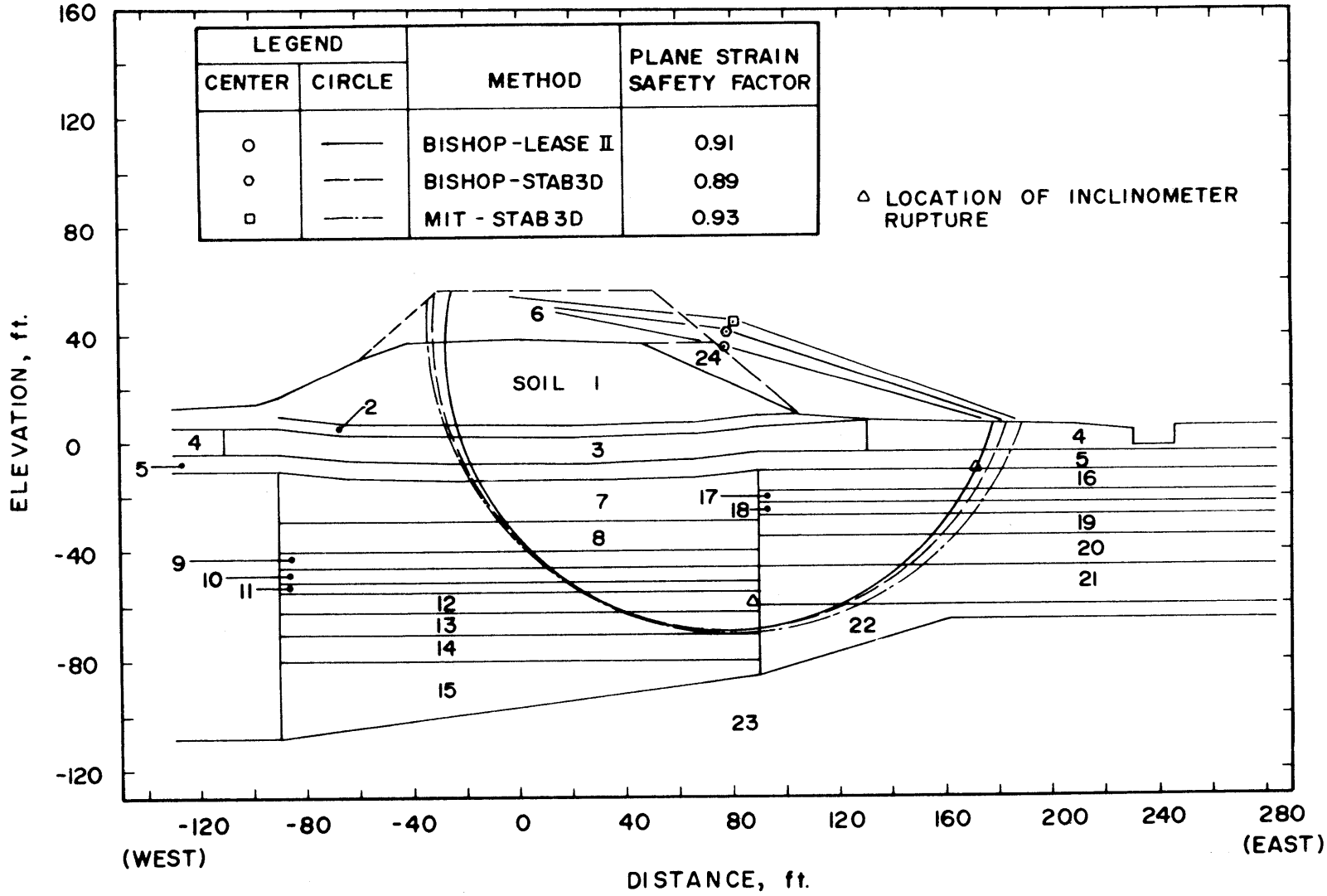


Figure 8.12 Field Vane Total Stress Stability Analysis, I-95, Station 263

Table 8.4 STAB3D Input Parameters Utilizing the Field Vane Strength Model for Boston Blue Clay, I-95 Station 263

Soil No.	γ_t (pcf)	c or s_u (psf)	$\bar{\phi}°$	K(1)	Soil Type
1	122	0	40	1.00	Embankment Sand
2	110	0	40	1.00	End-Dumped Sand
3	115	0	30	0.50	End Dumped Sand
4	75	300	0	-	Peat
5	113	0	35	0.46	Foundation Sand
6	122	0	37	1.00	Test Fill Sand
7	121	1270			
8	114	1188			
9	114	1075			
10	114	973			
11	114	871			
12	114	717			
13	114	594			
14	114	717			
15	114	1024	0	-	Boston Blue Clay
16	121	1936			
17	121	1639			
18	121	1331			
19	114	1127			
20	114	922			
21	114	758			
22	114	860			
23	120	0	40	0.36	Till
24	115	0	30	0.50	End-Dumped Sand

(1) $K = \frac{\text{out-of-plane stress}}{\text{vertical stress}}$

the factor of safety is less than 2% and, therefore, considered acceptable. Another comparison was made between the Modified Bishop method of analysis and the MIT method described in Chapter 6. Results in Fig. 8.12 show that the difference in the factor of safety determined from both methods is less than 4% and the corresponding critical circles are almost identical.

Two-Dimensional Analysis Based on SHANSEP-$S_u(\theta)$. A total stress stability analysis was then performed utilizing the SHANSEP-$S_u(\theta)$ strength model. The corresponding undrained shear strength parameters are given in Table 8.5 and Fig. 8.13. To obtain these values, the clay foundation was divided into two zones, one extending from 55 ft. West to 90 ft. East, and the other extending beyond 90 ft. East. The stress history used herein was developed by Ladd (1975b) before the embankment failure took place. For the first zone it was determined from the stress history profile at the center line as shown in Fig. 8.4 ($\bar{\sigma}_{vm}$ and "existing $\bar{\sigma}_{vc}$" lines). For the second zone, we selected the profiles of $\bar{\sigma}_{vm}$ and $\bar{\sigma}_{vo}$, for the soil "beyond 90' East" from Fig. 8.5. Knowing $\bar{\sigma}_{vm}$ and $\bar{\sigma}_{vo}$, the values of OCR were then computed and the strength ratios determined from Fig. 8.11. Table 8.6 gives the STAB3D SHANSEP-$S_u(\theta)$ input parameters.

The minimum two-dimensional factor of safety for this case equals 0.82. Figure 8.14 shows the critical circle and the distribution of the shear strength along this arc as com-

Table 8.5 SHANSEP-$S_u(\theta)$ Undrained Strength for Boston Blue Clay I-95 Station 263

El (ft)	$\bar{\sigma}_{vc}$ (psf)	$\bar{\sigma}_{vm}$ (psf)	OCR	$\frac{\tau_{ff}(V)}{\bar{\sigma}_{vc}}$	$\tau_{ff}(V)$ (psf)	$\bar{K}_s$	$\bar{b}/\bar{a}$
55' West to 90' East							
-12.5	5000	8750	1.75	0.39	1969	0.61	0.95
-20	5100	8000	1.57	0.36	1853	0.60	0.94
-30	4550	7000	1.54	0.36	1639	0.59	0.94
-40	4140	5600	1.35	0.33	1348	0.57	0.92
-50	3800	4300	1.13	0.29	1097	0.54	0.90
-60	3700	3750	1.01	0.26	971	0.52	0.88
-70	4150	4150	1.00	0.26	1091	0.52	0.88
-80	4700	4700	1.00	0.26	1236	0.52	0.88
-90	6000	6000	1.00	0.26	1578	0.52	0.88
Beyond 90' East							
-12.5	750	14000	18.7	2.06	1544	0.81	0.81
-20	1200	12000	10.0	1.39	1663	0.74	0.86
-30	1770	7000	3.95	0.73	1282	0.70	0.93
-40	2300	5000	2.17	0.46	1058	0.64	0.96
-50	2820	4000	1.42	0.34	962	0.58	0.93
-60	3330	4000	1.20	0.30	1007	0.55	0.91
-70	3850	3850	1.00	0.26	1013	0.52	0.88

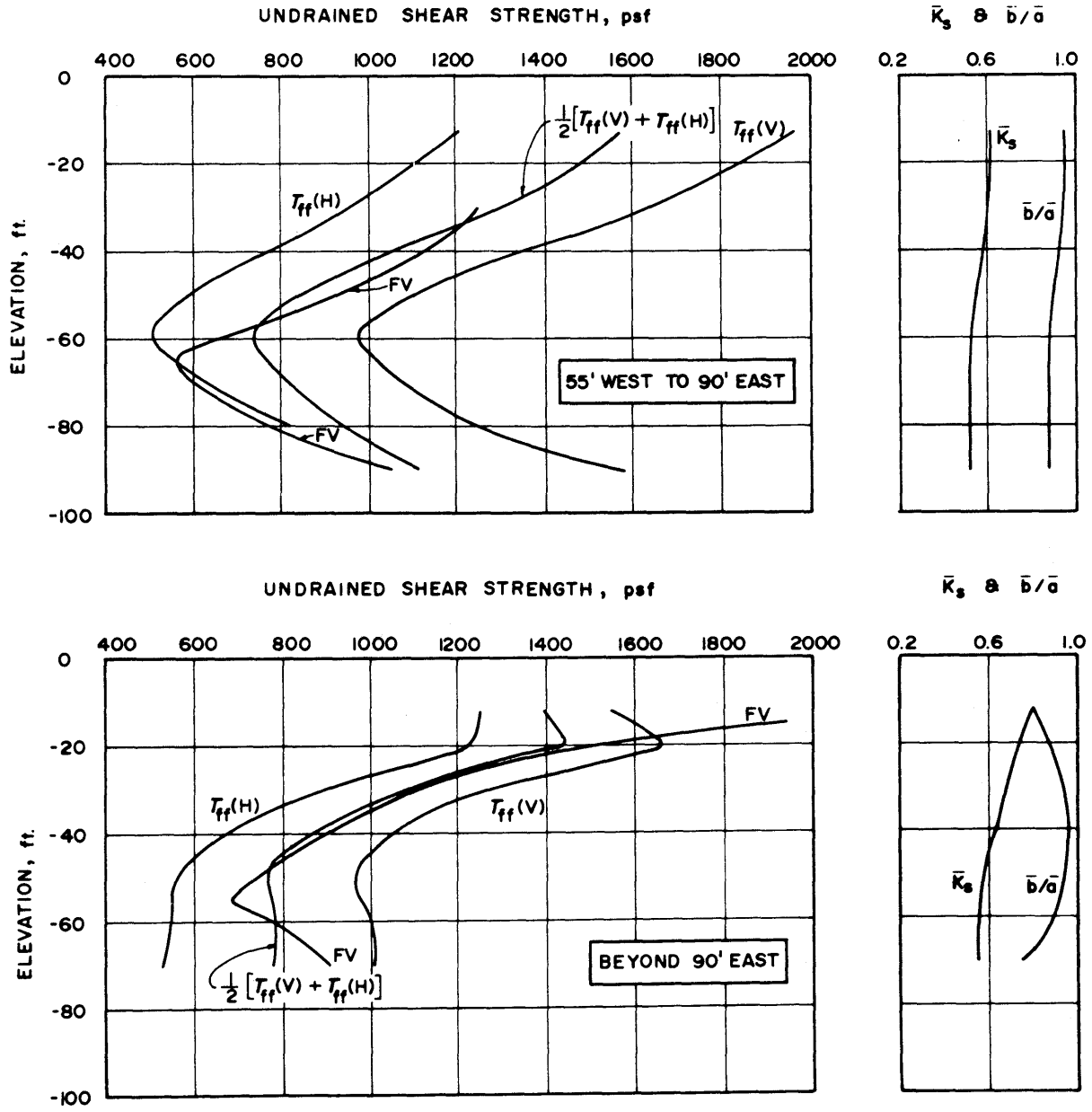


Figure 8.13 SHANSEP-$S_u(\theta)$ Undrained Strength for Boston Blue Clay, I-95 Station 263

Table 8.6 STAB3D Input Parameters Utilizing the SHANSEP-$S_u(\theta)$ Strength Model for Boston Blue Clay, I-95 Station 263

Soil No.	γ_t (pcf)	c or s_u (5) (psf)	$\bar{e}$ (1)	$\bar{d}$ (2)	f° (3)	$\bar{\phi}$°	K (4)	Soil Type
1	122	0				40	1.00	Embankment Sand
2	110	0				40	1.00	End-Dumped Sand
3	115	0				30	0.50	"
4	75	300	0	0	–	0	–	Peat
5	113	0				35	0.46	Foundation Sand
6	122	0				37	1.00	Test Fill Sand
7	121	1444	0.250	0.107				
8	114	1082	0.262	0.126				
9	114	977	0.278	0.154				
10	114	872	0.290	0.181				
11	114	798	0.303	0.199				
12	114	756	0.311	0.208				
13	114	793	0.316	0.226				
14	114	887	0.316	0.226	60	0	–	Boston Blue Clay
15	114	1071	0.316	0.226				
16	121	1407	0.114	0.311				
17	121	1428	0.149	0.260				
18	121	1292	0.163	0.208				
19	114	1071	0.183	0.126				
20	114	866	0.223	0.088				
21	114	772	0.270	0.135				
22	114	782	0.303	0.181				
23	120	0	0	0	–	40	0.36	Till
24	115	0	0	0	–	30	0.50	End-Dumped Sand

(1) $\bar{e} = \dfrac{1 - \bar{K}_s}{1 + \bar{K}_s}$ (2) $\bar{d} = 1 - \dfrac{\bar{b}^2}{\bar{a}^2}$ (3) f = angle between the major principal plane and the failure plane

(4) $K = \dfrac{\text{out-of-plane stress}}{\text{vertical stress}}$ (5) $s_u = 1/2[s_u(V) + s_u(H)]$

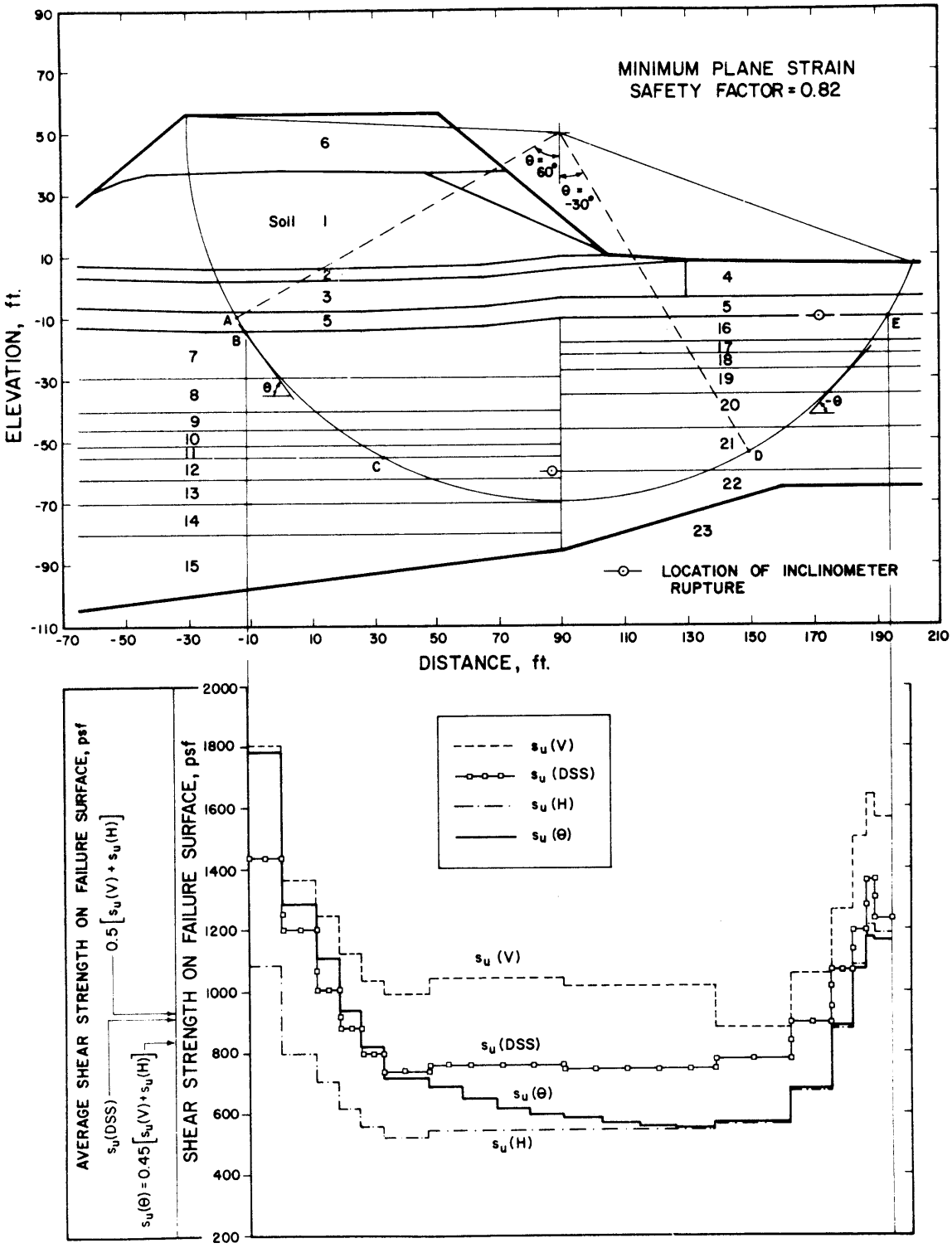


Figure 3.14 Results of Two-Dimensional Stability Analysis Utilizing the SHANSEP-$S_u(\theta)$ Strength Model

pared to the PSC, DSS and PSE strengths of each soil layer. In order to obtain this distribution, the angle between the failure plane and the major principal plane at failure (angle f in Chapter 5) was assumed equal to 60°. Therefore, at any point along the arc where the inclination of the failure surface to the horizontal is θ, the angle between the direction of the major principal stress at failure and the vertical direction, i, is given by (see Chapter 5):

$$i = f - \theta = 60° - \theta$$

The shear strength, $s_u(\theta)$, at a point where $\theta = 60°$ (point A in Fig. 8.14) is thus equal to $s_u(V)$ (corresponding to $i = 0$). Similarly, at point D, where $\theta = -30°$, the shear strength is equal to $s_u(H)$ ($i = 90°$). Let us now examine the variation of the shear strength along the portion of the failure arc between points B and E (Fig. 8.14) within the BBC. At point B, $\theta = 57°$, and hence $s_u(\theta)$ is slightly smaller than $s_u(V)$. As the angle i decreases, $s_u(\theta)$ decreases and approaches the DSS strength (point C in Fig. 8.14). Further reduction in the angle θ causes a decrease in strength up to point D where $s_u(\theta) = s_u(H)$. From point D to point E, $s_u(\theta)$ increases and remains close to $s_u(H)$.

The average shear strength along the failure arc between points B and E computed on the basis of the DSS strength and $0.5[s_u(V) + s_u(H)]$ is 915 psf and 930 psf, respectively. The corresponding average based on $s_u(\theta)$ is 839 psf, i.e., equal 90% of $0.5[s_u(V) + s_u(H)]$ average. Hence, in order to

account for strength anisotropy (including strain compatibility) in stability analyses involving BBC, an equivalent average strength equal to 0.45 [$s_u(H) + s_u(V)$] can be used. The strength based on DSS results will underestimate the $s_u(\theta)$ strengh by 10%.

Three-Dimensional Analysis. In evaluating the end effects on the stability of the I-95 test section, variations in the embankment cross section along the observed failure length (Sta 257+00 to Sta 267+30) are important. The fill elevation within the loaded section (Sta 261+50 to Sta 264 +50) was at 56.5 ft., and beyond the loaded area, the embankment was at its original elevation of 37.8 ft. In the analysis of this problem, two different cross sections were used, one at El. 56.5 ft., and the other at El. 37.8 ft. The transition zone between the two elevations, which had a length of about 20 ft. in plan, was neglected. For a detailed description of the analysis of embankments with variable cross sections using STAB3D, the reader is referred to Appendix A.

The shear surfaces described in Chapter 2 were used in this analysis: a cone attached to a cylinder and an ellipsoid attached to a cylinder. Stability computations were performed utilizing both the field vane (Fig. 8.3) and the SHANSEP-$S_u(\theta)$ strength models (Fig. 8.13). Results based on these strength models are shown in Fig. 8.15.

Based on the dependence of F/F^0 on 2L/DR illustrated by Fig. 8.15, the following can be concluded:

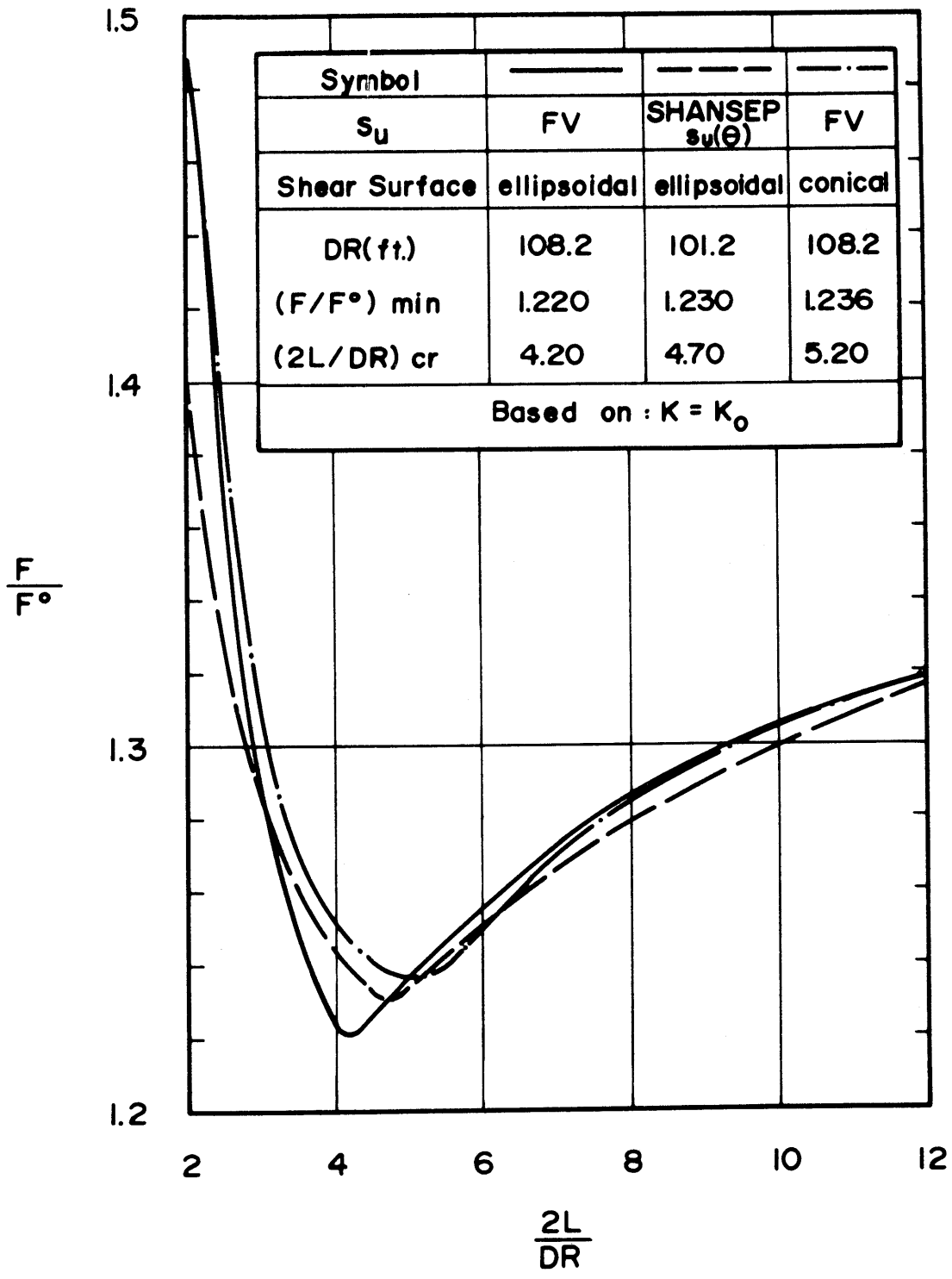


Figure 8.15 Three-Dimensional Effects for the I-95 Embankment Station 263

1. Using the FV strength data, the minimum value of $F/F^0 = 1.22$ corresponds to $2L/DR = 4.2$. Since, in this case, $F^0 = 0.89$ and DR = 108.2 ft., the minimum three-dimensional factor of safety is thus:

$$F_{min} = 1.22 \times 0.89 = 1.09$$

The corresponding failure length $2L = 4.2 \times 108.2 = 455$ ft.* This is substantially shorter than the observed failure length of 1030 ft., which has $2L/DR = 1030/108.2 = 9.52$. Figure 8.15 shows that for $2L/DR = 9.52$, the value of $F/F^0 = 1.30$, i.e., the three-dimensional factor of safety for the observed failure length $F = 1.30 \times 0.89 = 1.17$. Therefore, based on the minimum F/F^0 value, end effects increase the plane strain factor of safety by 22%, whereas based on the observed failure length, the end effects increase F^0 by 30%.

2. Using the SHANSEP-$S_u(\theta)$ strength model, the end effects equal 23% when the minimum value of F/F^0 is used and 30% when the observed failure length is used. The computed three-dimensional factor of safety, F = (1.23 to 1.30)(0.82 from Fig. 8.14) = 1.00 to 1.06. The failure length corresponding to the minimum three-dimensional factor of safety is 476 ft. (4.7 x 101.2).

3. From Fig. 8.15 it can be seen that ellipsoidal shear

---

*The total failure length (2L = 455 ft.) consists of a cylindrical part with length $2\ell_c = 220$ ft. and two end ellipsoids each having a length $\ell_e = 115$ ft.

surfaces give lower values of F/F^0 than conical surfaces. Therefore ellipsoidal shear surfaces are more likely to represent the actual failure surface.

In order to investigate the effect of the longitudinal (out-of-plane) stress, $\bar{\sigma}_\ell$, on the three-dimensional factor of safety, two computer runs were made utilizing the FV strength profile. In the first run, the K values, expressing the ratio of $\bar{\sigma}_\ell$ to $\bar{\sigma}_v$, for all soil layers having $\phi \neq 0$, were reduced from $K = K_o$ to $K = K_a = [(1 - \sin \bar{\phi})/(1 + \sin \bar{\phi})]$. In the second run we set $K = K_p = 1/K_a$. The results in Fig. 8.16 showed that a decrease in K reduces both the minimum factor of safety and the associated failure length. By decreasing K from K_o to K_a, F/F^0 decreased from 1.22 to 1.16 and the failure length decreased from 455 to 420 ft. Conversely, increasing K to K_p resulted in $F/F^0 = 1.42$ and a failure length of 1700 ft.

8.1.5 Summary and Conclusions for the I-95 Failure

The I-95 test section involved the construction to failure of an embankment on partially consolidated Boston Blue Clay. Total stress ($\phi = 0$, $c = s_u$) stability analyses performed using the viel vane, FV, and the SHANSEP-$S_u(\theta)$ strength models showed that the minimum plane strain factor of safety F^0 was equal to 0.89 and 0.82, respectively. The end effects were estimated by evaluating F/F^0 from three-dimensional analyses performed by the program STAB3D. From this case study, the following conclusions can be advanced:

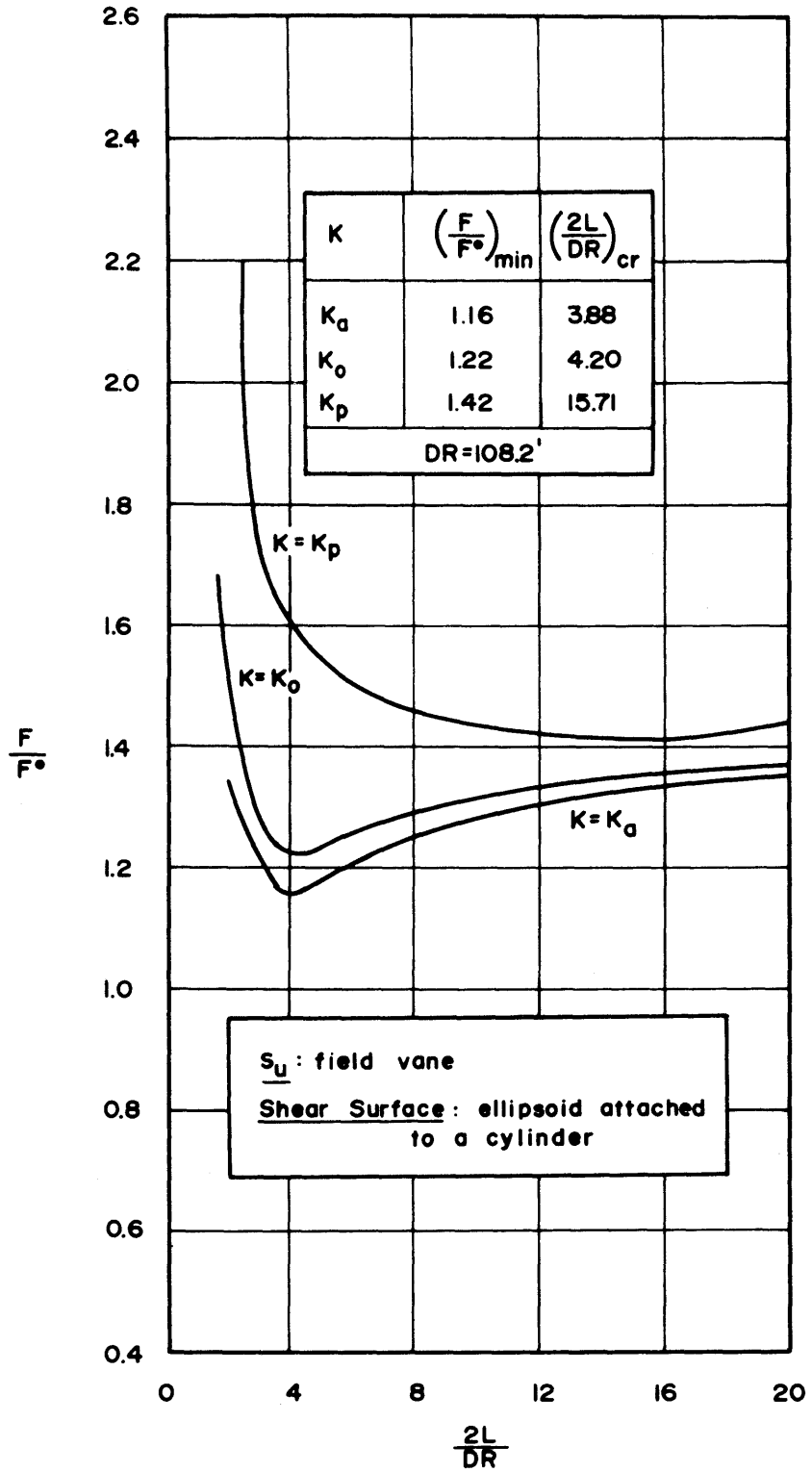


Figure 8.16 Effect of the Longitudinal Stress on the Stability of The I-95 Embankment Station 263

1. The SHANSEP-$S_u(\theta)$ strength model, which accounts for strength anisotropy and strain compatibility along a circular shear surface, yielded a three-dimensional factor of safety F^0 between 1 to 1.06 at failure and is, therefore, considered satisfactory.

2. The FV strength model overestimated the three-dimensional safety factor by about 9 to 17%. A FV correction factor, μ, between 0.85 and 0.92 should, therefore, be multiplied by the measured FV strength in embankment stability computations on Boston Blue Clay.

3. If the three-dimensional nature of the failure is neglected (by relying on plane-strain analyses), a correction factor $\mu = 1.1$ for the FV strength of Boston Blue Clay will be erroneously reached.

4. End effects expressed by the ratio F/F^0 are not significantly affected by the strength model used (see Fig. 8.15). However, the plane strain safety factor, F^0, increases by 9% when the FV strength is used instead of the SHANSEP-$S_u(\theta)$ strength model.

5. The end effects are affected by the longitudinal (out-of-plane) stress, $\bar{\sigma}_\ell$, because of the frictional fill materials in the embankment and the upper part of the foundation. An increase in K ($=\bar{\sigma}_\ell/\bar{\sigma}_v$) from K_a to K_o, and K_p, increases $(F/F^0)_{min}$ from 1.16 to 1.22 and 1.42, respectively. Since the actual value of K is difficult to estimate, we used $K = K_o$ in all of our analyses.

6. The computed failure length corresponding to $(F/F^0)_{min}$ is substantially shorter than the observed failure length. In general, the failure length is difficult to predict because of its sensitivity to the input parameters. For example, when K is increased from K_o to K_p, the failure length increased 500%, whereas the safety factor increased by only 22%.

7. Strength anisotropy of Boston Blue Clay can be accounted for in plane strain circular arc stability analyses by using an average shear strength equal to 0.45 times the sum of the vertical and horizontal strengths. The direct simple shear strength underestimates the average anisotropic strength by 10%.

8.2 EXPERIMENTAL TEST SECTION, PORTSMOUTH, NEW HAMPSHIRE

8.2.1 Site Description

The Experimental Test Section, ETS, at Portsmouth, New Hampshire, was conducted to investigate the shear strength and the consolidation characteristics of a soft, very sensitive marine illitic clay at the junction of Interstate Route I-95 and U.S. Route 4. The project is described in detail by Ladd (1972), and Ladd et al. (1972).*

Figures 8.17 and 8.18 show a cross section and a plan view of the embankment. Its west and east sides have slopes of 4:1 (4 horizontal to 1 vertical) and 8:1, respectively. The crest of the ETS was about 225 ft. long in order to approximate plane strain conditions. Based on a preliminary estimate of the in situ shear strength, the west slope was designed to fail at a height of about 15 ft. Since actual failure occurred when the embankment height was about 21.5 ft., a steeper slope above El. 33 ft. was required.

8.2.2 The Failure

A massive failure took place when the embankment elevation was at 41.5 ft. The crest dropped about 10 ft. and the toe heaved a similar amount along most of the embankment. The longitudinal extent of the shear surface was approximately

---

* The firm of Haley and Aldrich, Inc. was the soils consultant to the State of New Hampshire Department of Public Works and Highways for this project.

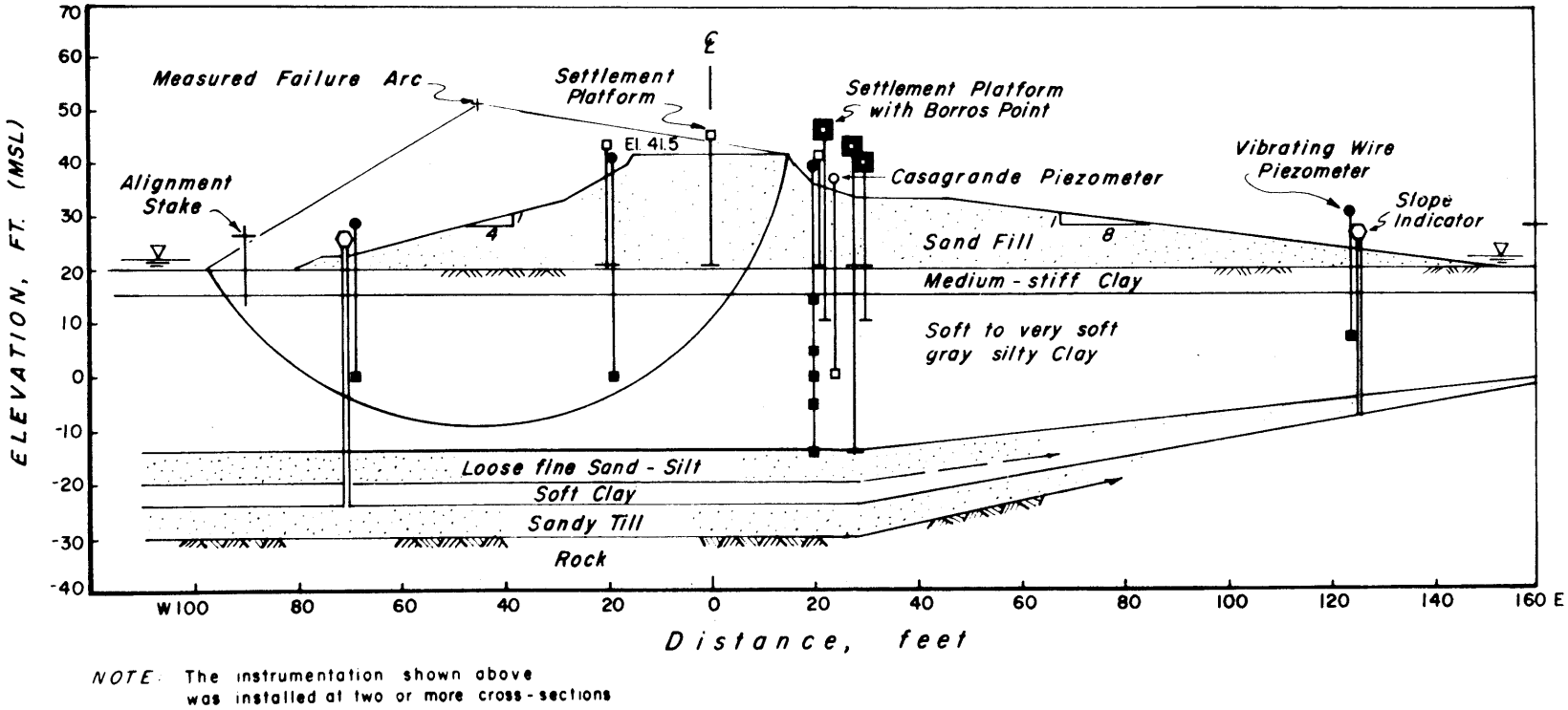


Figure 8.17 Cross Section Through Centerline of Experimental Test Section Looking North (From Ladd, 1972)

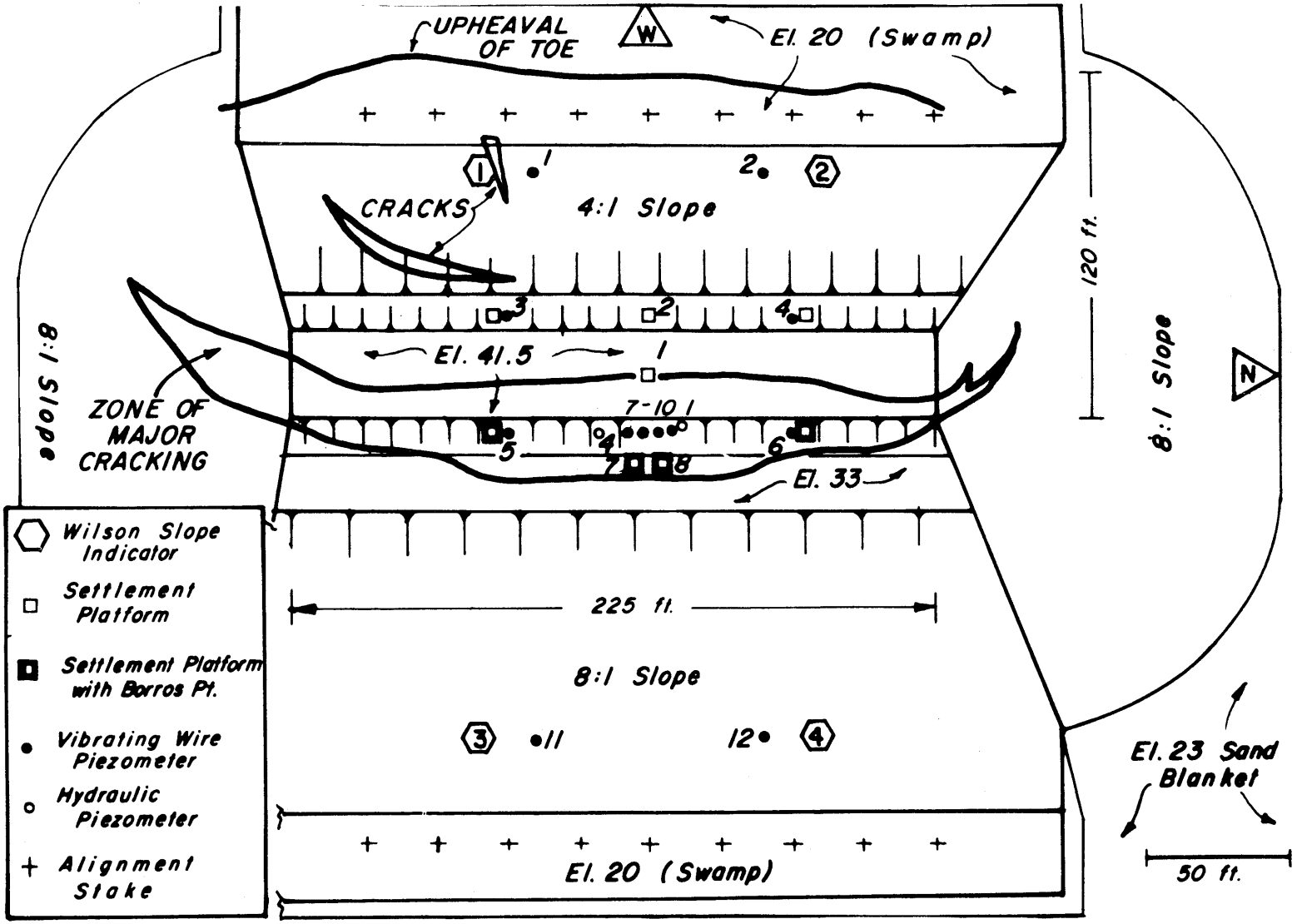


Figure 8.18 Plan of Experimental Test Section Showing Location of Instrumentation and Mode of Failure (From Ladd, 1972)

300 ft. (Fig. 8.18), and no visible cracks were observed in the embankment during the afternoon preceding the failure, which occurred at night.

8.2.3 Determination of the Soil Properties

Embankment Fill - The fill for the embankment consisted of a fairly clean, well graded sand. A unit weight, γ_t = 115 pcf and a friction angle, $\bar{\phi} = 40°$ were used for the embankment fill below El = 35.5 ft. Above this elevation we assumed γ_t = 110 pcf and $\bar{\phi} = 30$.

Foundation Clay - The clay stratum consists of 25 to 30 ft. (see Fig. 8.19) of soft, very sensitive marine illitic clay ($w_n = 50 \pm 5\%$, $w_\ell = 35 \pm 5\%$, $w_p = 20 \pm 2\%$). An extensive testing program to determine the clay properties, Ladd (1972), consisted of: 1 - standard auger and wash borings for soil identification and determination of the depth of the clay layer; 2 - in situ Geonor field vane, FV, tests; 3 - laboratory tests on specimens obtained from 3- and 5-inch undisturbed tube samples. These tests included: conventional incremental oedometer tests, unconfined compression tests on vertical (U_V) and horizontal (U_H) samples, isotropically consolidated - undrained triaxial compression tests with pore pressure measurements ($\overline{CIUC}$), anisotropically consolidated-undrained triaxial compression tests with pore pressure measurements ($\overline{CAUC}$), and K_o consolidated-undrained tests with pore pressure measurements under various stress systems including plane strain compression ($\overline{CK_oUPSC}$) plane strain extension ($\overline{CK_oUPSE}$) and Geonor direct simple shear ($\overline{CK_oUDSS}$).

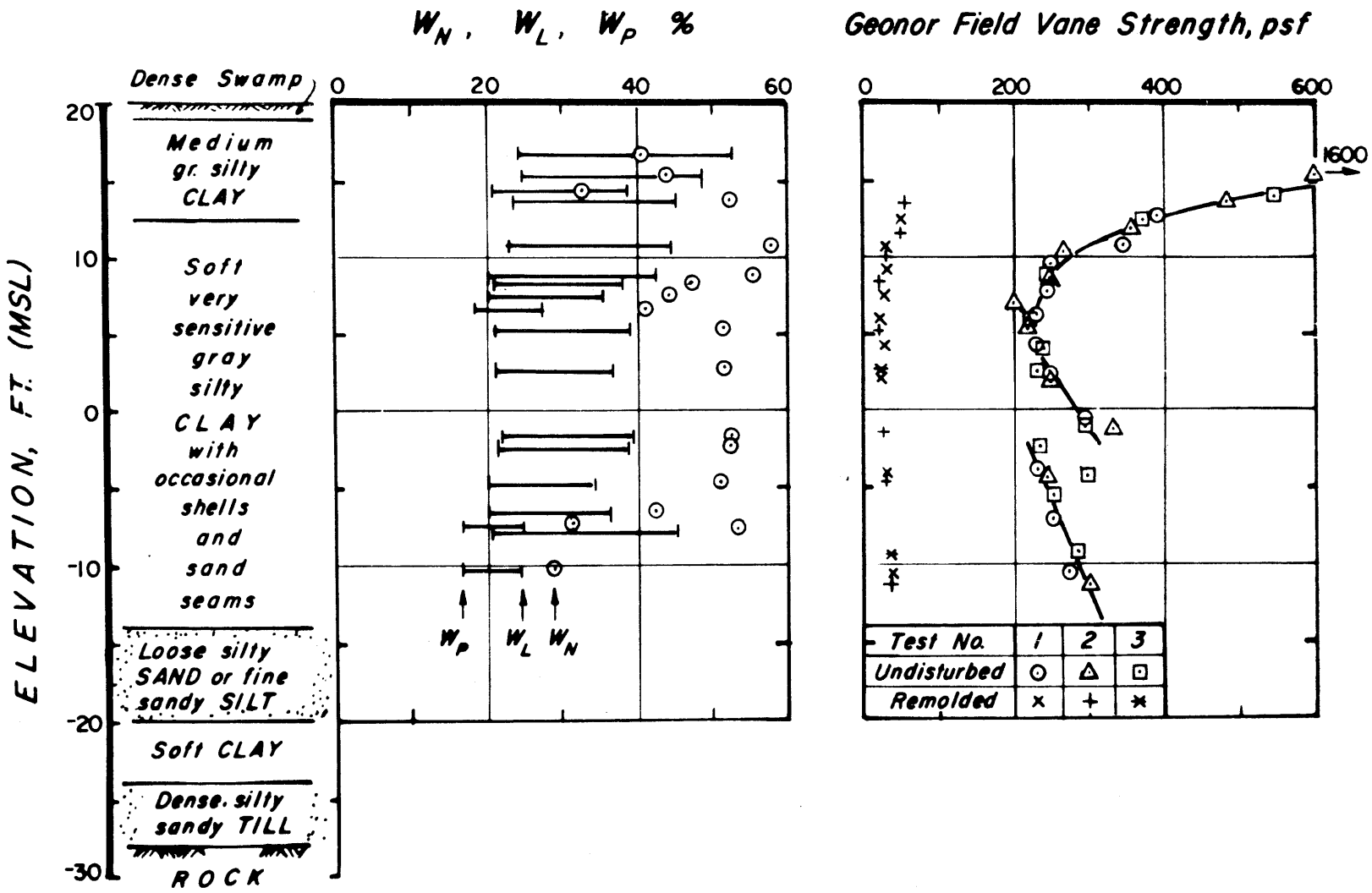


Figure 8.19 Soil Profile, Index Properties and Field Vane Strengths at Experimental Test Section (From Ladd, 1972)

Figure 8.20 shows the range of maximum past pressures, $\bar{\sigma}_{vm}$, used in the subsequent stability analyses. Part of the scatter is due to whether $\bar{\sigma}_{vm}$ was determined by using data at the end of primary consolidation (about 25 minutes) or data after 12 hrs (Ladd et al., 1972). Additional scatter is also caused by inevitable sampling and testing disturbances.

Geonor field vane, FV, test results are shown in Fig. 8.19. The sensitivity of the clay layer, defined as the ratio of the remolded to the undisturbed strengths, varied between 10-15. The FV profile used in subsequent stability analyses is shown in Fig. 8.19.

The normalized undrained shear strength ratios, $s_u/\bar{\sigma}_{vc}$, varied considerably with the stress system. The values obtained at OCR = 1 are (Ladd and Edgers, 1972):

$$\frac{s_u(PSC)}{\bar{\sigma}_{vc}} = 0.350;$$

$$\frac{s_u(PSE)}{\bar{\sigma}_{vc}} = 0.155; \quad \text{and}$$

$$\frac{s_u(DSS)}{\bar{\sigma}_{vc}} = 0.204,$$

where $s_u = 1/2(\sigma_1 - \sigma_3)_f$, except for DSS tests where $s_u = (\tau_h)_{max}$. Unfortunately, no tests were performed on overconsolidated Portsmouth Clay. However, Ladd et al. (1977) show

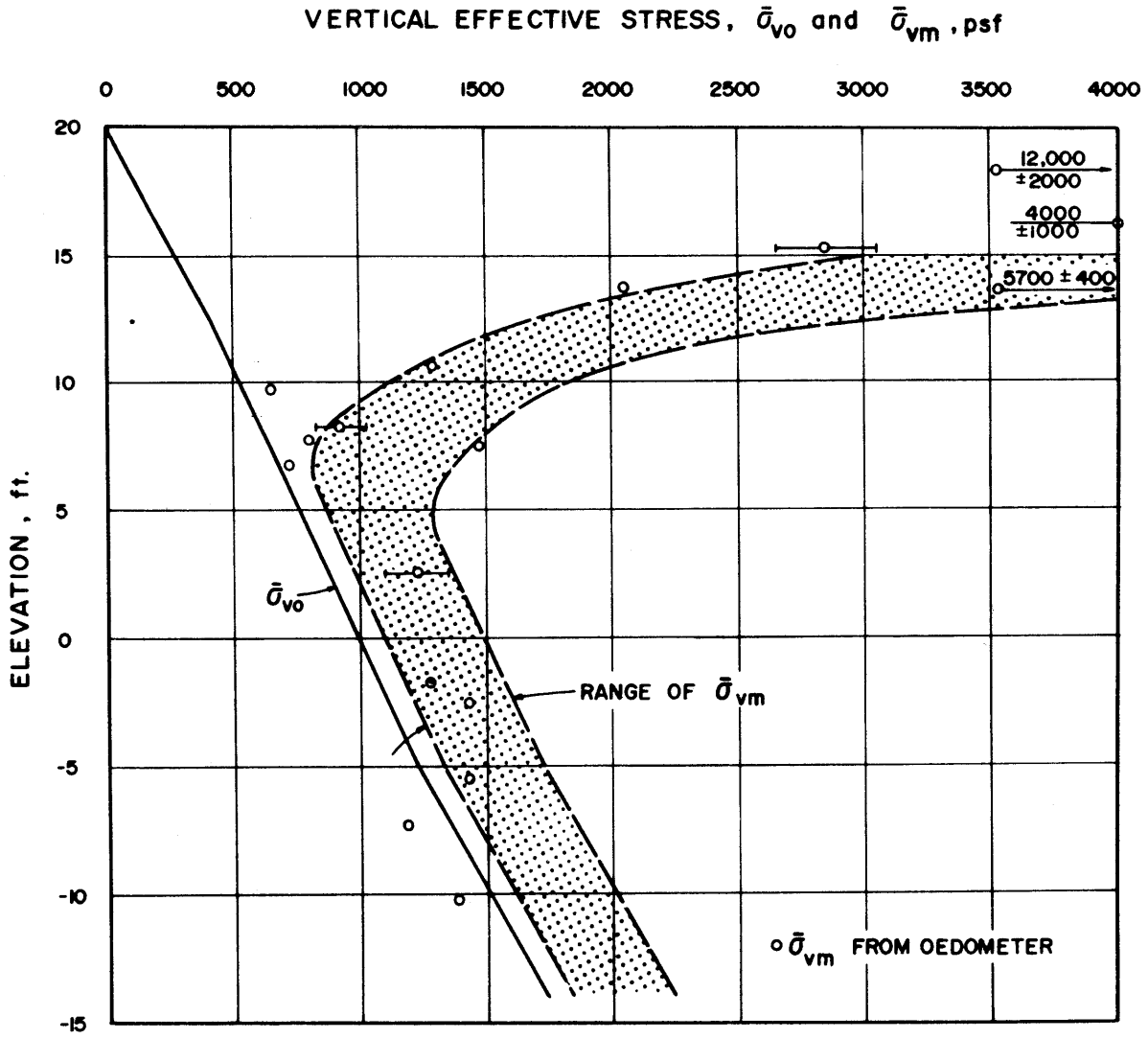


Figure 8.20 Stress History at Experimental Test Section
(After Ladd, 1972)

that the relationship [(s_u at $\bar{\sigma}_{vc}$)/(s_u at $\bar{\sigma}_{vm}$)] vs. OCR for 6 clays of widely different plasticity indices is roughly the same. Therefore, in order to estimate the shear strength at different OCR's, we used the results of reconsolidated Boston Blue Clay, BBC, which is a similar illitic, sensitive, silty clay. This was achieved by plotting [(s_u at $\bar{\sigma}_{vc}$)/(s_u at $\bar{\sigma}_{vm}$)] vs. log OCR (Fig. 8.21) utilizing the data given in Table 8.1 for BBC. For a particular stress system, $s_u/\bar{\sigma}_{vc}$ for the Portsmouth Clay at any OCR is thus estimated from the expression (see Ladd, 1975a for details):

$$s_u/\bar{\sigma}_{vc} = [s_u/\bar{\sigma}_{vc} \text{ at OCR} = 1 \text{ for the Portsmouth Clay}] \times [(s_u \text{ at } \bar{\sigma}_{vc})/(s_u \text{ at } \bar{\sigma}_{vm}) \text{ value in Fig. 8.21 at this OCR}] \times [\text{OCR}].$$

For example, to find the value of $s_u(\text{PSC})/\bar{\sigma}_{vc}$ at OCR = 4, we note that $s_u/\bar{\sigma}_{vc}$ at OCR = 1 for the Portsmouth Clay = 0.350. From Fig. 8.21, the ratio [(s_u at $\bar{\sigma}_{vc}$)/(s_u at $\bar{\sigma}_{vm}$)] at OCR = 4 for this stress system = 0.699. The required strength ratio is thus:

$$s_u(\text{PSC})/\bar{\sigma}_{vc} \text{ at OCR of } 4 = 0.35 \times 0.699 \times 4 = 0.978$$

This procedure was carried out up to OCR = 16 for the three stress systems under consideration. The computed shear strengths are given in Table 8.7. Since complete stress-strain data are not available for the PSC and PSE modes of failure for Portsmouth Clay, adjustments for strain compatibility were performed on the basis of BBC data in Figs. 8.6

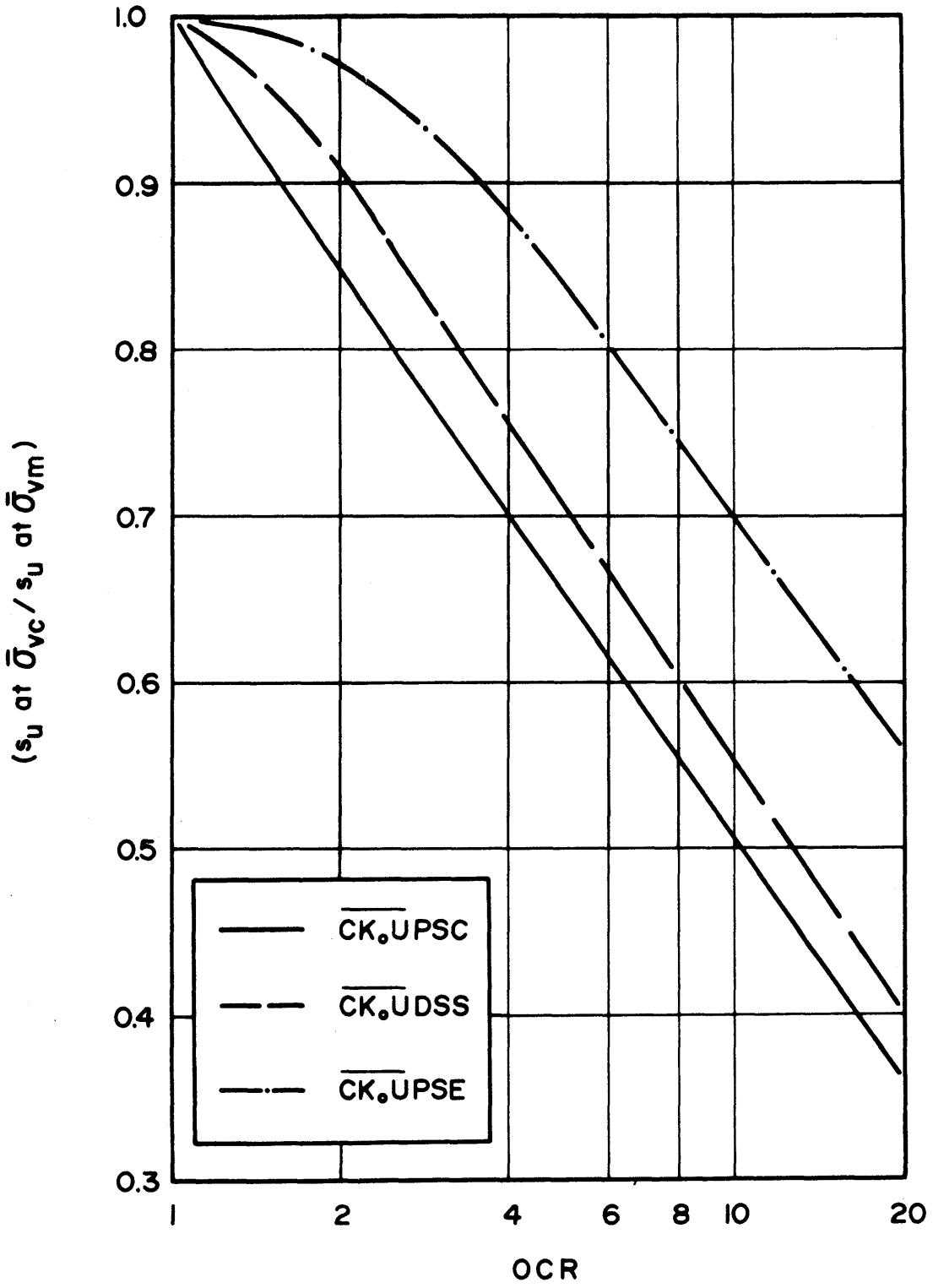


Figure 8.21 Decrease in Strength with Rebound for Boston Blue Clay

Table 8.7 Undrained Shear Strength Ratios for the Portsmouth Clay, N.H.

O C R	$\frac{s_u(PSC)}{\bar{\sigma}_{vc}}$ (1)	$\frac{s_u(DSS)}{\bar{\sigma}_{vc}}$ (2)	$\frac{s_u(PSE)}{\bar{\sigma}_{vc}}$ (1)
1	0.350	0.204	0.155
2	0.587	0.372	0.302
4	0.978	0.617	0.547
6	1.291	0.816	0.749
8	1.540	0.989	0.930
12	1.956	1.261	1.228
16	2.268	1.469	1.448

(1) $s_u = 1/2(\sigma_1 - \sigma_3)_f$

(2) $s_u = (\tau_h)_{max}$

and 8.7. The PSC strength was thus reduced by 10% for OCR < 8, the PSE strength was reduced by 6% for OCR < 6, and no reduction applied at higher OCR's. Similarly, no reduction was applied to the DSS strength.

Figure 8.22 gives the anisotropic undrained strength parameters as a function of OCR. The shear strength ratios plotted in Fig. 8.22 correspond to the shear stress on the failure plane at failure, τ_{ff}. The $\bar{b}/\bar{a}$ values were obtained according to the procedure presented earlier for the I-95 failure.

8.2.4 Stability Analyses

Total stress stability analyses ($\phi = 0$, $c = s_u$) were performed utilizing the field vane, FV, and the SHANSEP-$S_u(\theta)$ strengths as in the case of the I-95 failure.

Two-Dimensional Analysis Based on Field Vane Data. The FV profile used in the analysis is shown in Fig. 8.19. The input parameters for the computer program STAB3D are given in Table 8.8. The results of the FV stability analyses are shown in Fig. 8.23, where the FV plane strain factor of safety = 0.91. Fig. 8.23 also shows that good agreement exists between the results of STAB3D and ICES-LEASE II (Dawson, 1972). The MIT method, described in Chapter 6, gave the same factor of safety as the Modified Bishop analysis, but the corresponding circles are slightly different, and lie about 3 ft. below the actual failure circle.

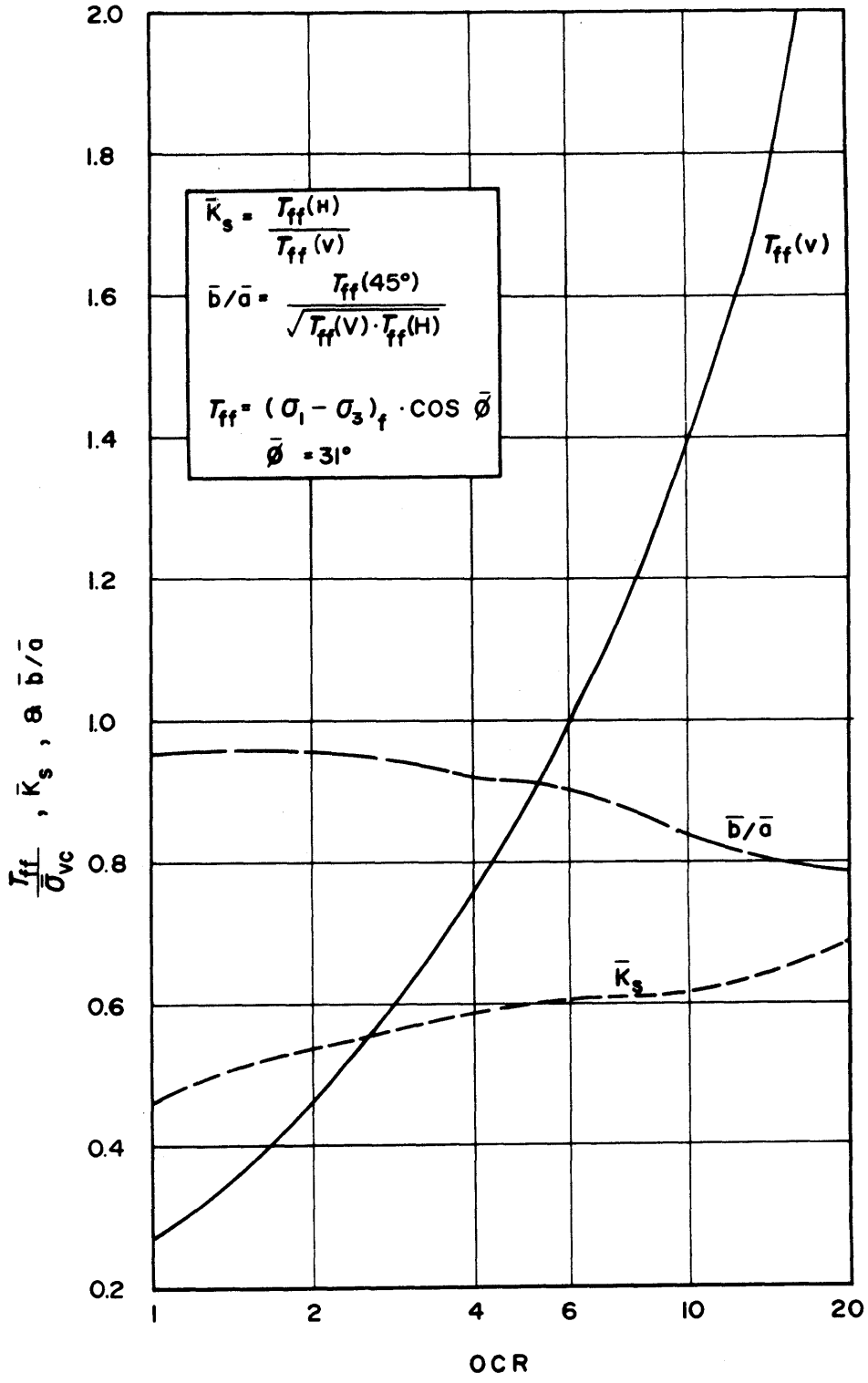


Figure 8.22 Anisotropic Undrained Strength Parameters For Portsmouth Clay, N.H.

Table 8.8 STAB3D Input Parameters Utilizing the Field Vane Strength Model for Portsmouth Clay

Soil No.	γ_t (pcf)	c or s_u (2) (psf)	$\bar{\phi}°$	K (1)	Soil Type
1	118	1000	0	—	Crust
2	130	0	40	0.357	Embankment Fill
3	115.5	0	40	0.357	Embankment Fill
4	110	0	30	0.500	Embankment Fill
5	130	0	30	0.500	Sand and Silt
6	62.4	0			Water
7	118	400			
8	109	240			
9	109	250	0	—	
10	109	300			Portsmouth Clay
11	109	235			
12	120	265			
13	120	300			

(1) $K = \frac{\text{out-of-plane stress}}{\text{vertical stress}}$

(2) From Ladd (1972)

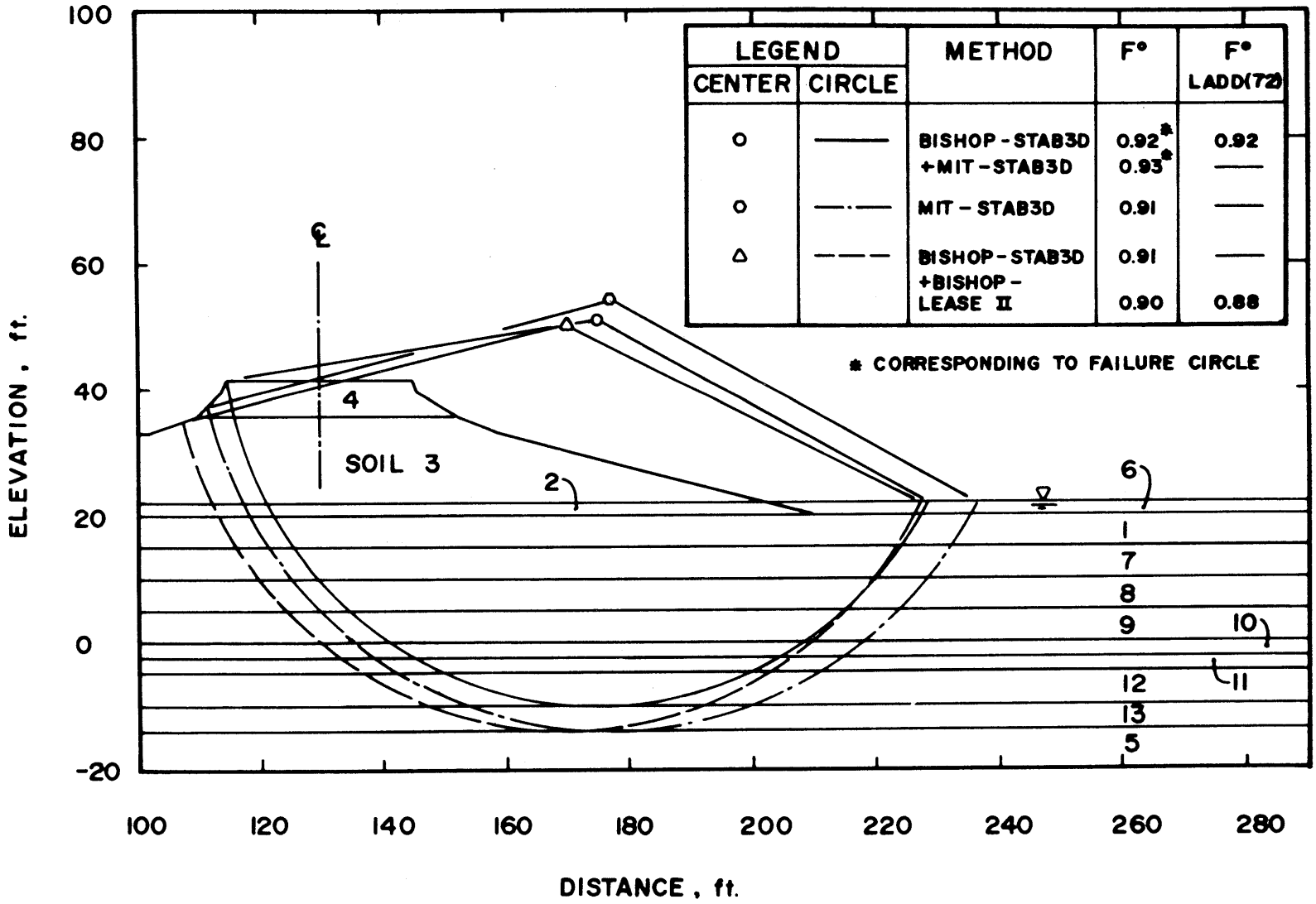


Figure 8.23 Field Vane Total Stress Stability Analysis of the Experimental Test Section, N.H.

Two-Dimensional Analysis Based on SHANSEP-$S_u(\theta)$ Data.

The SHANSEP strength profiles were computed on the basis of the minimum, average and maximum values of $\bar{\sigma}_{vm}$ shown in Fig. 8.20. These maximum past pressure values are slightly lower than those reported by Ladd (1972). The results of these computations are given in Table 8.9 and the strength profiles are illustrated in Fig. 8.24. Table 8.10 presents the input parameters used for the STAB3D analysis. Figure 8.25 shows the slope analyzed, the band in which the critical circles corresponding to different profiles of $\bar{\sigma}_{vm}$ fall, as well as the actual failure circle. The computed plane strain minimum safety factor, F^0, varies between 0.77 and 0.94 depending on $\bar{\sigma}_{vm}$. For the actual failure circle, F^0 varied between 0.78 and 0.96. The results of two-dimensional stability analyses are summarized in Table 8.11. The average shear strengths along the critical failure arc corresponding to the average $\bar{\sigma}_{vm}$ profile (Fig. 8.20) were computed. The average shear strength along the critical circle corresponding to the DSS, $0.5[s_u(V) + s_u(H)]$ and $s_u(\theta)$ strengths are 328, 310 and 266 psf, respectively. This means that strength anisotropy in circular arc analyses involving the Portsmouth Clay can be taken into consideration by using an equivalent average strength equal to $0.43\ [s_u(V) + s_u(H)]$. The DSS strength overestimates this strength by 23%.

Three-Dimensional Analysis. The end effects were determined by means of the program STAB3D assuming a uniform cross section for the embankment within the 300-foot long shear sur-

Table 8.9 SHANSEP-$S_u(\theta)$ Undrained Strength for Portsmouth Clay

El (ft)	$\bar{\sigma}_{vo}$ (psf)	Minimum $\bar{\sigma}_{vm}$ Profile						Average $\bar{\sigma}_{vm}$ Profile						Maximum $\bar{\sigma}_{vm}$ Profile					
		$\bar{\sigma}_{vm}$* (psf)	OCR	$\frac{\tau_{ff}(V)}{\bar{\sigma}_{vc}}$	$\tau_{ff}(V)$ (psf)	$\bar{K}_s$	$\bar{b}/\bar{a}$	$\bar{\sigma}_{vm}$* (psf)	OCR	$\frac{\tau_{ff}(V)}{\bar{\sigma}_{vc}}$	$\tau_{ff}(V)$ (psf)	$\bar{K}_s$	$\bar{b}/\bar{a}$	$\bar{\sigma}_{vm}$* (psf)	OCR	$\frac{\tau_{ff}(V)}{\bar{\sigma}_{vc}}$	$\tau_{ff}(V)$ (psf)	$\bar{K}_s$	$\bar{b}/\bar{a}$
15	275	3000	10.91	1.46	402	0.62	0.83	4500	16.36	2.00	550	0.66	0.80	5700	20.73	2.44	670	0.68	0.79
10	525	1100	2.10	0.48	252	0.54	0.95	1500	2.86	0.60	315	0.56	0.94	1800	3.43	0.68	357	0.57	0.93
5	775	875	1.13	0.30	229	0.48	0.96	1070	1.38	0.34	264	0.51	0.96	1275	1.65	0.40	310	0.52	0.96
0	1000	1100	1.10	0.29	287	0.48	0.95	1300	1.30	0.33	330	0.50	0.96	1500	1.50	0.37	370	0.52	0.96
-5	1225	1345	1.10	0.29	352	0.48	0.95	1545	1.26	0.32	392	0.50	0.96	1730	1.41	0.35	429	0.51	0.96
-10	1525	1625	1.07	0.28	427	0.47	0.95	1825	1.20	0.31	470	0.49	0.96	2025	1.33	0.34	519	0.50	0.96
-14	1750	1850	1.06	0.28	490	0.47	0.95	2050	1.17	0.30	525	0.48	0.96	2250	1.29	0.33	569	0.50	0.96

* $\bar{\sigma}_{vm}$ values are slightly lower than those reported by Ladd (1972)

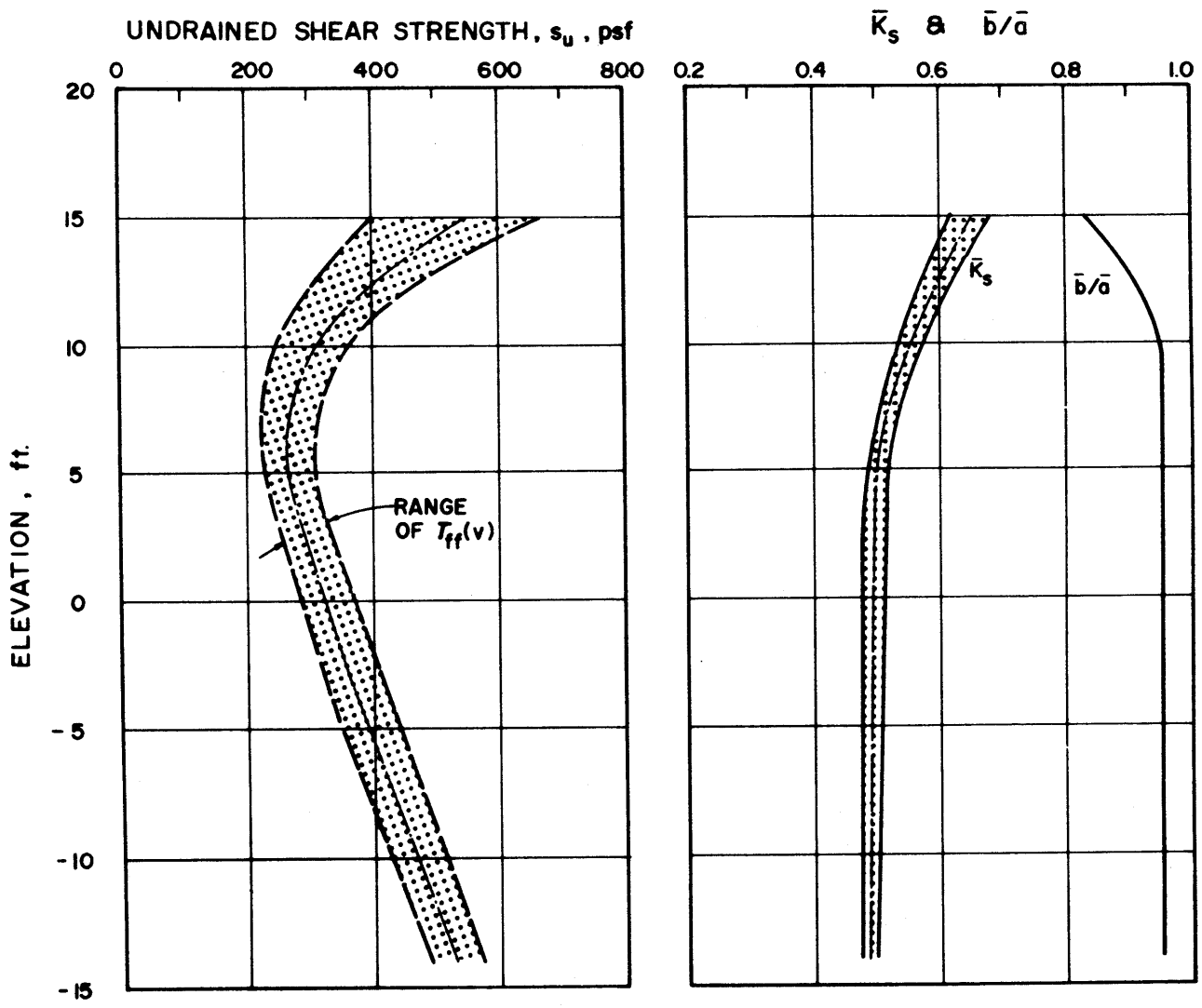


Figure 8.24 SHANSEP-$S_u(\theta)$ Undrained Strength for Portsmouth Clay

Table 8.10 STAB3D Input Parameters Utilizing the SHANSEP-$S_u(\theta)$ Strength Model for Portsmouth Clay, N.H.

Soil No.	γ_t (pcf)	Minimum $\bar{\sigma}_{vm}$			Average $\bar{\sigma}_{vm}$			Maximum $\bar{\sigma}_{vm}$			$f°$[4]	$\bar{\phi}°$	K[5]	Soil Type
		s_u[1] (psf)	$\bar{e}$[2]	$\bar{d}$[3]	s_u (psf)	$\bar{e}$	$\bar{d}$	s_u (psf)	$\bar{e}$	$\bar{d}$				
1	118	1000			1000			1000				0	-	Crust
2	130											40	0.357	Embankment Fill
3	115.5											40	0.357	"
4	110	0	0	0	0	0	0	0	0	0	-	30	0.500	"
5	130											30	0.500	Sand and Silt
6	62.4													Water
7	118	258	0.27	0.21	349	0.240	0.210	419	0.23	0.21				
8	109	182	0.32	0.10	221	0.310	0.100	259	0.29	0.10				
9	109	191	0.35	0.10	223	0.330	0.100	258	0.32	0.10	60	0	-	Portsmouth Clay
10	109	250	0.35	0.10	285	0.330	0.100	341	0.32	0.10				
11	109	326	0.35	0.10	356	0.340	0.100	394	0.33	0.10				

(1) $s_u = \frac{1}{2}[s_u(V) + s_u(H)]$ (2) $\bar{e} = \frac{1-\bar{K}_s}{1+\bar{K}_s}$ (3) $\bar{d} = 1 - \frac{\bar{b}^2}{\bar{a}^2}$

(4) $f°$ = angle between the major principal plane and the failure plane

(5) $K = \frac{\text{out-of-plane stress}}{\text{vertical stress}}$

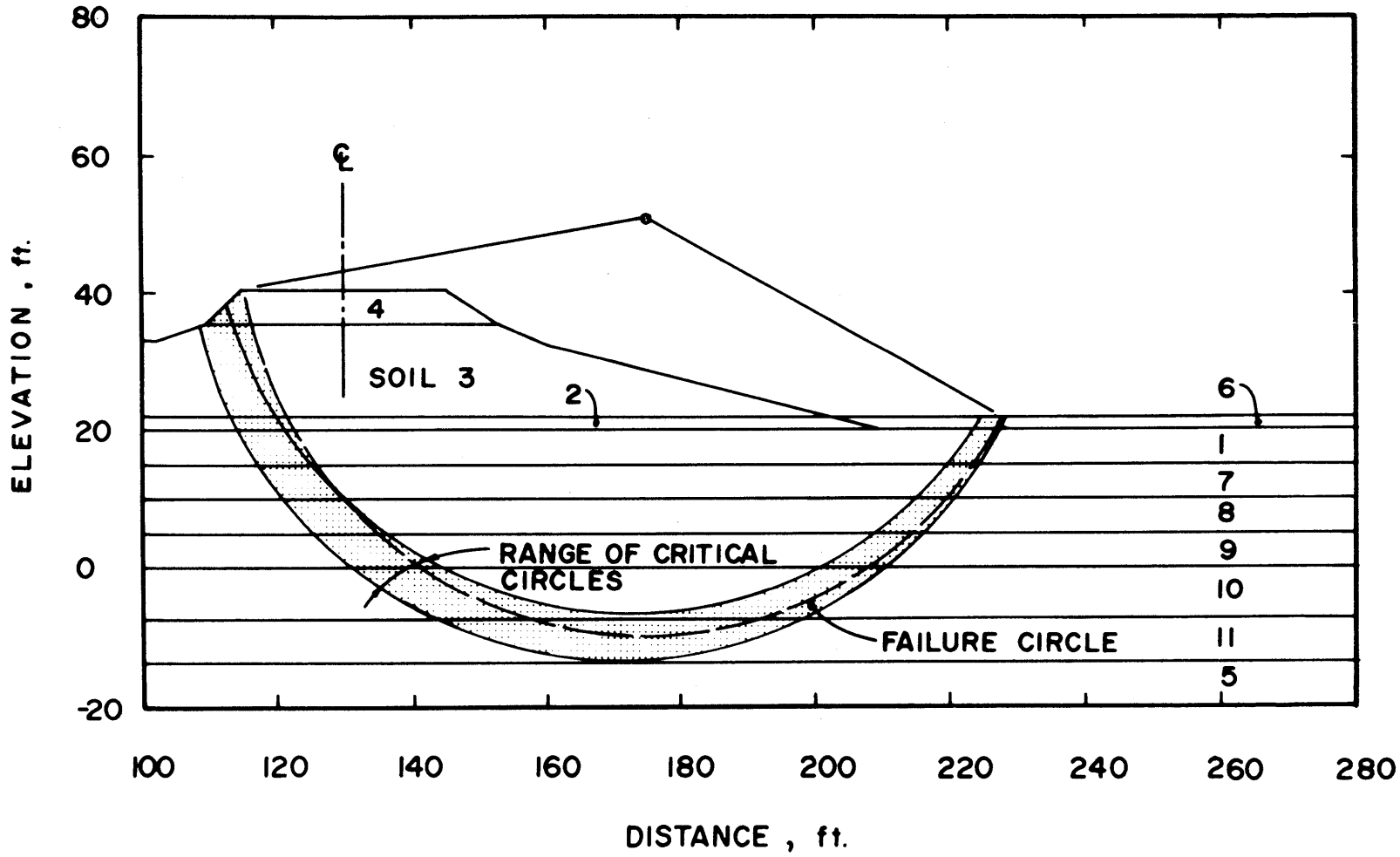


Figure 8.25 Results of Two-Dimensional Stability Analysis Utilizing the SHANSEP-$S_u(\theta)$ Strength Model, Experimental Test Section, N.H.

Table 8.11 Summary of Plane Strain Stability Analysis of the ETS, N.H.

Strength Model	Method of Analysis	Circle			Plane Strain Safety Factor	Remarks
		OX (ft)	OY (ft)	OR (ft)		
FV	Bishop	170.	50.12	64.13	0.91	STAB3D
FV	MIT	176.	54	68	0.91	STAB3D
FV	Bishop	169.5	50.5	64.5	0.90	LEASE II
FV	Bishop	175.	51	60.5	0.92*	STAB3D
FV	MIT	175.	51	60.5	0.93*	STAB3D
SHANSEP-$S_u(\theta)$	MODIFIED BISHOP	170.	58	66.2	0.77	Min. $\bar{\sigma}_{vm}$
		171.	51	65	0.85	Ave. $\bar{\sigma}_{vm}$
		171.5	51	65.5	0.94	Max. $\bar{\sigma}_{vm}$
		175.	51	60.5	0.78*	Min. $\bar{\sigma}_{vm}$
		175.	51	60.5	0.87*	Ave. $\bar{\sigma}_{vm}$
		175.	51	60.5	0.96*	Max. $\bar{\sigma}_{vm}$

* Corresponding to the actual failure circle

face. Figure 8.26 shows a plot of F/F^0 vs. 2L/DR obtained from the stability analyses utilizing the FV and SHANSEP-$S_u(\theta)$ strength models. The results show that:

1. Using the FV strength profile, the plane strain analysis gives DR = 42.4 ft. For a failure length 2L = 300 ft., we get $2L/DR \simeq 7.1$ and Fig. 8.26 shows that this corresponds to $F/F^0 = 1.1$, i.e., based on the actual failure length, end effects increase the FV plane strain factor of safety by 10%. The FV three-dimensional factor of safety F is thus equal to $0.91 \times 1.1 = 1.0$.

2. Using the SHANSEP-$S_u(\theta)$ strength model, the end effects (F/F^0 ratio) are independent of the $\bar{\sigma}_{vm}$ profile used (maximum vs. average vs. minimum).

3. The end effects (F/F^0 ratio) are virtually independent on the strength model used, i.e., FV vs SHANSEP-$S_u(\theta)$.

4. Using the SHANSEP-$S_u(\theta)$ strength model, the plane strain analysis gives DR = 44.1 ft., which is practically the same for the three critical circles corresponding to the three $\bar{\sigma}_{vm}$ profiles under consideration. The ratio 2L/DR is thus equal to 6.8, and Fig. 8.26 shows that the corresponding $F/F^0 \simeq 1.10$. The three-dimensional safety factor, F, for the minimum, average and maximum $\bar{\sigma}_{vm}$ profiles is thus = 0.85, 0.94 and 1.03, respectively. When the actual failure circle is used, the corresponding values of F are 0.86, 0.95 and 1.06, respectively.

5. Ellipsoidal shear surfaces gave lower factors of

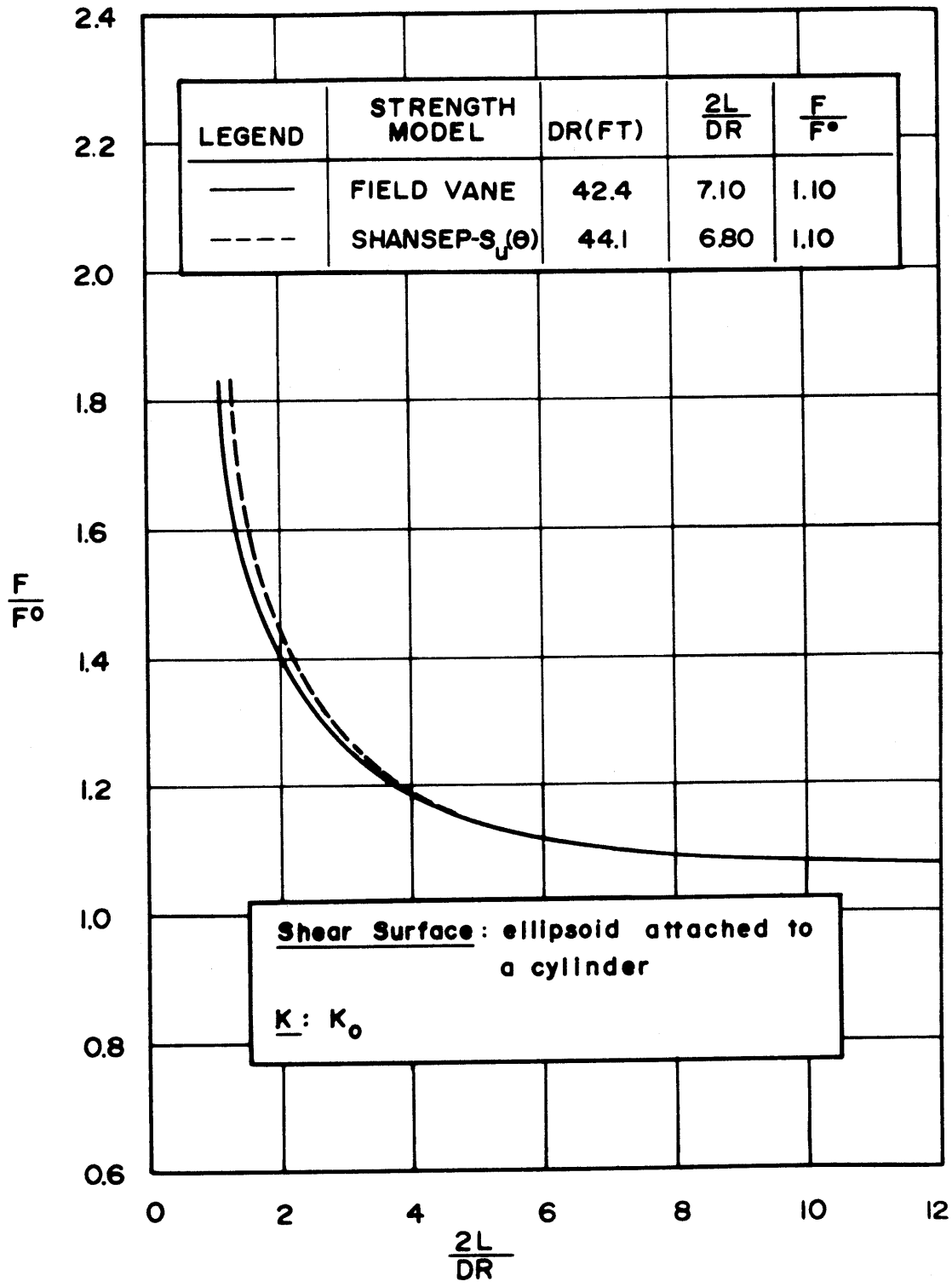


Figure 8.26 Three-Dimensional Effects for the Experimental Test Section, N.H.

safety than conical surfaces, and are, therefore, more likely to represent the actual shear surfaces.

In order to estimate the length of the cylindrical portion of the shear surface, $2\ell_c$, we determined F/F^0 for different values of $2\ell_c$, keeping the total failure length 2L = 300 ft. Results in Fig. 8.27 show that the critical cylinder length $2\ell_c$ = 220 ft. (= 5.20 x 42.4) when the FV strength is used, and $2_{\ell c}$ = 195 ft. (= 4.42 x 44.1) when the SHANSEP-$S_u(\theta)$ strength is used.

8.2.5 Summary and Conclusions for the ETS, Portsmouth, N.H.

This case study involves the failure of a 20-ft. embankment which was rapidly constructed over a 30-ft. deposit of soft, very sensitive marine clay. We performed two- and three-dimensional total stress stability analyses utilizing the field vane, FV, and the SHANSEP-$S_u(\theta)$ strength models. We found the FV plane strain factor of safety F^0 = 0.91, in agreement with stability computations conducted by Ladd (1972).

Due to a significant scatter in the maximum past pressures, the SHANSEP-$S_u(\theta)$ strengths were determined for three different $\overline{\sigma}_{vm}$ profiles representing the minimum, average and maximum estimated values of $\overline{\sigma}_{vm}$ (Fig. 8.20). Stability analyses based on these $\overline{\sigma}_{vm}$ profiles resulted in minimum plane strain factors of safety F^0 = 0.77, 0.85, and 0.94, respectively.

The end effects were obtained by determining the ratio F/F^0 corresponding to the observed failure length (Fig. 8.26).

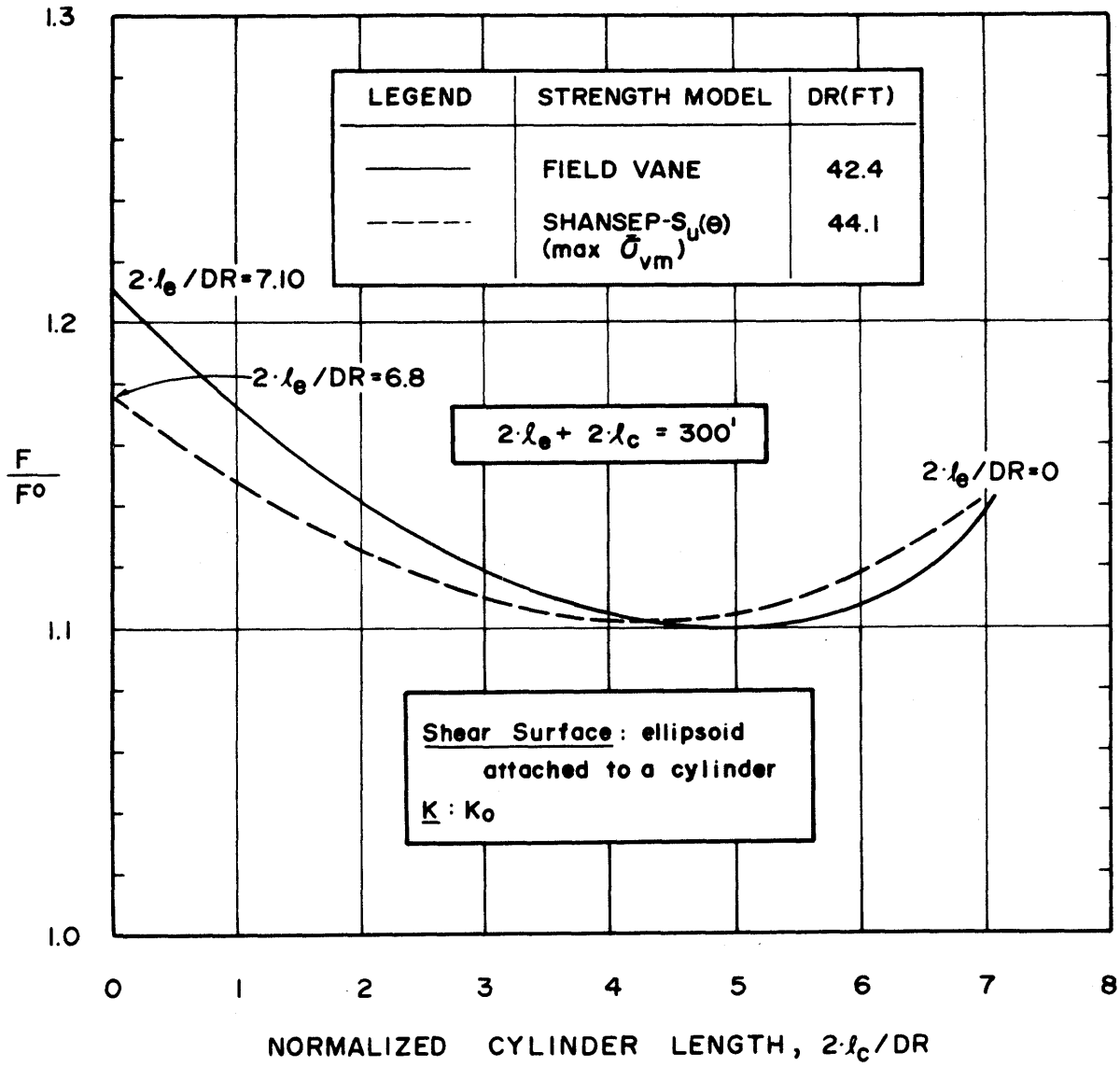


Figure 8.27 Determination of the Cylinder Length for the Experimental Test Section, N.H.

For both strength models considered, we found $F/F^0 \simeq 1.1$, i.e., the three-dimensional effects increase the plane strain factor of safety by 10%. The analysis of this case study also showed that:

1. The field vane strength profile yielded "perfect" results (F = 1.0). This suggests that no correction of the FV strength is required for stability analyses involving this Portsmouth Clay.

2. Three-dimensional factors of safety based on the SHANSEP-$S_u(\theta)$ strength are F = 0.85, 0.94 and 1.03 for the three profiles of $\bar{\sigma}_{vm}$ considered. This suggests that the actual $\bar{\sigma}_{vm}$ distribution is closer to the upper bound shown in Fig. 8.20. Simon (1972) reached the same conclusion by comparing the results of finite element analyses to the observed performance of the embankment. Furthermore, based on field settlement observations during consolidation under highway support fills, Ladd et al. (1972) concluded that the in situ maximum past pressures of the Portsmouth Clay was about equal to the upper limit of the range shown in Fig. 8.20 and possibly higher. This means that the SHANSEP strength model leads to an unconservative estimate (~5%) of the in situ undrained shear strength of the Portsmouth Clay.

3. As in the case of the I-95 embankment, the end effects, expressed by the F/F^0 ratio, are not sensitive to the strength model used in the stability analysis.

4. Strength anisotropy of Portsmouth Clay can be accoun-

ted for in plane strain circular arc stability analyses by using an equivalent average strength equal to 0.43 times the sum of the vertical and horizontal strengths.

8.3 NEW LISKEARD EMBANKMENT FAILURE, NEW LISKEARD, CANADA

8.3.1 Site Description

In 1960, the Ontario Department of Highways (now called the Ministry of Transportation and Communications) proposed construction of a bypass for Highway No. 11 near the town of New Liskeard in northern Ontario, Canada (see Fig. 8.28). The approaches to an Ontario Northland Railway (O.N.R.) crossing necessitated the construction of a 30-ft.-high embankment on a deep deposit of varved clay cemented in glacial Lake Barlow-Ojibway. Figure 8.29 presents a plan view and a profile of the construction site and the soil conditions. Nine feet of stiff silty clay overlie approximately 140 ft. of soft to medium stiff varved clay. A thin deposit of very dense silty sand and gravel is encountered above bedrock. Because of the low strength of the varved clay, a stage construction scheme was adopted for the approach embankments to the railroad overpass. The fill material consisted of gravelly sand with cobbles and boulders and traces of silt and sand, and was placed in two- to three-foot lifts.

8.2.2 Failure

On June 27, 1963, the embankment fill between Sta 804+50 and 807+75 failed without warning (no visible cracks) just after a lift had been completed. The movements were terminated within one minute. Figure 8.30 shows a plan of the failure area and an adjacent test section. The height of the fill

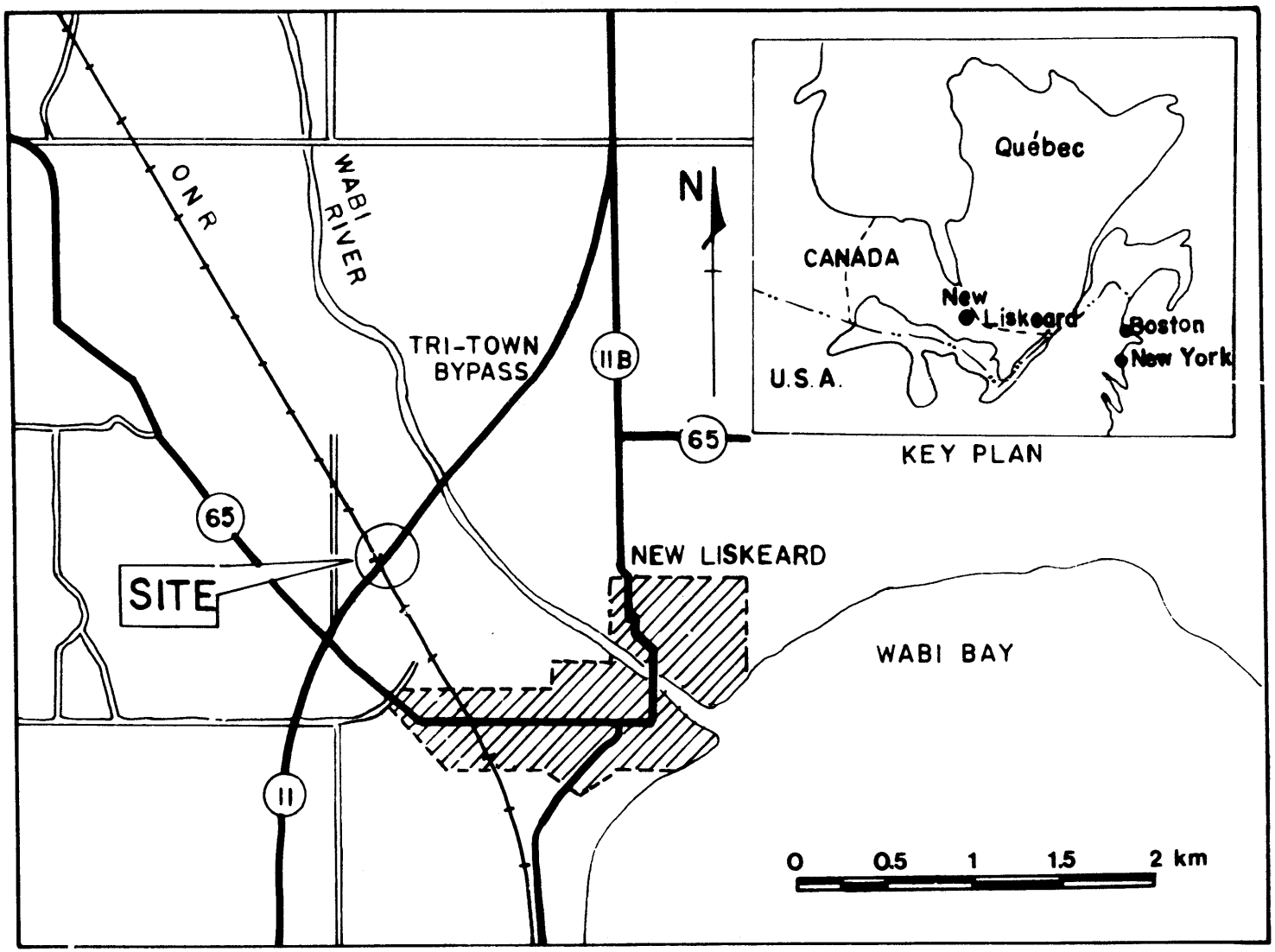
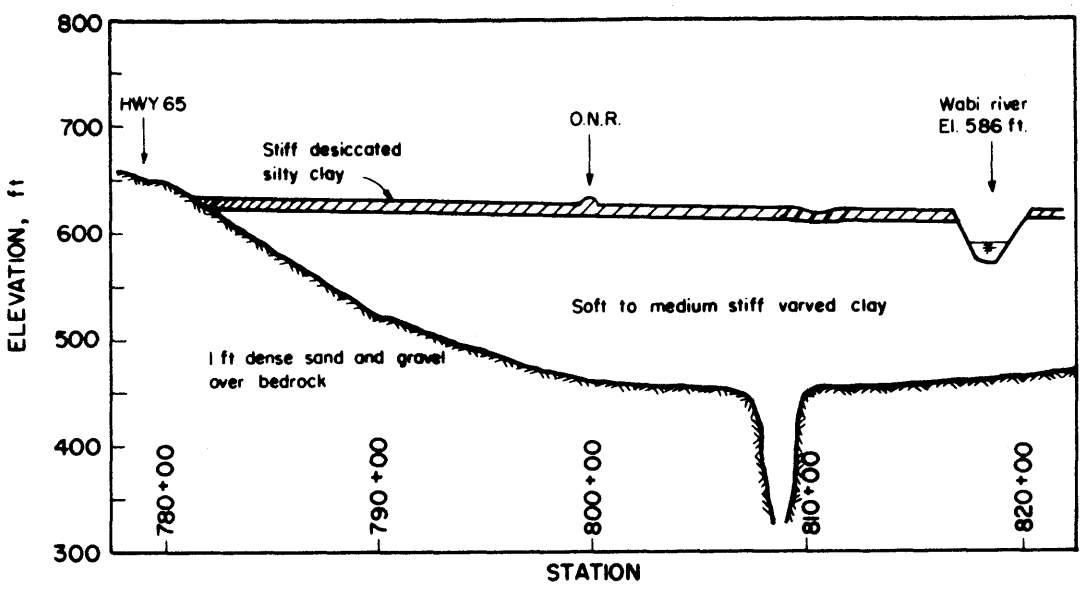
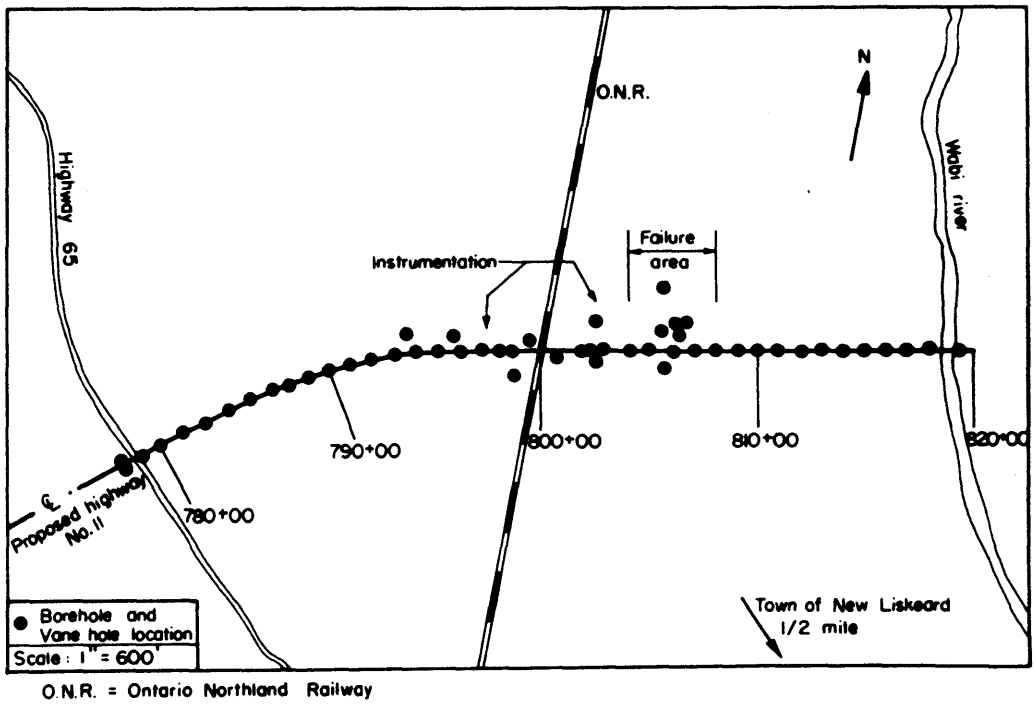


Figure 8.28 Project Location (From Lacasse et al., 1977)



PROFILE ALONG CENTERLINE OF NEW LISKEARD BYPASS



PLAN OF NEW LISKEARD BYPASS SHOWING BORE HOLE LOCATIONS

Figure 8.29 Description of Project and Soil Conditions (From Lacasse et al., 1977)

within the middle of the failure was 19 to 20 ft., gradually decreasing to 12 ft. at Sta 808+00. To the east of Sta 805 +25 the half-width of the embankment crest was 28 ft., whereas at the test section it increased to 45 ft.

The longitudinal extent of the shear surface was approximately 325 ft. and the average height of the fill within the region of failure was 18.5 ft. For a more complete description of the slide and the soil properties, the reader is referred to Lacasse and Ladd (1973) and Lacasse et al. (1977).

8.2.2 Soil Properties

Embankment Fill. The fill for the embankment consisted of a gravelly sand with cobbles, boulders and traces of silt and clay. A unit weight, γ_t = 130 pcf and a friction angle, $\overline{\phi}$ = 40°, were used for this embankment fill (Lacasse et al., 1977).

Foundation Clay. The soil profile consists of about 140 ft. of soft to medium varved clay having a 9-ft. silty clay crust. The undrained shear strength of this crust is estimated at 1000 psf in the upper 6 ft. and 800 psf below. The crust is underlain by varved clay consisting of alternating layers of "silt" and "clay" with approximate thicknesses of 1/2" and 3/8", respectively. The natural water content varies between 24 and 30% in the "silt" layers and between 60 and 80% in the "clay" portion. The corresponding values of the plasticity indices, P.I., are 10 $\pm$ 6% and 47 $\pm$ 13%, respectively (Lacasse and Ladd, 1973). The New Liskeard Varved

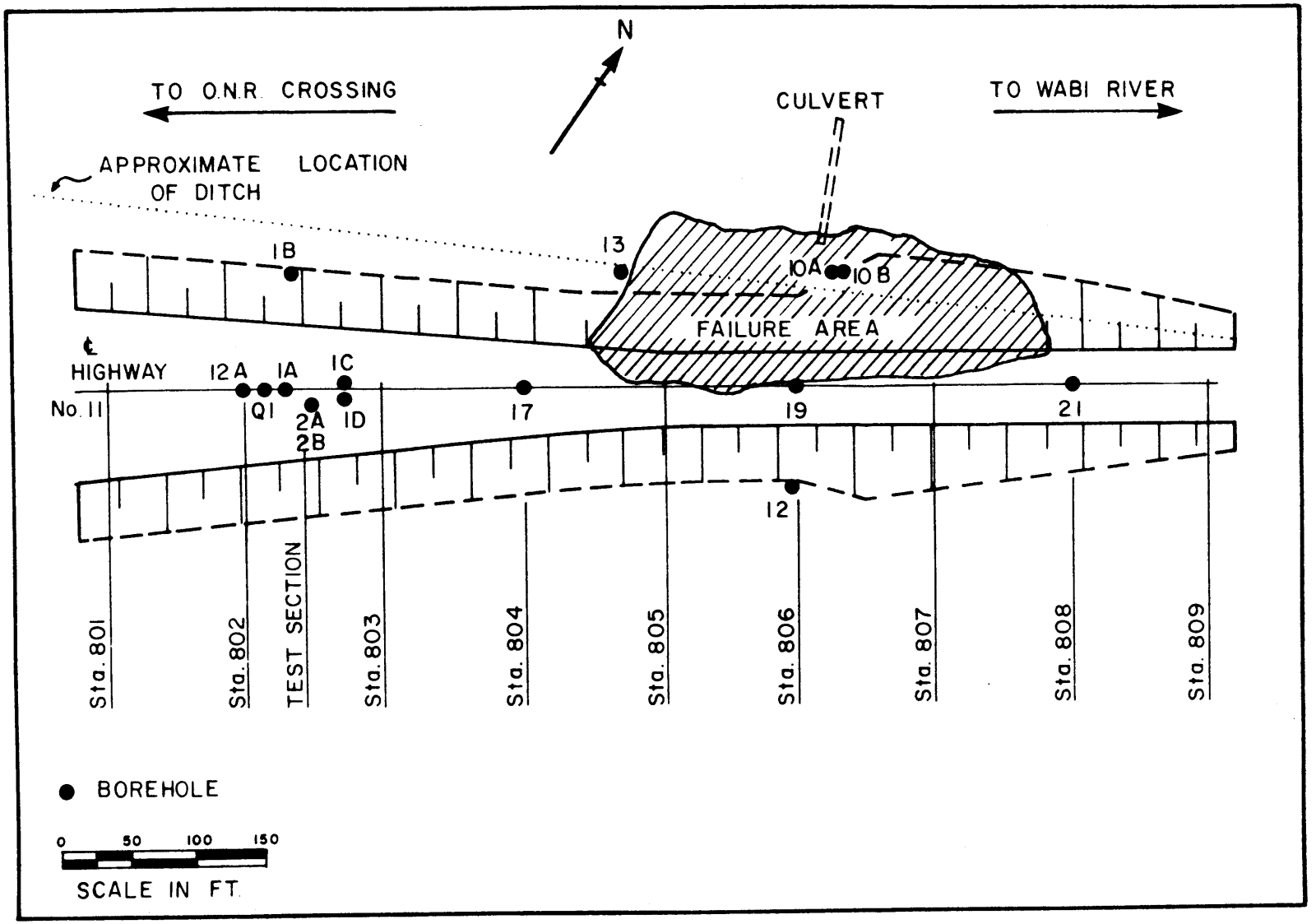


Figure 8.30 Plan of Test Section and Failure Area (From Lacasse et al., 1977)

Clay, NLVC, is believed to have a high degree of natural cementation.

Figure 8.31 presents the stress history of the NLVC deposit. Due to a downward seepage gradient of about 0.23, the initial vertical effective stress, $\bar{\sigma}_{vo}$, exceeds the hydrostatic value. Also shown on Fig. 8.31 is the range of maximum past pressures, $\bar{\sigma}_{vm}$, obtained from all available oedometer tests (see Lacasse and Ladd, 1973, for details).

Locations of field vane tests conducted along the alignment of Highway No. 11 are shown in Fig. 8.29. According to Lacasse et al. (1977), Stations 805+50 and 806+00 (Fig. 8.30) represented the most critical sections along the embankment. Stability analyses based on the same FV strength at both Stations showed that the factor of safety at Sta 805+50 is 2 to 3% lower than that at Sta 806 (Lacasse et al., 1977). Therefore, subsequent stability analyses will be restricted to Sta 805+50. The FV strength profile used in the stability analyses is shown in Fig. 8.32 and represents the average strength between Sta 804+50 and 808+00 (includes Borings 17, 19, 21, 12, 13 in Fig. 8.30). This profile is the FV profile denoted No. 1 by Lacasse et al. (1977).

Laboratory tests to evaluate the undrained shear strength of the NLVC included: unconfined compression (UC) tests, unconsolidated undrained triaxial compression tests (UU) and isotropically consolidated triaxial compression tests with pore pressure measurements ($\overline{CIUC}$). Lacasse and Ladd (1973)

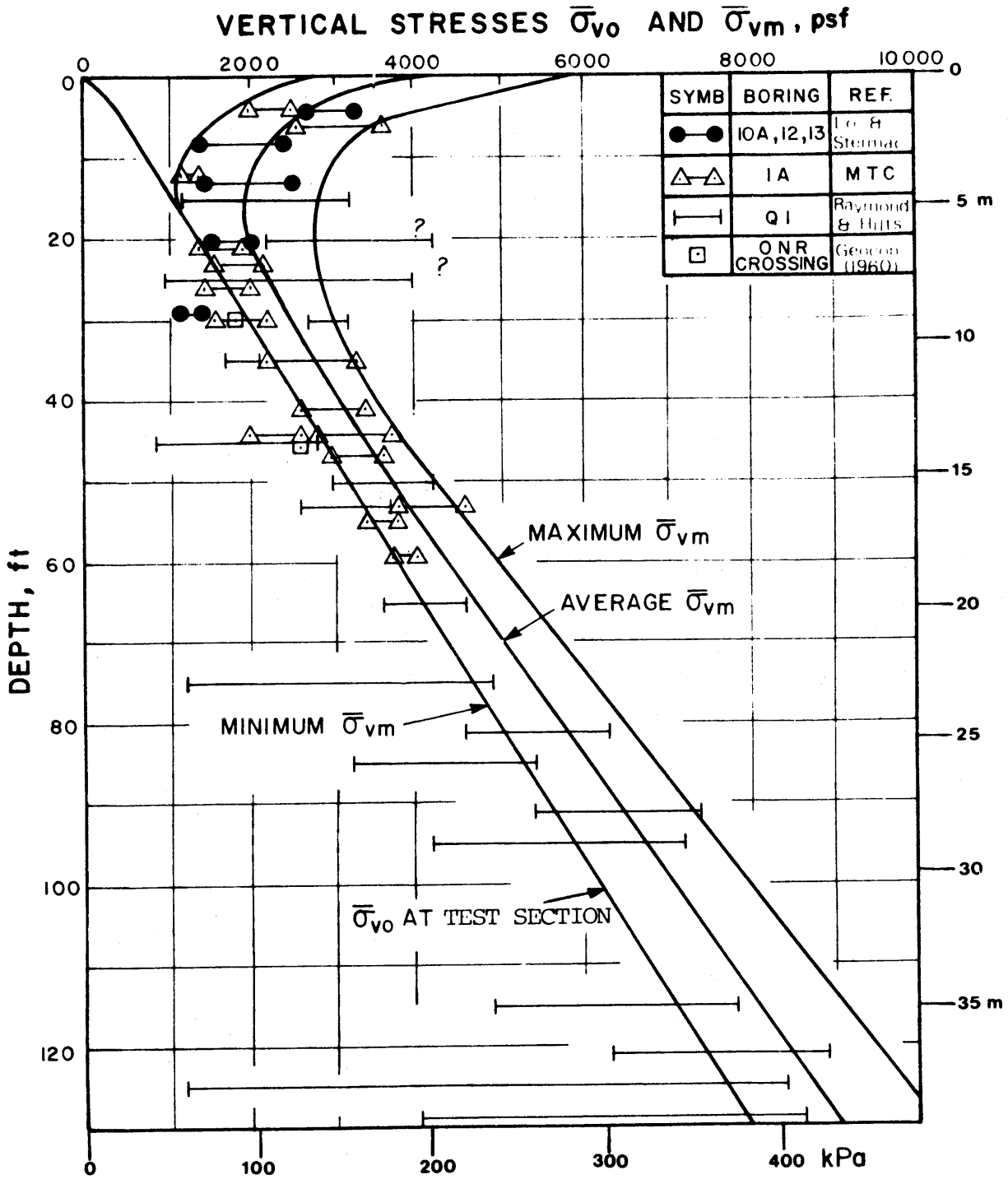


Figure 8.31 Maximum Past Pressures From Oedometer Tests
(From Lacasse et al., 1977)

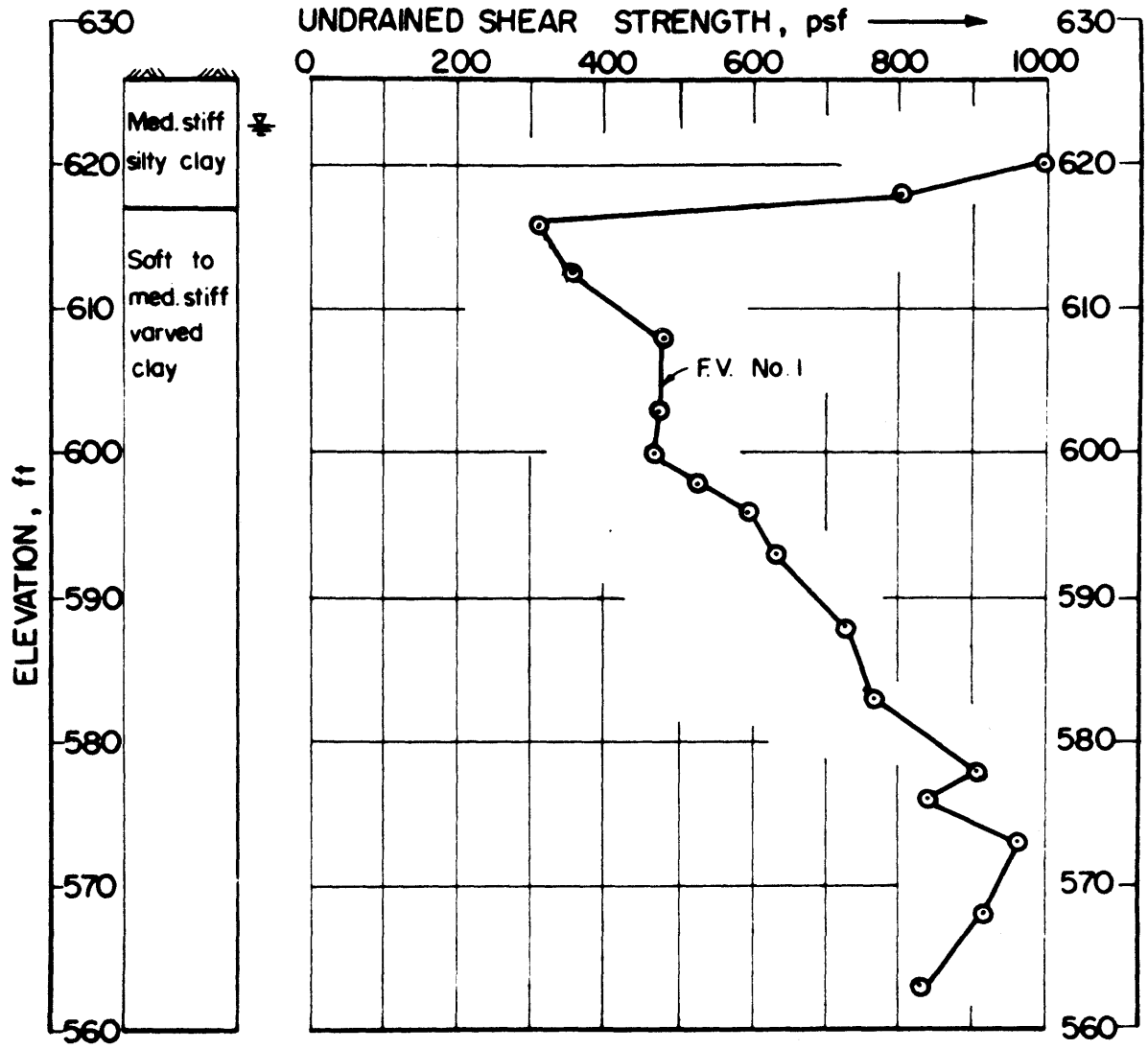


Figure 8.32 Average Field Vane Strength in Failure Area (From Lacasse and Ladd, 1973)

give the results of $\overline{CK_o}$UDSS tests run by Carlsen at the University of Toronto on samples from the Wabi river bank, about 0.3 miles east of the failure area. Based on these tests, the $s_u/\bar{\sigma}_{vc}$ for the normally consolidated "clay" samples is equal to 0.22.

Unfortunately, no data are available on the strength anisotropy for the NLVC. Hence, the SHANSEP-$S_u(\theta)$ strengths were estimated from test data on the noncemented Connecticut Valley Varved Clay, CVVC, reported by Ladd (1975a). This was achieved by assuming that the ratios $s_u(PSC)/s_u(DSS)$, and $s_u(PSE)/s_u(DSS)$ are the same for both types of clays.

The best estimates, after correcting for strain compatibility and strain rate effects, of the shear strength ratios, $s_u/\bar{\sigma}_{vc}$, at OCR = 1 for the CVVC are (see Ladd, 1975a for details):

$$\frac{s_u(PSC)}{\bar{\sigma}_{vc}} = 0.21$$

$$\frac{s_u(PSE)}{\bar{\sigma}_{vc}} = 0.20$$

$$\frac{s_u(DSS)}{\bar{\sigma}_{vc}} = 0.15$$

where s_u is the shear stress on the failure plane at failure, τ_{ff}. The corresponding ratios for the NLVC are thus:

$$\frac{s_u(PSC)}{\bar{\sigma}_{vc}} = 0.28$$

$$\frac{s_u(PSE)}{\bar{\sigma}_{vc}} = 0.26$$

$$\frac{s_u(DSS)}{\bar{\sigma}_{vc}} = 0.20$$

The ratio $s_u(DSS)/\bar{\sigma}_{vc}$ was reduced 10% from that given by Carlsen to account for strain rate effects. The large difference in the $s_u(DSS)/\bar{\sigma}_{vc}$ ratios (0.20 vs. 0.15) obtained for the New Liskeard and Connecticut Valley Varved Clays is believed to be due to the large degree of natural cementation exhibited by the NLVC.

The input parameters describing the extended Davis and Christian ellipsoidal model were obtained as follows:

1 - For OCR = 1,

$$\bar{K}_s = \left[\frac{\tau_{ff}(PSE)}{\bar{\sigma}_{vc}}\right] / \left[\frac{\tau_{ff}(PSC)}{\bar{\sigma}_{vc}}\right] = \frac{0.26}{0.28} = 0.93$$

2 - The direction of $\bar{\sigma}_{1f}$ in a DSS test was estimated as described earlier in the I-95 case study. The friction angle, $\bar{\phi}$, and cohesion intercept, $\bar{c}$, defining the Mohr-Coulomb envelope for NLVC were assumed equal to 23° and 0, respectively. These values fall between the upper and lower envelopes for the normally consolidated NLVC reported by Carlsen (see Lacasse et al., 1977). The Mohr circle drawn tangent to this

envelope and passing through the point representing the state of stress on the horizontal plane at failure shows that $\bar{\sigma}_{1f}$ makes an angle i = 28° with the vertical direction (Fig. 8.33).

3 - The ratios $\bar{b}/\bar{a}$ were obtained by trial and error from Eq. 5.8 such that $s_u/\bar{\sigma}_{vc}$ (at i = 28°) = τ_h(DSS)/$\bar{\sigma}_{vc}$. The corresponding value at OCR = 1 is 0.67. The shape of the elliptical strength plot is given in Fig. 8.34.

8.3.4 Stability Analyses

Total stress stability analyses (ϕ = 0, c = s_u) were performed utilizing the field vane and the SHANSEP-$S_u(\theta)$ strength models.

Two-Dimensional Analysis Based on Field Vane Data. Analyses employing the FV strength were conducted primarily to compare the results of the program STAB3D with those obtained by Lacasse et al. (1977) using the ICES LEASE-I computer program (Bailey and Christian, 1969). The FV strength profile is shown in Fig. 8.32. The input parameters for STAB3D are given in Table 8.12. The value of the safety factor obtained from STAB3D for this case = 1.16, which is about 4% higher than that determined by Lacasse et al. (1977) with almost identical failure circles (Fig. 8.35). The Modified Bishop and MIT methods of analyses yielded exactly the same failure surface and factor of safety.

One explanation for the "small" difference between the results of LEASE-I and STAB3D may be due to the methods used

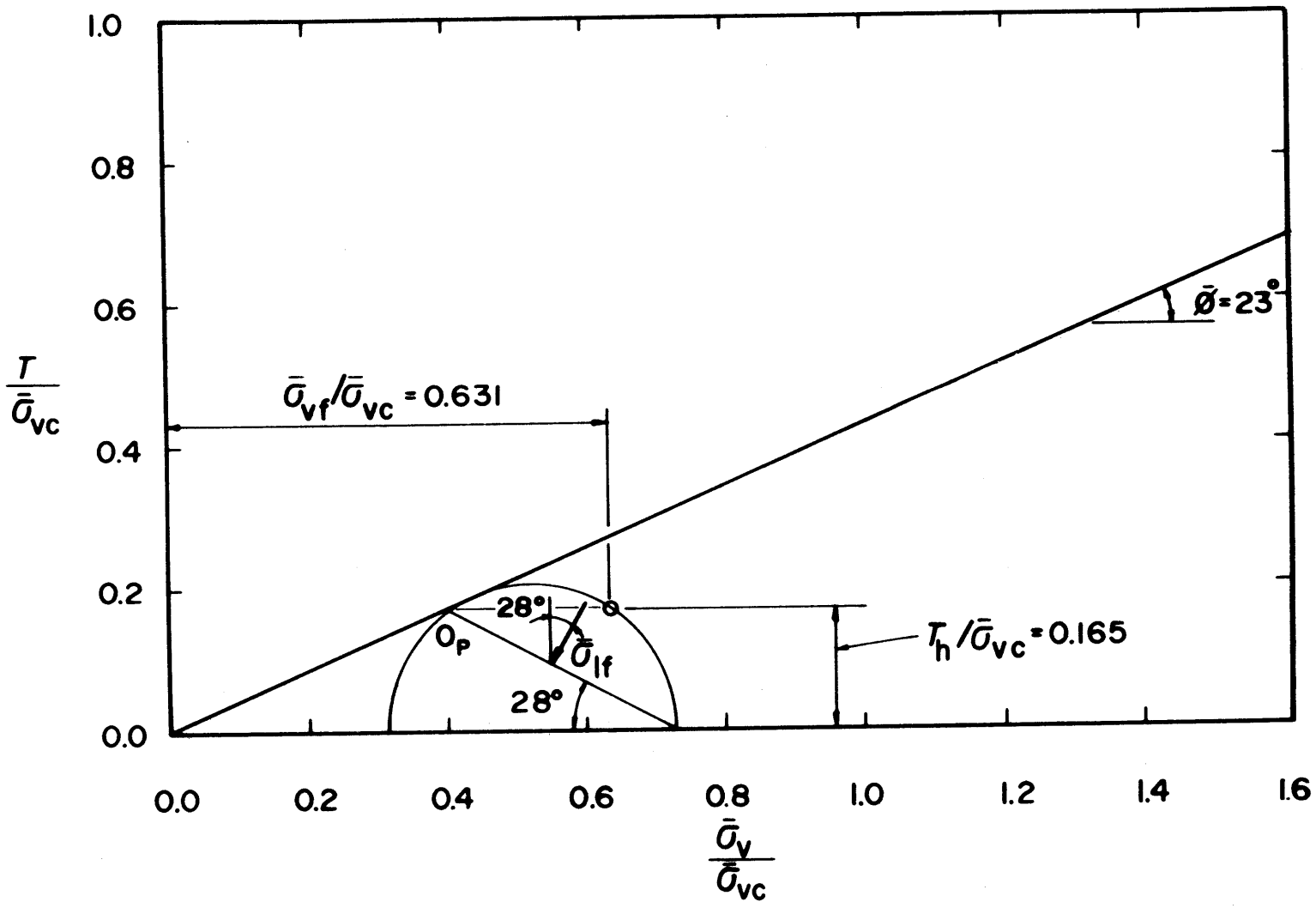


Figure 8.33 Interpretation of the $\overline{CK_oUDSS}$ Test Results for the Normally Consolidated New Liskeard Varved Clay

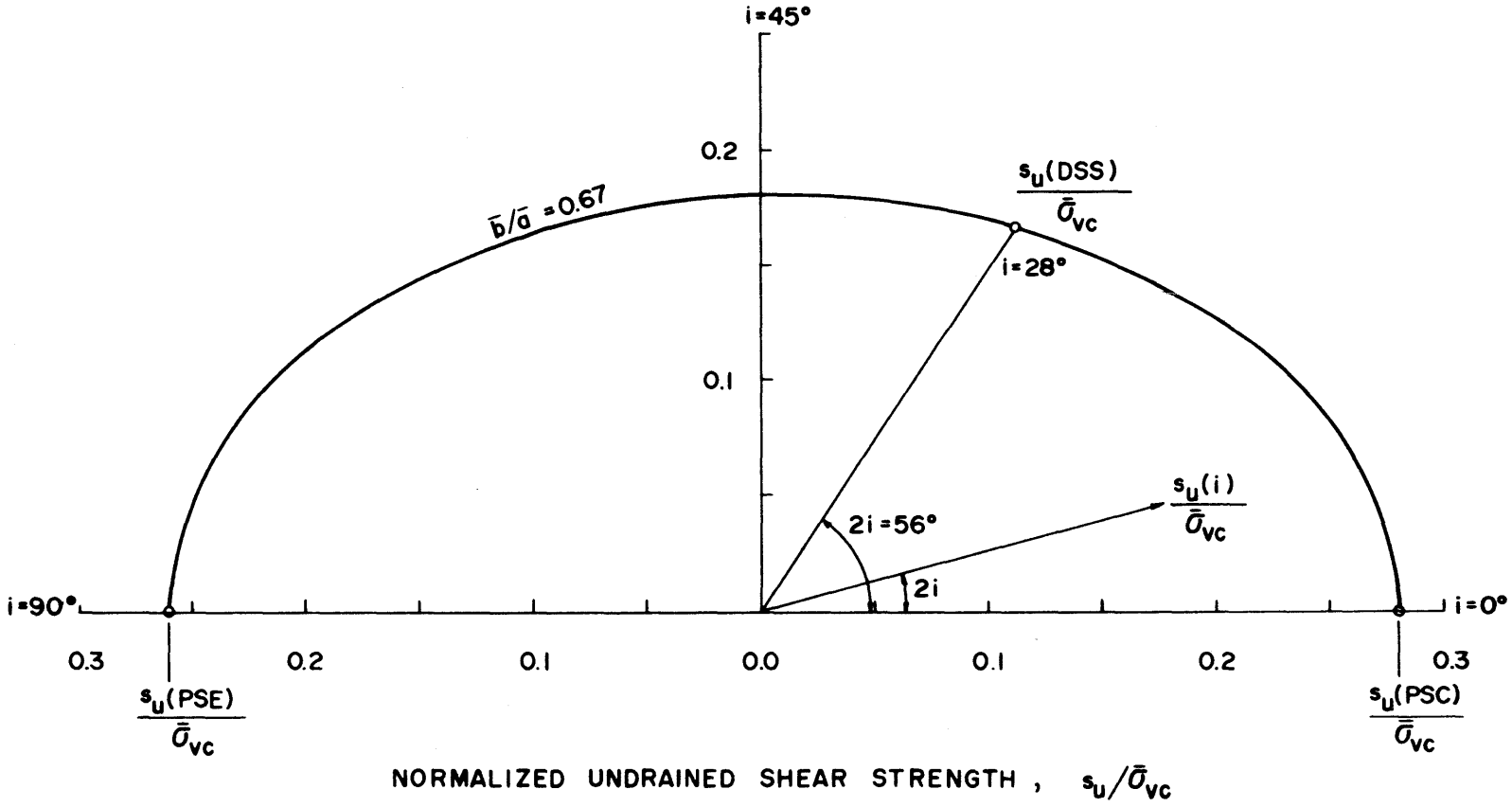


Figure 8.34 Normalized Polar Strength Plot for the Normally Consolidated New Liskeard Varved Clay

Table 8.12 STAB3D Input Parameters Utilizing the Field Vane Strength Model for New Liskeard Varved Clay

Soil No.	γ_t (pcf)	c or s_u (psf)	$\overline{\phi}^0$	K (1)	Soil Type
1	130	0	40	1.00	Embankment Fill
2	115	1000			Crust
3	115	800			Crust
4	105	330			
5	105	390			
6	105	460			
7	105	475	0	—	New Liskeard Varved Clay
8	110	535			
9	110	645			
10	110	725			
11	110	795			
12	110	882			

(1) $K = \dfrac{\text{out-of-plane stress}}{\text{vertical stress}}$

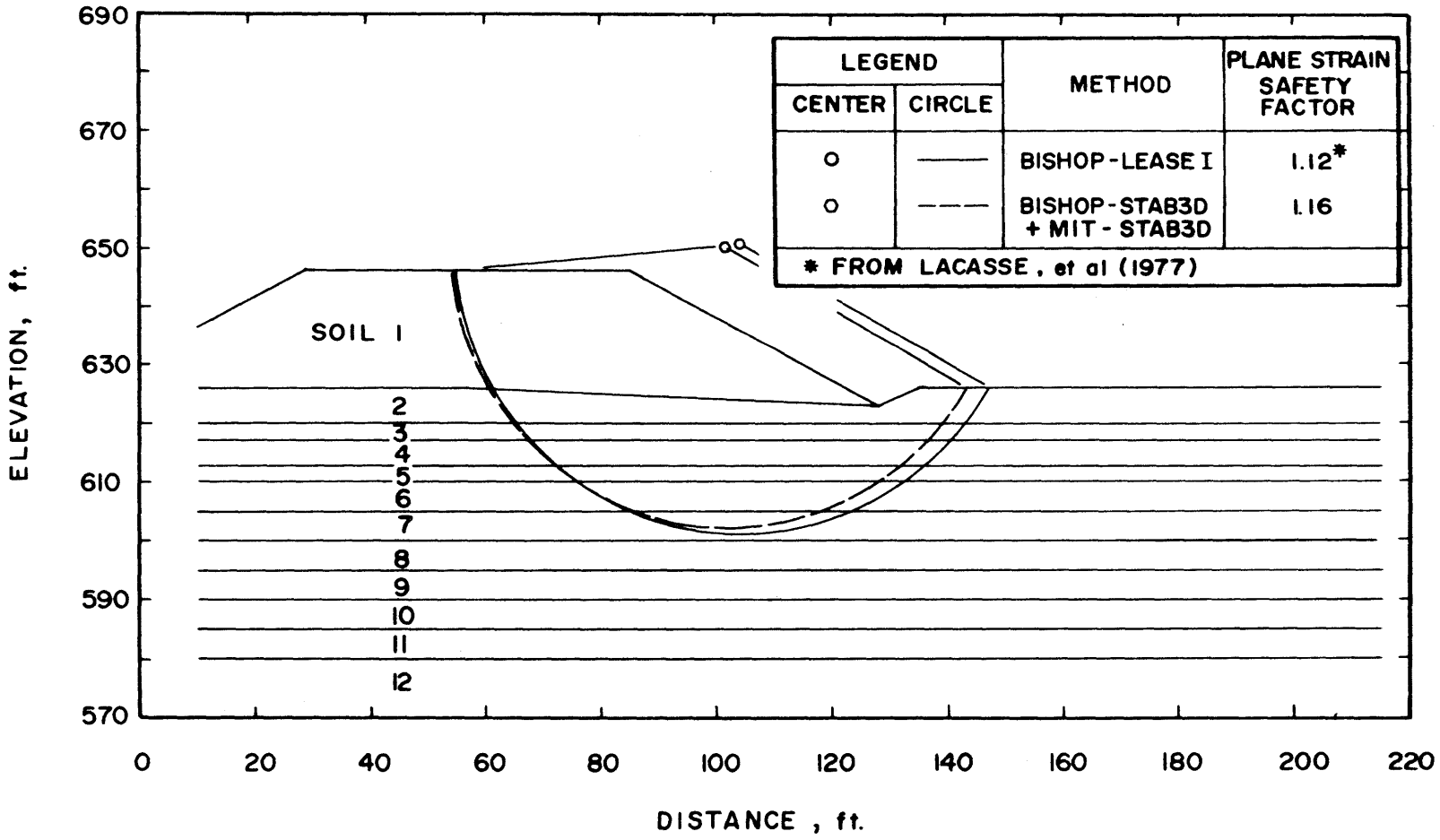


Figure 8.35 Field Vane Total Stress Stability Analysis, New Liskeard Embankment

to divide the slope surface into slices. LEASE-I (and also LEASE-II) divides the width of the slope surface (defined as the difference between the x coordinates of the left and right ends) into a prescribed number of slices. On the other hand, STAB3D divides the sliding mass, which is bounded by the slope surface and the failure arc, into a prescribed number of slices. This difference between the two programs causes LEASE to consider more than one soil at the base of a slice, and, therefore, may introduce errors in selecting the strength parameters for this slice, especially if more than two soils are encountered (Bailey and Christian, 1969). STAB3D avoids this difficulty by dealing with one soil at the base of each slice.

Two-Dimensional Analysis Based on SHANSEP-$S_u(\theta)$ Data. Based on both laboratory and field strength tests, Ladd and Lacasse (1973) concluded that the soil at the failure area is slightly weaker than that at the adjacent test section (Sta 802+50). This may imply a lower than average maximum past pressure to exist within the failure area.* Hence, the SHANSEP-$S_u(\theta)$ strength profile was obtained utilizing the minimum $\bar{\sigma}_{vm}$ profile in Fig. 8.31. The corresponding anisotropic undrained strength parameters are given in Table 8.13 and plotted in Fig. 8.36. The input parameters for STAB3D are given in Table 8.14.

---

*For normally consolidated and slightly overconsolidated clay, $s_u/\bar{\sigma}_{vm}$ = constant.

Table 8.13 SHANSEP-$S_u(\theta)$ Undrained Strength for New Liskeard Varved Clay Based on the Minimum $\bar{\sigma}_{vm}$ Profile

El. (ft)	$\bar{\sigma}_{vo}$ (psf)	$\bar{\sigma}_{vm}$ (psf)	OCR	$\tau_{ff}/\bar{\sigma}_{vc}$			τ_{ff} (psf)			$\bar{K}_s$	$\bar{b}/\bar{a}$
				DSS	PSC	PSE	DSS	PSC	PSE		
615	820	1160	1.41	0.26	0.37	0.34	213	303	279		
612	1000	1060	1.06	0.205	0.29	0.27	205	290	270		
610	1140	1140	1				228	319	296		
605	1420	1420	1				284	398	369		
600	1760	1760	1				352	493	458		
595	2020	2020	1				404	566	525		
590	2320	2320	1	0.20	0.28	0.26	464	650	603	0.93	0.67
585	2620	2620	1				524	734	681		
580	2920	2920	1				584	818	759		
570	3540	3540	1				708	991	920		
550	4760	4760	1				952	1333	1238		

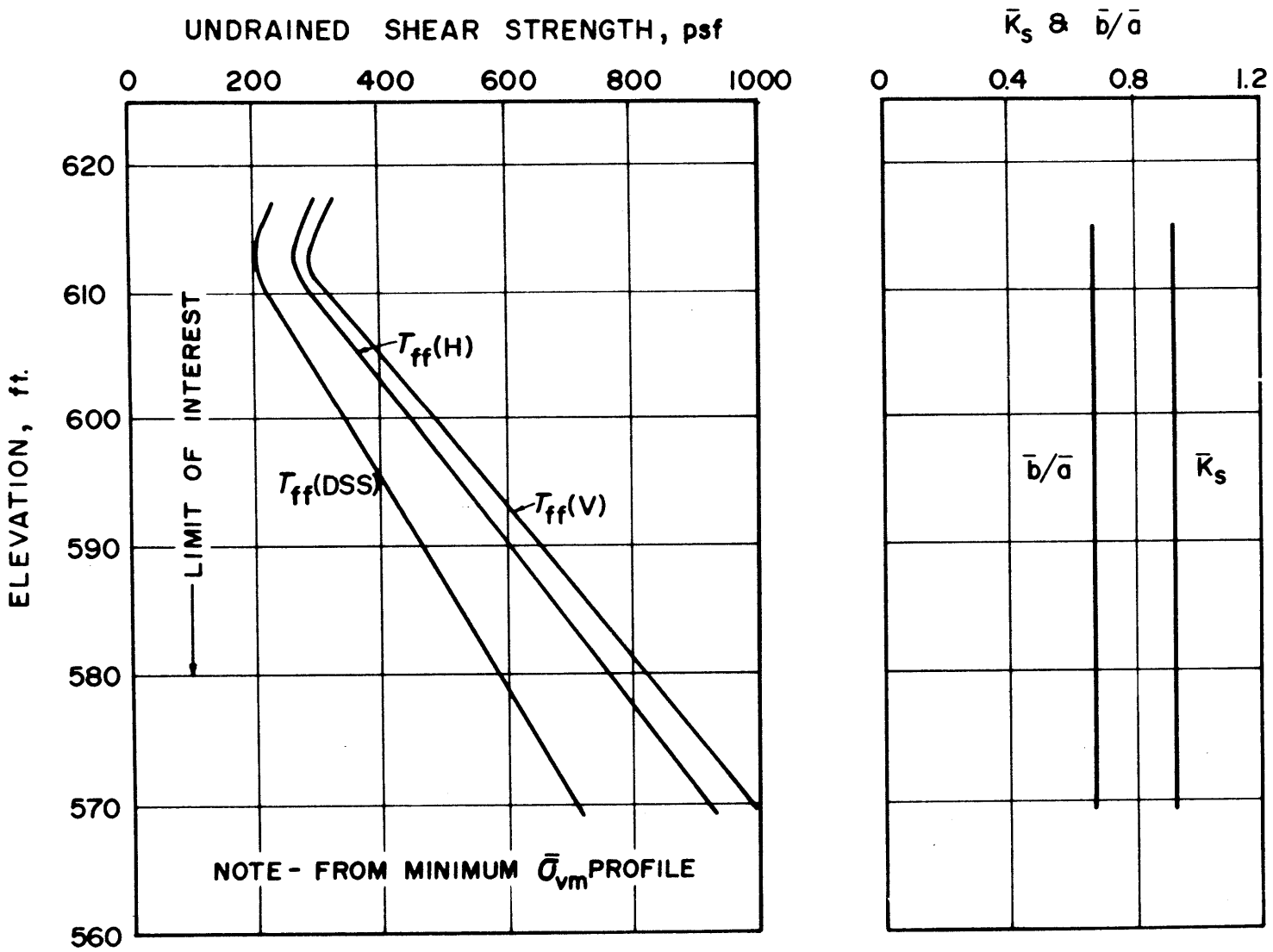


Figure 8.36 SHANSEP-$S_u(\theta)$ Undrained Shear Strength for the New Liskeard Varved Clay

Table 8.14 STAB3D Input Parameters Utilizing the SHANSEP-$S_u(\theta)$ Strength Model for New Liskeard Varved Clay

Soil No.	γ_t (pcf)	s_u (psf) (1)	$\bar{e}$ (2)	$\bar{d}$ (3)	f° (4)	$\bar{\phi}$°	K (5)	Soil Type
1	130	0	0	0	—	40	1	Embankment Fill
2	115	1000	0	0	—			Crust
3	115	800	0	0	—			Crust
4	105	299						
5	105	293						
6	105	346						
7	105	430						
8	110	511	0.036	0.551	60	0	—	New Liskeard Varved Clay
9	110	587						
10	110	668						
11	110	749						
12	110	873						

(1) $s_u = 0.5[s_u(V) + s_u(H)]$

(2) $\bar{e} = \dfrac{1 - \bar{K}_s}{1 + \bar{K}_s}$

(3) $\bar{d} = 1 - \dfrac{\bar{b}^2}{\bar{a}^2}$

(4) f = angle between major principal plane and failure plane

(5) $K = \dfrac{\text{out-of-plane stress}}{\text{vertical stress}}$

Based on the SHANSEP-$S_u(\theta)$ strength, the minimum factor of safety, $F^0 = 0.94$, and the corresponding critical circle is shown in Fig. 8.37. The distribution of the shear strength along the critical shear surface is also shown in Fig. 8.37. The average shear strength along the circular arc (between points A and B in Fig. 8.37) within the NLVC for the DSS, $0.5[s_u(H) + s_u(v)]$ and $s_u(\theta)$ strengths is = 271, 368, and 292 psf, respectively. This shows that, for this case, the DSS strength will underestimate the average anisotropic strength by about 7%. Strength anisotropy of the NLVC can be accounted for in plane strain circular arc stability analysis by using an equivalent average strength equal to $0.40\ [s_u(V) + S_u(H)]$. However, it should be noted that for varved clays, the strength is at or near minimum for horizontal failures. Hence, the use of $[s_u(V) + s_u(H)]$ to account for strength anisotropy in noncircular (wedge-type) shear surfaces where large portions of the failure surface are horizontal, may be unsafe.

Three-Dimensional Analysis. The end effects were evaluated by means of the program STAB3D assuming the embankment cross section at Sta 805+50 to be uniform within the failure zone (Sta 804+50 to Sta 807+75). The analyses were performed employing the FV and the SHANSEP-$S_u(\theta)$ strengths together with the three-dimensional shear surfaces described in Chapter 2. The results in Fig. 8.38 show that:

1. Using the FV strength profile, plane strain analyses give DR = 34.8 ft. Hence, for a failure length, 2L = 325 ft.,

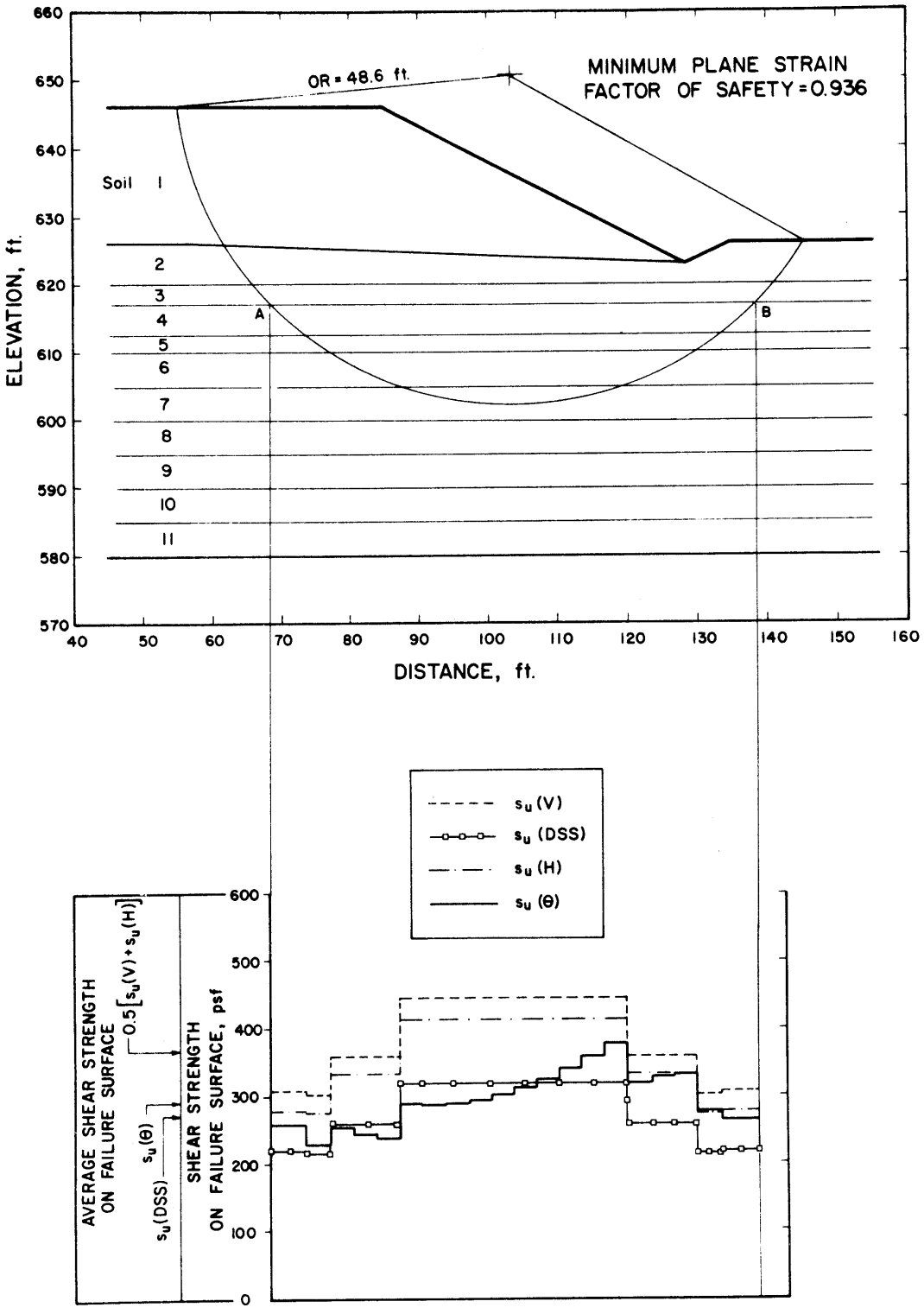


Figure 8.37 Results of Two-Dimensional Stability Analysis Utilizing the SHANSEP-$S_u(\theta)$ Strength Model

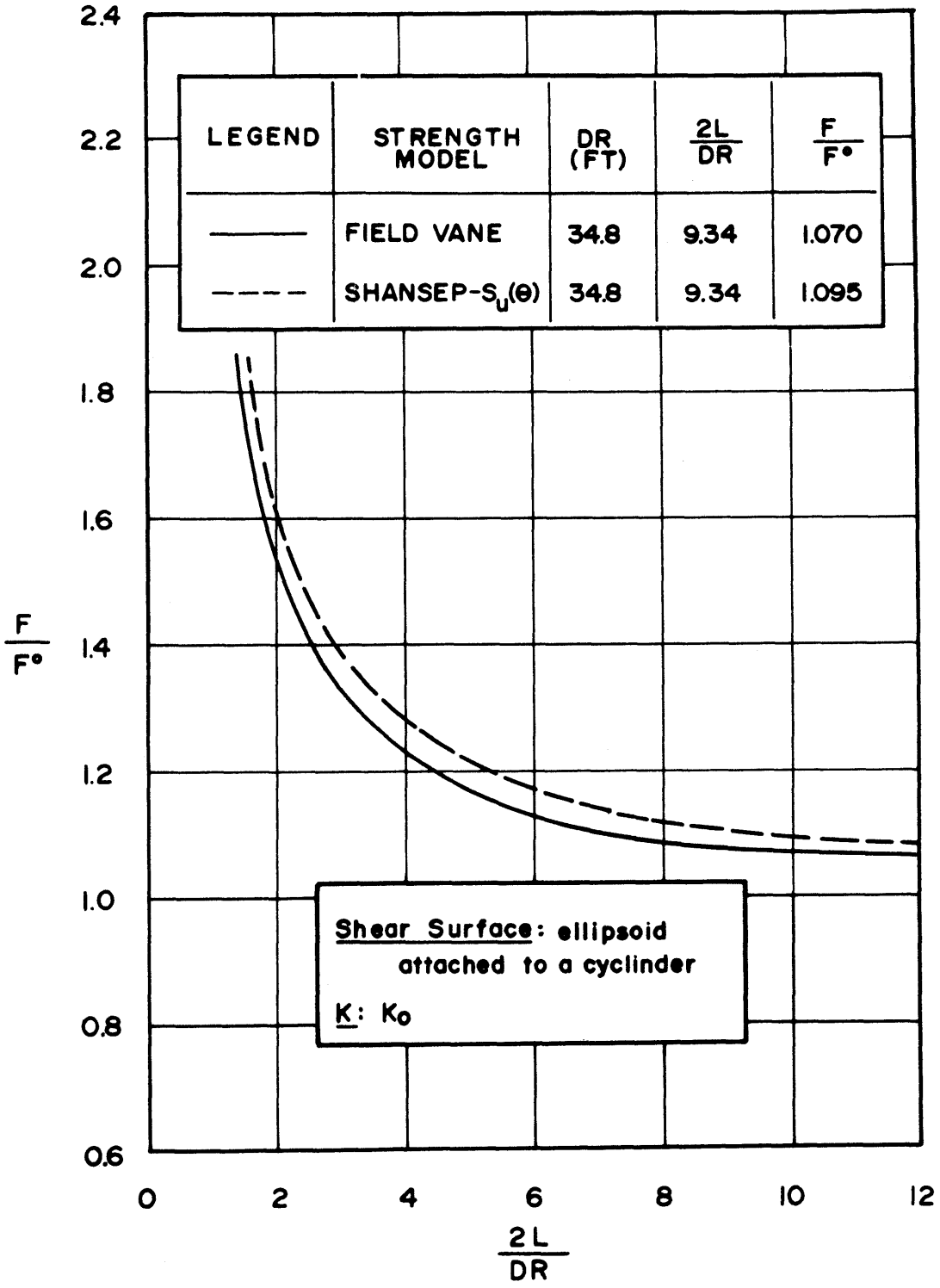


Figure 8.38 Three-Dimensional Effects for the New Liskeard Embankment

2L/DR = 9.34. The corresponding F/F^0 from Fig. 8.38 = 1.07, i.e., based on the actual failure length, end effects increase the FV plane strain safety factor by 7%. The FV three-dimensional factor of safety is equal to 1.16 x 1.07 = 1.24.

2. Similarly, using the SHANSEP-$S_u(\theta)$ strength model, the plane strain analysis yields DR = 34.8 ft. Hence, for a 2L/DR value of 9.34, one finds from Fig. 8.38 that the corresponding F/F^0 = 1.095, and the three-dimensional SHANSEP-$S_u(\theta)$ factor of safety = 1.03.

3. Ellipsoidal shear surfaces gave consistently lower values of the factor of safety than conical surfaces. Hence, they are more likely to simulate the geometry of the actual failure surface.

4. The end effects (F/F^0 ratio) are virtually independent of the strength model used, i.e., FV vs. SHANSEP-$S_u(\theta)$.

8.3.5 Summary and Conclusions for the New Liskeard Case Study

Total stress stability analyses were performed on a 20-foot-high embankment which was rapidly constructed to failure on a deep deposit of saturated varved clay at New Liskeard, Canada. Two strength models were considered: the first being the measured field vane strength, and the second utilizing the SHANSEP approach combined with the extended Davis and Christian elliptical relationship (see Chapter 5). Two- and three-dimensional analyses were carried out using the computer program STAB3D.

The results of the two-dimensional analyses yielded FV and SHANSEP-$S_u(\theta)$ factors of safety = 1.16 and 0.94, respectively. The SHANSEP-$S_u(\theta)$ strengths were based on the minimum estimated $\bar{\sigma}_{vm}$ profile in Fig. 8.31. Fair agreement was obtained between the results of the two programs STAB3D and ICES LEASE-I, and exact agreement between the Modified Bishop and MIT methods of analysis.

The end effects (F/F^0) were found to increase the FV and SHANSEP-$S_u(\theta)$ plane strain factors of safety by 7 and 9.5% respectively. Based on the results of these analyses, we conclude that:

1. The SHANSEP-$S_u(\theta)$ strength model, based on the minimum $\bar{\sigma}_{vm}$ profile (Fig. 8.31), which accounts for strength anisotropy and strain compatibility along the circular shear surface, yielded a three-dimensional factor of safety, F, equal to 1.03 at failure. The strengths based on an average $\bar{\sigma}_{vm}$ profile overpredicts the factor of safety at failure (Lacasse et al., 1977).

2. Based on the FV strength, the factor of safety at failure, F = 1.24. Therefore, a FV correction factor = 0.81 should be used with the field vane strengths in performing circular arc stability analyses on the New Liskeard Varved Clay.

3. End effects expressed by the ratio F/F^0 are not significantly affected by the strength model used (Fig. 8.38).

4. The effect of strength anisotropy in circular arc stability analyses involving the New Liskeard Varved Clay can

be approximately taken into consideration by using an equivalent strength of 0.40 [s_u(V) + s_u(H)]. The DSS strength will underestimate the average anisotropic strength by 7%

8.4 FORE RIVER TEST SECTION, PORTLAND, MAINE

8.4.1 Site Description

The extension of Interstate I-295 into Portland and South Portland, Maine, required the construction of large embankments on soft clay deposits located in the Fore River area. To assist in the design of the highway, a test section was constructed to evaluate different methods of vertical sand drain installation. A plan of the Fore River Test, FRT, section is shown in Fig. 8.39. The embankment, which consisted of granular fill, was first to be raised to El. 10 over an area 240 ft. square prior to installation of the sand drains in the inner 120-ft.-square area of the embankment. Fill was then to be placed to El. 20 over the central area.

The original ground surface elevation averaged -3 ft. (MSL). The soft organic clay extends to El. -25 $\pm$ 8 ft. and overlies a silty sand and gravel layer which has an artesian pressure of five feet (Fig. 8.40). The project is described in detail by Ladd et al. (1969)*.

8.4.2 The Failure

During the first stage filling to El. 10, an unexpected failure occurred along the northern edge of the test section in the area indicated by the cross-hatched portion of Fig.

---

*Detailed studies of the slope failure were performed by Haley and Aldrich, Inc., consultants to the Maine State Highway Commission, the authority responsible for the project.

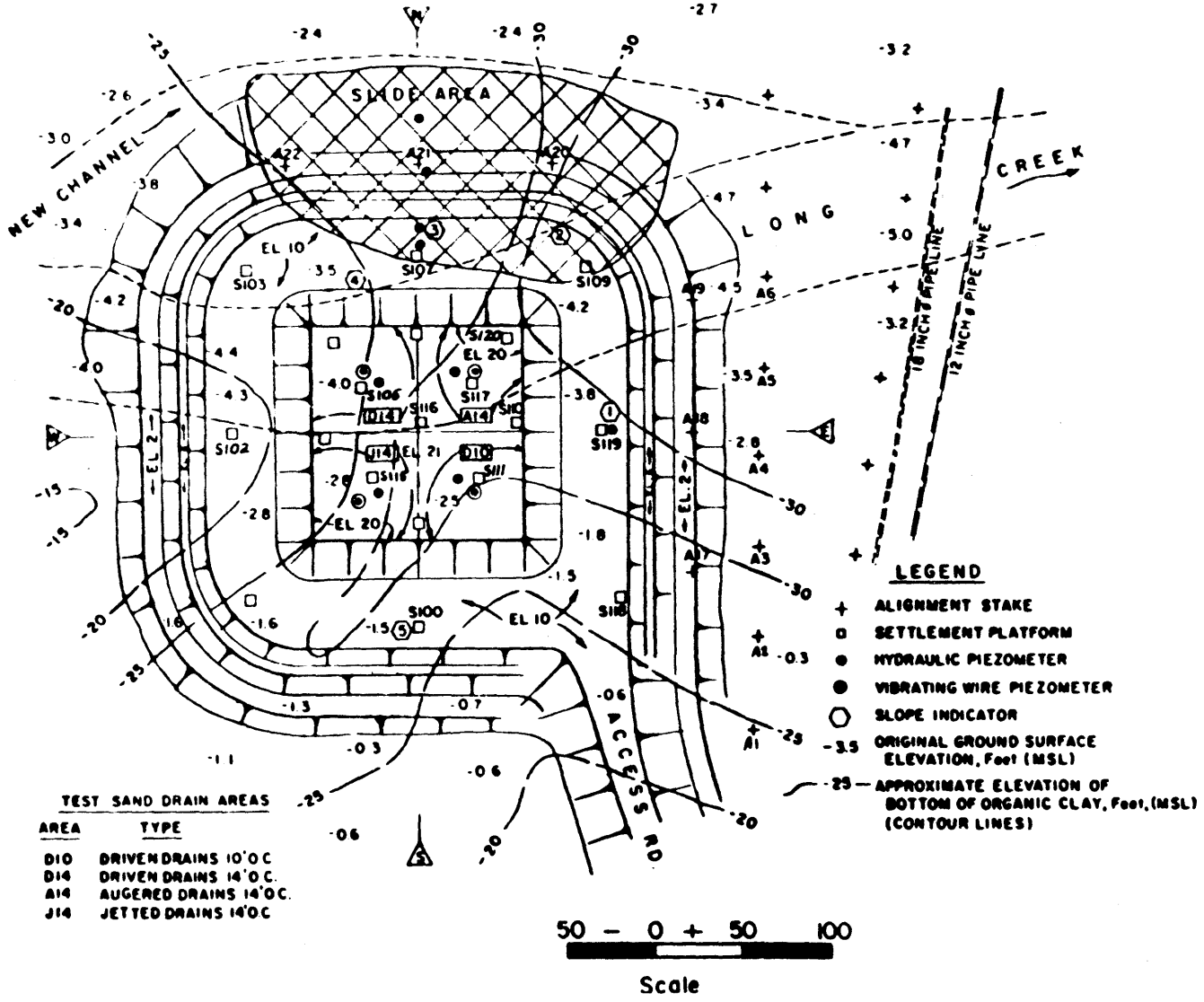


Figure 8.39 Plan View of Fore River Test Section (From Ladd et al., 1969)

8.39. Settlement platforms existing within the slide area (S107 and S109 in Fig. 8.39) dropped 1.5 to 3.5 ft. and continued to settle for two weeks after the failure had taken place (Ladd et al., 1969). The longitudinal extent of the shear surface was approximately 240 ft.

8.4.3 Soil Properties

Embankment Fill. The granular embankment fill consisted of a clean gravelly sand with an estimated total unit weight γ_t = 125 pcf and a friction angle $\overline{\phi}$ = 30° below the ground water table (El. 4). The fill above the water table has $\overline{\phi}$ = 30° and γ_t = 110 pcf in the upper five and half feet and γ_t = 130 pcf below.

Foundation Clay. The Maine Organic Clay is a soft organic clay with varying amounts of broken shells, organic matter and sand lenses and pockets. The natural water content, w_n, varied from 30 to 80%, and the plasticity index, P.I.= 32 $\pm$ 8%,

Due to the existence of 5 feet of artesian pressure in the sand layer underlying the clay stratum, the initial vertical effective stress is lower than that based on hydrostatic conditions (Fig. 8.40). Several incremental oedometer tests were conducted to estimate the distribution of the maximum past pressures. Results of Casagrande construction method based on data at the end of primary consolidation are shown in Fig. 8.40.

The results of field vane, FV, tests from nine borings at the FRT site showed considerable scatter (Fig. 8.40). The

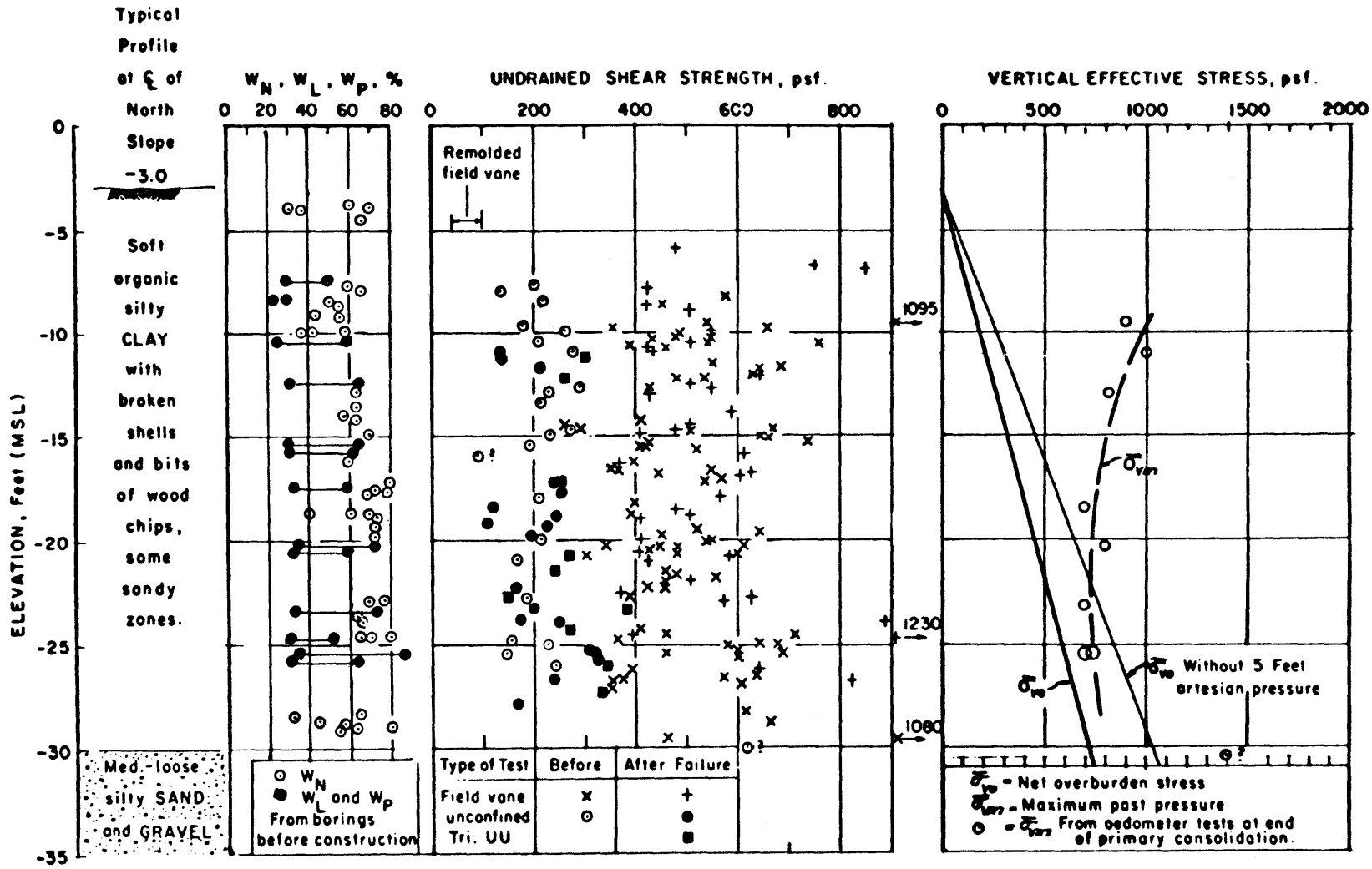


Figure 8.40 Soil Properties of the Maine Organic Clay (from Ladd et al., 1969)

rate of rotation on these FV tests was 40 times faster than that recommended by the ASTM specification (Ladd et al., 1969). The FV strength of the clay = 525 $\pm$ 150 psf over the entire thickness of the layer.

Several K_o consolidated undrained tests under direct simple shear and triaxial compression stress systems revealed that the undrained shear strength behavior of the clay is essentially isotropic (Ladd et al., 1969 and Simon, 1972). Hence, stability analyses were performed using both DSS and FV strength data. The shear strength ratios $s_u/\bar{\sigma}_{vc}$, for different OCR's were reported by Ladd and Edgers (1972) and are given in Fig. 8.41. Table 8.15 shows that the DSS shear strength is quite uniform over the entire clay layer with an average of 210 psf.

8.4.4 Stability Analyses

Two-Dimensional Analysis. Total stress stability analyses (ϕ = 0 and c = s_u) were performed utilizing the field vane and SHANSEP-DSS strengths. The STAB3D input parameters for both strength models are given in Table 8.16. The results of plane strain analyses are shown in Fig. 8.42. The critical circle is the same for both strength profiles and independent of the method of analysis. The factor of safety, F^0, obtained by the MIT method, is 1% less than that obtained by the Modified Bishop method.

Three-Dimensional Analysis. The end effects were evaluated by means of the program STAB3D assuming a uniform embank-

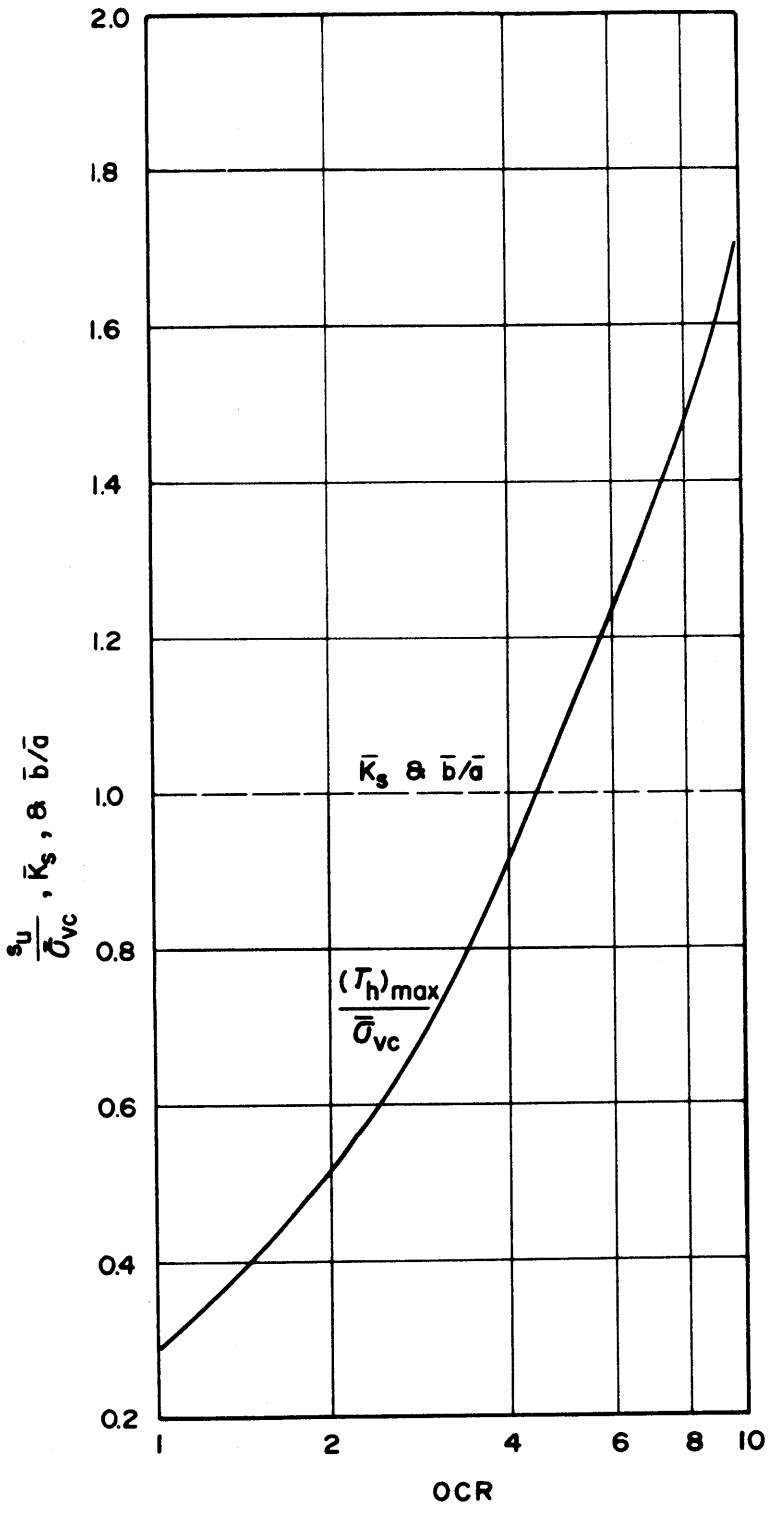


Figure 8.41 Anisotropic Shear Strength Parameters for the Maine Organic Clay

Table 8.15 SHANSEP-DSS Undrained Strength for Maine Organic Clay*

El (ft)	$\bar{\sigma}_{vo}$ (psf)	$\bar{\sigma}_{vm}$ (psf)	OCR	$\frac{s_u}{\bar{\sigma}_{vc}}$	s_u (psf)
-10	185	1000	5.40	1.14	211
-15	315	800	2.55	0.65	205
-20	450	740	1.65	0.45	203
-25	590	740	1.25	0.35	207
-30	730	765	1.05	0.30	219

Average s_u = 210 psf

* From Ladd et al. (1969)

Table 8.16 STAB3D Input Parameters for Fore River Test Section, Me.

Soil No.	γ_t (pcf)	SHANSEP-DSS Strength				s_u(FV)	$\bar{\phi}^\circ$	K	Soil Type
		s_u (psf)	$\bar{e}$	$\bar{d}$	f°				
1	110	0				0	30	0.50	Embankment Fill
2	130	0				0	30	0.50	Embankment Fill
3	130	0				0	30	0.50	Underwater Fill
4	125	0	0	0	–	0	30	0.50	Underwater Fill
5	62.4	0				0	0		Water
6	103	210				525	0	–	Maine Clay
7	120	0				0	40		Sand and Gravel

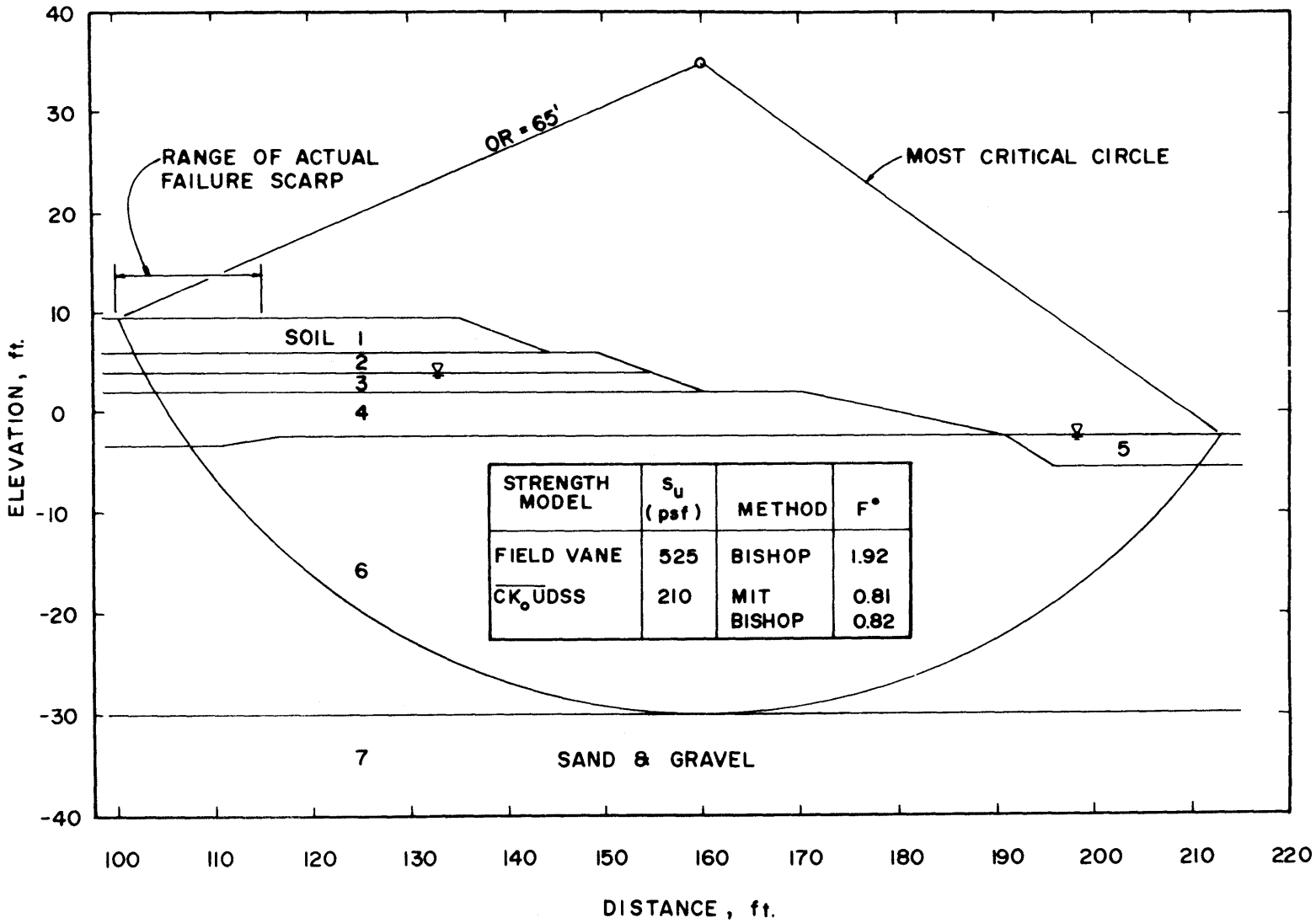


Figure 8.42 Results of Two-Dimensional Stability Analysis, Fore River Test Section, Me.

ment cross section within the 240-foot-long shear surface. Plane strain analyses yielded a value of DR = 33.5 ft. For a failure length, 2L, of 240 ft., we get 2L/DR = 7.20. The corresponding F/F^0 ratio from Fig. 8.43 = 1.07, i.e., three-dimensional effects increase the plane strain factor of safety by 7%. Hence, the FV and SHANSEP-DSS three-dimensional factors of safety are 2.05 and 0.86, respectively. The results of the analysis showed that ellipsoidal shear surfaces gave lower factors of safety than conical ones, and, therefore, they are more likely to simulate the geometry of the actual slope failure.

8.4.5 Summary and Conclusions for the FRT Case Study

This case study consists of a 20 ft. embankment constructed on a tidal mudflat deposit of soft, silty, slightly organic clay. Laboratory tests showed that the foundation clay has an isotropic undrained shear strength. Total stress stability analyses were performed utilizing the SHANSEP-DSS as well as the FV strength models.

The results of the two-dimensional analyses yielded FV and SHANSEP-DSS factors of safety, F^0 = 1.92 and 0.80, respectively. Excellent agreement was obtained between the Modified Bishop and the MIT methods of analysis.

The end effects (F/F^0) were found to increase the FV and SHANSEP-DSS plane strain factors of safety by 7%. Thus, the corresponding three-dimensional factors of safety = 2.05 and 0.86, respectively. This means that the FV strength should

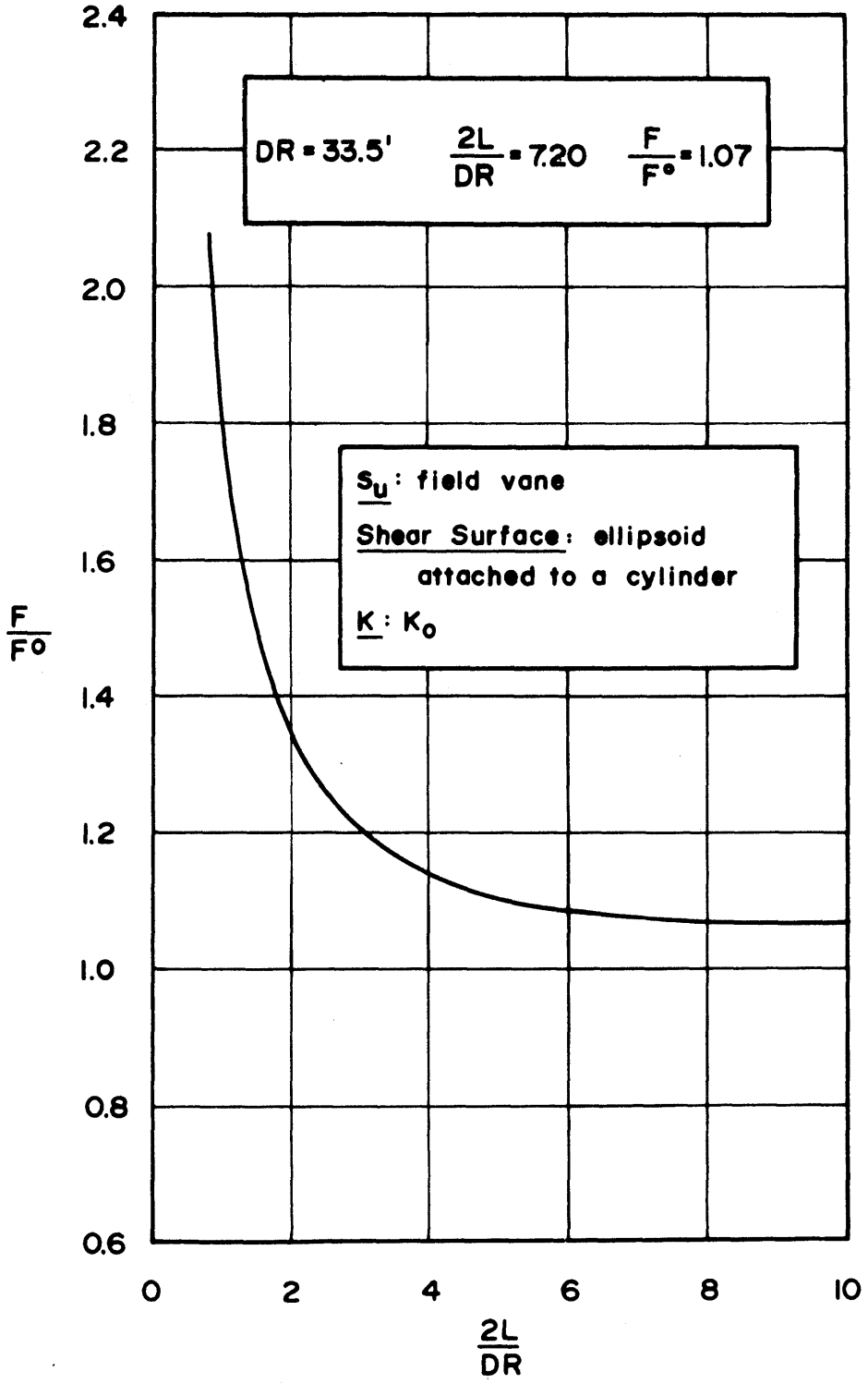


Figure 8.43 Three-Dimensional Effects for the Fore River Test Section

be reduced by a correction factor, $\mu = 0.49$ (1/2.05) in stability computations on Maine Organic Clay. Furthermore, the SHANSEP-DSS strength of 210 psf corresponds to $F = 0.86$ and is about 16% too low.

8.5 DESIGN OF EMBANKMENTS USING THE FIELD VANE STRENGTH

In order to use field vane data, $s_u(FV)$ in stability computations, Bjerrum (1972) introduced the concept of a correction factor, μ, such that the design strength for embankments, $s_u(design)$, can be estimated by the product $\mu \times s_u(FV)$. To determine μ for different clays, Bjerrum obtained the plane strain factor of safety, F^o, based on $s_u(FV)$ for a number of embankments which were loaded to failure and plotted $\mu (= 1/F^o)$ versus the plasticity index, P.I., as shown in Fig. 8.44 by the open triangles.* Since 1972, additional embankment failures have been reported in the literature. The FV correction factors for these failures are shown in Fig. 8.44 (open circles).

However, since all of these cases correspond to three-dimensional failures, where end effects can be significant, more appropriate values of μ should be based on three-dimensional factors of safety at failure, F, rather than F^0. For example, based on the field vane data at I-95, Table 8.17 shows that $F^0 = 0.89$ and $F = 1.17$. Without consideration of end effects, Bjerrum's method estimates $\mu = \frac{1}{0.89} = 1.12$, whereas the actual value to provide the best estimate of the shear strength for designs, s_u (design), should be $\mu = \frac{1}{1.17} =$

---

*Figure 8.44 gives the correction factors for cases where the failure length is reported .

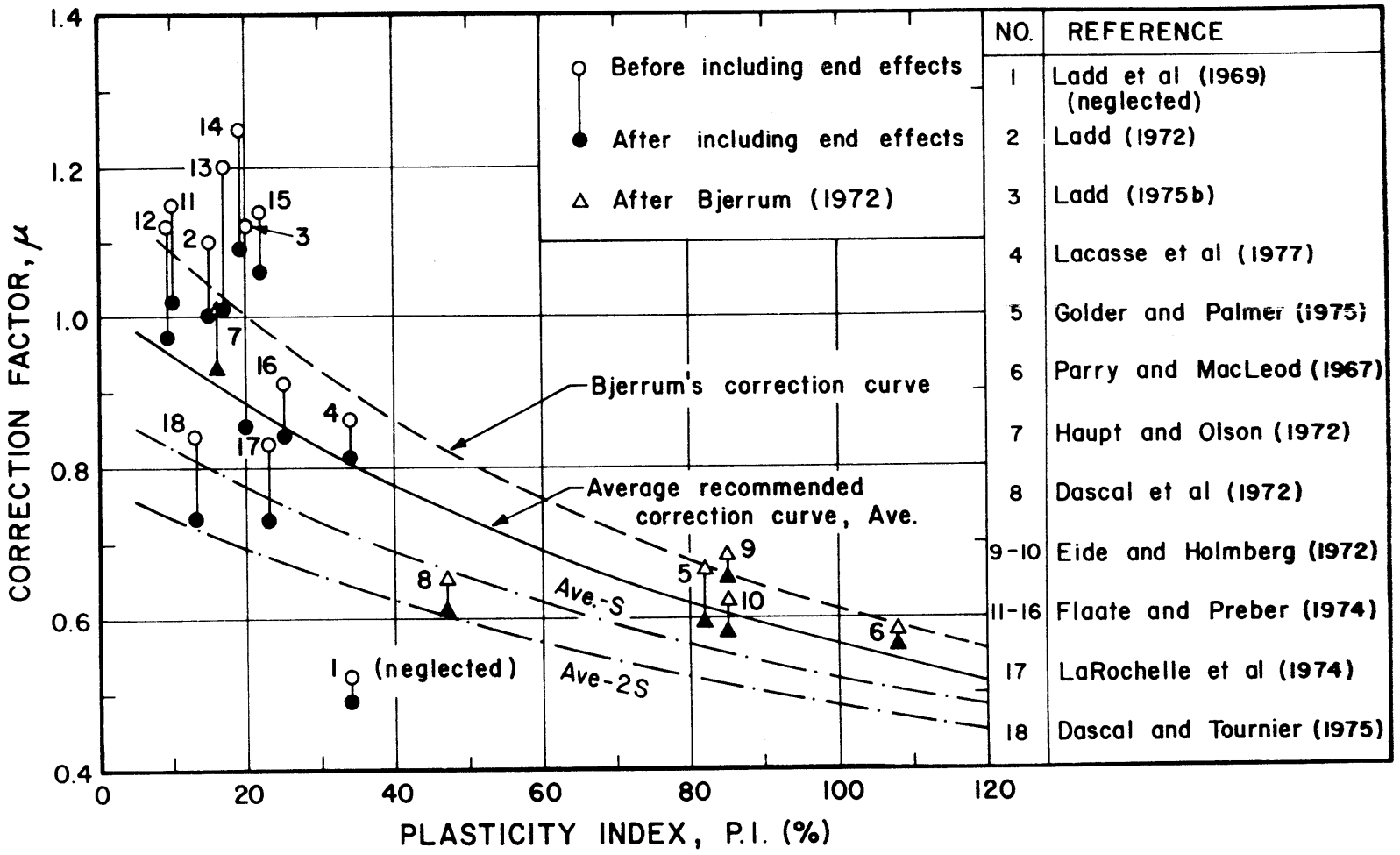


Figure 8.44 Field Vane Correction Factor

0.85. The difference between the two values of μ is clearly due to end effects which apply to the particular mode of failure that took place at I-95. Therefore, in the design of embankments on BBC, s_u (design), can be estimated on the basis of field vane data and a correction factor, μ(design) = 0.85. This s_u (design) should be used in the analysis of three-dimensional failures. Furthermore, this s_u (design) should also be used in the two-dimensional analysis of plane strain failures.

Table 8.17 shows the appropriate correction factors, μ, for the four case histories considered herein (numbers 1 through 4) as well as for 14 additional embankment failures reported in the literature. For each of these 14 cases, the correction factor was computed as follows:

1. The values of DR and F^0 were obtained from the results of plane strain analyses performed by the initial investigators of these case studies. DR is defined as the difference between the maximum and minimum radii of the shear surface .

2. Based on the actual failure length, 2L, reported in the literature, the value of 2L/DR was computed and the end effects, F/F^0, obtained from Fig. 3.4.

3. Knowing F^0 and F/F^0, the three-dimensional factor of safety, F, was determined and the correction factor $\mu = 1/F$ was computed.

It is important to note that Fig. 3.4 applies to homogeneous slopes of uniform cross sections, and is, therefore,

Table 8.17 Field Vane Correction Factors

No.	P.I. (%)	Two-Dimensional Analysis			Three-Dimensional Analysis				μ(5)	References
		F^0	μ^0(1)	DR(2) (ft)	2L(3) (ft)	2L/DR	F/F^0	F (4)		
1	34	1.92	0.52	33.5	240	7.20	1.07	2.05	0.49	Ladd et al. (1969)
2	15	0.91	1.10	42.4	300	7.10	1.10	1.00	1.00	Ladd (1972)
3	20	0.89	1.12	108.2	1030	9.54	1.30	1.17	0.85	Ladd (1975b)
4	34	1.16	0.86	34.8	325	9.34	1.07	1.24	0.81	Lacasse et al. (1977)
5	82	1.52	0.66	32.0	215	6.72	1.11	1.69	0.59	Golder and Palmer (1955)*
6	108	1.65	0.60	15.0	300	20.00	1.04	1.72	0.58	Parry and MacLeod (1967)*
7	16	0.99	1.01	60.0	500	8.33	1.08	1.07	0.93	Haupt and Olson (1972)*
8	47	1.53	0.65	34.0	400	10.95	1.06	1.63	0.61	Dascal et al. (1972)*
9	85	1.46	0.68	22.0	250	11.36	1.06	1.55	0.65	Eide and Holmberg (1972)*
10	85	1.61	0.62	25.5	250	9.80	1.07	1.72	0.58	"
11	8	0.87	1.15	10.0	54	5.40	1.13	0.98	1.02	Flaate and Preber (1974)
12	8	0.89	1.12	8.8	40	4.55	1.15	1.03	0.97	"
13	17	0.83	1.20	10.0	50	5.00	1.14	0.99	1.01	"
14	20	0.80	1.25	7.6	35	4.61	1.15	0.92	1.09	"
15	22	0.88	1.14	6.0	50	8.33	1.07	0.94	1.06	"
16	25	1.10	0.91	8.7	72	8.28	1.08	1.19	0.84	"
17	23	1.20	0.83	20.0	100	5.00	1.14	1.37	0.73	La Rochelle et al. (1974)
18	13	1.19	0.84	60.0	282	4.70	1.15	1.37	0.73	Dascal and Tournier (1975)

(1) $\mu^0 = 1/F^0$ (2) $DR = R_{max} - R_{min}$ (3) 2L = Total length of failure

(4) F/F^0 obtained from Fig. 3.4, except for cases 1 through 4.

* case studies considered by Bjerrum (1972)

believed to underestimate the end effects. For example, in case of the I-95 failure, the procedure based on Fig. 3.4 gives $F/F^0 = 1.07$, whereas the results of the detailed analysis in Table 8.18 gives $F/F^0 = 1.30$, i.e., Fig. 3.4 underestimated the end effects by about 20%.*

The solid circles in Fig. 8.44 represent the corrected values of μ vs. P.I. The solid line in Fig. 8.44 corresponds to the least squares fit for the cases considered,** and is about 10% lower than the correction curve recommended by Bjerrum. A more detailed analysis of the failures taking into consideration nonhomogeneity of the soil and variability in embankment cross section is expected to increase the deviation of the new curve from Bjerrum's.

Figure 8.45 shows the relationship between the average values of μ vs. P.I. together with the bands corresponding to $\pm$ 1 and 2 standard deviations, s, of the data used. In practical design, the average curve, $\mu_{ave.}$, should be used to obtain s_u (design). After an allowable factor of safety, F_{all}, is selected, Fig. 8.45 can be used again to evaluate the reliability of the embankment by plotting $\mu_{all} = \mu_{ave.}/F_{all}$ at the P.I. of the clay under consideration. If the point lies below the 2s band, the chances of a failure taking place is reasonably

---

*This large difference is believed to be due to the unusual loading conditions associated with the I-95 embankment.

**On the basis of a linear regression analysis between $1/\mu$ vs. P.I.

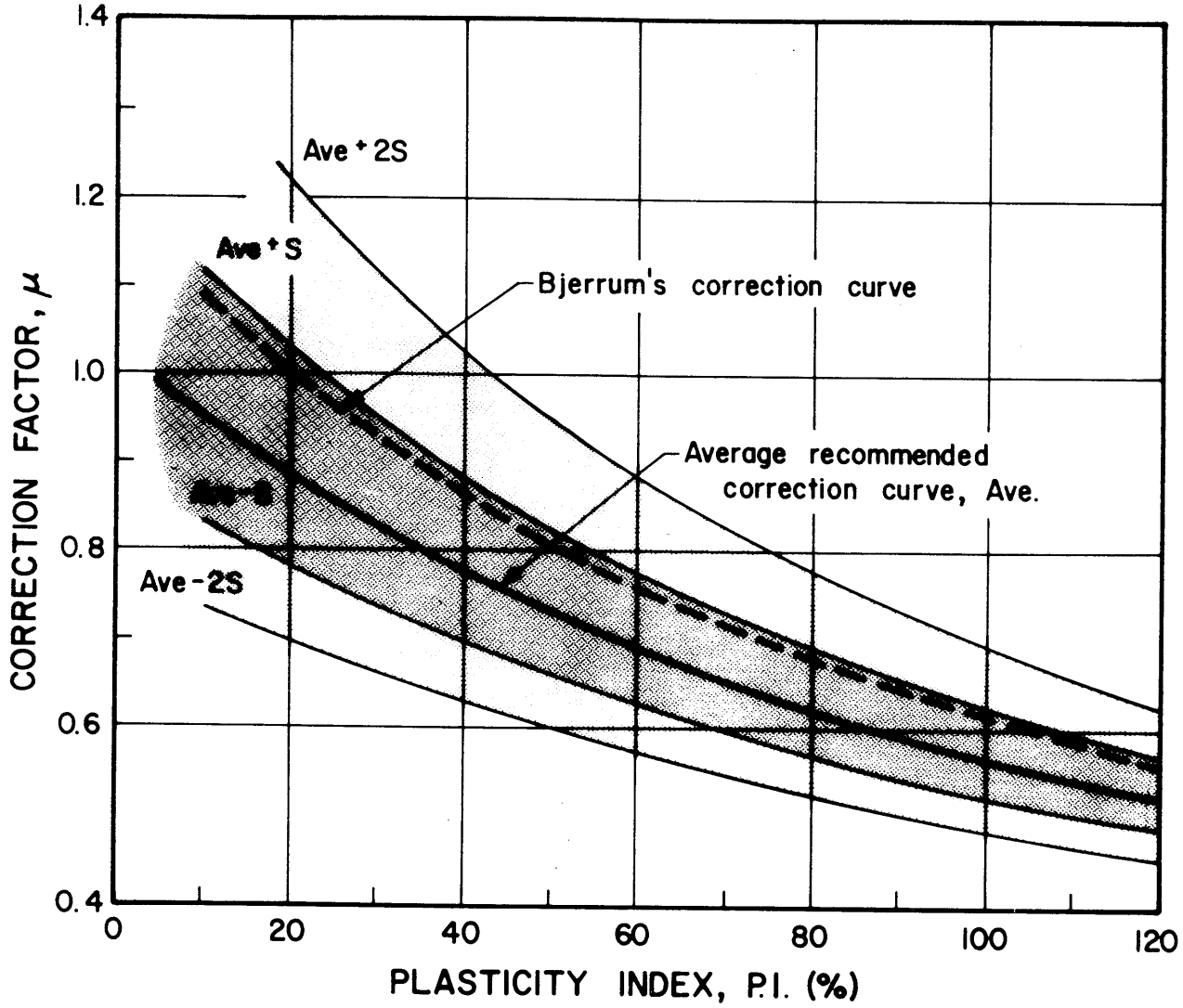


Figure 8.45 The Use of the Field Vane Strength in the Design of Embankments

low (below 3%, say).* If the point lies within the 2s and outside 1s band, the possibility of an embankment failure exists (between 3% and 17%, say). If the point lies within the 1s band, the probability of an embankment failure is high (17% to 50%).**

---

*Assuming a normal distribution.

** A more thorough three-dimensional analysis of all case studies in Table 8.17 is expected to increase the failure probabilities presented above.

8.6 SUMMARY AND CONCLUSIONS

This chapter presents four case studies of embankments rapidly loaded to failure on saturated clay foundations. Two- and three-dimensional total stress ($c = s_u$ and $\phi = 0$) circular arc stability analyses were performed utilizing two strength models: 1) the (uncorrected) field vane strength, s_u (FV) and 2) the Stress History and Normalized Soil Engineering Properties (Ladd and Foott, 1974) strength, which accounts for strain compatibility along the shear surface and strength anisotropy based on Davis and Christian's (1971) elliptical model extended to three dimensions, SHANSEP-$S_u(\theta)$. Table 8.18 presents a summary of the results where one observes that:

1. The end effects F/F^0, increase the plane strain factor of safety, F^0, by a maximum of 30% (I-95 case) and a minimum of 7% (FRT case). Therefore, when three-dimensional effects are neglected in the analysis of test fills, the back-calculated in situ shear strength can be slightly to significantly overestimated.

2. The SHANSEP-$S_u(\theta)$ strength model, which accounts for strength anisotropy and strain compatibility along the circular shear surface, yielded factors of safety close to unity at failure (except for the FRT case). However, the results of this model are influenced by the stress history of the soil deposit as well as the failure length. Based on the

Table 8.18 Summary of Results from Case Studies

Case Study	Foundation Clay	Two-Dimensional Analysis				Three-Dimensional Analysis								Correction Factor Applied to Field Vane Strength, μ[4]	Comments
		Field Vane Strength FV		SHANSEP-$S_u(\theta)$*		$2L$[2] (ft)	Field Vane Strength, FV				SHANSEP-$S_u(\theta)$				
		F^0(Bishop)	F^0(MIT)	F^0(Bishop)	α[1]		DR[3] (ft)	2L/DR	F/F^0	F	DR (ft)	2L/DR	F/F^0	F	
1. I-95 Embankment, Saugus, Mass.	partially consolidated Boston Blue Clay (P.I. = 20%)	0.89	0.93	0.82	0.45	1030	108.2	9.52	1.30	1.17	101.2	10.18	1.30	1.06	0.85 Corresponding to observed failure length
							108.2	4.20	1.22	1.09	101.2	4.70	1.23	1.00	0.92 Corresponding to minimum F/F^0 ratio.
2. Experimental Test Section, Portsmouth, N.H.	soft, very sensitive marine illitic clay (P.I. = 15%)	0.91	0.91	0.77	-	300	42.4	7.10	1.10	1.00	44.1	6.80	1.10[5]	0.85	1.00 Minimum $\bar{\sigma}_{vm}$
				0.85	0.45									0.94	Average "
				0.94	-									1.03	Maximum "
															Observed failure length
3. New Liskeard Embankment, New Liskeard, Canada	soft to medium stiff varved clay (P.I. = 10-47%)	1.16	1.16	0.94	0.40	325	34.8	9.34	1.07	1.24	34.8	9.34	1.095	1.029	0.81 F/F^0 corresponding to observed failure length. Minimum $\bar{\sigma}_{vm}$ for SHANSEP-$S_u(\theta)$
4. Fore River Test Section, Portland, Me.	soft, silty, slightly organic clay (P.I.= 34%)	1.92	1.92	0.80[6]	-	240	33.5	7.20	1.07	2.05	33.5	7.20	1.07	0.86	0.49 F/F^0 corresponding to observed failure length.

(1) s_u(equivalent) = $\alpha[s_u(V) + s_u(H)]$ (2) 2L = Total failure length (3) DR = $R_{max} - R_{min}$

(4) $\mu = 1/F(FV)$ (5) F/F^0 independent of $\bar{\sigma}_{vm}$ (6) based on $\overline{CK_oU}$DSS strength

* Based on average $\bar{\sigma}_{vm}$ profile except as noted.

observed failure length and the best estimate of the stress history profile at the I-95 site, the three-dimensional factor of safety at failure, F = 1.06. Hence, the SHANSEP-$s_u(\theta)$ model for the I-95 site is considered satisfactory. On the other hand, the best estimate of the stress history profile (corresponding to the average $\overline{\sigma}_{vm}$ profile) underestimated F for the Experimental Test Section and the Fore River Test section case studies, and overestimated it for the New Liskeard Embankment failure.*

3. Strength anisotropy can be accounted for in plane strain circular arc stability analyses by using an equivalent strength, $s_u(equ)$, given by:

$$s_u(equ) = \alpha[s_u(V) + s_u(H)]$$

For nonlayered soils, e.g., Boston Blue Clay and Portsmouth Clay, α was found equal to 0.45, whereas for the New Liskeard Varved Clay, $\alpha = 0.40$. However, it should be noted that for varved clays, the strength is at or near its minimum for horizontal failures. Hence, the use of $[s_u(V) + S_u(H)]$ to account for strength anisotropy in noncircular (wedge type) shear surfaces, where a large portion of the failure surface is horizontal, may be unsafe.

4. End effects, expressed by the ratio F/F^0, were not

---

*Based on results from Lacasse et al., 1977.

significantly affected by the strength model used, i.e., FV vs. SHANSEP-$S_u(\theta)$. This means that for routine investigations of three-dimensional effects, the FV strength can generally be used without significant errors. This will reduce the computational time by an order of magnitude.

5. The end effects are affected by the longitudinal (out-of-plane) stress, $\bar{\sigma}_\ell$, because of the frictional properties of the fill material. In the I-95 case study, an increase in $K(= \bar{\sigma}_\ell/\bar{\sigma}_v)$ from K_a to K_o and K_p increases the minimum ratio of F/F^0 from 1.16 to 1.30 and 1.42, respectively (Fig. 8.16). Since the actual value of K is difficult to estimate, we recommend the use of $K = K_o$.

6. Following Bjerrum's procedure (1972), and in order to use the field vane data, $s_u(FV)$, in the design of embankments, Fig. 8.44 gives a plot of a FV correction factor, μ, versus the plasticity index, P.I., of the clay. The design strength for embankments can then be estimated by the product $\mu \times s_u(FV)$. These correction factors were obtained based on the results of <u>three-dimensional analyses</u> (F at failure) for the four case studies investigated herein, and for fourteen additional embankment failures reported in the literature. Figure 8.44 shows that the new correction curve based on F is about 10% lower than Bjerrum's curve, which was based on F^0. However, including the end effects in the correction factor, μ, did not significantly affect the scatter in μ.

CHAPTER 9

SUMMARY AND CONCLUSIONS

This thesis investigates the three-dimensional stability of slopes. The classical circular arc method of analysis is extended to three-dimensional problems by replacing the cylindrical shear surfaces considered in plane strain failures by two types of shear surfaces of revolution. The first consists of a cone attached to a cylinder and the second consists of an ellipsoid attached to a cylinder. The factor of safety is computed by means of a computer program (STAB3D) developed for performing three-dimensional analyses. Solutions are presented in the form of design charts for the following problems:

1. The undrained stability of homogeneous slopes which may exhibit an anisotropic shear strength.

2. The undrained stability of slopes with homogeneous cross sections and a variable shear strength along their axis.

3. The undrained stability of homogeneous slopes with isotropic strength subjected to surcharge loads.

4. The drained stability of homogeneous slopes.

Four case studies of embankments rapidly loaded to failure on saturated clay foundations are thoroughly analyzed. The three-dimensional factor of safety, which accounts for strength anisotropy and strain compatibility along the shear surface, is compared to the actual value of unity at failure.

Conclusions regarding the selection of an adequate shear strength for stability computations on clay foundations are then derived. The remainder of this chapter presents a summary of the results obtained from this study.

A. Undrained Stability of Homogeneous Slopes

Three-dimensional analyses conducted on homogeneous isotropic cohesive slopes having a uniform cross section show that:

1. The end effects (expressed by the ratio F/F^0) increase the factor of safety, F^0, obtained by means of a conventional two-dimensional solution. This increase depends on the ratio between the length of failure, 2L, and the depth of failure, DR, defined as the difference between the maximum and minimum radii of the shear surface. Fig. 3.4 shows that, for long shallow failures where 2L/DR exceeds eight, the increase in the factor of safety is less than 5% and can, therefore, be neglected. On the other hand, for short deep failures where 2L/DR is less than two, the increase in the factor of safety can exceed 20% and the use of a three-dimensional analysis is thus recommended.

2. For a certain ratio of 2L/DR, the slope angle β has little influence on the increase in the factor of safety due to end effects. For a value of 2L/DR equal to six, the increase in the factor of safety due to end effects is about 8% for $\beta = 10°$, whereas the corresponding increase for $\beta = 90°$ is about 12% (Fig. 3.4).

3. For flat slopes, the three-dimensional effects (the ratio F/F^0) are influenced by the bedrock location expressed by the parameter n in Fig. 3.4. In case of $\beta = 45°$ ($\cot \beta = 1$), when n increases from 1 (toe failures) to 2, the F/F^0 value at $2L/DR = 4$ decreases by about 7%.

Clays often exhibit a significant anisotropy in their undrained shear strength, Ladd et al. (1977). Results of slope stability analyses based on the Davis and Christian (1971) model for strength anisotropy show that:

1. The plane strain factor of safety, F^0, can be significantly affected by the strength anisotropy. This effect becomes more pronounced when the anisotropy parameters b/a and K_s, as well as the slope angle β decrease. For the case of a vertical cut in an anisotropic soil with $K_s = b/a = 0.5$, Fig. 5.6 shows that analyses based on the undrained shear strength for compression in the vertical direction, $s_u(V)$, will overestimate the factor of safety by about 45%. However, this error can be reduced to 8% when the average strength, $(0.5[s_u(V) + s_u(H)])$, is used.

2. End effects (F/F^0) are not significantly affected by strength anisotropy.

B. Undrained Stability of Slopes with Homogeneous Cross Sections and Variable Strength Along Their Axis

The end effects in slopes having a uniform shear strength along their axis increase the plane strain factor of safety.

The critical failure length is thus infinite and corresponds to the plane strain solution. Hence, in order to better simulate the field conditions, where actual failures are three-dimensional, the variation of the shear strength along the slope axis was considered. This was achieved by means of a deterministic analysis followed by a probabilistic approach.

In the deterministic analysis a sinusoidal variation of the shear strength along the slope axis was considered. Results in Fig. 7.7 show that:

1. The parameters m and δ representing the amplitude and the normalized half wave length of the strength model, respectively, determine the mode of failure. For a given value of m and large values of λ, a failure with finite length will take place. In this case, three-dimensional effects reduce the plane strain factor of safety and, if neglected, can lead to unsafe designs. By decreasing the value of λ, the factor of safety increases and the critical failure length decreases until a certain value of λ, beyond which the minimum factor of safety equals the plane strain factor of safety and the failure has an infinite length.

2. For finite failure lengths, the factor of safety decreases when either m or λ increases.

3. For slopes with homogeneous cross sections, finite failure lengths are shorter than half the wave length, δ, of the strength variation.

In the probabilistic analysis, the reliability of embankments is estimated. The soil model considered is statistically homogeneous and the inherent variability of the shear strength constitutes the major uncertainty in the factor of safety. Analyses were carried out assuming two types of probability distributions (the Gaussian and sinusoidal distributions) and three models for the spatial variability of the shear strength.

The results of the probabilistic analysis show that:

1. For the case of the sinusoidal strength variation, both the deterministic and probabilistic models give exactly the same results. The wave amplitude factor, m, of the deterministic model is equivalent to $\bar{m}$ in the probabilistic approach. The parameter $\bar{m}$ is the product of the reliability index, R_i, (corresponding to a certain probability of failure) and the coefficient of variation of the shear strength, $\tilde{c}/\bar{c}$.

2. The failure length of a slope depends on the autocorrelation distance, δ^*, describing the spatial variability of the shear strength, and $\bar{m}$ $(= R_i \frac{\tilde{c}}{\bar{c}})$. This is similar to the case of the deterministic analysis where the failure mode is affected by δ and m.

3. For fixed values of $\bar{m}$ and δ^*, the effect of different shear strength spatial variability models on the minimum factor of safety is not significant.

C. Undrained Stability of Slopes Subjected to Surcharge Loads

The undrained stability ($\phi = 0$, $c = s_u$) of homogeneous slopes subjected to infinitely long line and strip loads, as well as line loads of finite length and square loaded areas, were considered. Results show that:

1. The critical surcharge load to cause failure of a cohesive slope of height H possessing a uniform strength, c, and a unit weight, γ (Fig. 4.1) depends on six dimensionless parameters grouped into two categories. The first describes the slope and consists of the stability number, $\gamma H/c$, the slope angle β, and the bedrock location expressed by the parameter n. The second set of parameters describes the load by means of the width ratio, B/H, length ratio, L_p/H, and the normalized edge distance from the edge of the slope, A/H.

2. For a slope subjected to a surcharge load, failure can take place according to one of two modes: a) Bearing capacity, where the failure surface does not intersect the slope (bearing capacity theories for horizontal ground surfaces are applicable to such modes of failure); and, b) slope failure, where the critical shear surface extends beyond the crest and hence involves part of the slope.

3. Results for line loads show that three-dimensional effects become significant whenever L_p/H is less than unity and are especially important when the factor of safety of the slope due to own weight only is close to unity. For many

practical situations, three-dimensional effects would increase the plane strain critical load by a factor of 5 to 10.

D. Drained Stability of Homogeneous Slopes

The drained stability of slopes where the shear strength obeys the Mohr-Coulomb criterion was considered. In such cases, the stability problem is statically indeterminate and the normal effective stresses, $\bar{\sigma}_N$, along the shear surface must be assumed in order to estimate the factor of safety. This was achieved by adopting simplified procedures which are aimed at estimating "reasonable" bounds on $\bar{\sigma}_N$.

Two methods of analysis were used to estimate $\bar{\sigma}_N$: The Ordinary Method of Slices (OMS), and the MIT method (MIT). In the OMS, all interslice forces are neglected and $\bar{\sigma}_N$ is obtained from equilibrium in a direction normal to the base of the slice. In two dimensions, the MIT method assumes that the vertical overburden stress is either a major or a minor principal stress at failure, depending on whether the inclination of the base angle, θ, is positive or negative, respectively. In three dimensions, the longitudinal (out-of-plane) effective stress, $\bar{\sigma}_\ell$, is also assumed to be a principal stress and given by the ratio $K(= \bar{\sigma}_\ell/\bar{\sigma}_v)$. Knowing the principal stresses, $\bar{\sigma}_N$ can be easily computed.

A parametric study was performed for different slope angles, β, and frictional strength parameter, $\lambda_{c\phi}(= \frac{\gamma H}{\bar{c}} \tan \bar{\phi})$, to evaluate the effect of these assumptions on the two- and

three-dimensional factors of safety. The results show that:

In two Dimensions

1. Similar to the Ordinary Method of Slices (OMS), the MIT method provides an explicit expression for the plane strain factor of safety, F^0, and thus avoids the iteration required by the Modified Bishop (MB) method. This reduces the computer time significantly and enables extensions of the method to three dimensions to be easily performed. However, the MIT method predicts factors of safety that are closer to the ones predicted by the widely used Modified Bishop method than the OMS.

2. The distribution of $\bar{\sigma}_N$ along the shear surface according to the MIT method appears reasonable for all values of θ, even for "deep" circles (large negative values of θ). For this case, the MB method predicts infinite passive resistance for $\theta \leq \bar{\phi} - 90°$, and the OMS predicts a very small passive resistance which tends to zero at $\theta = -90°$.

In Three Dimensions

1. The results obtained by the extended OMS to three dimensions are shown in Fig. 6.3 where F/F^0 is plotted vs. 2L/DR. The method predicts that failure of frictional slopes ($\lambda_{c\phi} = 100$) takes place along very short and deep shear surfaces contrary to typical observed failure modes. This arises because the extended OMS assumes the effective longitudinal stress, $\bar{\sigma}_\ell$, to be equal to zero. This assumption underestim-

ates the frictional resistance on vertical planes, becomes significant when $\lambda_{c\phi}$ increases, and, therefore, is not considered satisfactory.

2. The results obtained by the MIT method (Fig. 6.4) show that when K = 0, the results are very similar to the extended OMS: F/F^0 is less than unity, and the critical failure length is very short. This confirms the earlier conclusions that the extended OMS yields unrealistic results because the longitudinal stresses are neglected.

3. An increase in the longitudinal effective stress, $\bar{\sigma}_\ell$, increases the end effects, i.e., F/F^0 increases when K increases. Furthermore, this effect of $\bar{\sigma}_\ell$ increases as the frictional strength parameter, $\lambda_{c\phi}$, increases, and vanishes for frictionless slopes ($\lambda_{c\phi} = 0$).

4. An increase in the frictional component of the shear strength reduces the end effects, i.e., F/F^0 decreases as $\lambda_{c\phi}$ increases (Fig. 6.3). In the case of K = 0.3 and $\lambda_{c\phi} = 100$, which corresponds to a highly frictional slope near the active state in the longitudinal direction, end effects (F/F^0) are not significant when $2L/DR \geq 3$.

5. The end effects increase slightly with slope angle β.

Finally, four case studies of embankments rapidly loaded to failure on saturated clay foundations were analyzed. Two- and three-dimensional total stress ($c = s_u$ and $\phi = 0$) circular arc stability analyses were performed utilizing two strength models: 1) the (uncorrected) field vane strength,

s_u(FV) and 2) the Stress History and Normalized Soil Engineering Properties (Ladd and Foott, 1974) strength, which accounts for strain compatibility along the shear surface and strength anisotropy based on Davis and Christian's (1971) elliptical model extended to three dimensions, SHANSEP-$S_u(\theta)$. The results show that:

1. The end effects, F/F^0, increase the plane strain factor of safety, F^0, by a maximum of 30% (I-95 case) and a minimum of 7% (Fore River Test section, FRT, case). Therefore, when three-dimensional effects are neglected in the analysis of test fills, the back-calculated in situ shear strength can be slightly to significantly overestimated.

2. The SHANSEP-$S_u(\theta)$ strength model, which accounts for strength anisotropy and strain compatibility along the circular shear surface, yielded factors of safety close to unity at failure (except for the FRT case). However, the results of this model are influenced by the stress history of the soil deposit as well as the failure length. Based on the observed failure length and the best estimate of the stress history profile at the I-95 site, the three-dimensional factor of safety at failure, F = 1.06. Hence, the SHANSEP-$S_u(\theta)$ model for the I-95 site is considered satisfactory. On the other hand, the best estimate of the stress history profile (corresponding to the average $\bar{\sigma}_{vm}$ profile) underestimated F for the Experimental Test Section and the Fore River Test section case studies, and overestimated it for the New Liskeard Embankment failure.

3. Strength anisotropy can be accounted for in plane strain circular arc stability analyses by using an equivalent strength, $s_u(equ)$, given by:

$$s_u(equ) = \alpha[s_u(V) + s_u(H)]$$

For nonlayered soils, e.g., Boston Blue Clay and Portsmouth Clay, α was found equal to 0.45, whereas for the New Liskeard Varved Clay, $\alpha = 0.40$. However, it should be noted that for varved clays, the strength is at or near its minimum for horizontal failures. Hence, the use of $[s_u(V) + s_u(H)]$ to account for strength anisotropy in noncircular (wedge type) shear surfaces, where a large portion of the failure surface is horizontal, may be unsafe.

4. The end effects, expressed by the ratio F/F^0, were not significantly affected by the strength model used, i.e., FV vs. SHANSEP-$S_u(\theta)$. This means that for routine investigations of three-dimensional effects, the FV strength can generally be used without significant errors. This will reduce the computational time by an order of magnitude.

5. The end effects are affected by the longitudinal (out-of-plane) stress, $\bar{\sigma}_\ell$, because of the frictional properties of the fill material. In the I-95 case study, an increase in $K(= \bar{\sigma}_\ell/\bar{\sigma}_v)$ from K_a to K_o and K_p increases the minimum ratio of F/F^0 from 1.16 to 1.22 and 1.42, respectively (Fig. 8.16).

6. Following Bjerrum's procedure (1972), and in order to use the field vane data, $s_u(FV)$, in the design of embankments,

Fig. 8.44 gives a plot of the FV correction factor, μ, versus the plasticity index, P.I., of the clay. The design strength for embankments can be estimated by the product $\mu \times s_u(FV)$. These correction factors were obtained based on the results of three-dimensional analyses (F at failure) for the four case studies investigated herein, and for fourteen additional embankment failures reported in the literature. Figure 8.44 shows that the new correction curve based on F is about 10% lower than Bjerrum's curve, which was based on F^0. However, including the end effects in the correction factor, μ, did not significantly affect the scatter in μ.

REFERENCES

Abramowitz, M., and Stegun, I.A., editors, Handbook of Mathematical Functions with Formulas, Graphs and Mathematical Tables, 10th ed., National Bureau of Standards, Applied Mathematics Series 55, 1972, pp. 295-330.

Anagnosti, P., "Three-Dimensional Stability of Fill Dams," Proceedings, 7th International Conference on Soil Mechanics and Foundations Engineering, Mexico City, Vol. 2, 1969, pp. 275-280.

Bailey, W.A., and Christian, J.T., "ICES LEASE-I, a Problem Oriented Language for Slope Stability Analysis," User's Manual, Research Report R69-22, Department of Civil Engineering, Massachusetts Institute of Technology, 1969, 56 p.

Barboteu, G., "Reliability of Earth Slopes," thesis presented to the Massachusetts Institute of Technology at Cambridge, Massachusetts, in 1972, in partial fulfillment of the requirements for the degree of Master of Science.

Bishop, A.W., "The Use of the Slip Circle in the Stability Analysis of Slopes," Geotechnique, London, England, Vol. 5, No. 1, March 1955, pp. 7-17.

Bishop, A.W., "The Strength of Soils as Engineering Materials," Geotechnique, London, England, Vol. 16, No. 2, 1966, pp. 89-130.

Bishop, A.W. and Morgenstern, N., "Stability Coefficients for Earth Slopes," Geotechnique, London, England, Vol. 10, No. 4, December 1960, pp. 129-150.

Bjerrum, L., "Embankments on Soft Ground," State-of-the-Art Report, Proceedings, ASCE Specialty Conference on Performance of Earth and Earth-Supported Structures, Lafayette, Vol. 2, 1972, pp. 1-54.

Bowles, J.E., "Spread Footings," Chapter 15, Foundation Engineering Handbook, Winterkorn, H.F., and Fang, H.Y., editors, Van Nostrand Reinhold Company, New York, N.Y., 1975, p. 493.

Bowles, J.E., Foundation Analysis and Design, 2nd ed., McGraw-Hill Book Company, New York, N.Y., 1977, pp. 131-133.

Casagrande, A., and Carillo, N., "Shear Failure of Anisotropic Materials," Journal of the Boston Society of Civil Engineers, 1944, pp. 122-135.

Chen, W.F., Limit Analysis and Soil Plasticity, Elsevier Scientific Publishing Company, New York, N.Y., 1975.

Chen, W.F., Snitbhan, N., and Fang, H.Y., "Stability of Slopes in Anisotropic, Nonhomogeneous Soils," Canadian Geotechnical Journal, Vol. 12, No. 1, 1975, pp. 146-151.

Crandall, S.H., Engineering Analysis: A Survey of Numerical Procedures, McGraw-Hill Book Company, New York, N.Y., 1956.

Dascal, O., et al., "Failure of a Test Embankment on Sensitive Clay," Proceedings, ASCE Specialty Conference on Earth and Earth-Supported Structures, Lafayette, Vol. 1, Part 1, 1972, pp. 129-158.

Dascal, O., and Tournier, J., "Embankment on Soft and Sensitive Clay Foundation," Journal of the Geotechnical Engineering Division, ASCE, Vol. 101, No. GT3, March 1975, pp. 297-314.

Davis, E.H., and Christian, J.T., "Bearing Capacity of Anisotropic Cohesive Soils," Journal of Soil Mechanics and Foundations Division, ASCE, Vol. 97, No. SM5, May 1971, pp. 753-769.

Dawson, A.W., "LEASE II: A Computerized System for the Analysis of Slope Stability," thesis presented to the Massachusetts Institute of Technology, at Cambridge, Massachusetts, in 1972, in partial fulfillment of the requirements for the degree of Civil Engineer.

Eide, O., and Holmberg, S., "Test Fills to Failure on the Soft Bangkok Clay," Proceedings, ASCE Specialty Conference on Earth and Earth-Supported Structures, Lafayette, Vol. 1, Part 1, 1972, pp. 159-180.

Fellenius, W., "Calculation of the Stability of Earth Dams," Transactions, 2nd Congress on Large Dams, Vol. 4, Washington D.C., 1936, pp. 445-459.

Flaate, K., and Preber, T., "Stability of Road Embankments in Soft Clay," Canadian Geotechnical Journal, Vol. 11, No.1, 1974, pp. 72-88.

Giger, M.W., and Krizek, R.J., "Stability of Vertical Corner Cut with Concentrated Surcharge Load," Journal of the Geotechnical Engineering Division, ASCE, Vol. 102, No. GT1, January 1976, pp. 31-40.

Gilbert, L.W., "A Probabilistic Analysis of Embankment Stability Problems," thesis presented to the Massachusetts Institute of Technology, at Cambridge, Massachusetts, in 1974, in partial fulfillment of the requirements for the degree of Master of Science.

Golder, H.Q., and Palmer, D.J., "Investigation of a Bank Failure at Scrapsgate, Isle of Sheppey, Kent," Geotechnique, London, England, Vol. 5, No. 1, March 1955, pp. 55-73.

Hansen, J. Brinch, "Comparison of Methods for Stability Analysis; Three-Dimensional Effect in Stability Analysis; Resistance of a Rectangular Anchor Slab," The Danish Geotechnical Institute Bulletin, No. 21, Copenhagen, 1966, 13 p.

Haupt, R.S., and Olson, J.P., "Case History - Embankment Failure on Soft Varved Silt," Proceedings, ASCE Specialty Conference on Earth and Earth-Supported Structures, Lafayette, Vol. 1, Part 1, 1972, pp. 1-28.

Hill, R., The Mathematical Theory of Plasticity, The Clarendon Press, Oxford, England, 1950, pp. 317-340.

Hovland, H.J., "Three-Dimensional Slope Stability Analysis Method," Journal of the Geotechnical Engineering Division, ASCE, Vol. 103, No. GT9, September 1977, pp. 971-986.

Janbu, N., "Stability Analysis of Slopes with Dimensionless Parameters," thesis presented to Harvard University, at Cambridge, Massachusetts, in 1954, in partial fulfillment of the requirements for the degree of Doctor of Philosophy.

Janbu, N., "Slope Stability Computations," Embankment-Dam Engineering, Casagrande Volume, Hirschfeld, R.C., and Poulos, S.J., editors, John Wiley and Sons, Inc., New York, N.Y., 1973, pp. 47-86.

Lacasse, S.M., and Ladd, C.C., "Behavior of Embankments on New Liskeard Varved Clay," Research Report R73-44, No. 327, Department of Civil Engineering, Massachusetts Institute of Technology, Cambridge, Massachusetts, 1973, 270 p.

Lacasse, S.M., Ladd, C.C., and Barsvary, A.K., "Undrained Behavior of Embankments on New Liskeard Varved Clay," Canadian Geotechnical Journal, Vol. 14, No. 3, August 1977, pp. 367-388.

Ladd, C.C., "Strength Parameters and Stress-Strain Behavior of Saturated Clays," Research Report R71-23, No. 278, Department of Civil Engineering, Massachusetts Institute of Technology, Cambridge, Massachusetts, 1971.

Ladd, C.C., "Test Embankment on Sensitive Clay," Proceedings, ASCE Specialty Conference on Performance of Earth and Earth-Supported Structures, Lafayette, Vol. 1, Part 1, 1972, pp. 101-128.

Ladd, C.C., "Advanced Soil Mechanics," Unpublished Lecture Notes, Massachusetts Institute of Technology, Cambridge, Massachusetts, 1970.

Ladd, C.C., "Foundation Design of Embankments Constructed on Connecticut Valley Varved Clays," Research Report R75-7, No. 343, Department of Civil Engineering, Massachusetts Institute of Technology, Cambridge, Massachusetts, 1975a, 439 p.

Ladd, C.C., "Proceedings of the Foundation Deformation Prediction Symposium," Research Report R75-32, No. 512, Vol. 2, Appendix B, Department of Civil Engineering, Massachusetts Institute of Technology, Cambridge, Massachusetts, 1975b, pp. B-1 - B-111

Ladd, C.C., Aldrich, J.P., Jr., and Johnson, E.G., "Embankment Failure on Organic Clay," Proceedings, 7th International Conference on Soil Mechanics and Foundation Engineering, Mexico City, Vol. 2, 1969, pp. 627-634.

Ladd, C.C., et al., "Consolidated-Undrained Plane Strain Shear Tests on Boston Blue Clay," Research Report R71-13, No. 273, Department of Civil Engineering, Massachusetts Institute of Technology, Cambridge, Massachusetts, 1971, 243 p.

Ladd, C.C., and Edgers, L., "Consolidated-Undrained Direct-Simple Shear Tests on Saturated Clays," Research Report R72-82, No. 284, Department of Civil Engineering, Massachusetts Institute of Technology, Cambridge, Massachusetts, 1972, 354 p.

Ladd, C.C., Rixner, J.J., and Gifford, D.C., "Performance of Embankments with Sand Drains on Sensitive Clay," Proceedings, ASCE Specialty Conference on Performance of Earth and Earth-Supported Structures, Lafayette, Vol. 1, Part 2, 1972, pp. 211-242.

Ladd, C.C., and Foott, R., "New Design Procedure for Stability of Soft Clays," Journal of the Geotechnical Engineering Division, ASCE, Vol. 100, No. GT7, July 1974, pp. 763-786.

Ladd, C.C., et al., "Stress-Deformation and Strength Characteristics," State-of-the-Art Report Session 1, Proceedings, 9th International Conference on Soil Mechanics and Foundations Engineering, Tokyo, Vol. 2, 1977, pp. 421-494.

Lambe, T.W., and Whitman, R.V., Soil Mechanics, John Wiley and Sons, Inc., New York, N.Y., 1969.

LaRochelle, P., Trak, B., Tavenas, F., and M. Roy, "Failure of a Test Embankment on a Sensitive Champlain Clay Deposit," Canadian Geotechnical Journal, Vol. 11, No. 1, 1974, pp. 142-164.

Lo, K.Y., "Stability of Slopes in Anisotropic Soils," Journal of Soil Mechanics and Foundations Division, ASCE, Vol. 91, No. SM4, July 1965, pp. 85-106.

Lorente de No, C., "Stability of Slopes with Curvature in Plan View," Proceedings, 7th International Conference on Soil Mechanics and Foundations Engineering, Mexico City, Vol. 2, 1969, pp. 635-638.

Lowe, John III, and Karafiath, L., "Stability of Earth Dams upon Drawdown," Proceedings, First Panamerican Conference on Soil Mechanics and Foundation Engineering, Mexico City, Vol. 2, 1960, pp. 537-552.

Massachusetts Institute of Technology, "Proceedings of the Foundation Deformation Prediction Symposium," Research Report R75-32, No. 512, Vol. 1, Department of Civil Engineering, Massachusetts Institute of Technology, Cambridge, Massachusetts, 1975, 157 p.

Matsuo, M., and Kuroda, K., "Study on the Soil Exploration System for Stability Analysis of Embankments," Transactions, Japanese Society of Civil Engineers, Vol. 3, Part 2, 1971, pp. 218-219.

Matsuo, M., and Kuroda, K., "Probabilistic Approach to Design of Embankments," Soils and Foundations, Japanese Society of Soil Mechanics and Foundation Engineering, Vol. 14, No. 2, June 1974, pp. 1-17.

Marsal, R.J., and de Arellano, L.R., "Performance of El Infiernillo Dam," Journal of the Soil Mechanics and Foundations Division, ASCE, Vol. 93, No. SM4, July 1967, pp. 265-298.

Meyerhof, G.G., "The Ultimate Bearing Capacity of Foundations on Slopes," Proceedings, 4th International Conference on Soil Mechanics and Foundation Engineering, Vol. 1, London, 1957, pp. 384-386.

Morgenstern, N.R., and Price, V.E., "The Analysis of the Stability of General Slip Surfaces," Geotechnique, London, England, Vol. 15, No. 1, March 1965, pp. 79-93.

Morla Catalan, J., and Cornell, C.A., "Earth Slope Reliability by a Level-Crossing Method," Journal of the Geotechnical Engineering Division, ASCE, Vol. 102, No. GT6, June 1976, pp.591-604.

Parry, R.H.G., and McLeod , J.H., "Investigation of Slip Failure in Flood Levee at Launceston, Tasmania," Proceedings, 5th Australia-New Zealand Conference on Soil Mechanics and Foundation Engineering, Auckland, 1967, pp. 294-300.

Prandtl, L., "Ueber die Haerte Plastischer Koerper," Goettinger Nachr., Math.-Phys. Kl, 1920, 74 p.

Ranganatham, B.V., and Matthai, A.C., "Anisotropy and its Effect on the Stability of Earth Masses under the $\phi_u = 0$ Condition," Proceedings, 3rd Asian Regional Conference on Soil Mechanics and Foundations Engineering, Haifa, Vol. 1, 1967, pp. 348-352.

Ranganatham, B.V., Sani, A.C., and Sreenivasulu, V.,"Strength Anisotropy on Slope Stability and Bearing Capacity of Clays," Proceedings, 7th International Conference on Soil Mechanics and Foundations Engineering, Mexico City, Vol. 2, 1969, pp. 659-667.

Reti, G.A., and Djou, S.K., "Slope Stability Analysis," Computer Program No. EP-5A, Dames and Moore Consulting Firm, San Francisco, 1969, 46 p.

Sambhandharaksa, Surachat, "Stress-Strain-Strength Anisotropy of Varved Clays," thesis presented to the Massachusetts Institute of Technology, at Cambridge, Massachusetts, in 1977, in partial fulfillment of the requirements for the degree of Doctor of Science.

Scott, R.F., Principles of Soil Mechanics, Addison-Wesley Publishing Company, Inc., Reading, Massachusetts, 1963.

Sherard, J.L., et al., Earth and Earth-Rock Dams, John Wiley and Sons, Inc., New York, N.Y., 1963.

Shield, R.T., "On the Plastic Flow of Metals under Conditions of Axial Symmetry," Proceedings, Royal Society of London, Series A, Vol. 233, 1955, pp. 267-287.

Shield, R.T., and Drucker, D.C., "The Application of Limit Analysis to Punch-Indentation Problems," Journal of Applied Mechanics, ASME, 1953, pp. 453-460.

Silva, F., "Stability of an Embankment on a Partially Consolidated Foundation - Interstate I-95," thesis presented to the Massachusetts Institute of Technology, at Cambridge, Massachusetts, in 1975, in partial fulfillment of the requirements for the degree of Master of Science.

Simon, R.M., "Analysis of Embankment Construction by Finite Elements," thesis presented to the Massachusetts Institute of Technology, at Cambridge, Massachusetts, in 1972, in partial fulfillment of the requirements for the degree of Doctor of Philosophy,

Skempton, A.W., "The Bearing Capacity of Clays," Proceedings, Building Research Congress, London, 1951, pp. 180-189.

Spencer, E., "A Method of Analysis of the Stability of Embankments Assuming Parallel Inter-Slice Forces," Geotechnique, London, England, Vol. 17, No. 1, March 1967, pp. 11-26.

Steiner, W., "Three-Dimensional Stability of Frictional Slopes," thesis presented to the Massachusetts Institute of Technology, at Cambridge, Massachusetts, in 1977, in partial fulfillment of the requirements for the degree of Master of Science.

Taylor, D.W., "Stability of Earth Slopes," Journal of the Boston Society of Civil Engineers, 1937, pp. 337-386.

Turnbull, W.J., and Hvorslev, M.J., "Special Problems in Slope Stability," Journal of the Soil Mechanics and Foundations Division, ASCE, Vol. 93, No. SM4, July 1967, pp. 499-528.

Thomson, W.T., Vibration Theory and Application, 3rd ed., Prentice Hall, Inc., Englewood Cliffs, New Jersey, 1965, pp. 324-325.

Vanmarcke, E.H., "Probabilistic Modeling of Soil Profiles," Journal of the Geotechnical Engineering Division, ASCE, Vol. 103, No. GT11, November 1977a, pp. 1227-1246.

Vanmarcke, E.H., "On the Reliability of Earth Slopes," Journal of the Geotechnical Engineering Division, ASCE, Vol. 103, No. GT11, November 1977b, pp.1247-1265.

Veneziano, D., Camacho, D.H., and Antoniano, J., "Three-Dimensional Models of Slope Stability," Research Report R77-17, No. 570, Department of Civil Engineering, Massachusetts Institute of Technology, Cambridge, Massachusetts, 1977, 42 p.

Whitman, R.V., and Bailey, W.A., "Use of Computers for Slope Stability Analysis," Journal of the Soil Mechanics and Foundations Division, ASCE, Vol. 93, No. SM4, July 1967, pp. 475-498.

Wissa et al., "Consolidation at Constant Rate of Strain," Journal of Soil Mechanics and Foundations Division, ASCE, Vol. 97, No. SM10, October 1971, pp. 1393-1413.

Wright, S.G., "A Study of Slope Stability and the Undrained Shear Strength of Clay Shales," thesis presented to the University of California, at Berkeley, in 1969, in partial fulfillment of the requirements for the degree of Doctor of Philosophy.

Wu, T.H., and Kraft, L.M., "Safety Analysis of Slopes," Journal of the Soil Mechanics and Foundations Division, ASCE, Vol. 96, No. SM2, March 1970, pp. 609-630.

Yucemen, M.S., Tang, W.H., and Ang, A.H-S, "A Probabilistic Study of Safety and Design of Earth Slopes," Technical Report No. 402, Department of Civil Engineering, University of Illinois, Urbana, 1973.

BIOGRAPHY

Amr Sayed Azzouz, son of Dr. and Mrs. Sayed Azzouz, was born in Cairo, Egypt on September 27, 1947. He attended high school in Maadi, Egypt. In 1964 he was a member of the American Field Service Exchange Program, where he spent one year in California and attended Lakewood High School, near Long Beach. After obtaining a Bachelor of Science in Civil Engineering from Cairo University in July 1970, he worked as a teaching associate at Cairo University for two years. His duties involved teaching several undergraduate fluid mechanics and hydraulics courses.

In 1972 he went to Northwestern University in Evanston, Illinois, and he obtained a Master of Science in Civil Engineering in August 1974, with a thesis entitled, "Statistical Analysis of Index Properties and Compressibility of Soils." During his stay at Northwestern he assisted in teaching two undergraduate fluid mechanics courses.

In 1974 he began his studies toward the degree of Doctor of Science at Massachusetts Institute of Technology. Since his arrival at M.I.T. he has been involved in geotechnical research and teaching.

In 1972 he married Ms. Moushira Rasmy, and they have a son, born in 1975.

His publications include:

"Statistical Evaluation of Soil Index Properties and Constrained Modulus" with R. B. Corotis and R. J. Krizek, Second International Conference on Application of Statistics and Probability in Soil and Structural Engineering, Aachen, Germany, 1975, pp. 273-294.

"End Effects on the Stability of Cohesive Slopes," with M. M. Baligh, Journal of the Geotechnical Engineering Division, ASCE, November, 1975, pp. 1105-1117.

"Regression Analysis of Soil Compressibility" with R. J. Krizek and R. B. Corotis, Soils and Foundations, 16(2), 1976, pp. 19-30.

"Consolidation Around Sand Drains in Non-Darcian Soils," with R. J. Krizek and H. A. Elnaggar, Acta Technica Academiae Scientarum Hungaricae, Tomus 82 (1-2), 1976, pp. 99-119.

"Design Charts for Three-Dimensional Stability of Cohesive Slopes Subjected to Surcharge Loads," with M. M. Baligh, Publication No. R76-19, Order No. 540, Department of Civil Engineering, Massachusetts Institute of Technology, Cambridge, Mass., 1976, 69 p.

"Stability of Vertical Corner Cut with Concentrated Surcharge Load," with M. M. Baligh, Journal of the Geotechnical Engineering Division, discussion, ASCE, December, 1976, pp. 1286-1288.

"Line Loads on Cohesive Slopes," with M. M. Baligh and C. C. Ladd, Ninth International Conference on Soil Mechanics and Foundation Engineering, Tokyo, 1977.

APPENDIX A

COMPUTER PROGRAM STAB3D

The computer program STAB3D* is capable of performing two-and three-dimensional stability analysis of arbitrary slopes by the method of slices. In two-dimensions, the shear surface is assumed to be a cylinder. In three-dimensions, two different types of shear surfaces can be used: a cone attached to a cylinder; and an ellipsoid attached to a cylinder. The two dimensional analysis can be performed according to one of three methods: the ordinary method of slices (Fellenius, 1936); the modified Bishop method (Bishop, 1955); and the MIT method described in Chapter 6. The three-dimensional analysis can only be performed according to the MIT method.

The program will locate the surface having the minimum factor of safety at each of a specified set of trial centers. Alternatively, a search routine is provided that can be useful in locating the center and shape of the critical failure surface. Explicitly defined surfaces can also be analyzed.

Analyses can be performed by either the total or the

---

*The two-dimensional option of STAB3D is based on the computer program No. EP-5A written by Reti, G. and Djou, K. (1969) for the Dames and Moore consulting firm.

effective stress method, depending on the input of appropriate soil strength properties.

This appendix gives the STAB3D user's manual. In this manual, each card or group of cards is identified by a name, the format used on the card(s), the meaning of the variables and notes.

A.1 USER'S MANUAL

1. IDENTIFICATION CARD (18A4)

Note	Columns	Entry
(1)	1 - 72	Enter the program heading information for use in labeling the output.

NOTES:

(1) Begin each new data case with a new identification card.

2. MASTER CONTROL CARDS

2.1 Card 1 (7F 10.3)

Note	Columns	Entry
(1)	1 - 10	Number of water lines.
(2)	11 - 20	Pore pressure definition code: Code = positive number equal to number of piezometric lines. Pore pressure is defined by piezometric level. Code = 0; pore pressure is defined by coefficient r_u given with two-dimensional soil properties data. Code = -1; pore pressure is defined by top flow line, given as the water line data.
(3)	21 - 30	Number of slope geometry lines.
(4)	31 - 40	Method of analysis: Code = 1; Ordinary Method of Slices Code = 2; Modified Bishop method Code = 3; MIT method
(5)	41 - 50	Type of analysis; Code = 0; two-dimensional analysis Code = 1; three-dimensional analysis
(6)	51 - 60	Data input code.
(7)	61 - 70	Unit weight of water: Code = 0; default set to 62.4 pcf.

NOTES:

(1) Number of water lines. This is a count of the number of lines used to define the water surface within and outside the slope. A maximum of 10 straight-line segments can be used to define the water surface.

(2) Pore pressure definition code. This code defines the method used to specify pore pressures in the slope. Three options are available:

Code = positive number; the pore pressure is defined by the piezometric level in the slope. For seepage through soils, the piezometric head is defined as pressure head. The pore pressure along any point on the failure circle is equal to the vertical distance from that

point to the piezometric line above that point (see Fig. A.1a). For this case, the code number is the count of the number of straight line segments used to define the piezometric level for the slope. A maximum of 10 straight-line segments can be used for this purpose.

Code = 0; the pore pressure is defined by the pore pressure ratio, r_u, given with the two-dimensional soil properties in Section 6 of this manual. r_u is equal to the ratio of the pore pressure within a soil layer to the total overburden stress applied to that layer, or:

$$r_u = \frac{u}{\gamma_t \cdot h}$$

where,

u = pore pressure

γ_t = total unit weight of the soil

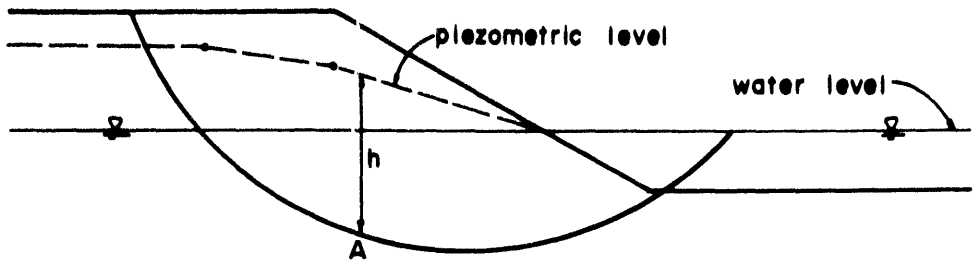
h = depth to point (see Fig. A.1b)

Code = - 1; the pore pressure is defined by the phreatic surface given with the water lines listed later in Section 3. The phreatic line corresponds to the top flow line of a flow net. Such a boundary flow line has the special characteristic that at all points of the line the pressure head is zero.

In the program the pore pressure at any point in the slope is computed as the unit weight of water multiplied by the vertical distance times the cosine squared of the slope of the phreatic line directly above the point in question. (See Fig. A.1c.) This is an approximation unless the phreatic line is a straight line. The error is usually on the conservative side for phreatic lines which curve down (concave down). The actual pore pressure for such a downward curving phreatic line is less than the one computed by the above described approximation. For an upward curving phreatic line, the approximation is less conservative than the actual condition, however, upward curving flow lines are relatively rare in slope seepage.

(3) Number of slope geometry lines. This is a count of the number of straight-line segments which will be used to define the slope geometry. A maximum of 80 lines can be used for this purpose. The slope geometry lines must include any water surface located outside the slope. Internal water lines must be included if the soil properties are different above and below the line.

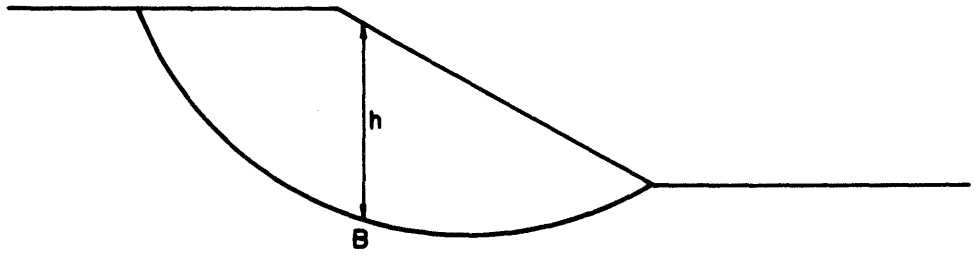
(4) Method of analysis. Two-dimensional analysis can be performed according to one of three methods; the Ordinary Method of Slices; the Modified Bishop method; and the MIT method. For a description of these methods including the limitations and the assumptions involved, the user is referred to Chapter 6. For three-dimensional problems, the analysis must be performed according to the MIT method, and hence a "3" must be specified in columns 31 to 40. If a different entry is specified, execu-



$u_A = \gamma_w h$

γ_w = unit weight of water

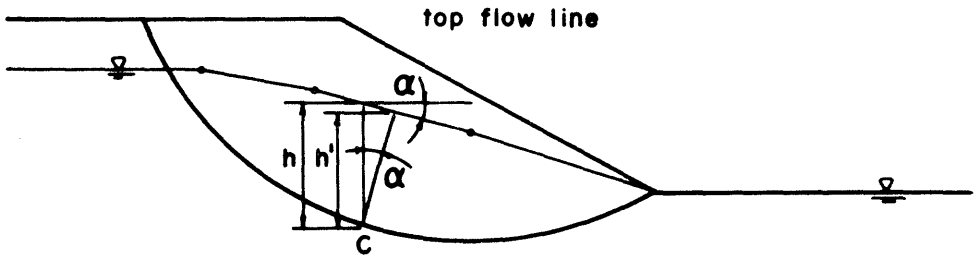
a) PORE PRESSURE SPECIFIED BY PIEZOMETRIC LEVEL



$u_B = r_u \gamma_t h$

γ_t = total weight of soil

b) PORE PRESSURE SPECIFIED BY PORE PRESSURE COEFFICIENT r_u



$u_c = \gamma_w h \cos^2\alpha = \gamma_w h'$

c) PORE PRESSURE SPECIFIED BY TOP FLOW LINE

Figure A.1 Pore Pressure Specification in STAB3D

tion of the program will terminate.

(5) Type of analysis. In running a three-dimensional analysis, the program STAB3D provides also the plane strain factor of safety, according to the MIT method, for each surface analyzed.

(6) Data input code. This code number allows the user to reanalyze a slope without reentering all the data from the previous problem:

Code = 1; all new data.

Code = 2; same water and piezometric lines. Other new data (after the end of Section 2, proceed to Section 5).

Code = 3; same water, piezometric lines, slope geometry data. After the end of Section 2, proceed to Section 6 to input the two-dimensional soil properties.

Code = 4; same water, piezometric lines, slope geometry and soil properties data. Proceed to Section 7 to input the variation of soil properties along the axis of the slope after the end of Section 2.

Code = 5; after the end of Section 2, proceed to Section 8 to input the cross-sectional variation data.

Code = 6; after the end of Section 2, proceed to Section 9 to input the line load data.

(7) Unit Weight of Water. This field is used to enter the unit weight of water if it is different from 62.4 pounds per cubic foot. This allows the use of different water unit weight to account for sea water, special fluids, etc., and to perform the slope stability analysis in the metric system. Since all other values on the input data are independent of the system of measurement, slope stability analyses to be performed in the metric system need only to have the unit weight of water adjusted to correspond to the units used throughout the rest of the analysis.

2.2 Card 2 (5F 10.3)

Note	Columns	Entry
(1)	1 - 10	Number of horizontal layers forming the slope.
	11 - 20	Offline plotting code: Code = 1; a deck of cards containing the data for plotting the end effects (F/F^0) vs. the normalized failure length (2L/DR) is punched. Code = 0; no data is punched.
	21 - 30	Online plotting code: Code = 1; an online plot of (F/F^0) vs. (2L/DR) is provided. Code = 0; no plot is obtained.
	31 - 40	Units code: Code = 1; data is given in ton-meter units. Code = 0; data is given in pound-foot units
	41 - 50	Strength anisotropy code: Code = 1; the strength of any soil layer within the soil deposit is anisotropic. Code = 0; the strength of all soil layers is isotropic.

NOTES:

(1) The maximum number of layers is equal to 30.

2.3 Card 3(7F 10.3)

Skip cards 3 and 4 of this section if running a two-dimensional analysis.

Note	Columns	Entry
(1)	1 - 10	z-coordinate at which the failure surface is centered.
(2)	11 - 20	The maximum z-coordinate of the embankment.
(2)	21 - 30	The minimum z-coordinate of the embankment.
(3)	31 - 40	Specified cylinder length (enter zero if the cylinder length is to be varied).
	41 - 50	Printing code: Code = 0; results are only printed for the shear surface yielding the minimum three-dimensional factor of safety. Code = 1; results are printed for all surfaces analyzed. Code = 2; results are printed for failure surfaces attached to a specific cylinder.
(4)	51 - 60	Cylinder number forming the shear surfaces for which the detailed information is printed (enter zero if code above is not equal to 2).
(5)	61 - 70	Number of different cross sections to be analyzed.

NOTES:

(1) For running three-dimensional analysis, the user must specify the z-coordinate, along the embankment axis, at which the failure surface is centered, z_c. This is particulary important for the case when the shear strength is varying along the axis of the embankment. In this case, z_c should be taken at a location where the shear strength is low. Different z_c locations will ultimately yield the location of the most critical shear surface.

(2) The user must also specify the maximum and minimum z-coordinates of the embankment, z_u and z_ℓ, respectively. The embankment length is then given by $z_u - z_\ell$.

Knowing z_ℓ, z_c and z_u, the three-dimensional analysis is carried out according to the following procedure:

a) half the cylinder length, ℓ_c, is allowed to vary between a minimum of zero and a maximum equal to the distance between z_c and the

closest end of the embankment. Within this distance 10 cylinders of varying lengths are considered.

b) The remaining distance between a given ℓ_c and the closest end of the embankment determines the range over which the length of the conical (or ellipsoidal) attachments vary. Within this distance, 10 cones (or ellipsoids) are considered.

c) For each combination of a cone (or ellipsoid) and a cylinder, STAB3D computes the three-dimensional factor of safety, F.

(3) STAB3D offers the user the option of specifying the cylinder length forming the three-dimensional shear surface. In this case, the cylinder length is set equal to the specified cylinder length and the cone (or ellipsoid) length is then varied according to the procedure described above.

(4) As was mentioned previously, 10 different cylinders are considered within the distance between z_c and the closest end of the embankment. These cylinders are numbered 1 to 10, with the number 1 assigned to the cylinder with zero length. When the printing code in columns 41 through 50 is 2, results are only printed for the failure surfaces consisting of one of the above cylinders plus the conical (or ellipsoidal) attachments. The user's selection of this cylinder number is entered in columns 51 through 60.

(5) This entry is provided for the analysis of embankments of varying cross sections. STAB3D has the capability of analyzing embankments with a maximum of two different cross sections.

2.4 Card 4 (3F 10.3)

Skip this card if running a two-dimensional analysis.

Note	Columns	Entry
(1)	1 - 10	Number of segments dividing the failure surface in the third dimension (leave blank if equals 20).
	11 - 20	Code for strength variation along the embankment axis: Code = 1; strength of any layer is nonuniform. Code = 0; strength of all layers is uniform.
(2)	21 - 30	Code for line load variation along the embankment axis: Code = 1; line load is varying. Code = 0; no variation in the line load.

NOTES:

(1) This is equivalent to the number of slices in two-dimensional analysis. Results in Chapter 3 show that good results are obtained when 20 segments are used.

(2) This option allows the user to input line loads of finite length.

3. WATER LINE DATA

Proceed to Section 5 if number of water lines (Section 2) is equal to 0.

3.1 Card 1 (5F 10.3)

Note	Columns	Entry
(1)	1 - 10	Line number.
	11 - 20 21 - 30	x and y coordinates of the left point of the line.
	31 - 40 41 - 50	x and y coordinates of the right point of the line.

NOTES:

(1) The x and y coordinates of the ends of straight-line segments defining the water line within and outside the slope are entered in this section of the manual. The number of water lines to be used must be equal to the line count given on Card 2.1. No vertical water lines are allowed but very steeply inclined lines (slopes up to 1 horizontal to 10 vertical) can be used to approximate near vertical lines. Water line segments can intersect the other types of lines (such as piezometric lines or soil geometry lines) in the slope. Water line limits should extend far enough left and right to allow for the analysis of large circles extending in each direction. Enter as many cards as there are water lines (maximum = 10).

4. PIEZOMETRIC LINE DATA

Proceed to Section 5 if pore pressure definition code (Section 2) is 0 or -1.

4.1 Card 1 (5F 10.0)

Note	Columns	Entry
(1)	1 - 10	Line number.
	11 - 20 21 - 30	x and y coordinates of the left point of the line.
	31 - 40 41 - 50	x and y coordinates of the right point of the line.

NOTES:

(1) If a positive "Pore Pressure Definition Code" was used in Card 2.1, then the x and y coordinates of the ends of straight-line segments defining the piezometric line are entered in this section. The number of piezometric line segments must be equal to the line count given on Card 2.1. Again, no vertical lines are allowed but near vertical lines can be used (see Section 3). Piezometric line segments should extend across the entire slope geometry and can be located above the slope surface, if necessary. The height of the piezometric line should correspond to the pressure head of water in the slope based on the unit weight of water given on Card 2.1. Enter as many cards as there are piezometric lines (maximum = 10).

5. SLOPE GEOMETRY DATA

5.1 Card 1 (7F 10.0)

Note	Columns	Entry
(1)	1 - 10	Line number.
	11 - 20	x and y coordinates of the left point of the line
	21 - 30	
	31 - 40	x and y coordinates of the right point of the line.
	41 - 50	
	51 - 60	Soil number laying above this line.
	61 - 70	Soil number laying below this line.

NOTES:

(1) The x and y coordinates of the ends of straight-line segments used to define the slope geometry are recorded in this section of the manual. Up to 80 lines can be used to specify slope geometry. The x and y coordinate system should be established so that the entire slope is located along positive values of the coordinate system and that the slope fails by rotation in the counter-clockwise direction. No slope geometry lines should intersect one-another and no vertical lines can be used. Vertical lines can be approximated by near vertical lines (inclined approximately 10 vertical to 1 horizontal). The slope geometry lines need not be listed in any particular order. Enter as many cards as there are lines (maximum = 80).

6. TWO-DIMENSIONAL SOIL PROPERTIES

Data for each soil layer is given on two cards. Enter as many two-card sets as there are soil layers (maximum = 30).

6.1 Card 1 (7F 10.3)

Note	Columns	Entry
	1 - 10	Layer number.
	11 - 20	Total unit weight of soil.
	21 - 30	Friction angle of soil, in degrees.
(1)	31 - 40	Strength parameter a.
(1)	41 - 50	Strength parameter d.
(1)	51 - 60	Strength parameter e.
(2)	61 - 70	Angle between the failure plane and the major principal plane at failure.

NOTES:

(1) Strength anisotropy is treated in STAB3D according to the Davis and Christian model described in Chapter 5. The input parameters needed are:

$$a = 1/2[s_u(V) + s_u(H)]$$

$$d = 1 - b^2/a^2$$

$$e = (1 - K_s)/(1 + K_s)$$

where

$s_u(V)$ = undrained shear strength for plane strain compression shear

$s_u(H)$ = undrained shear strength for plane strain extension shear

$K_s = s_u(H)/s_u(V)$

$b/a = \dfrac{s_u(45°)}{\sqrt{s_u(V) \cdot s_u(H)}}$, where $s_u(45°) = s_u$ for plane strain shear with $i = 45°$.

For the case of isotropic strength enter a = isotropic strength and d = e = 0. Similarly, for frictional material, enter a = cohesion intercept, $\underline{c}$ and d = e = 0.

(2)This is the angle needed to relate the inclination of the failure surface to the angle which the major principal stress at failure makes with the vertical.

6.2 Card 2 (2F 10.3)

Note	Columns	Entry
	1 - 10	Pore pressure ratio, r_u.
(1)	11 - 20	Ratio of longitudinal effective stress to vertical effective stress (leave blank if running a two-dimensional analysis, or if layer has $\phi = 0$ and $c = s_u$)

NOTES:

(1) For frictional materials ($\phi \neq 0$), the shear strength depends on the normal stress on the failure plane at failure. In two dimensions, the MIT method assumes that the vertical overburden stress is a major, or minor, principal stress at failure depending on whether the inclination of the base of the slice is positive or negative, respectively (see Chapter 6 for details). In three-dimensions, the longitudinal (out-of-plane) effective stress, $\bar{\sigma}_\ell$, is also assumed to be a principal stress and given by the ratio $K(= \bar{\sigma}_\ell/\bar{\sigma}_v)$. This completely defines the principal stress tensor, and hence the normal effective stress on the base of the failure surface, $\bar{\sigma}_N$, can be easily computed. This $\bar{\sigma}_N$ can then be used in conjunction with the Mohr-Coulomb criterion to determine the shear strength.

Go to next section if only one cross section is to be analyzed, otherwise input soil properties for Section 2. In this case, the user needs to input data only for layers whose properties differ between cross sections 1 and 2 according to the format described above. Two blank cards indicate the end of the data.

7. THREE-DIMENSIONAL SOIL PROPERTIES

Skip this section if running a two-dimensional analysis or if there is no variation of the strength along the axis of the slope (Section 2.4). Data for the strength variation of each layer is given in two groups. Input as many groups as there are layers.

7.1 Group 1 (only 1 card, 7F 10.3)

Note	Columns	Entry
	1 - 10	Layer number
(1)	11 - 20	Number of data points describing the variation of the shear strength along the axis of the embankment.
(2)	21 - 30	Code indicating whether data expressing the variation of the strength for this layer is given or generated from data for the previous layer: Code = 0; data is given. Code = 1; data is generated from that for the previous layer.
	31 - 40	Scaling factor used to adjust the strength parameter "a" generated from the previous layer. Leave blank if code in columns 21 - 30 is 0.
	41 - 50	Scaling factor used to adjust the strength parameter "d" generated from the previous layer. Leave blank if code in columns 21 - 30 is 0.
	51 - 60	Scaling factor used to adjust the strength parameter "e" generated from the previous layer. Leave blank if code in columns 21 - 30 is 0.

NOTES:

(1) The strength variation is taken into consideration by inputing a curve of shear strength vs. the distance z along the embankment axis for each soil layer. A maximum of 15 points can be used to describe each curve.

(2) The data describing the variation of the strength for a particular layer can be generated from data for a previous layer. The generated data points for any layer will have the same values of the coordinate z and the strength parameters a, d and e as those of the previous layer. The user can then use the scaling factors in columns 31 through 60 to adjust the values of the generated a, d, and e. The user, however, must give the data for the first layer.

7.2 Group 2

Skip this group of cards if code in columns 21 - 30 is 1, i.e., data describing the strength variation for this layer is generated from data for the previous layer.

Card 1 (4F 10.3)

Note	Columns	Entry
	1 - 10	z-coordinate of 1st point.
	11 - 20	Value of "a" at 1st point.
	21 - 30	Value of "d" at 1st point.
	31 - 40	Value of "e" at 1st point.

Card 2 (4F 10.3)

Note	Columns	Entry
(1)	1 - 10	z-coordinate of 2nd point.
	11 - 20	Value of "a" at 2nd point.
	21 - 30	Value of "d" at 2nd point.
	.. ..	.. ..

NOTES:

(1) Input as many cards as required to fully describe the strength variation of this layer (maximum = 15).

8. CROSS-SECTIONAL VARIATION

Skip this section if there is no variation in cross sections, i.e., the number of different cross sections to be analyzed (Card 2.3) equals 1. Data for the cross-sectional variation is given in two groups.

8.1 Group 1 (only 1 card, F 10.3)

Note	Columns	Entry
(1)	1 - 10	Number of data points describing the cross-sectional variation.

NOTES:

(1) As was mentioned previously, STAB3D is capable of analyzing the stability of embankments with variable cross sections. A maximum of two different cross sections can be handled in STAB3D. The central cross section is given the number 1 and the other cross section the number 2. The user has to input the curve describing the cross-sectional variation. This is achieved by inputing a z-coordinate and the cross section number corresponding to this z. A maximum of 10 points can be used to describe the variation.

8.2 Group 2

Card 1 (6F 10.3)

Note	Columns	Entry
	1 - 10	z-coordinate of 1st point.
	11 - 20	Cross section number at 1st point (either 1 or 2).
	21 - 30	z-coordinate of 2nd point.
	31 - 40	Cross section number at 2nd point.
	41 - 50	z-coordinate of 3rd point.
	51 - 60	Cross section number at 3rd point.

Card 2 (6F 10.3)

Note	Columns	Entry
(1)	1 - 10	z-coordinate of 4th point.
	11 - 20	Cross section number at 4th point
	.. ..	

NOTES:

(1) Input as many cards as required to describe the cross-sectional variation, three points per card.

9. LINE LOADS

Data for line loads are given in three groups.

9.1 Group 1 (only 1 card, F 10.3)

Note	Columns	Entry
(1)	1 - 10	Number of line loads.

NOTES:

(1) A maximum of 12 line loads can be used. Proceed to Section 10 if number of line loads = 0.

9.2 Group 2 (only 1 card, 5F 10.3)

Enter as many group 2 and 3 cards as there are column loads.

Note	Columns	Entry
	1 - 10	x-coordinate of the load
	11 - 20	Value of the load: if using pound-foot units, enter the value of the load in kips, if using ton-meter units, enter the value of the load in tons.
(1)	21 - 30	Number of data points describing the variation for this load along the z-axis.
	31 - 40	Code indicating whether data for this load is given or generated from data for the previous load: = 0; data is given for this load, = 1; data is generated.
	41 - 50	Scaling factor to adjust the magnitude of the generated load.

NOTES:

(1) This option is provided to allow the user to input line loads of finite length (Card 2.4). This is achieved by inputing the line load as a function of the distance along the embankment axis. A maximum of 10 points can be used to describe this.

IF CODE IN COLUMNS 21 - 30 OF CARD 2.4 IS EQUAL TO ZERO, LEAVE COLUMNS 21 - 50 BLANK AND GO BACK TO GROUP 9.1 TO INPUT THE DATA FOR THE NEXT LINE LOAD.

9.3 Group 3

Skip this group if code in columns 31 - 40 is equal to 1.

Card 1 (6F 10.3)

Note	Columns	Entry
	1 - 10	z-coordinate of 1st point.
	11 - 20	Value of load at point 1.
	21 - 30	z-coordinate of 2nd point.
	31 - 40	Value of load at point 2.
	------	.. ..
	51 - 60	Value of load at point 3.

Card 2 (6F 10.3)

Note	Columns	Entry
(1)	1 - 10	z-coordinate of 4th point.
	.. ..	.. ..

NOTES:

(1) Input as many cards to fully describe the vairation of each line load, 3 points per cards and a maximum of 10 points.

10. ANALYSIS INFORMATION

Card 1 (F 10.3)

Note	Columns	Entry
(1)	1 - 10	Mode of program operation.

NOTES:

(1) The slope stability analysis can be performed using the various degrees of program control. The computer can be instructed to analyze the stability of a single circle (in two-dimensions) or of a series of single circles, the data for each of which is given by the user. Conversely, the user can instruct the computer to automatically locate the minimum factor of safety for the slope. The following four options are available:

Option 1. Single Circle Analysis

The user provides the computer with a series of circle centers and radii. The computer analyzes these circles one at a time in turn and prints the factor of safety for each specified circle. To use this option, enter Mode of program operation = 1 and list the centers and radii you wish to analyze in Section 10.1 of this manual. The number of circles which can be analyzed in this manner is unlimited.

Option 2. Single-Center--Automatic Radius Variations

Here, the user specifies a center and the upper and lower boundaries between which he wishes the computer to vary the radii of the circles to be analyzed. The engineer also specifies the radius change increments to be used to cover the distance between the two radius boundaries. To use this option, enter "2" for mode of program operation (Section 10) and record the x and y coordinates of the center, the radius boundaries and radius increments in Section 10.2. (Again, the number of analyses using this option is unlimited.)

Option 3. Automatic Center and Radius Variations.

Here, both the center locations and the circle radii are varied automatically by the computer. The circle center locations are moved within the boundaries of a predetermined rectangular search area (centers located on the boundary line of the search area are also included in the analysis). The circle radii are varied between upper and lower boundaries--as described above. To use this option, enter mode of program operation Number "3" (Section 10). Record the x and y coordinates of the boundaries of the circle center search area, the desired spacing of the circle centers, the y coordinates of the horizontal lines which will be the upper and lower boundaries of the radii and record the step size by which the radii are to be changed in Section 10.3.

Option 4. Automatic Search for Minimum FS

To use this option, enter Mode of program operation Number "4" (Section 10). In Section 10.4, the user specifies a starting point for the "search." The search proceeds in a series of "steps" with the first one starting in a "northeast" direction. The initial search step size to be used has to be specified by the user in Section 10.4. The search continues until a circle center whose FS is smaller than the FS of the 4 centers which surround it is located. If the factor of safety "tolerance" specified in Section 10.4 of the manual is not satisfied at this point, the search continues with a reduced step interval. If the maximum number of trials specified is reached before a satisfactory factor of safety is found, the search is discontinued. For this version of STAB3D, three-dimensional analysis can only be performed according to Option 2. For each center, the difference between the maximum and minimum radii specified in Section 10.2 is divided by the number of segments given on Card 2.4 to determine the value of the radius change increment.

In addition, the user can also select to print out the detailed computations of the analysis of the stability of a particular surface. These options are only available for the two-dimensional analysis. Their use is described in more detail below.

Printout Options

The following three options are available for specifying the amount of detail to be printed regarding the search procedure used by the computer in locating the minimum factor of safety:

1. Printout Option (1) Print all the data used in the analyses and the final result of the search for the minimum factor of safety.

2. Printout Option (2) Print all the data used in the analyses, the minimum factor of safety obtained for each circle center after having varied the radius, and the final results of the search for the minimum factor of safety.

3. Printout Option (3) Print all data used in the analyses, and the factor of safety computed for each center and for each radius examined during the analysis. Finally, print the final results of the search in terms of the minimum factor of safety obtained for the slope.

Analysis Output Options

The following two options are available to specify the amount of detail to be printed regarding the analysis of each circle:

1. Analysis Option (0) For each circle it analyzes, the computer prints a one-line entry which displays basic information about the circle. This information includes the location and radius of the circle, the computed factor of safety and as much additional data as can be displayed on one printed line.

2. Analysis Option (1) This option produces a detailed printout of the computations used to analyse the critical circle, and

detailed information is printed about each soil slice. The computer also prints the overall driving and resisting components for each circle segment located within a particular soil layer and for the entire critical circle. Finally, this option also displays the iteration procedure (for the Modified Bishop method) for converging on the final factor of safety for the critical circle. This option produces several pages of output for the critical circle. It should be used when the computer calculation is to be checked manually. It should be noted that these printout and analysis options are only valid for two-dimensional analyses. Printout options for three-dimensional analyses are given on Card 2.2.

The following table summarizes the output options which are available:

Printout/ Analysis	Analysis Option (0)	Analysis Option (1)
Printout Option (1)	Data + Results for Critical Circle	Data + Details of Analysis for Critical Circle
Printout Option (2)	Data + Minimum FS for Each Center	Data + Minimum FS for Each Center Details of Analysis for Critical Circle
Printout Option (3)	Data + FS for all Circles Analyzed	Data + FS for all Circles Analyzed Details of Analysis for Critical Circle

10.1 Mode Number 1

Card 1 (6F 10.3)

Note	Columns	Entry
	1 - 10	Center number.
	11 - 20	Radius number.
	21 - 30	x coordinate of the center.
	31 - 40	y coordinate of the center.
	41 - 50	Radius of the circle.
	51 - 60	Analysis option code (see Section 10).

Enter as may cards as the number of centers to be analyzed. A blank card indicates the end of the analysis.

Proceed to Section 11.

10.2 Mode Number 2

Card 1 (7F 10.3)

Note	Columns	Entry
	1 - 10	Center number.
	11 - 20	Leave blank.
	21 - 30	x and y coordinates of center.
	31 - 40	
	41 - 50	Maximum radius.
	51 - 60	Minimum radius.
	61 - 70	Radius change increment.

Card 2 (F 10.3)

Note	Columns	Entry
	1 - 10	Analysis option code (see Section 10).

Enter as many two-card groups as there are centers to be analyzed. Two blank cards indicate the end of the analysis.

Proceed to Section 11.

10.3 Mode Number 3

Card 1 (7F 10.3)

Note	Columns	Entry
	Boundaries of circle center variation zone.	
	1 - 10	Minimum x
	11 - 20	Maximum x
	21 - 30	Minimum y.
	31 - 40	Maximum y.
	Variation step increment.	
	41 - 50	x increment.
	51 - 60	y increment.
	61 - 70	Enter the number 1.

Card 2 (5F 10.3)

Note	Columns	Entry
	1 - 10	y coordinate of tangent to maximum radius.
	11 - 20	y coordinate of tangent to minimum radius.
	21 - 30	Radius change increment
	31 - 40	Printout option code (see Section 10).
	41 - 50	Analysis option code.

Proceed to Section 11.

10.4 Mode Number 4

Card 1 (6F 10.3)

Note	Columns	Entry
	1 - 10	Maximum number of centers (max. 40).
		Search starting coordinates
	11 - 20	x coordinate.
	21 - 30	y coordinate.
		Initial search step
	31 - 40	x increment.
	41 - 50	y increment.
	51 - 60	Factor of safety tolerance.

Card 2 (5F 10.3)

Note	Columns	Entry
	1 - 10	y coordinate of tangent to maximum radius.
	11 - 20	y coordinate of tangent to minimum radius.
	21 - 30	Radius change increment.
	31 - 40	Printout option code (see Section 10).
	41 - 50	Analysis option code (see Section 10).

11. END OF INFORMATION

Note	Columns	Entry
	1 - 10	End of Job Code: Code = 1; another problem follows. Code = 2; all analyses completed.